

JAPANESE CONTRIBUTIONS TO IAEA INTOR WORKSHOP,  
PHASE TWO A, PART 3  
CHAPTER VI : ELECTROMAGNETICS

February 1988

Masao KASAI<sup>\*1</sup>, Bunko IKEDA<sup>\*2</sup>, Ryuta SAITO<sup>\*2</sup>, Toshinari ANDO  
Noboru FUJISAWA, Mitsuru HASEGAWA<sup>\*2</sup>, Takashi HASHIZUME<sup>\*3</sup>  
Toshio IDA<sup>\*1</sup>, Fumio IIDA<sup>\*4</sup>, Hiromasa IIDA, Akihisa KAMEARI<sup>\*1</sup>  
Masayuki KONNO<sup>\*5</sup>, Fushiki MATSUOKA<sup>\*6</sup>, Nobuharu MIKI  
Shigetomo NAKAGAWA<sup>\*3</sup>, Hideo NAKAJIMA, Masana NISHIKAWA<sup>\*1</sup>  
Kanji OTA<sup>\*2</sup>, Kichiro SHINYA<sup>\*7</sup>, Shohei SUZUKI<sup>\*4</sup>, Eisuke TADA  
Shigeru TADO<sup>\*2</sup>, Katsuyoshi TOYODA<sup>\*2</sup>, Toshihide TSUNEMATSU  
Koju UEDA<sup>\*2</sup>, Yoshihiro WACHI<sup>\*7</sup>, Masao YAMADA, Minoru YAMANE<sup>\*2</sup>  
and Kiyoshi YOSHIDA

JAERI-M レポートは、日本原子力研究所が不定期に公刊している研究報告書です。  
入手の間合わせは、日本原子力研究所技術情報部情報資料課（〒319-11茨城県那珂郡東海村）あて、お申しこしください。なお、このほかに財団法人原子力弘済会資料センター（〒319-11 茨城県那珂郡東海村日本原子力研究所内）で複写による実費頒布をおこなっております。

JAERI-M reports are issued irregularly.

Inquiries about availability of the reports should be addressed to Information Division  
Department of Technical Information, Japan Atomic Energy Research Institute, Tokai-mura, Naka-gun, Ibaraki-ken 319-11, Japan.

©Japan Atomic Energy Research Institute, 1988

編集兼発行 日本原子力研究所  
印 刷 いばらき印刷(株)

JAPANESE CONTRIBUTIONS TO IAEA INTOR WORKSHOP

PAHSE TWO A PART 3

CHAPTER VI : ELECTROMAGNETICS

Masao KASAI<sup>\*1</sup>, Bunko IKEDA<sup>\*2</sup>, Ryuta SAITO<sup>\*2</sup>  
Toshinari ANDO<sup>+1</sup>, Noboru FUJISAWA, Mitsuru HASEGAWA<sup>\*2</sup>  
Takashi HASHIZUME<sup>\*3</sup>, Toshio IDA<sup>\*1</sup>, Fumio IIDA<sup>\*4</sup>  
Hiromasa IIDA, Akihisa KAMEARI<sup>\*1</sup>, Masayuki KONNO<sup>\*5</sup>  
Fushiki MATSUOKA<sup>\*6</sup>, Nobuharu MIKI, Shigetomo NAKAGAWA<sup>\*3</sup>  
Hideo NAKAJIMA<sup>+1</sup>, Masana NISHIKAWA<sup>\*1</sup>, Kanji OTA<sup>\*2</sup>  
Kichiro SHINYA<sup>\*7</sup>, Shohei SUZUKI<sup>\*4</sup>, Eisuke TADA<sup>+1</sup>  
Shigeru TADO<sup>\*2</sup>, Katsuyoshi TOYODA<sup>\*2</sup>, Toshihide TSUNEMATSU<sup>+1</sup>  
Koju UEDA<sup>\*2</sup>, Yoshihiro WACHI<sup>\*7</sup>, Masao YAMADA  
Minoru YAMANE<sup>\*2</sup> and Kiyoshi YOSHIDA<sup>+1</sup>

Department of Large Tokamak Research  
Naka Fusion Research Establishment  
Japan Atomic Energy Research Institute  
Naka-machi, Naka-gun, Ibaraki-ken

(Received January 11, 1988)

This report corresponds to Chapter VI of Japanese contributions to IAEA INTOR Workshop, Phase Two A, Part 3, and consists of two parts, i.e. Critical Issues and Innovations. The critical issues contains the analyses on poloidal field coils, operation scenario, closed loop plasma control and plasma disruptions. The innovations contains feasibility studies on high current density and high field for TF coil, use of Nb<sub>3</sub>Sn for PF coils, forced flow subcooled He II superconducting coils, allowable

---

+1 Department of Thermonuclear Fusion Research

\*1 Mitsubishi Atomic Power Industries, Inc.

\*2 Mitsubishi Electric Corporation

\*3 Kawasaki Heavy Industry, Ltd.

\*4 Hitachi, Ltd.

\*5 Fuji Electric Corporation, Ltd.

\*6 Mitsubishi Heavy Industries, Ltd.

\*7 Toshiba Corporation

stresses in the structural material of the magnetic system and non-metallic structural materials, and design guidelines of toroidal field coil sizing.

Keywords: INTOR, Critical Issues, Innovations, PF Coil, Operation Scenario, Closed Loop Plasma Control, Plasma Disruptions, TF Coil, Nb<sub>3</sub>Sn PF Coil, Forced Flow Subcooled He II Coil, Non-metallic Structural Materials, Design Guidelines of TF Coil

I A E A I N T O R ワークショップ，  
フェーズⅡA，パート3 報告書  
第Ⅵ章 電磁過渡現象解析及びマグネット

日本原子力研究所那珂研究所臨界プラズマ研究部

笠井 雅夫<sup>\*1</sup>・池田 文構<sup>\*2</sup>・斎藤 龍太<sup>\*2</sup>・安藤 俊就<sup>+1</sup>  
藤沢 登・長谷川 満<sup>\*2</sup>・橋爪 隆<sup>\*3</sup>・井田 俊雄<sup>\*1</sup>  
飯田 文雄<sup>\*4</sup>・飯田 浩正・亀有 昭久<sup>\*1</sup>・今野 雅行<sup>\*5</sup>  
松岡 不識<sup>\*6</sup>・三木 信晴・中川 茂友<sup>\*3</sup>・中嶋 秀夫<sup>+1</sup>  
西川 正名<sup>\*1</sup>・太田 完治<sup>\*2</sup>・新谷 吉郎<sup>\*7</sup>・鈴木 昌平<sup>\*4</sup>  
多田 栄介<sup>+1</sup>・田戸 茂<sup>\*2</sup>・豊田 勝義<sup>\*2</sup>・常松 俊秀<sup>+1</sup>  
上田 孝寿<sup>\*2</sup>・和智 良裕<sup>\*7</sup>・山田 政男・山根 実<sup>\*2</sup>  
吉田 清<sup>+1</sup>

(1988年1月11日受理)

本報告書はIAEA主催のINTORワークショップ，フェーズⅡA，パート3における日本の報告書の第Ⅵ章に相当するものであり，クリティカルイッシュとイノベーションの節から成っている。クリティカルイッシュでは，ポロイダルコイルに関する解析，オペレーションシナリオ，プラズマのフィードバック制御，およびディスラプション解析について述べられている。またイノベーションでは，トロイダルコイルの高電流密度化，高磁場化の検討，ポロイダルコイルへのNb<sub>3</sub>Snの適用性検討，サブクールHeⅡの強制循環冷却コイルの検討，コイル支持材の許容応力の検討，非金属構造材の可能性，トロイダルコイル寸法に関するデザインガイドラインについてまとめられている。

---

那珂研究所：〒311-01 茨城県那珂郡那珂町大字向山801-1

+1 核融合研究部

\*1 三菱原子力工業（株）

\*2 三菱電機（株）

\*3 川崎重工業（株）

\*4 （株）日立製作所

\*5 富士電機（株）

\*6 三菱重工業（株）

\*7 （株）東芝

## Contents

I. Critical Issues .....	1
1. Poloidal Field Coils .....	1
1.1 Benchmark Calculation for Static Plasma Equilibrium (A. Kameari, M. Kasai) .....	1
1.2 Comparative Studies on Single null (SND) versus Double null (DND) Poloidal Divertors (N. Fujisawa) .....	14
1.3 Some Features with the TNS Plasma Equilibrium (K. Ueda) ...	20
2. Operation Scenario Analysis .....	28
2.1 Analyses of the quasi steady state operation scenario (M. Kasai, T. Ida, M. Nishikawa, A. Kameari) .....	28
2.2 Comparison of the PF coil system requirements for vertical and horizontal accesses (M. Kasai) .....	30
3. Closed Loop Plasma Control .....	33
3.1 Stability analysis by deformable plasma (T. Tsunematsu, M. Kasai) .....	33
3.2 Development of analysis code for plasma current, position and shape (PCPS) control system (A. Kameari, B. Ikeda) .....	39
3.3 Simulation studies on plasma position control for the next generation tokamak machines with up-down asymmetry (M. Kasai, A. Kameari, F. Matsuoka, K. Shinya, H. Iida, N. Fujisawa) .....	53
3.4 Estimation of AC losses in cryogenic structures generated with plasma vertical position control (M. Kasai, F. Matsuoka, A. Kameari) .....	74
3.5 Effect of ferromagnetic steel on plasma position control (A. Kameari) .....	83
3.6 Review of control experimental results (A. Kameari) .....	86
3.7 Electromagnetic measurements of plasma (K. Ota, M. Kasai) .....	91
4. Plasma Disruptions .....	94
4.1 Analyses of the loop voltages on PF coil induced at plasma disruptions (M. Kasai, A. Kameari) .....	94
4.2 Analyses of a coil quench (PF and TF) triggered by plasma disruption (M. Hasegawa, M. Yamane, R. Saito, K. Toyoda, B. Ikeda) .....	97

4.3	Protection by shunt resistor for JFT-2M vacuum vessel against disruptions (M. Kasai, M. Yamada)	111
II.	Innovations	113
1.	High Current Density and High Field for Toroidal Field Coil (S. Suzuki, K. Toyoda, F. Iida, N. Miki, T. Ando)	113
1.1	General guidelines for INTOR TF coil design	113
1.2	Generalized graph to select current density	119
1.3	Conductor and coil manufacturing	123
1.4	Analysis of quench protection	124
2.	The Use of Nb <sub>3</sub> Sn for PF Coils (K. Toyoda, N. Miki, T. Ando)	130
2.1	Basic conditions for design of central solenoid (OH) coils	130
2.2	Conductor design	130
2.3	OH coil design	134
2.4	OH coil design criteria	137
3.	Forced Flow Subcooled HeII Superconducting Coils (FFSSC) (Y. Wachi, N. Miki, E. Tada)	138
3.1	Non-copper critical current density	138
3.2	Conductor design	141
3.3	Comparison of cooling system	146
3.4	Conclusions	147
4.	Design Guidelines of Toroidal Field Coil Sizing (R. Saito, B. Ikeda, S. Tado, N. Miki)	148
4.1	Formulation of TF coil	148
4.2	Feasibility study of the wedging support TF coil	164
4.3	Design guidelines for TF coil sizing	174
5.	Allowable Stresses in the Structural Material of the Magnetic System (T. Hashizume, N. Miki, K. Yoshida, H. Nakajima)	177
6.	Non-metallic Structural Materials (T. Hashizume, S. Nakagawa, M. Kasai, A. Kameari, N. Miki, K. Yoshida)	186
6.1	Study of the application of non-metallic structural materials in the magnet systems	186
6.2	Proposal of composites with required properties	191
6.3	Advantages of non-metallic structural materials for INTOR	203
6.4	Applicability of FRP to magnet component	204

## 目 次

I. クリティカルイッシュ	1
1. ポロイダル磁場コイル	1
1.1 プラズマ平衡のベンチマーク計算 (亀有, 笠井)	1
1.2 シングルヌル, ダブルヌルダイバータの比較 (藤沢)	14
1.3 TNSプラズマ平衡 (上田)	20
2. オペレーション シナリオ解析	28
2.1 非定常オペレーション シナリオ解析 (笠井, 井田, 西川, 亀有)	28
2.2 垂直, 水平アクセスに対する PF コイル系の比較 (笠井)	30
3. プラズマ制御	33
3.1 デフォーマブル プラズマモデルによる安定性解析 (常松, 笠井)	33
3.2 プラズマ電流, 位置, 形状制御系のコード開発 (亀有, 池田)	39
3.3 プラズマ位置制御のシミュレーション (笠井, 亀有, 松岡, 新谷, 飯田, 藤沢)	53
3.4 極低温構造材中の AC ロス (笠井, 松岡, 亀有)	74
3.5 プラズマ位置制御に対する磁性鋼の効果 (亀有)	83
3.6 プラズマ制御実験結果のまとめ (亀有)	86
3.7 プラズマ電磁気計測 (太田, 笠井)	91
4. プラズマディスラプション	94
4.1 PF コイルの 1 ターン誘起電圧 (笠井, 亀有)	94
4.2 コイルクエンチ解析 (長谷川, 山根, 斎藤, 豊田, 池田)	97
4.3 シャント抵抗体による JFT-2 M 真空容器の保護 (笠井, 山田)	111
II. イノベーション	113
1. 超電導トロイダル磁場コイルの高磁場, 高電流密度化の検討 (鈴木, 豊田, 飯田, 三木, 安藤)	113
1.1 トロイダル磁場コイル設計上の考察点	113
1.2 電流密度の選定法	119
1.3 導体, コイル製作上の問題点	123
1.4 クエンチ保護解析	124
2. ポロイダル磁場コイルへの Nb <sub>3</sub> Sn の適用 (豊田, 三木, 安藤)	130
2.1 コイル設計の基本条件	130
2.2 導体設計	130
2.3 コイル設計	134
2.4 INTOR OH コイルの電流密度設計基準	137
3. He II 冷却超電導コイルの検討 (和智, 三木, 多田)	138



3.1	超電導材料の臨界電流密度比較 .....	138
3.2	He I, He II 冷却導体の電流密度 .....	141
3.3	冷却系 (He I, He II) の比較 .....	146
3.4	結 論 .....	147
4.	トロイダル磁場コイル支持方式の検討 (斎藤, 池田, 田戸, 三木) .....	148
4.1	バックリングシリンダ方式とウェッジ方式の比較 .....	148
4.2	ウェッジ支持方式の検討 .....	164
4.3	INTOR TF コイルの電流密度設計基準 .....	174
5.	マグネット支持構造材の許容応力 (橋爪, 三木, 吉田, 中嶋) .....	177
6.	非金属構造材応用 (橋爪, 中川, 笠井, 亀有, 三木, 吉田) .....	186
6.1	マグネット系への非金属構造材の適用検討 .....	186
6.2	適用上の問題点 .....	191
6.3	適用上期待される効果 .....	203
6.4	結 論 .....	204

## I. CRITICAL ISSUES

## 1. Poloidal Field Coils

## 1.1 Benchmark Calculation for Static Plasma Equilibrium

The benchmark problems for static plasma defined at the INTOR workshop (10-21, March 1986) are calculated by the MHD equilibrium calculation code 'EQUICIR'[1]. In this code, coil currents are calculated by the minimization of the following object function in the iteration of the equilibrium calculation.

$$J = \sum_{i=1}^{Np} w_i^p \{ \psi(r_i, z_i) - \psi^s \}^2 + w_{null}^R \left( \frac{\partial \psi}{\partial r} \right)_{null}^2 + w_{null}^Z \left( \frac{\partial \psi}{\partial z} \right)_{null}^2 + \mu_0^2 \sum_{j=1}^{NC} w_j^I I_j^2 \quad (1.1)$$

The  $(r_i, z_i)$ 's are positions fit to plasma surface. The flux function is given by,

$$\psi(r, z) = \psi_p(r, z) + \sum_{j=1}^{NC} \phi_j(r, z) I_j \quad (1.2)$$

here,  $\psi_p$ ,  $\phi_j$  and  $I_j$  are plasma flux function, flux function of j-th unit coil current and j-th coil current, respectively. The second and third terms are evaluated at null point. The weights  $w_i^p$ 's,  $w_{null}^R$ ,  $w_{null}^Z$  and  $w_j^I$ 's are selected so that desired plasma shape and null point are obtained and the coil currents are reasonably small. The object function J is minimized for  $I_j$ 's and  $\psi^s$  by the least square method. The coil currents are restricted by the volt-second condition,

$$V_s = \sum_{j=1}^{NC} M_{pj} I_j \quad (1.3)$$

here,  $M_{pj}$ 's are mutual inductances between plasma and coils. The definition of volt-second is equivalent to the benchmark definition.

The toroidal current of plasma is given by,

$$j_p = C \left\{ \beta_p \frac{r}{R_p} + (1-\beta_p) \frac{R_p}{r} \right\} (\psi - \psi_s) \quad (1.4)$$

Here  $\beta_p$ ,  $R_p$  and  $\psi_s$  are input poloidal beta, plasma major radius and flux function at surface limited at null point, respectively.  $C$  is determined so that total toroidal current is equal to the defined plasma current,  $I_p$ .

The definitions of resultant parameters are shown in Table 1.1.1.

(a) Symmetric double null divertor configuration

The input parameters  $I_p$ ,  $R_p$ ,  $a_p$ ,  $\beta_p$  and  $V_s$  are 8MA, 5.0 m, 1.2 m, 1.5 and 0V·sec, respectively. And surface fitting points are inner point  $(R_p - a_p, 0) = (3.8 \text{ m}, 0)$ , outer point  $(R_p + a_p, 0) = (6.2 \text{ m}, 0)$  and null point  $(4.6 \text{ m}, 2.6 \text{ m})$ . The weights  $w_i^p$ 's,  $w_{\text{null}}^R$ ,  $w_{\text{null}}^Z$  and  $w_j^I$ 's are selected to be 1, 1, 1 and  $10^{-4}$ , respectively. The mesh size of equilibrium calculation is 10 cm. Results are shown in Fig. 1.1.1, and Table 1.1.2. The total coil current is 88.3 MAT. The position error of the surface points are less than 1 cm.

(b) Single null divertor configuration

The input parameters and weights are same as (a). Surface fitting points are inner point  $(R_p - a_p, \delta_{ax}) = (3.8 \text{ m}, 0.5 \text{ m})$ , outer point  $(R_p + a_p, \delta_{ax}) = (6.2 \text{ m}, 0.5 \text{ m})$ , upper point  $(R - \delta_{ua} a_p, \delta_{ax} + \kappa_{ua} a_p) = (4.76 \text{ m}, 2.3 \text{ m})$  and null point  $(4.6 \text{ m}, -2.1 \text{ m})$ . Result are shown in Fig. 1.1.2 and Table 1.1.3. Total coil current is 113.5 MAT. The position errors of the surface points are less than 4 cm. The resultant vertical position of magnetic axis  $\delta_{ax}$  is 0.343 and out of range of the error definition ( $\delta_{ax} = 0.5 \pm 0.05 \text{ m}$ ). The position is determined by the surface shape and it is difficult to fit the axis position and the elongation simultaneously. The upper triangularity  $\delta_{up}$  is 0.154 and also out of range ( $\delta_{up} = 0.2 \pm 0.02$ ). The uppermost point is calculated at mesh and mesh size is 10 cm which corresponds to the error of triangularity 0.08. So, finer mesh or interpolation of surface shape is necessary to calculate more accurate triangularity.

The total coil current is strongly depend on the accuracy of the surface fitting. Figure 1.1.3 shows the dependence of the total coil current and position errors of fitting points on the weights of coil currents. Figure 1.1.4 shows the configurations at  $w_j^I = 10^{-3}$  and  $10^{-6}$ . The 9 points in the upper half of plasma are given to fit the plasma

surface. The total current increases drastically where  $w_j^I$  is less than  $10^{-5}$  although the surface fitting becomes more accurate. Figure 1.1.5 shows each coil current and shows that the currents of coils (9,4,5), which mainly induce divertor field, strongly depend on the accuracy of the surface fitting.

#### Reference

- [1] H. Ninomiya, K. Shinya and A. Kameari, Optimization of Current in Field-shaping Coils of a Non-Circular Tokamak, 8th Symp. on Engineering Problems of Fusion Research (1979)

Table 1.1.1 Definition of resultant parameters

1. Mutual inductance between plasma and coils

$$M_{pi} = \frac{2\pi}{I_p} \int j_p \phi_i ds$$

$j_p(r, z)$  : Plasma toroidal current density

$\phi_i(r, z)$  : flux function of i-th coil unit current

2. Self inductance of plasma

$$L_p = \frac{2\pi}{I_p^2} \int j_p \psi_p ds$$

3. Normalized internal inductance

$$l_i = \frac{\langle B_p^2 \rangle}{\bar{B}_p^2}, \quad \langle B_p^2 \rangle = \frac{\int B_p^2 dv}{V}, \quad \bar{B}_p = \frac{\int B_p dl}{\int dl}$$

$B_p(r, z)$  : poloidal field

$V$  : plasma volume

4. Calculated poloidal beta

$$\beta_{pcal} = \frac{\frac{\langle P \rangle}{\bar{B}_p^2}}{2\mu_0}, \quad \langle P \rangle = \frac{\int p dv}{V}$$

$p(r, z)$  : plasma pressure

5. Averaged vertical field

$$\bar{B}_v = \frac{1}{I_p} \int B_z j_p ds$$

$B_z(r, z)$  : external vertical field

6. Averaged n-value

$$\bar{n} = -\frac{1}{I_p \bar{B}_v} \int j_p \frac{\partial B_r}{\partial z} r ds = -\frac{1}{I_p \bar{B}_v} \int j_p \frac{\partial B_z}{\partial r} r ds$$

$B_r(r, z)$  : external horizontal field

7. Field averaged plasma major radius

$$\bar{R}_p = \frac{1}{I_p \bar{B}_v} \int j_p B_z r ds$$

Table 1.1.2 Results for (a) Symmetric double null divertor configuration

No.	Coil position		Current (MAT)	Mutual inductance Mpi ( $\mu$ H)
	R (m)	Z (m)		
1	1.43	$\pm 0.23$	1.7375	0.7807
2	1.43	$\pm 2.93$	10.923	0.5015
3	1.80	$\pm 5.20$	9.9268	0.4270
4	3.70	$\pm 6.20$	15.683	1.1892
5	11.00	$\pm 1.20$	5.895	5.067
$\Sigma  I_i $			88.333	
Null point				
			$R_{null}$ (m)	4.6078
			$Z_{null}$ (m)	$\pm 2.6093$
Inner point				
			$R_{in}$ (m)	3.7986
Outer point				
			$R_{out}$ (m)	6.1999
Magnetic axis				
			$R_{ax}$ (m)	5.1954
Elongation at surface				
			$\kappa$	2.1733
		at = 0.9	$\kappa_{0.9}$	1.7952
Triangularity at surface				
			$\delta$	0.3260
		at = 0.9	$\delta_{0.9}$	0.1149
Safety factor at axis				
			$q_0$	0.6871
		at = 0.9	$q_{0.9}$	2.257
Plasma self-inductance				
			$L_p$ ( $\mu$ H)	11.4426
Normalized internal inductance				
			$l_i$	1.1845
Beta poloidal				
			$\beta_{pca1}$	1.7500
Averaged vertical field				
			$\overline{B}_v$ (T)	-0.5428
Averaged n-value				
			$\overline{n}$	-1.7789
Averaged major radius				
			$\overline{R}_p$ (m)	5.2133

Table 1.1.3 Results for (b) single null divertor configuration

No.	Coil position		Current (MAT)	Mutual inductance	
	R (m)	Z (m)		Mpi (μH)	
1	7.69	5.83	-7.6420	3.3117	
2	4.28	6.31	19.397	1.5801	
3	2.19	5.83	9.6315	0.5628	
4	2.38	-5.70	10.732	0.5676	
5	5.05	-6.19	20.770	1.7397	
6	11.70	-4.74	-19.324	3.4911	
7	1.43	-0.54	8.9919	0.7581	
8	1.43	2.68	5.9283	0.5887	
9	1.43	-3.76	11.079	0.3761	
$\sum  I_i $			113.50		
Null point			$R_{null}$ (m)	4.6005	
			$Z_{null}$ (m)	-2.0873	
Inner point			$R_{in}$ (m)	3.7652	
			$Z_{in}$ (m)	0.2	
Outer point			$R_{out}$ (m)	6.2121	
			$Z_{out}$	0.4	
Upper point			$R_{up}$ (m)	4.8	
			$Z_{up}$ (m)	2.3127	
Magnetic axis			$R_{ax}$ (m)	5.1940	
			$Z_{ax}$ (m)	0.3425	
Elongation	at surface lower		$\kappa_{low}$	1.9912	
		upper	$\kappa_{up}$	1.6146	
		at = 0.9	$\kappa_{0.9}$	1.5875	
Triangularity	at surface lower		$\delta_{low}$	0.3177	
		upper	$\delta_{up}$	0.1543	
		at = 0.9	$\delta_{0.9}$	0.1503	
Safety factor at axis			$q_0$	0.6003	
			$q_{0.9}$	2.257	
Plasma self-inductance			$L_p$ (μH)	11.8292	
Normalized internal inductance			$l_i$	1.1261	
Beta poloidal			$\beta_{pcal}$	1.6651	
Averaged vertical field			$\overline{B}_V$ (T)	-0.5619	
Averaged n value			$\overline{n}$	-1.5117	
Averaged major radius			$\overline{R}_p$ (m)	5.1983	

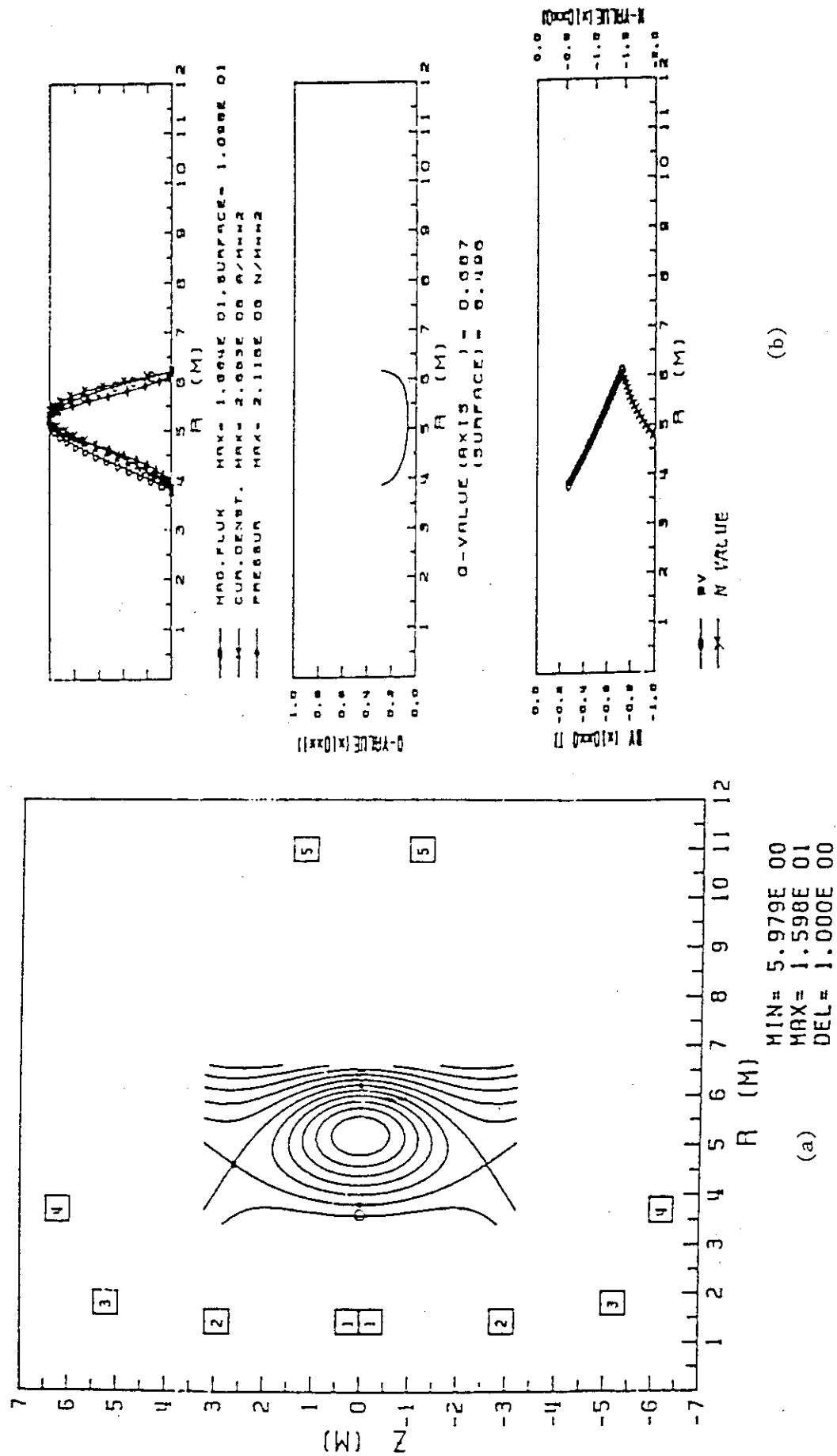


Fig. 1.1.1 Symmetric double null divertor configuration. (a) Equilibrium configuration, (b) distributions of flux function, plasma current density, plasma pressure, safety factor, vertical field and n-value and (c) external field distribution.



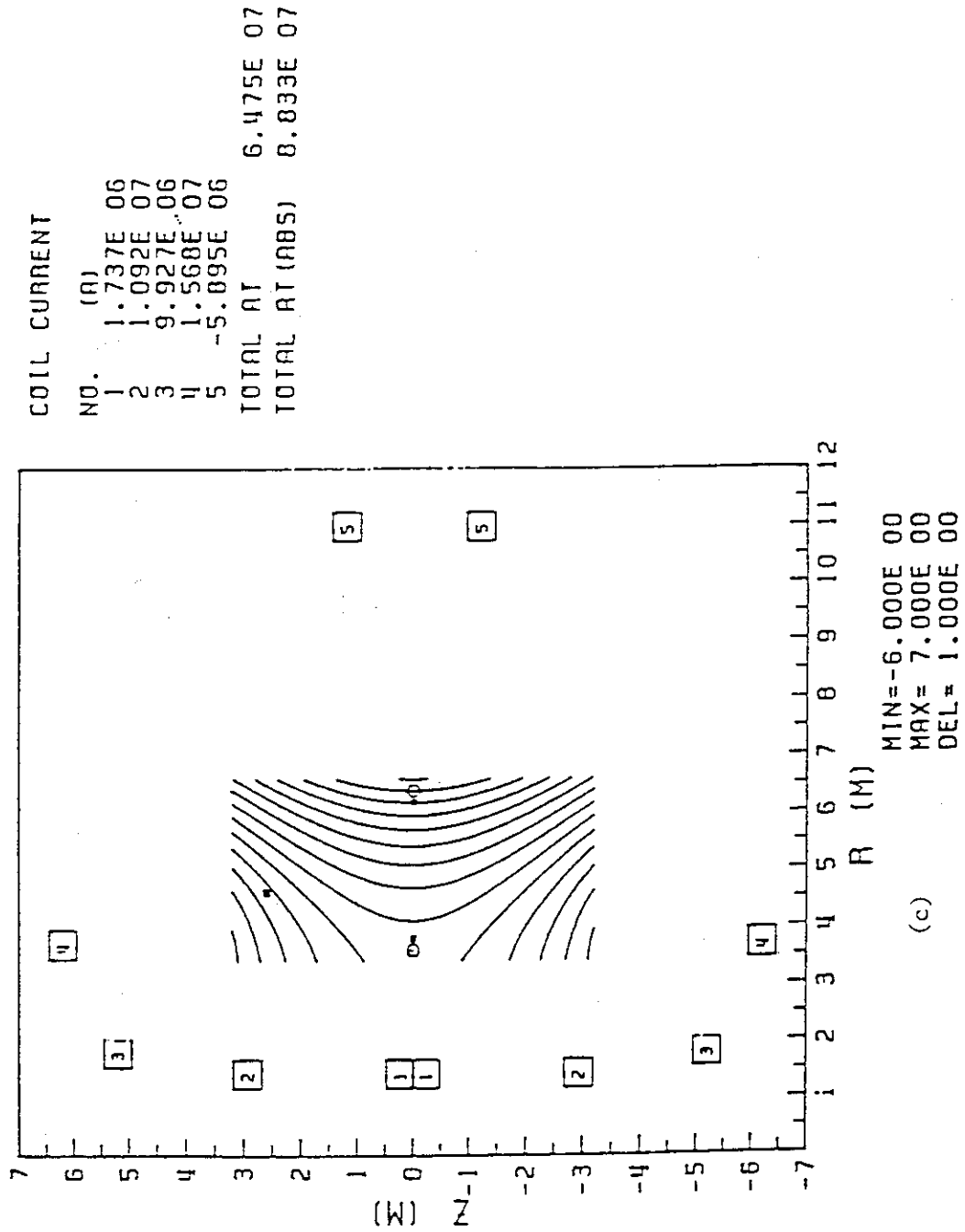


Fig. 1.1.1 (continued)

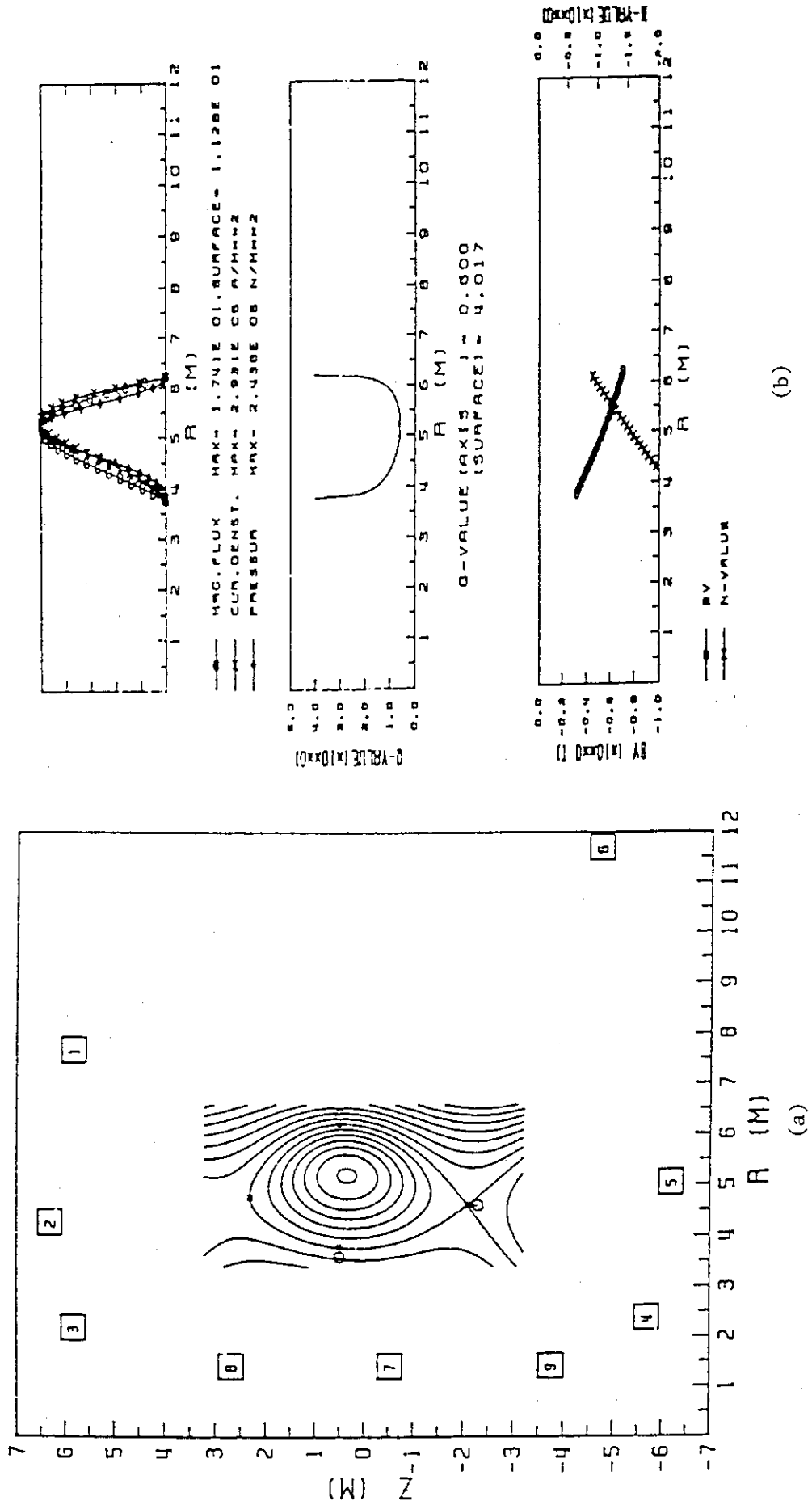


Fig. 1.1.2 Single null divertor configuration. (a) Equilibrium configuration, (b) distributions of flux function, plasma current density, plasma pressure, safety factor, vertical field and n-value and (c) external field distribution.

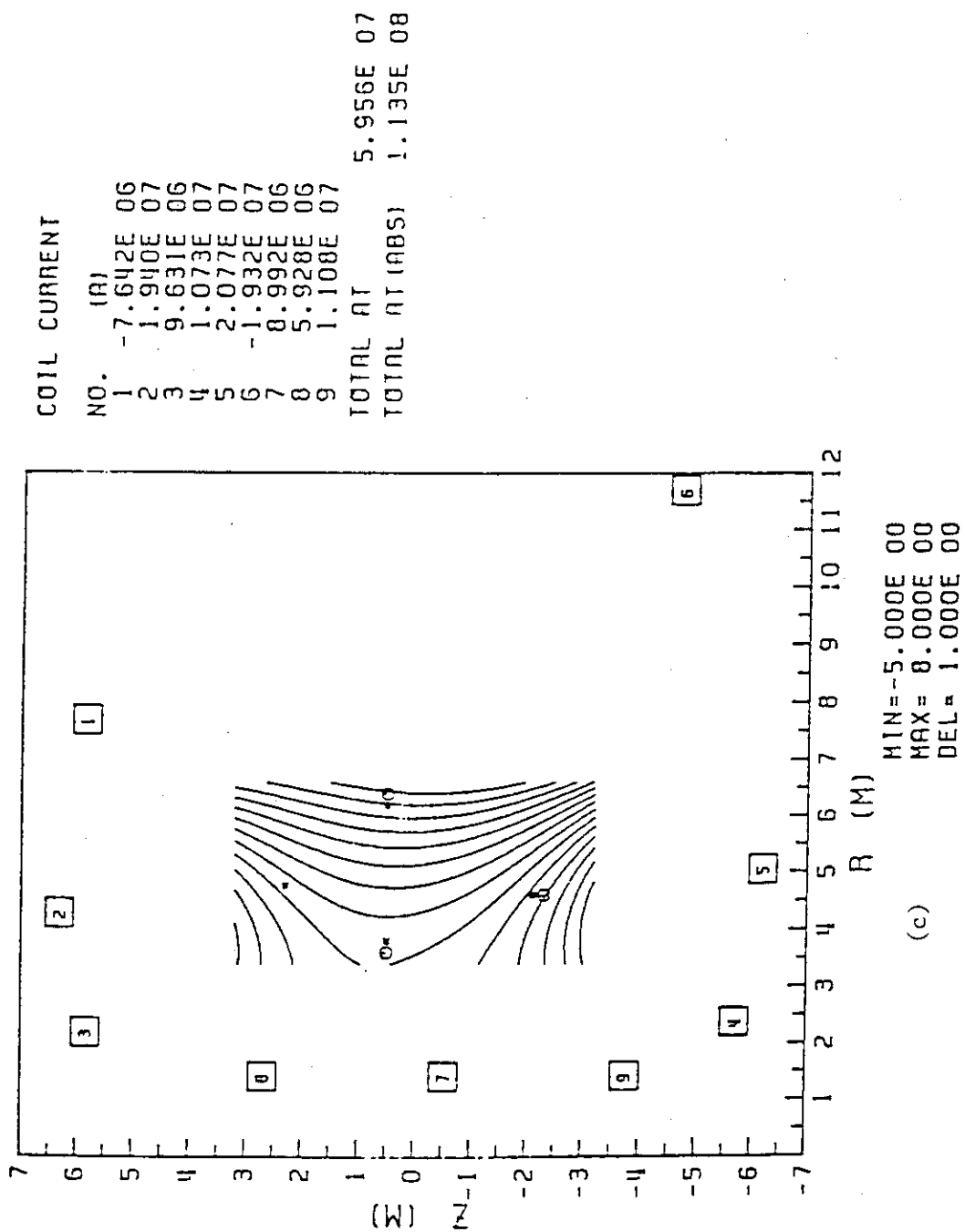


Fig. 1.1.2 (continued)

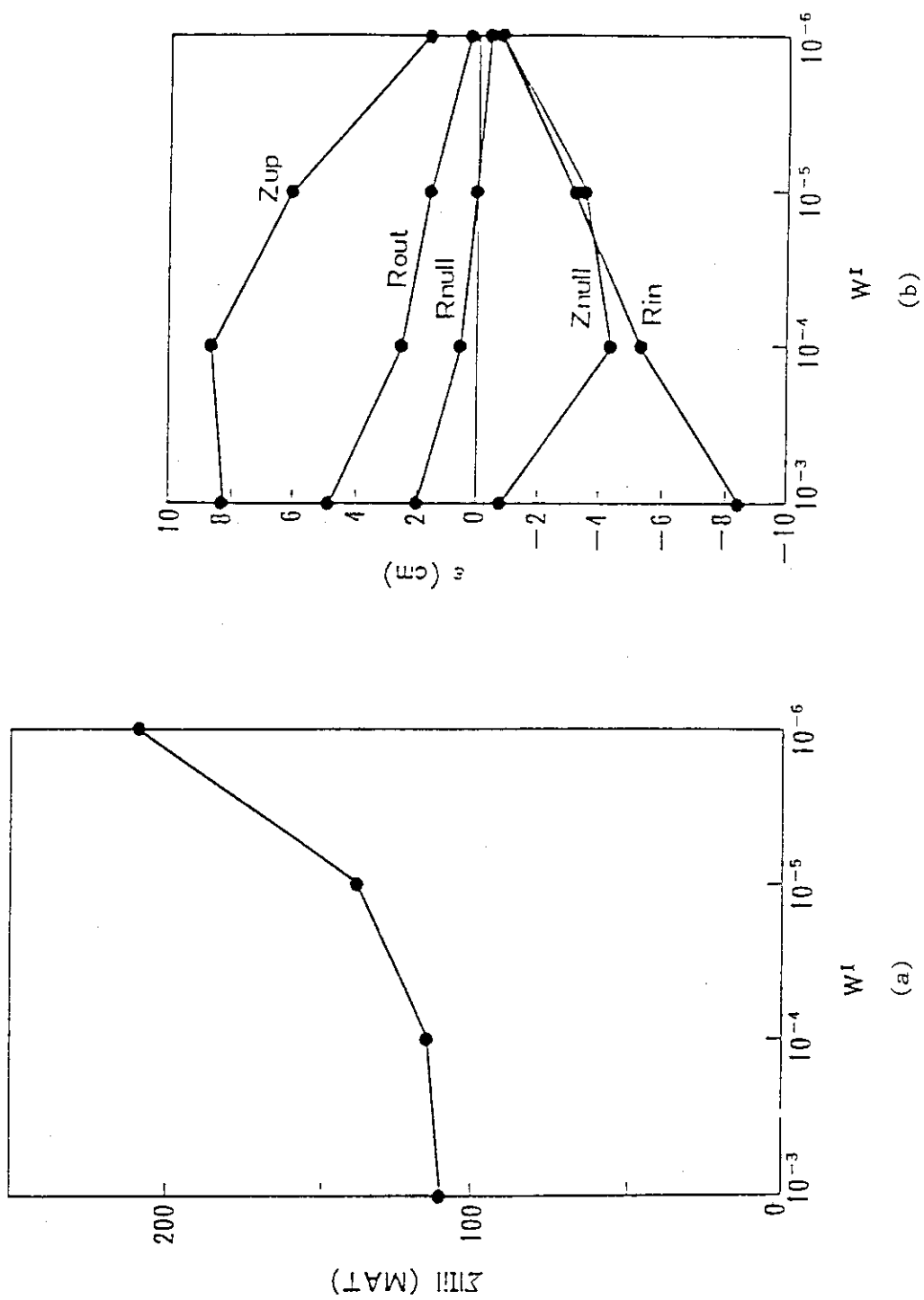


Fig. 1.1.1.3 Dependence of (a) total coil current and (b) fitting errors of surface points on the weights  $w_1$  of coil currents.

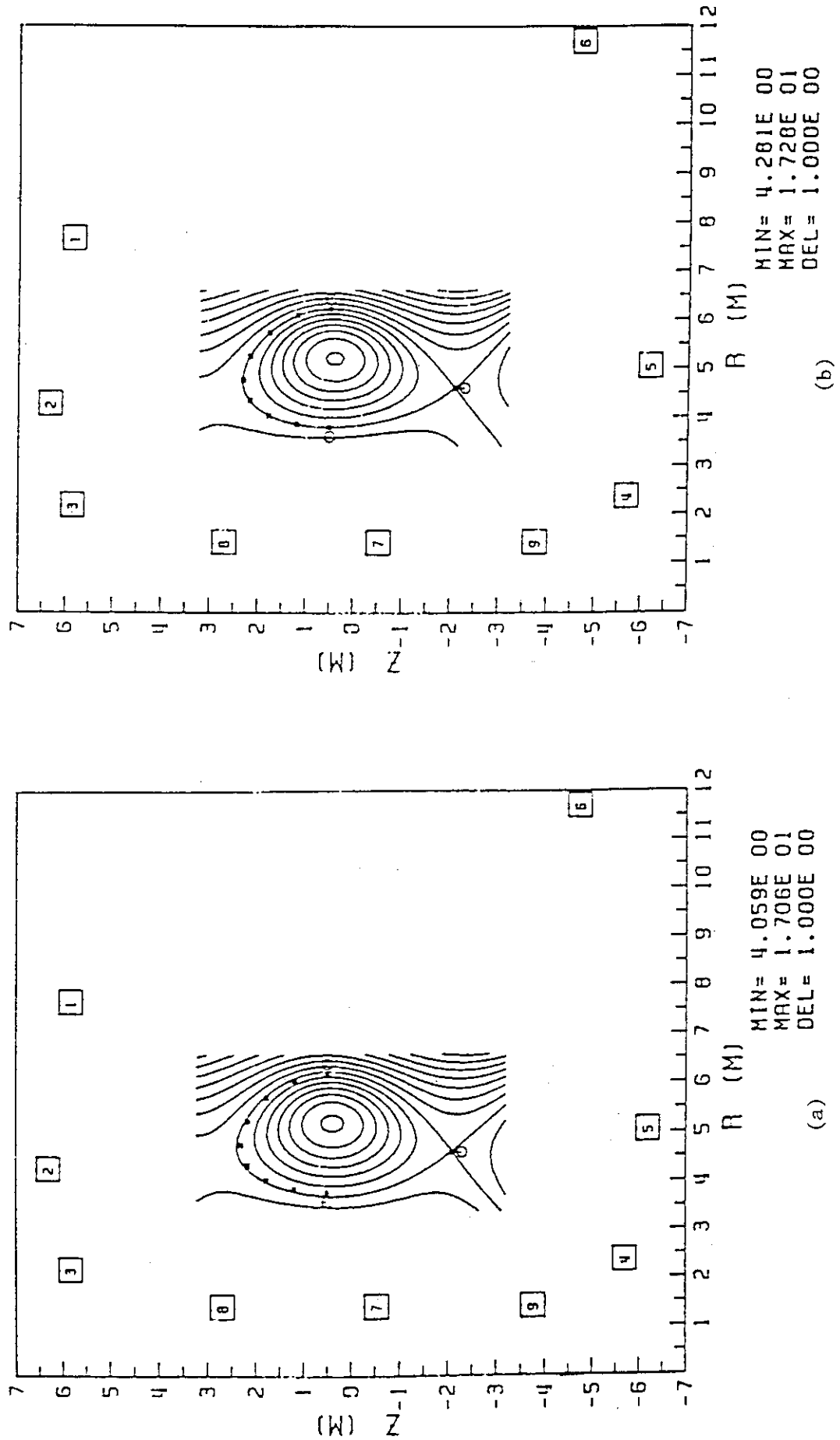


Fig. 1.1.4 Configurations at (a)  $w^I=10^{-3}$  and (b)  $w^I=10^{-6}$ .

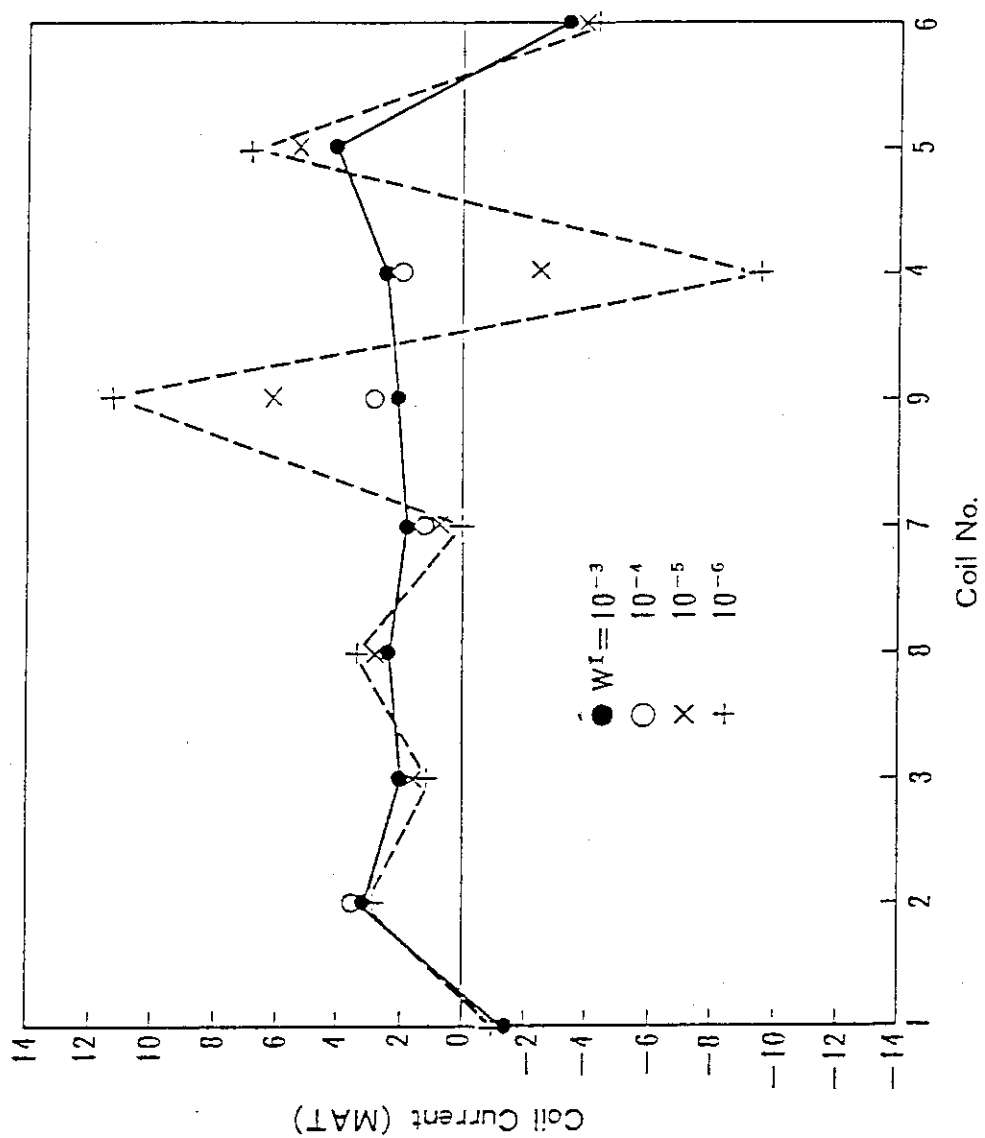


Fig. 1.1.1.5 Coil current at different  $w^I$ 's.

## 1.2 Comparative Studies on Single null (SND) versus Double null (DND) Poloidal Divertors

### 1.2.1 Introduction

Fusion Experimental Reactor (FER) will succeed the large tokamak JT-60 to realize ignited DT plasma and to demonstrate engineering feasibility of fusion reactors. Synthetic comparative studies on impurity control concepts for FER were carried out to select a reference option. Four options evaluated are: (a) double null poloidal divertor (DND), (b) single null poloidal divertor (SND), (c) pumped limiter with medium edge temperature (PLM), (d) pumped limiter with low edge temperature using a cold mantle (PLL). Plasma parameters of those four options are determined by keeping plasma confinement performance, i.e. confinement time and allowable beta value.

Four reactor concepts corresponding to those four impurity control options are assumed to have the following common features. The number of toroidal field (TF) coils is 14, which satisfies a field ripple limit of 0.75% at a plasma edge. Both toroidal and poloidal field (PF) coils are superconducting coils with a pool boiling method. All PF coils are located outside of the TF coils. A tritium breeding blanket with  $\text{Li}_2\text{O}$  as breeding material with its breeding efficiency above unity is installed all around the plasma column. Plasmas are heated to ignition by a hybrid heating of radio frequency and neutral beam injection heatings, and seven heating ports are provided at every two TF coils.

Results of the comparative studies are summarized in Table 1.2.1. It is recommended for the impurity control option for FER that the single null divertor should be a reference option and that the double null divertor and pumped limiter with the cold mantle should be retained as a back-up option. Those three options will be continued to be studied from both of engineering and physics viewpoints.

### 1.2.2 Comparative studies of physics of features

#### 1.2.2.1 Plasma parameters

The main plasma parameters for four options for impurity control are selected so that they have same plasma performance, and are listed in Table 1.2.1. The energy confinement time is evaluated with the INTOR

scaling with some margins. The allowable beta limit is assumed to follow the theoretical beta maximum derived from ballooning instability, and to have some risk, i.e., the maximum beta value is assumed to exceed the theoretical one to some extent. All plasmas satisfy D-T ignition.

The plasma elongation and the safety factor are set 1.5 and 2.5, respectively. A burn time is 100 s and plasma current is inductively driven, which is supplied by hybrid PF coils with their maximum field, 8 T. The maximum experienced field of TF coils is 12 T. The width of a gap between a separatrix surface and a first wall is assumed to be 15 cm on a midplane of both of inboard and outboard sides for the DND option, and to be 15 cm at outboard and 30 cm at inboard for the SND and two limiter options. Plasma with a cold mantle are also assumed to have a layer with its width 20 cm inside a separatrix.

#### 1.2.2.2 Physics data bases

##### Impurity control

A divertor configuration produced with the exterior PF coils to the TF coils is quite different from the conventional one. It is featured by a significantly wide divertor throat and no particular divertor chamber, so that it is called an open-type divertor. The divertor obtained in the Doublet III device is just an open-type one, and the results from it provide important data bases for a design of next tokamaks. The data bases of the open-type divertor are well assessed in the INTOR Workshop, Phase 2A (Part 2). The most remarkable feature, different from the conventional type, is a dense and cold plasmas formed in front of the divertor plate. The dense and cold divertor plasma brings about several advantages to impurity control such as quite low sputtering erosion of a divertor plate which directly results in reduction of metal impurities in the main plasma, neutral gas compression near the plate which reduces the pumping requirement, coexistence with the so-called H-mode discharges, enhanced radiation in the divertor region which leads to reduction of heat load to the plate. Such a dense and cold divertor plasma is demonstrated to be reproduced in a FER divertor operation by an computational code, which can of course well explain the present divertor experiments.

A pumped limiter with medium temperature was studied in the INTOR workshop, Phase 2A (Part 1). It is found that limiter material is



limited to low-Z and therefore its erosion becomes quite large. Then, behaviors of impurities have a key role in a physics aspect. At present impurity transport is uncertain and credible impurity control is an open question.

The pumped limiter with a cold mantle is an attractive option, which brings a lot of engineering advantages and could survive in future tokamak reactors. A present problem is, same as the pumped limiter without a cold mantle, uncertainty in impurity behaviors in plasma.

#### Beta limit

Theoretical studies on a beta limit due to ballooning instabilities show that a triangular deformation of a plasma cross section is advantageous in increasing beta limit. In a elongated D-shaped plasma configuration, enhancement of the triangularity induced proximity of a magnetic null point to a plasma boundary. For limiter configurations and single null divertor, therefore, their triangularities must be moderate. On the other hand, the double null configuration can increase its deformation and attain slightly higher beta value than other three options, although the enhancement of triangularity needs larger currents of PF coils.

#### 1.2.3 Comparative studies of engineering features

Comparative studies of engineering features for four impurity control options are conducted as qualitatively as possible to elucidate engineering gains and losses. The results are summarized in Table 1.2.1. Some details of engineering comparative studies are in a reference [13th SOFT (Sep., 1984, Italy) 5P03].

Table 1.2.1 Summary of comparative studies for four impurity control options

Items assessed	Summaries
<p>1. Physics data bases</p> <p>Impurity control</p> <p>Divertor</p> <p>Pumped limiter</p> <p>Medium temperature</p> <p>Low temperature</p> <p>Beta limit</p>	<p>Impurities, particularly metal, are well controlled with an open-type divertor owing to a dense and cold divertor plasma.</p> <p>Concerns on impurity control are large due to a large amount of sputtering and uncertainty of impurity transport.</p> <p>Insufficient data base, but if a cold mantle coexists with a hot plasma, such a concept is attractive.</p> <p>Double null divertor is somewhat superior to single null due to an available large triangularity.</p>
<p>2. Reactor structure</p> <p>Size</p> <p>Maintainability</p> <p>Single</p> <p>Double</p>	<p>TF coil sizes of four options are almost same.</p> <p>Plates, installed at bottom, can be retracted with one straight radial motion through every window.</p> <p>Plates, installed at top and bottom, are retracted with two straight (radial and oblique) motions through every two windows.</p>

Items assessed	Summaries
Earthquake-proof Single Double	Fairly good Somewhat difficult, when vacuum pumps are installed at top.
3. Collector plate Life	Limiter with a cold mantle is maximum (full life). Divertor is reasonable (1 ~ 2 years). Limiter without a cold mantle is low (less than one year).
4. TF Coil Stress due to out-of-plane Force AC loss	Limiters are almost half of divertors. Single divertor is reduced by 20% from double divertor. Same as a case of stress mentioned above.
5. PF Coil Stored energy MG peak power	Limiters are about half of divertors. Single divertor decrease by 20-30% from double divertor. Limiters are less than half of divertors. Single divertor is almost same as double divertor.

Items assessed	Summaries
6. Vertical position control	Double divertor and limiter with a cold layer are somewhat unfavorable to single divertor and limiter with medium temperature.
7. Tritium breeding	Double divertor is slightly disadvantageous compared with other three options.
8. Vacuum pumping	Double divertor needs approximately half of pumping speed of other three options.

\* Synthetic judgement

1. Pumped limiter without a cold mantle should be excluded because of its uncertainty of impurity control and short life of collector plates. (However, the latter difficulty is eased in a fairly low fluence reactor)
2. Pumped limiter with a cold mantle has a lot of engineering advantages, although physics uncertainties are large. Especially a long life of collector plate is preferable.
3. Double null divertor is not preferable in almost all items compared with single null divertor, especially, double is fairly more difficult in replacement of plates than single. The followings, however, should be kept in mind. 1) Allowable beta value of double null divertor is best, 2) No definite engineering items are found which reasonably exclude double divertor concept.
4. AC loss of TF coils and PF power supply are crucial items in a conventional tokamak reactor with inductive current drive, however their importance is significantly reduced when a scenario of RF current drive is used in a start-up phase.

### 1.3 Some Features with the TNS Plasma Equilibrium

The INTOR plasma equilibrium had been studied in previous papers.<sup>[1]-[12]</sup> Here, some of their contents are described as follows.

(1) The INTOR conceptual designs are based and performed under an important postulate that the poloidal field coils should not be linked with the toroidal field coils and then should be located outside them, in order to facilitate INTOR's remote assembly and maintenance.

(2) Moreover, a constraint from the portwindow size for remote assembly and maintenance of the torus had been given for the poloidal coil locations. The portwindows opened in the direction of radius had several meters in vertical width on both the upper and lower part of midplane.

(3) Ampere-turns required for the poloidal field coils on high  $\beta$  were powerfully determined to be as little as possible. On the determinations had been studied some evaluation functions for optimization of their ampere-turns, too.

(4) In the Phase I, the design studies had been concentrated on the poloidal coils only for the divertor configuration and, in the Phase II A, for the pump limiter configuration.

Main conclusions are described on the following.

(1) Expected reactor size as the INTOR from the studies about the poloidal field coils was found to attain more than 24 m in diameter and 14 m in height.

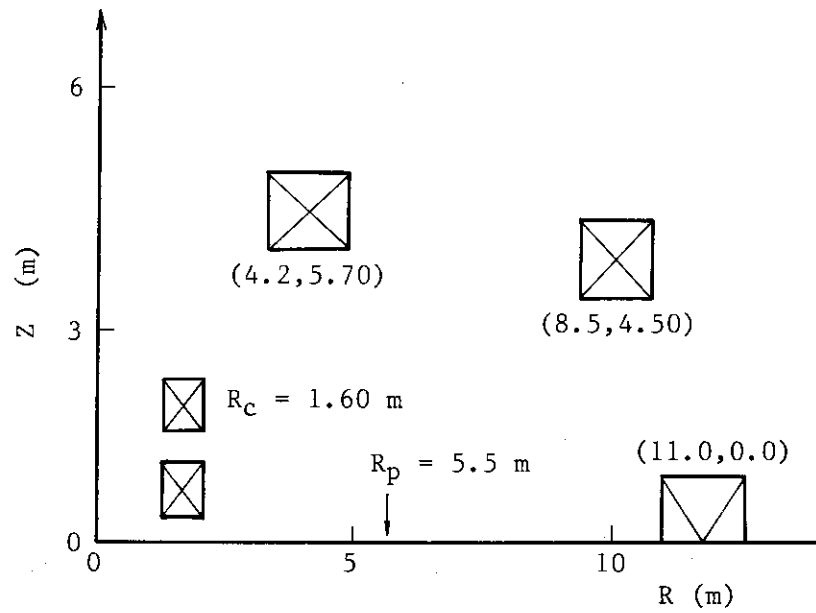
(2) The total ampere-turns of the poloidal coils had been reduced into a range of 80 - 90 MAT for the divertor and, 70 - 80 MAT for the pump limiter, where the plasma had been in the following parameters 3.5 m in major radius, 1.2 m in minor radius, 6.4 MA in the maximum plasma currents, 1.6 in elongation and 0.2 - 0.3 in triangularity.

(3) The n-index in a strong relation with the vertical positional instability decreases with increasing elongation, and increases with increasing triangularity, as well known. Under the above mentioned plasma parameters the n-index was found to be equal to -1.1 - -1.3 at the major radius.

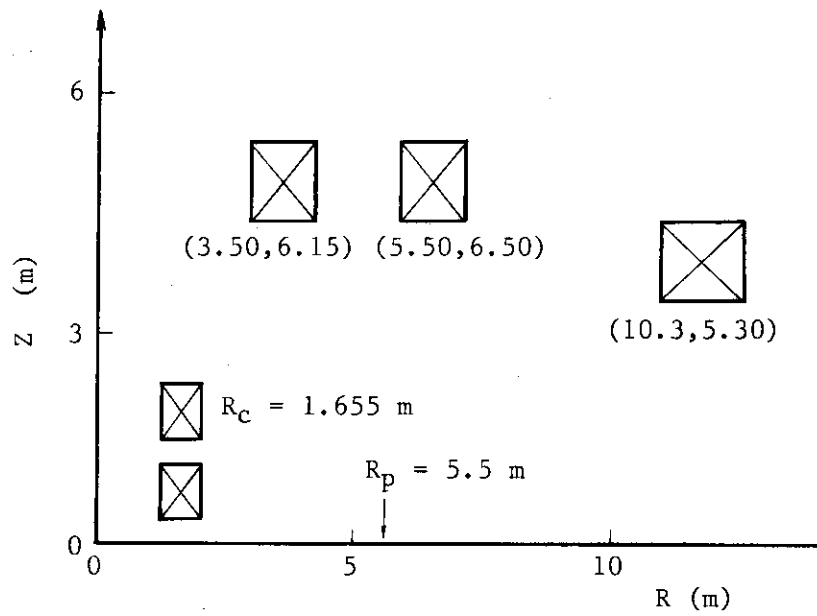
The above-mentioned contents were obtained from the INTOR reference design. Likely some results had been obtained parallel from the national reference design, too. Their concrete contents can be known from Fig. 1.3.1~Fig. 1.3.9.

## References

- [1] N. Fujisawa, M. Sugihara, K. Shinya and K. Ueda : Report of Physics Group Tasks for IAEA INTOR Workshop, Japan, JAERI October 20-31 (1980)
- [2] N. Fujisawa, M. Sugihara and K. Ueda : Report of Physics Group Tasks for IAEA INTOR Workshop, Japan, JAERI Mar. 30 - Apr. 11 (1981)
- [3] K. Ueda, S. Nishio, M. Hatayama, S. Saito, M. Sugihara and N. Fujisawa : Task 1.2.4 in Japanese Contribution for Session IV of INTOR Workshop, Phase II.A, March 22 - April 2 (1982)
- [4] International Tokamak Reactor Zero Phase : Report of the International Tokamak Reactor Workshop Organized by IAEA and Held in Four Sessions in Bienna, 5-6 Feb., 11 June - 6 July, 1-23 Oct. and 10-19 Dec. (1979)
- [5] INTOR Summary Report of Session 3 Phase II.A Group F : Magnetics and Electromagnetics, December (1981)
- [6] H. Ninomiya, A. Kameari and K. Shinya : JAERI-M 9127 (September 13, 1980)
- [7] K. Shinya and H. Ninomiya : JAERI-M 9278 (December 22, 1980)
- [8] H. Ninomiya, K. Shinya and A. Kameari : Proc. 8th Symp. on Engineering Problems of Fusion Research, Vol.1, 75 (1979)
- [9] K. Lackner, W. Schneider and U. Seidel : Poloidal Field Design for INTOR, December (1981)
- [10] O. Gruber and K. Lackner : Poloidal Field Design Calculations for INTOR Divertor and Limiter Versions in the Report of European Contributions to the 5th Workshop Meeting on INTOR Phase II.A
- [11] T.G. Brown, B.A. Cramer, G.M. Fuller, R.J. Kalsi, M.H. Kunselman, P.H. Sager, V.C. Srivastava and C.A. Trachsel : INTOR Reactor Design Studies, July (1982)
- [12] K. Ueda, S. Nishio, N. Fujisawa, M. Sugihara and S. Saito : JAERI-M 82-217 (1983)



(a) Ideal coil arrangement



(b) FER coil arrangement

Fig. 1.3.1 Two coil arrangements used in a study of plasma equilibrium

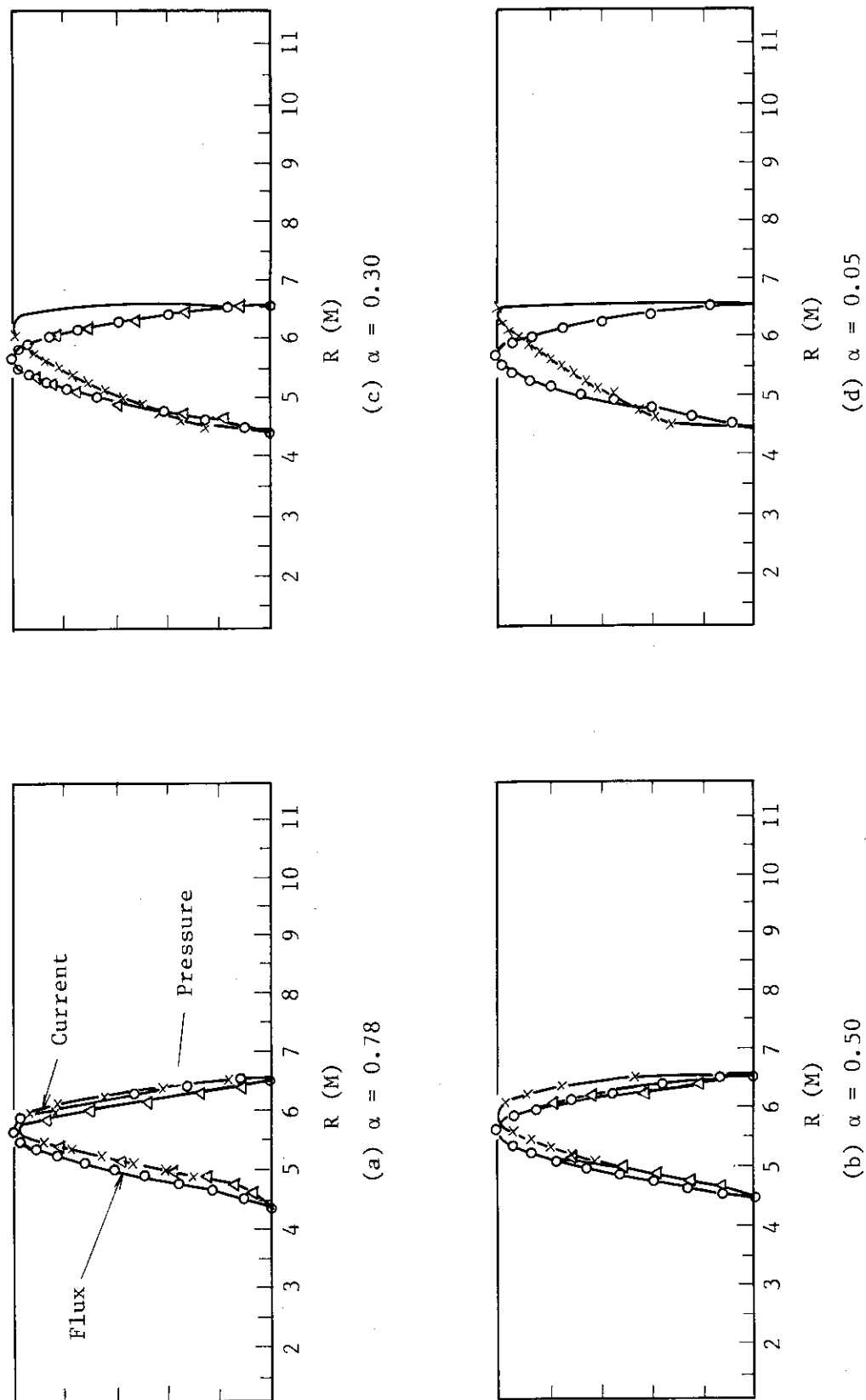


Fig. 1.3.2 Dependence of plasma current distribution upon profile factor  $\alpha$  on high beta



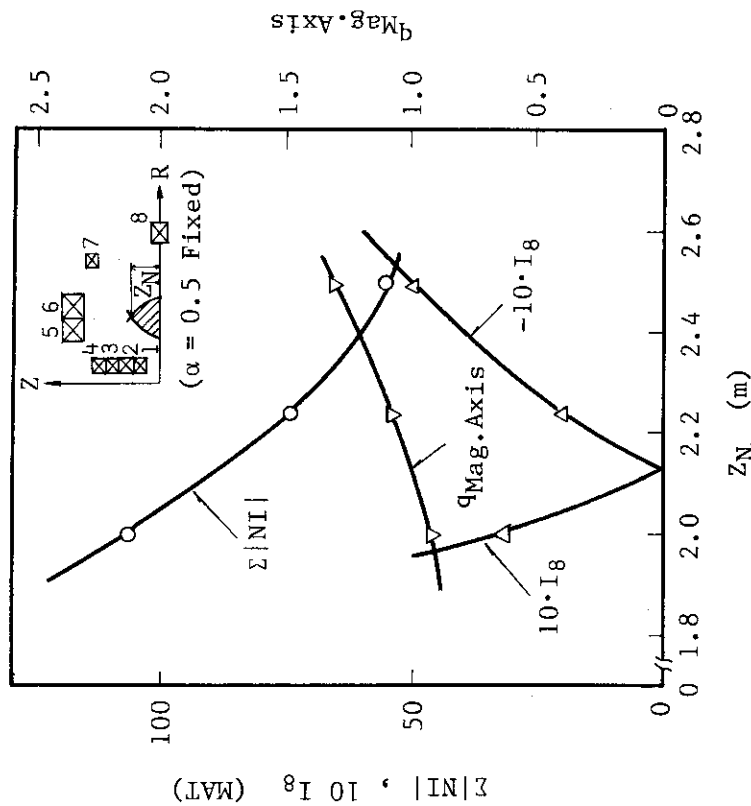


Fig. 1.3.3  $|NI|$ ,  $q_{Mag.Axis}$  and  $I_8$  as a function of  $Z_N$

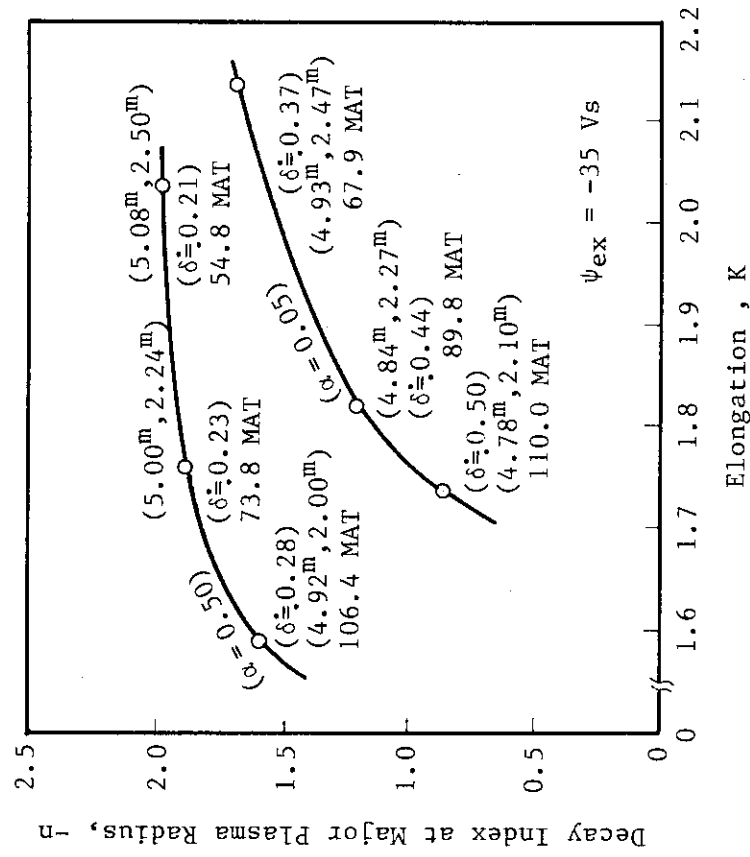


Fig. 1.3.4 Decay index,  $n$  as a function of elongation,  $K$ , for both cases of  $\alpha = 0.50$  and  $0.05$  (Ideal coil arrangement)

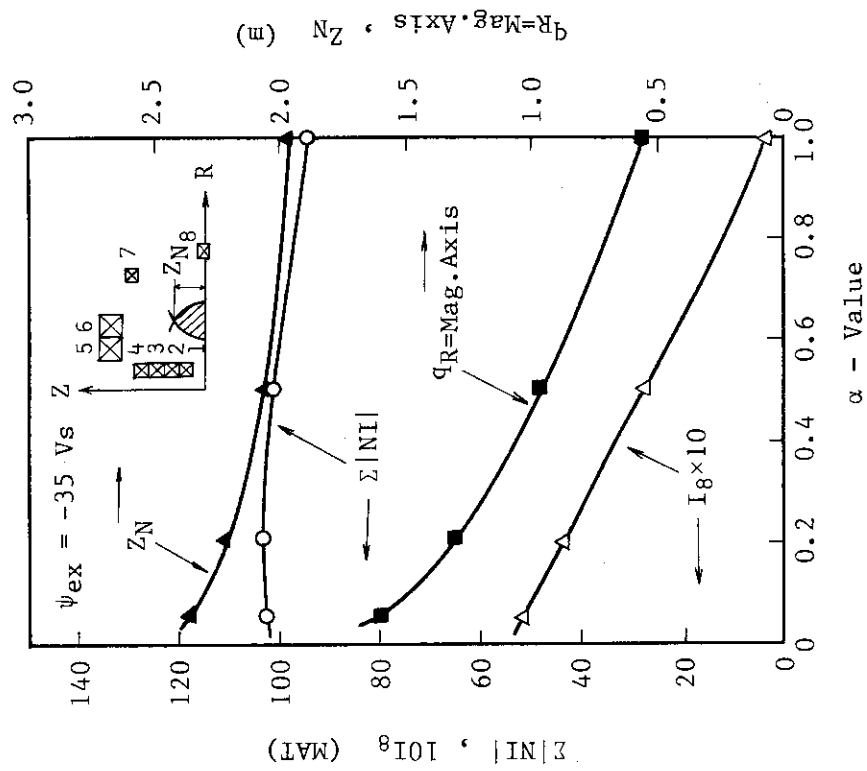


Fig. 1.3.6  $\Sigma|NI|$  and  $I_8$  as a function of  $\alpha$

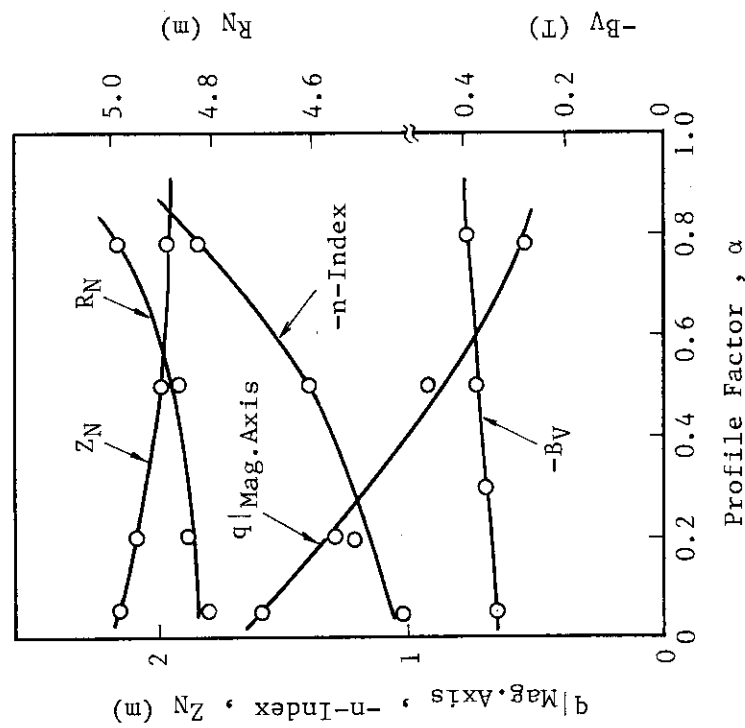


Fig. 1.3.5 Dependence of null point ( $R_N, Z_N$ )  $n$ -index and safety factor upon profile factor on high beta in case of ideal coil arrangement

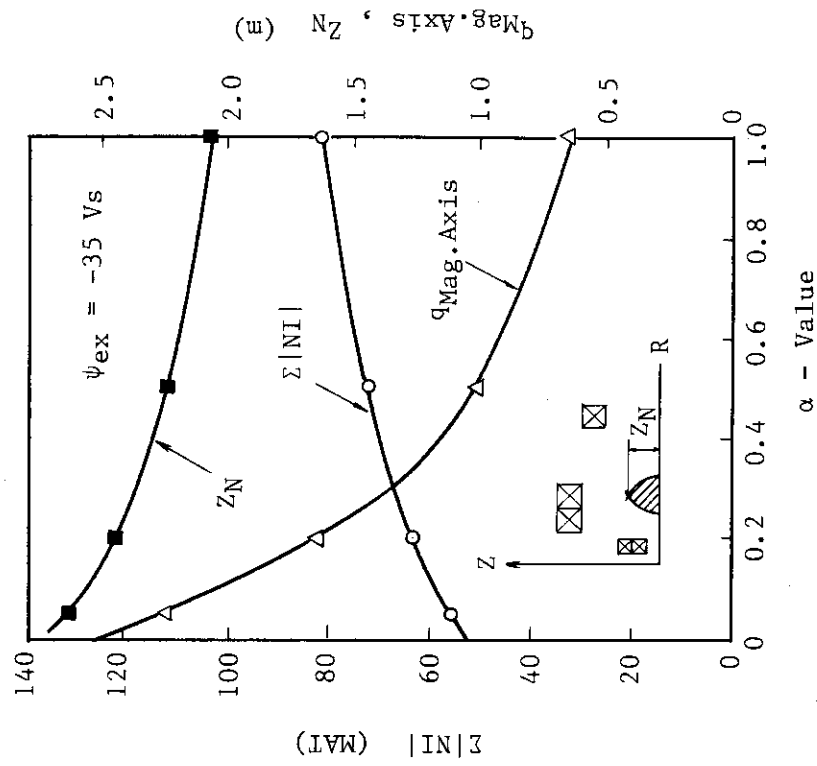


Fig. 1.3.8  $\Sigma|NI|$ ,  $q_{Mag.Axis}$  and  $Z_N$  as a function of  $\alpha$  in case of FER configuration

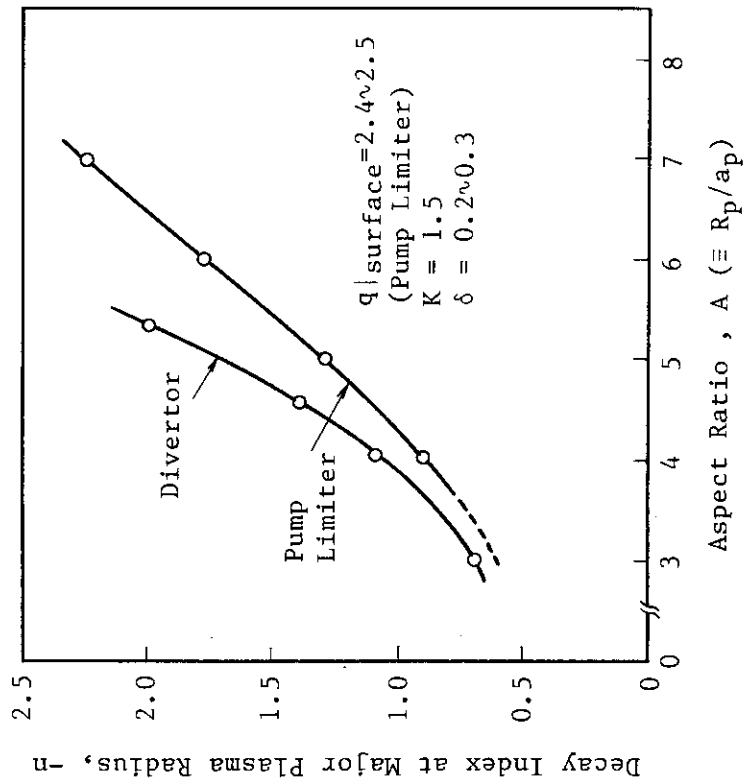
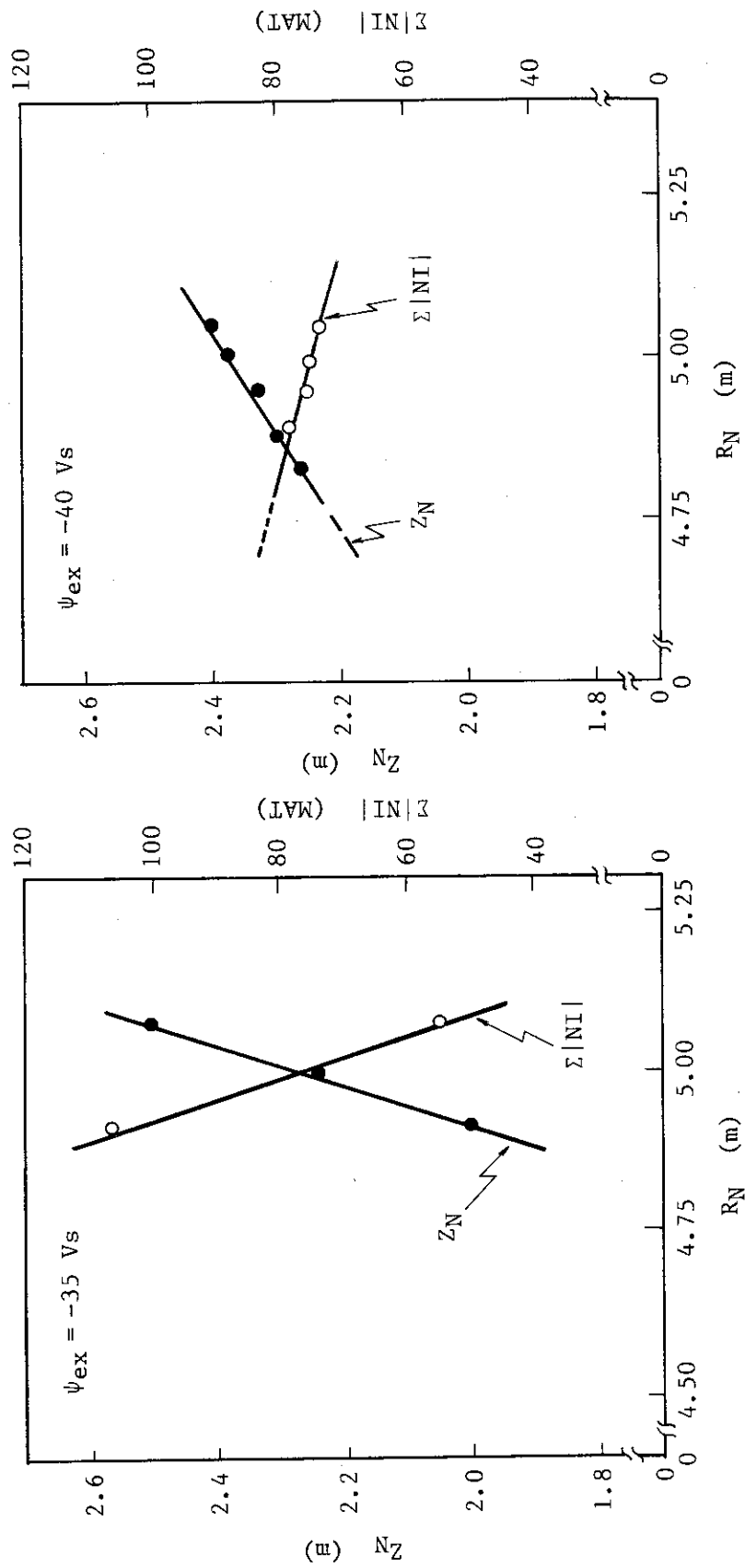


Fig. 1.3.7 Dependence of decay index,  $n$  upon Aspect ratio,  $A$  ( $\equiv R_p/a_p$ ) in both cases of divertor and pump limiter



(a) Ideal coil arrangement

(b) FER coil configuration

Fig. 1.3.9 Relation of null position ( $R_N, Z_N$ ) with total sum of absolute current,  $\Sigma|NI|$

## 2. Operation Scenario Analysis

### 2.1 Analyses of the quasi steady state operation scenario

A possible burning time is compared between inductive and quasi steady state operation scenarios for the next generation tokamak reactors as functions of plasma elongation and triangularity. Figure 2.1.1 shows the difference in a possible burning time between the two operation scenarios mentioned above,  $\Delta\tau_{\text{burn}}$ . Plasma parameters are set so as to obtain an ignition condition for each plasma elongation and triangularity by using ASDEX H mode scaling with ignition margin 2.5. Peak fields in poloidal field coils are limited to less than 10 T in these calculations. The burning time difference,  $\Delta\tau_{\text{burn}}$ , decreases with the increases of plasma elongation and triangularity as shown in Fig. 2.1.1. The possible burning time of inductive operation case,  $\tau_{\text{burn}}^{\text{Ind}}$ , is set to 500 sec in this figure. The check calculations are also carried out to survey the  $\tau_{\text{burn}}^{\text{Ind}}$  dependence by charging  $\tau_{\text{burn}}^{\text{Ind}}$  from 50 sec to 700 sec and the results show that the  $\Delta\tau_{\text{burn}}$  dose not strongly depend on  $\tau_{\text{burn}}^{\text{Ind}}$  (error is approximately 5 ~ 10%). The large difference of a possible burning time can be expected between inductive and quasi steady state operation scenarios in the machines with relatively low elongation and triangularity plasma such as the INTOR reference design and the FER (JAERI's Fusion Experimental Reactor) '85 design. On the other hand, only a small difference in  $\Delta\tau_{\text{burn}}$  is expected in the machines with high elongation and triangularity plasmas such as the double null divertor option of the NET design.

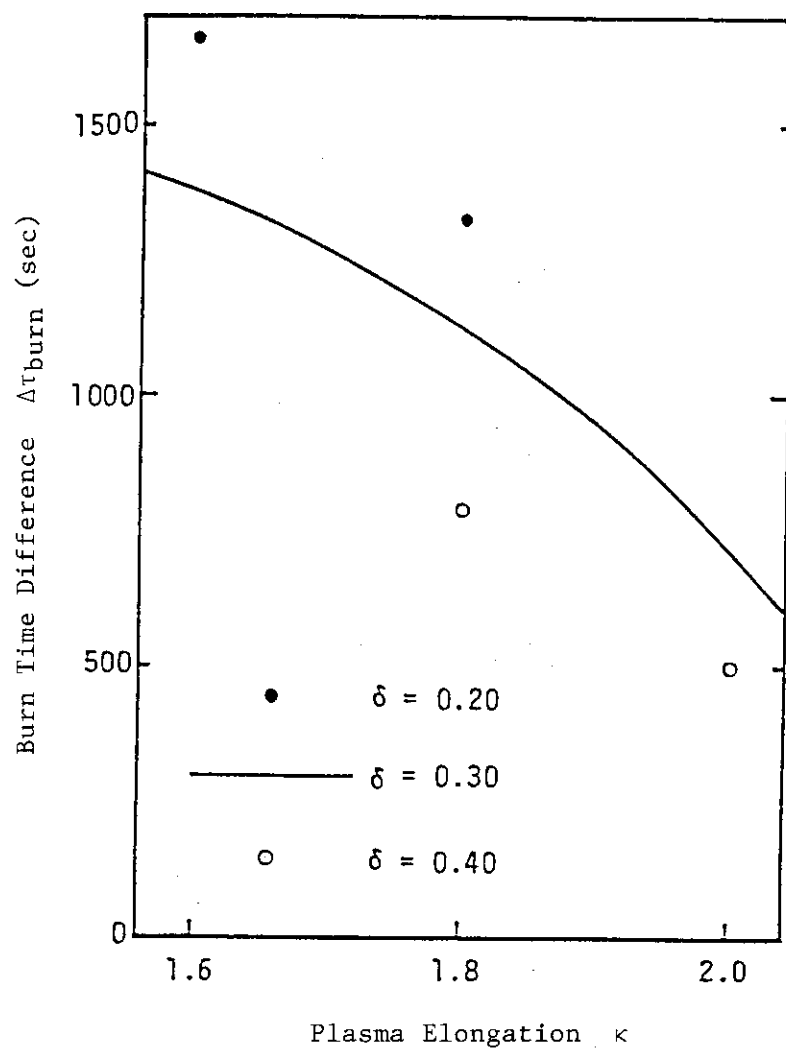


Fig. 2.1.1 Difference of possible burn time between quasi steady state operation and inductive operation as a functions of plasma elongation and triangularity.

## 2.2 Comparison of the PF coil system requirements for vertical and horizontal accesses

The requirements for PF coil system are compared between horizontal (radial) access case and vertical (oblique) one. The result is summarized in Table 2.2.1. The plasma configuration is a single null divertor one with elongation  $\kappa = 1.8$  and triangularity  $\delta = 0.35$ . A quasi-steady state operation is adopted and a burn time is fixed at  $\sim 1500$  sec in both cases. Though the peak stored energy of PF coils is less in the case of oblique access by  $\sim 30\%$  than in the case of radial access, the difference of relative capital cost is only  $\sim 3\%$ . At higher elongation than  $\kappa \gtrsim 1.8$ , the requirements for the PF coil system are relieved largely in the case of oblique access, though those in the case of radial access are larger (i.e. at  $\kappa = 2.0$ , the peak stored energies in the cases of oblique access and radial access are  $\sim 6$  GJ and  $\sim 16$  GJ, respectively.). On the other hand, at such lower elongation as  $\kappa \lesssim 1.6 \sim 1.7$ , the requirements for the PF coil system of the radial access case are very close to the ideal case with no restriction on the PF coil arrangement (i.e. at  $\kappa = 1.6$ , difference of the peak stored energy and total Ampere turn of the PF coil system are less than several percent between the radial access and the ideal cases).

Figures 2.2.1(a) and (b) show the cross-sectional views of radial access type and oblique access type of reactors, respectively. The PF coil locations in the case of oblique access are relatively close to the ideal PF coil locations at higher plasma elongation ( $\kappa \gtrsim 1.7 \sim 1.8$ ) compared with the case of radial access. However, at lower plasma elongation ( $\kappa \lesssim 1.6 \sim 1.7$ ), the PF coil locations in the radial access case are more preferable than those in the oblique access case.

In summarizing, the radial access for remote maintenance is more preferable at  $\kappa \lesssim 1.6 \sim 1.7$  and the oblique access is more preferable at  $\kappa \gtrsim 1.7$  from the view point of the PF coil system requirements.

Table 2.2.1 Comparison between radial and oblique acceses  
( $\kappa = 1.8$ ,  $\delta = 0.35$ )

	Radial Access	Oblique Access
Plasma Major Radius (m)	4.97	5.01
Plasma Minor Radius (m)	1.52	1.50
Plasma Current (MA)	10.9	10.7
Toroidal Field (T)	4.43	4.51
Total Weight (ton)	11350	10990
TF Coil Weight (ton)	3030	2750
PF Coil Weight (ton)	1150	1020
Peak Stored Energy (GJ)	11.65	7.84
Power Capacity (MVA)	787	675
Total Ampere Turn (MAT)	115	101
Relative Capital Cost	1.0	0.970



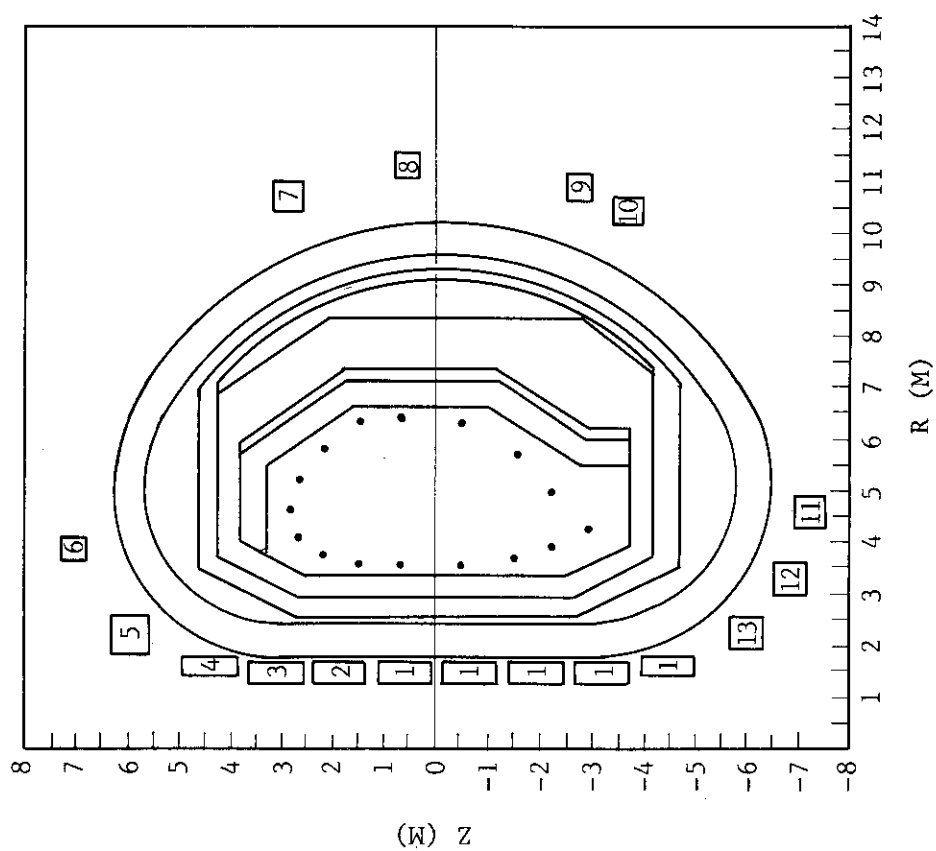


Fig. 2.2.1(b) Oblique access type reactor

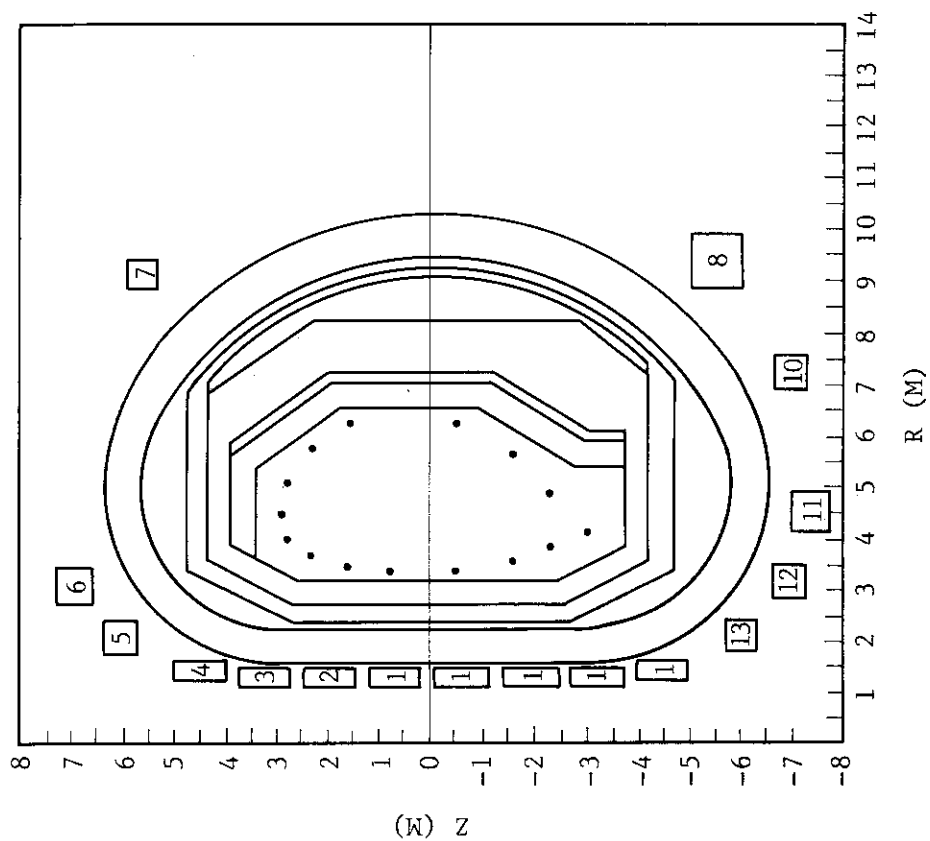


Fig. 2.2.1(a) Radial access type reactor

### 3. Closed Loop Plasma Control

#### 3.1 Stability analysis by deformable plasma

A deformable plasma model provides somewhat different features on the plasma positional instability from a rigid plasma model [1], [2]. The comparison study between a rigid and a deformable plasma model was done during the last INTOR phase (Phase 2A, Part 2). The analysis by the full MHD equation shows the different dependency of the triangularity on the stability boundary from the analysis by the rigid plasma model, especially in the region of high elongation and high triangularity [1]. In this study, the conducting wall was assumed to be placed at infinity (no conducting wall) and the flat profile was assumed on plasma current distribution. Here, we improve the assumption on plasma current profile to obtain more realistic results, and analyze the effect of the conducting wall on plasma positional instability by using deformable plasma model.

We estimate the critical position of the conducting wall for a given elongation,  $\kappa$ , by using the linearized ideal MHD model. The equilibrium used in this analysis is for  $q_0=1$ ,  $q_s \sim 3$ ,  $\beta_j=1.5$  and  $A=4$  in up and down symmetry (double-null divertor configuration) where  $q_0$ ,  $q_s$  and  $\beta_j$  denote the safety factor at the magnetic axis and at the plasma surface and the poloidal beta value, respectively. The toroidal current density is given by

$$J_\varphi = -\mu_0 R \frac{dP}{d\psi} - \frac{1}{R} F \frac{dF}{d\psi}$$

$$\frac{dP}{d\psi}(\bar{\psi}) = P_0 \beta_1 (1 - \bar{\psi}^{j_1})$$

and

$$F \frac{dF}{d\psi}(\bar{\psi}) = R_0^2 \left( \frac{1}{\beta_1} - 1 \right) \mu_0 \frac{dP}{d\psi}(\bar{\psi})$$

The parameters  $P_0$  and  $j_1$  are used to adjust  $q_0$  and  $q_s$  to prescribed values. The shape of the cross section is specified by using the functional form:

$$R = R_0 + a \cos(\theta + \delta \sin \theta)$$

and

$$Z = \kappa a \sin\theta$$

where  $\kappa$ ,  $\delta$ , and  $a$  denote the ellipticity, triangularity and the horizontal minor radius. Figures 3.1.1, 3.1.2 and 3.1.3 show the examples of the equilibria for  $\kappa=1.6$ , 1.8 and 2.0 with  $\delta=0.3$ :

(a) contour of poloidal flux function, (b) contour of toroidal current density, (c) plasma pressure, (d) safety factor and (e) toroidal current on the horizontal midplane, the total plasma current is  $I_p \sim 7\text{MA}$ , 8.3MA and 10MA for  $\kappa=1.6$ , 1.8 and 2.0 respectively, when we take the reference parameters of INTOR plasma ( $R_0=4.9\text{m}$ ,  $a=1.2\text{m}$  and  $B_T=5.5\text{T}$ ). For the stability analysis of the  $n=0$  modes, the conducting wall is placed at the equidistant position from the plasma surface (Fig. 3.1.4). The parameter,  $b_w/b_p$ , is used to specify the position of the conducting wall.

Figure 3.1.5 shows the critical position of the conducting wall as the function of  $\kappa$ . The effect of the triangularity,  $\delta$ , is within  $\pm 0.05$  for  $0 \leq \delta \leq 0.4$ . In this analysis, we used the marginal growth rate  $\gamma/\omega_A \sim 10^{-4}$  ( $\omega_A = B_T / \sqrt{\mu_0 \rho_0 R_0}$ ) which corresponds to the characteristic time of  $\tau$  lms for the INTOR parameter. For the case of highly elongated cross section,  $\kappa \geq 2.0$ , the conducting wall has to be located within  $b_w/b_p \leq 1.3$  to suppress the rapid displacement within lms. This analysis used the perfect conducting wall around the plasma. However, the wall has cuts both to the toroidal and the poloidal directions. For the quantitative estimation, we have to take account of the realistic wall, which may give more pessimistic stabilization. This analysis is preliminary one. We have to make more detailed analysis including the effect of current profile and further deformation of the cross section etc.

#### References

- [1] Japanese Contribution to the INTOR Phase Two A Part 2 Workshop Group C Transient Electromagnetics), May 21 - June 1, 1984.
- [2] T. Ozeki, M. Azumi, S. Seki, T. Tsunematsu, S. Tokuda and T. Takizuka, JAERI-M 86-022 (in Japanese), 1986.

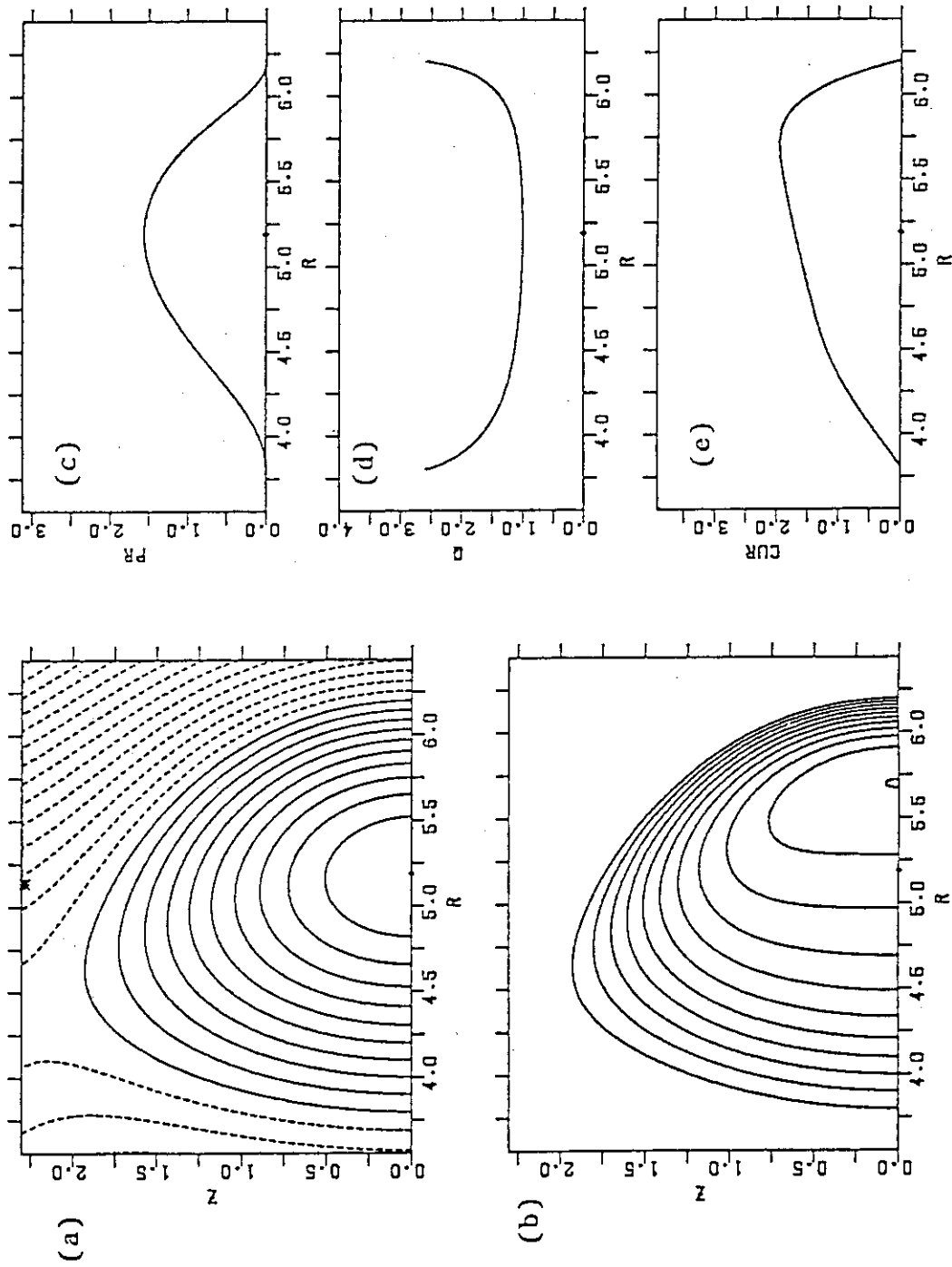


Fig. 3.1.1 Equilibrium for  $q_0=1$ ,  $q_s=3.0$ ,  $A=4$ ,  $\kappa=1.6$  and  $\delta=0.3$  : (a) flux surface, (b) contour of toroidal current, (c) plasma pressure, (d) safety factor and (e) toroidal current density on the horizontal midplane.

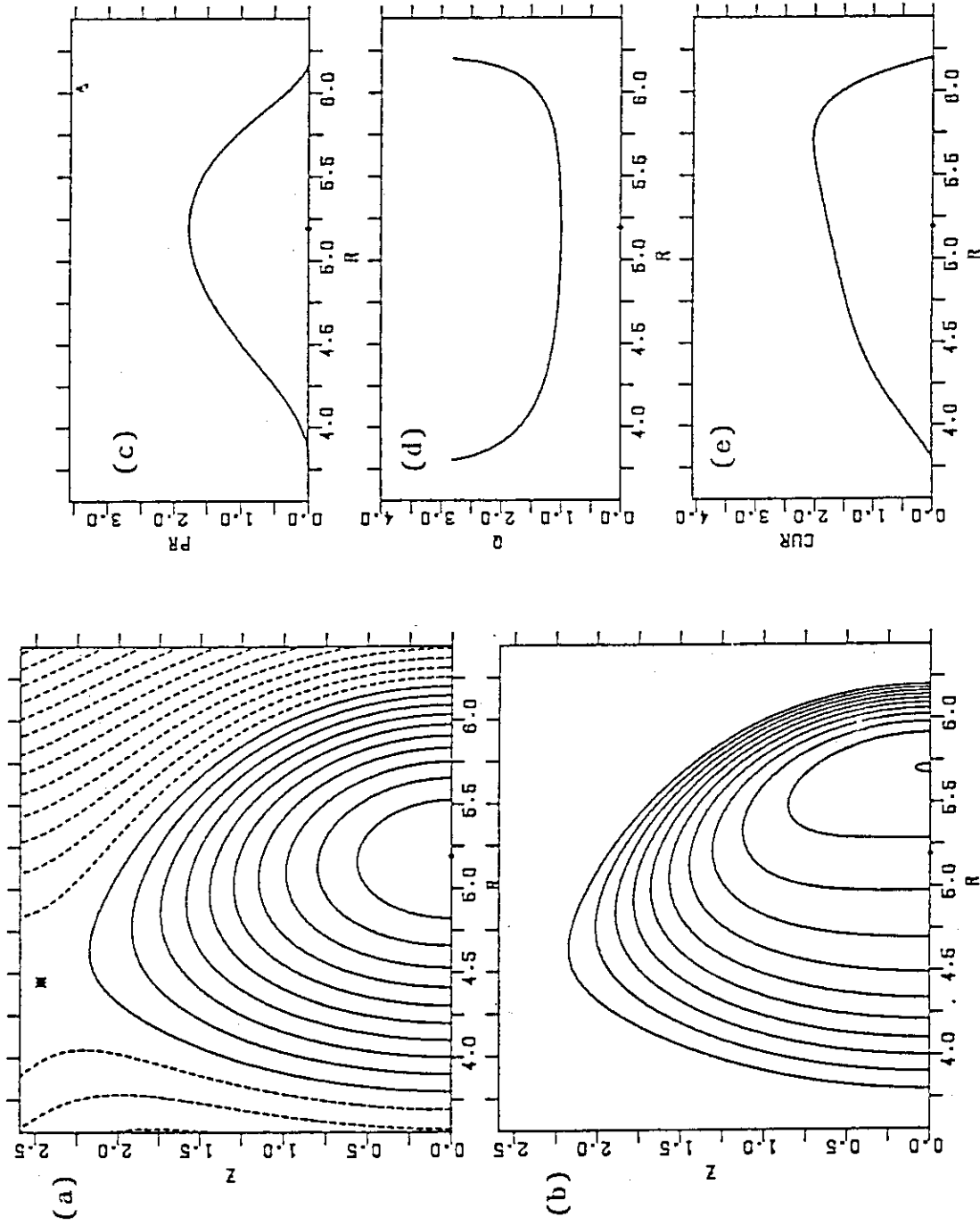


Fig. 3.1.2 Equilibrium for  $q_0=1$ ,  $q_s=3.0$ ,  $A=4$ ,  $\kappa=1.8$  and  $\delta=0.3$  : (a) flux surface, (b) contour of toroidal current, (c) plasma pressure, (d) safety factor and (e) toroidal current density on the horizontal midplane.

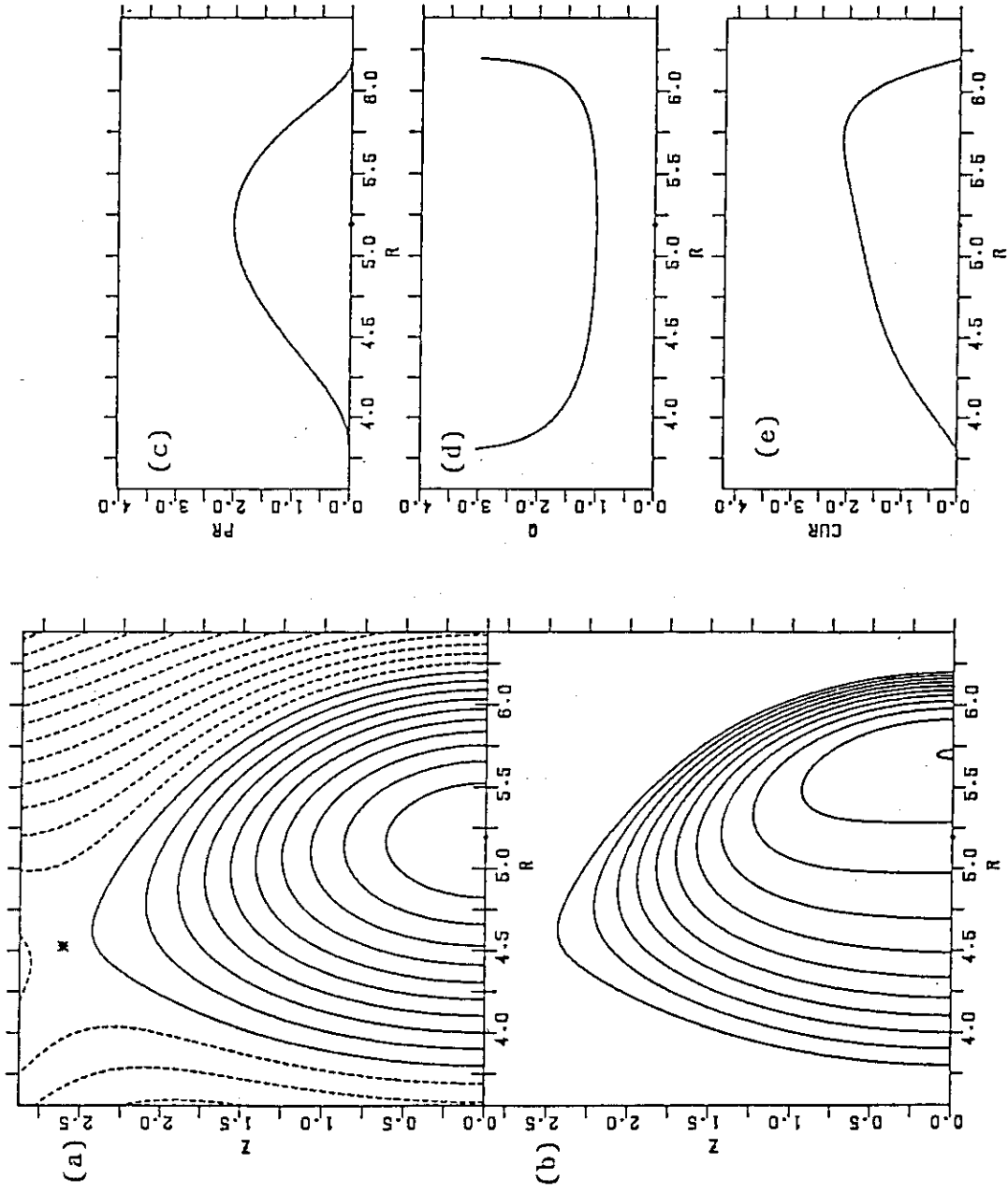


Fig. 3.1.3 Equilibrium for  $q_0=1$ ,  $q_s=3.0$ ,  $A=4$ ,  $\kappa=2.0$  and  $\delta=0.3$  : (a) flux surface, (b) contour of toroidal current, (c) plasma pressure, (d) safety factor and (e) toroidal current density on the horizontal midplane.

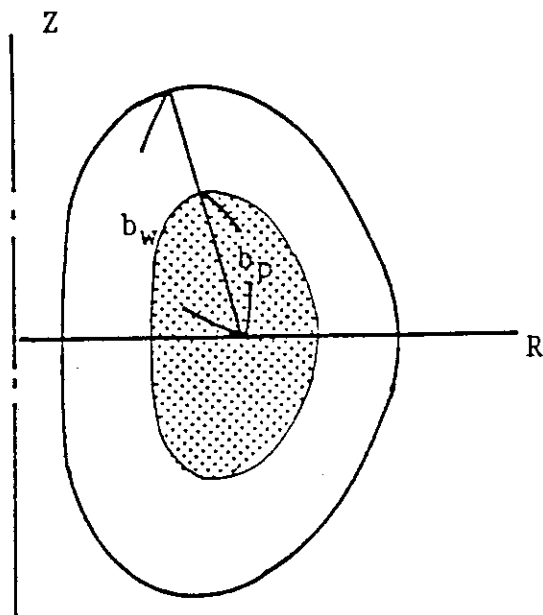


Fig. 3.1.4 Plasma surface and conducting wall. The radii,  $b_w$  and  $b_p$ , denote ones for the top of the dee from the magnetic axis.

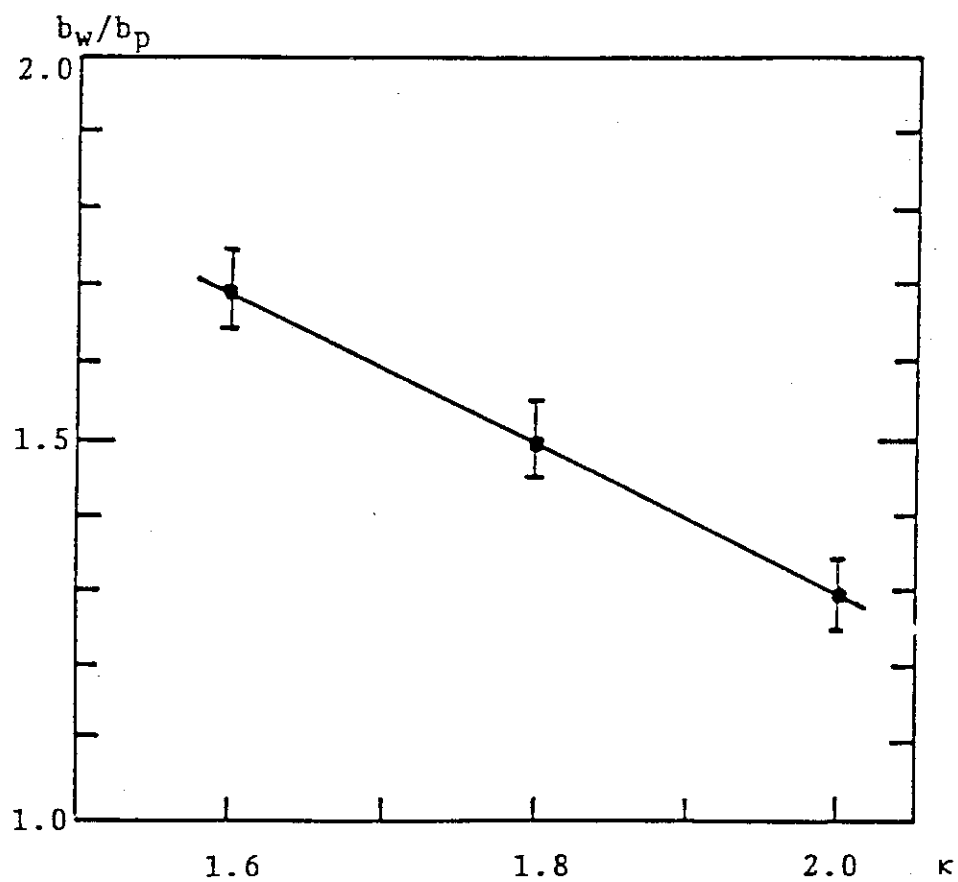


Fig. 3.1.5 Critical  $b_w/b_p$  vs.  $\kappa$ . Effect of  $\delta$  is within  $\pm 0.05$ .

### 3.2 Development of analysis code for plasma current, position and shape (PCPS) control system

#### Introduction

At this design stage of INTOR class tokamak reactor, evaluations of requirements for the plasma current, position and shape control system is important. The system includes plasma, structural components (first wall, blanket, shield, vacuum vessel, stabilizing shell and others), PF and active control coils, power supplies, detectors, computers and others. Our proposal is a development of an analysis code which specifies the requirement for the each components and total control system.

The scheme of the reference design of PCPS control system in FER is shown in Fig.3.2.1. The plasma current, position and shape are mainly controlled by the slow PF coil system in time scale of sec order. The PF control system controls the plasma by preprogram and feedback during discharges. The CF control system is dedicated to stabilization of vertical instability and fast feedback control of plasma vertical and radial position in the time scale of 10 to 100 msec orders. To build up the system, it is necessary to analyze not only the each system but also global behavior of the total system.

We have been devoted to our main effort to analysis of the vertical position control and to specify the requirements to the control system because the instability is critical in the design of the elongated plasma tokamak. The analyses are performed using rigid plasma displacement model. The growth time of the vertical instability may be affected by the effect of plasma deformation and is studied partially as shown in section 3.1. In the experiments of present-day tokamaks (JFT-2M, Doublet III, JET and others), it seems that the instability ( $n=0, n$ : toroidal mode number) is determined by the vertical instability caused by curvature of external field (decay index) and effects of



deformation is small. And the vertical position is enough controlled in these machines.

The shape control is performed slowly by PF control system in time scale of sec order in FER. We have no mean for the fast control of the plasma shape in the reference design. The introduction of fast feedback of the plasma shape will cause difficult coil systems or high control power. The scheme of shape control by PF control system is applicable under the situation where the vertical position is successfully stabilized and controlled by CF control system to sec order.

In the study of shape control, we focus to the feedback control of static equilibrium evolution. The main task in the study will be to formulate of MHD equilibrium equations, circuit equations among plasma current, coil currents and eddy current and transfer functions of power supply, computers and detectors and to develop a simulation code for the analysis of the time evolution of the total system. In general, to simulate the plasma totally, we should consider plasma particle and heat transports, magnetic field diffusion, pressure balance, interaction with wall and so on in one or two dimensional space. In this case, the associated analysis code will become to be very large. In the design study of a PCPS control system, more practical plasma model with a concentrated constants is desirable.

Here, we intend to formulate the equations in general form to construct the equation system at first, to formulate analytically using assumptions of high aspect ratio and small perturbations of plasma current, position and shape, and to reduce a linear system equation to have a good prospect of the system structure.

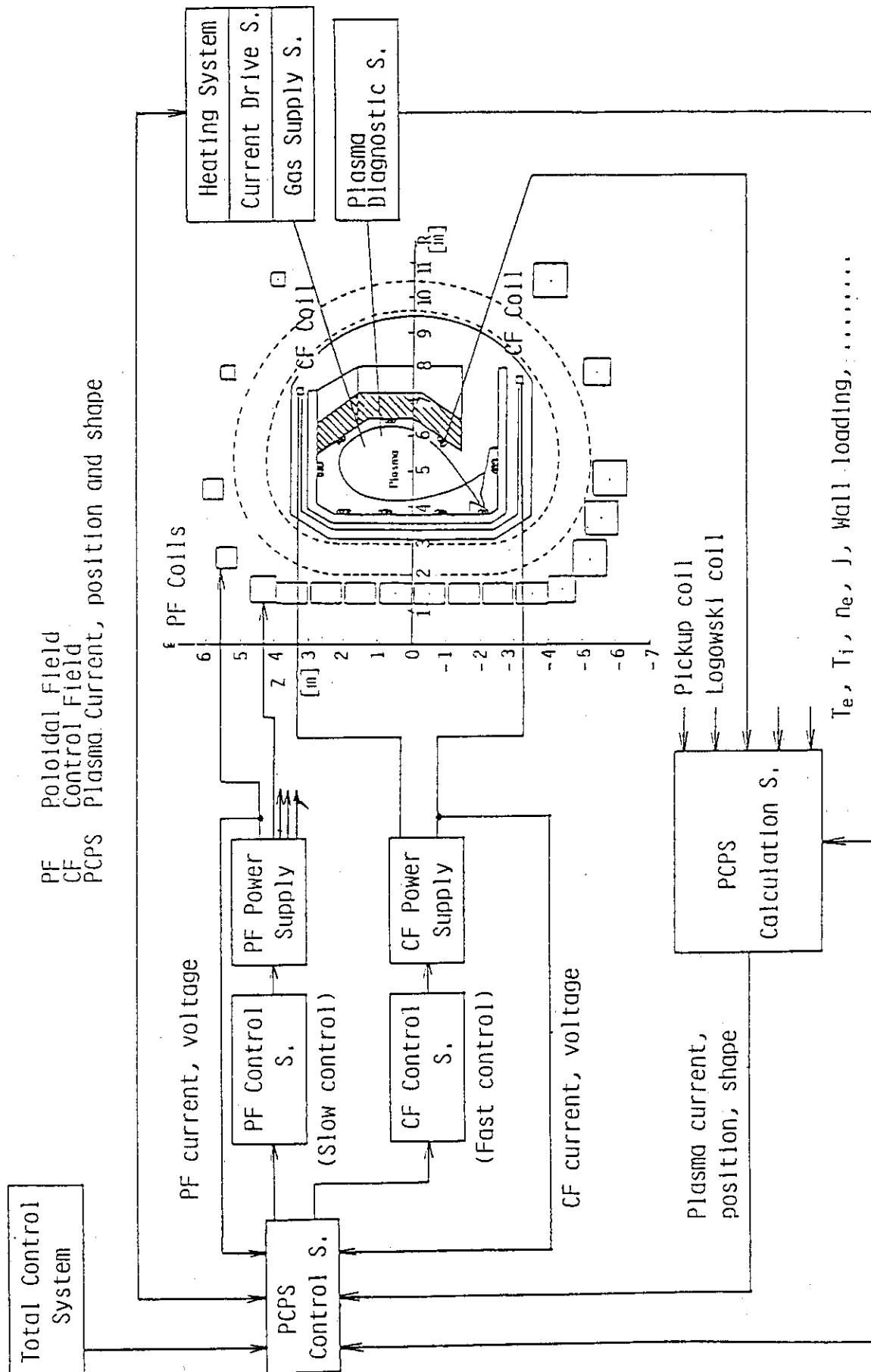


Fig. 3.2.1 Plasma current, position and shape (PCPS) control system

### 3.2.1 General formulation of plasma equilibrium and circuit equations

A MHD equilibrium state is expressed by a plasma current  $I_p$ , shape parameters  $S$ , plasma internal parameters  $X$ . The shape parameters  $S$  correspond to plasma position  $(R_p, Z_p)$ , an elongation  $k$ , a triangularity  $\delta$  and so on. Otherwise, positions on plasma surface and null points can be selected as shape parameters  $S$ . The plasma internal parameters  $X$  characterize the plasma state, and are a minor radius (half width) of a plasma  $a_p$ , a poloidal beta  $\beta_p$ , a normalized internal inductance  $l_i$  and so on. A mean minor radius  $a_p$  is included as an internal parameter because it is not fixed only by an external field and is related to limiter positions and conditions such as flux conservation.

The MHD equilibrium equation in an external field is formulated as

$$B_{ex} = I_p b(S, X). \quad (1)$$

Here  $B_{ex}$  are external field parameters which express the external field applied to the plasma. The components of  $B_{ex}$  can be magnitudes of multipole fields of the external field, such as vertical, quadrupole and hexapole field. The external field is proportional to  $I_p$  if the plasma shape and internal parameters are fixed. The functions  $b$  express the dependency of the external field on the plasma shape and internal parameters, and are generally non-linear functions of  $S$  and  $X$ . The ohmic heating field does not appear in Eq.(1) because of no field in the plasma region. In the formulation, it is important that independent variables are selected as the components of parameters  $B_{ex}$ ,  $S$  and  $X$ .

On the other hand, parameters  $B_{ex}$  are linearly related to external currents  $I_{ex}$  of coils and eddy currents as,

$$B_{ex} = \mathcal{V} I_{ex}. \quad (2)$$

A each component of the matrix  $\mathcal{V}$  is a magnitude of each field component generated by each external current. Generally, fields generated by eddy currents in surrounding conductors is not axisymmetric, so the fields by

eddy currents is averaged over the toroidal direction. By substituting Eq.(2) to Eq.(1), A plasma equilibrium equation is reduced to

$$I_p b(S, X) = \gamma I_{ex}. \quad (3)$$

In the next step, the circuit equation for plasma current is formulated to be of the form

$$(L_p \dot{I}_p) + R_p I_p + \dot{\Phi}_p = 0. \quad (4)$$

Here,  $(\dot{\phantom{x}})$  denotes time derivative.  $L_p$  is a plasma self-inductance and is generally a function of parameters  $S$  and  $X$ , i.e.  $L_p(S, X)$ .  $R_p$  is a plasma one-turn resistance and is one of the plasma internal parameters  $X$ .  $\Phi_p$  is a magnetic flux linked by a plasma column and is expressed as

$$\Phi_p = {}^t M_p(S, X) I_{ex}. \quad (5)$$

Each component of  $M_p$  is a mutual inductance between a plasma and an external current.  $({}^t)$  denotes a transposition of matrix. Substituting Eq.(5) into Eq.(4) forms

$$(L_p \dot{I}_p) + ({}^t M_p \dot{I}_{ex}) + R_p I_p = 0. \quad (6)$$

The circuit equations for external currents are formulated as

$$M_{ex} \dot{I}_{ex} + (M_p \dot{I}_p) + R_{ex} I_{ex} = V_{ex}. \quad (7)$$

The matrix  $M_{ex}$  is a inductance matrix between external currents. The  $M_{ex}$  is a constant matrix if the current paths are fixed. The second term in Eq.(7) expresses an induced voltage resulting from plasma time evolution. The  $R_{ex}$  is a resistance matrix of external currents. The components of  $V_{ex}$  are applied voltages to external currents. Applied voltages to eddy currents are zero. The  $R_{ex}$  is assumed to be a constant in time in this formulation.

In the last step, the equations for the evolution of plasma

internal parameters  $X$  are required to be formulated. In the equations, the heat and particle transports in the plasma, magnetic field diffusion, interactions between plasma and first wall, external heating injections and so on should be taken into account. For simplicity, we assume that the equations are expressed as

$$G(X, \dot{X}, S, \dot{S}, I_p, \dot{I}_p, Y, \dot{Y}) = 0. \quad (8)$$

The  $Y$  represents externally applied actions such as a heating injection.

For example, if a flux conservation and adiabatic condition are assumed, the following equations are derived.

$$k a_p^2 / R_p = \text{constant}, \quad (9)$$

$$\beta_p I_p^{2\gamma} a_p^{2\gamma-2} R_p^\gamma = \text{constant}. \quad (10)$$

Here, the  $\gamma$  is a specific heat ratio.

Equations (3), (6), (7) and (8) are the equations to be solved and non-linear equations. Here we linearize these equations. Each parameters is separated into reference and perturbation terms as

$$\begin{aligned} S &= S_0 + \delta S, \quad X = X_0 + \delta X, \quad I_p = I_{p0} + \delta I_p, \quad I_{ex} = I_{ex0} + \delta I_{ex}, \\ R_p &= R_{p0} + \delta R_p, \quad Y = Y_0 + \delta Y, \quad V_{ex} = V_{ex0} + \delta V_{ex}. \end{aligned} \quad (11)$$

The suffix 0 denotes values to a reference plasma state. The reference state satisfies the followings.

$$\begin{aligned} I_{p0} b_0 &= \nu I_{ex0}, \\ L_{p0} \dot{I}_{p0} + t_{M_{p0}} \dot{I}_{ex0} + R_{p0} I_{p0} &= 0, \\ M_{ex} \dot{I}_{ex0} + M_{p0} \dot{I}_{p0} + R_{ex} I_{ex0} &= V_{ex0}, \end{aligned}$$

$$G_0 = 0. \quad (12)$$

Where it is assumed that  $X_0$  and  $S_0$  do not change in time. The linearized equations for perturbation terms are followings.

$$\begin{aligned} b_0 \delta I_p + b_{S0} \delta S + b_{X0} \delta X &= \mathcal{V} \delta I_{ex}, \\ L_{p0} \dot{\delta I}_p + \delta L_p I_{p0} + t_{M_{p0}} \dot{\delta I}_{ex} + t_{\delta M_p} I_{ex0} + \mathcal{R}_{p0} \delta I_p + \delta \mathcal{R}_p I_{p0} &= 0, \\ M_{ex} \dot{\delta I}_{ex} + M_{p0} \dot{\delta I}_p + \delta M_p I_p + R_{ex} \delta I_{ex} &= \delta V_{ex}, \\ \delta G &= G_{X0} \delta X + G_{X0} \dot{\delta X} + G_{S0} \delta S + \dots = 0. \end{aligned} \quad (13)$$

Where the notation such as the matrix  $b_{S0}$  denotes that

$$b_{S0} = \left. \frac{\partial b}{\partial S} \right|_{S=S_0}.$$

And  $\delta L_p$  and  $\delta M_p$  are written as

$$\begin{aligned} \delta L_p &= t_{L_{pS0}} \delta S + t_{L_{pX0}} \delta X, \\ \delta M_p &= M_{pS0} \delta S + M_{pX0} \delta X. \end{aligned} \quad (14)$$

### 3.2.2 Analytical formulation of plasma equilibrium and circuit equations

We are concerned with obtaining concrete expressions for the plasma equilibrium and circuit equations in the previous section. Here, the expressions are formulated using Fourier expansion of the flux function and the plasma boundary, and also the usual expansion in the inverse aspect ratio[1]. The formulation has applicable limits to the aspect ratio and plasma displacement and deformation. But the formulation is relatively simple and easy to look insight of the dependency among parameters. In the first step to develop analysis model of PCPS control system, this simple formulation seems to be adequate. The formulation can be replaced by more accurate method of numerical calculation solving MHD equilibrium, because the structure of the equations will not change.

At first, the Grad-Shafranov MHD equilibrium equation is given by

$$\frac{\partial^2 \Psi}{\partial R^2} - \frac{1}{R} \frac{\partial \Psi}{\partial R} + \frac{\partial^2 \Psi}{\partial Z^2} = -\mu_0 R j_p, \quad (15)$$

with

$$j_p = R \frac{\partial P}{\partial \Psi} + \frac{1}{\mu_0 R} F \frac{\partial F}{\partial \Psi},$$

in the usual axisymmetric cylindrical coordinate (R,Z).  $\Psi$  is a poloidal flux function and  $j_p$  is a plasma current density in the toroidal direction. P and F are plasma pressure and poloidal current function, respectively, and are functions of  $\Psi$ . Each component of magnetic field is expressed in term of  $\Psi$  and F as

$$B_R = -\frac{1}{R} \frac{\partial \Psi}{\partial Z}, \quad B_Z = \frac{1}{R} \frac{\partial \Psi}{\partial R}, \quad B_\varphi = \frac{F}{R}. \quad (16)$$

The plasma current density  $j_p$  in Eq.(15) is assumed to be expressed as

$$j_p = j_0 \left\{ \frac{R}{R_0} \beta_p + \frac{R_0}{R} (1 - \beta_p) \right\} \left\{ J_{0\sigma} + (1 - J_{0\sigma}) \frac{\Psi - \Psi_s}{\Psi_0 - \Psi_s} \right\}, \quad (17)$$

where  $j_0$ ,  $\Psi_0$  and  $\Psi_s$  are current density on the magnetic axis and

poloidal flux function on the magnetic axis and at the plasma surface, respectively. The  $R_p$  and the  $\beta_p$  are plasma major radius and poloidal beta, respectively. The  $J_{0\sigma}$  is a parameter describing a plasma current distribution and takes a value of 0 to 1.  $J_{0\sigma}=0$  and  $J_{0\sigma}=1$  correspond to parabolic and flat current distributions, setting a normalized internal inductance  $l_i=1$  and  $l_i=0.5$ , respectively.

The toroidal coordinate  $(\rho, 0)$  illustrated in Fig.3.2.2 is used where  $R_p$  is the plasma geometrical major radius. Equation (15) is expanded by an inverse aspect ratio  $\epsilon (=r_p/R_p)$  to the first order in the same way shown in Ref.[1]. An up-down symmetry is assumed for simplicity and the plasma boundary is expressed in the form

$$\rho_\sigma = r_p \{1 + \sum_{n=1} (\epsilon_{0n} + \epsilon_{1n}) \cos(n\theta)\}. \quad (18)$$

Here,  $r_p$  is the mean minor radius of plasma and here  $\epsilon_{0n}$  and  $\epsilon_{1n}$  are the zero and first order shape parameters, respectively.

As a result, flux functions in vacuum region of  $\Psi_e$  and  $\Psi_p$ , which represent the external magnetic field and the magnetic field generated by the plasma current, are expressed as

$$\Psi_e(\rho, 0) = \sum_{n=0} [C_{0n} + C_{1n} - r_p/R_p C_{0n-1} (\rho/2r_0)^2] (\rho/r_0)^n \cos(n\theta), \quad (19)$$

$$\begin{aligned} \Psi_p(\rho, 0) = & -D_0 (\ln(8R_p/\rho) - 2) \\ & + [D_{11} + (r_0 D_0 / 2R_p) \{ \ln(8R_p/\rho) - 1 \} (\rho/r_0)^2] (\rho/r_0)^{-1} \cos(0) \\ & + \sum_{n=2} [D_{0n} + D_{1n} - r_0/R_p D_{0n-1} (\rho/2r_0)^2] (\rho/r_0)^{-n} \cos(n\theta). \end{aligned} \quad (20)$$

where  $r_0$  is a characteristic length. The relations between plasma shape and internal parameters and field coefficients (parameters) are given by,

$$C_{0n} = -(D_0/2) (r_0/r_p)^n s_n \epsilon_{0n}, \quad (n \geq 2) \quad (21)$$



$$C_{11} = -(D_0 r_0 / 2R_p) [\ln(8R_p / r_p) + \beta_p + l_i / 2 - 3/2 + w_1 \beta_p \varepsilon_{02}], \quad (22)$$

$$C_{1n} = -(D_0 / 2) (r_0 / r_p)^n \times [s_n \varepsilon_{1n} + (r_p / R_p) \{t_n \varepsilon_{0n-1} + u_n \varepsilon_{0n+1} + v_n \beta_p \varepsilon_{0n-1} + w_n \beta_p \varepsilon_{0n+1}\}], \quad (n > 2) \quad (23)$$

and

$$D_{0n} = -(D_0 / 2) (r_0 / r_p)^{-n} s_n' \varepsilon_{0n}, \quad (n > 2)$$

$$D_{11} = -(D_0 r_p / 2R_p) (r_0 / r_p)^{-1} [-\beta_p - l_i / 2 + 1/2 + t_1' \varepsilon_{02} + w_1' \beta_p \varepsilon_{02}],$$

$$D_{1n} = -(D_0 / 2) (r_0 / r_p)^{-n} \times [s_n' \varepsilon_{1n} + (r_p / R_p) \{t_n' \varepsilon_{0n+1} + u_n' \varepsilon_{0n-1} + v_n' \beta_p \varepsilon_{0n-1} + w_n' \beta_p \varepsilon_{0n+1}\}], \quad (n > 2)$$

$$D_0 = -(\mu_0 R_p I_p / 2\pi). \quad (24)$$

Where coefficients  $s_n$ ,  $s_n'$ ,  $t_n$ ,  $t_n'$ ,  $u_n$ ,  $u_n'$ ,  $v_n$ ,  $v_n'$ ,  $w_n$  and  $w_n'$  are functions of  $J_{0\sigma}$  and depend on a plasma internal inductance  $l_i$ . The coefficient  $C_{00} + C_{10}$  has no relation with the plasma equilibrium because it shows OH field. Equations (21), (22) and (23) express the relations between plasma shape and internal parameters and external field parameters, which corresponds to Eq.(1). Equation (22) expresses the relation between the vertical field and the radial position of plasma. Equations of Eq.(21) and (23) express the relations of the zero and first order between plasma deformation and multipole magnetic fields. The last terms of Eqs.(22) and (23) show mutual couplings among Fourier components of deformation and external field because of the toroidal effect.

External fields are usually given in a fixed coordinate system located in space. The expression of external field given by Eq.(19) in the toroidal coordinate of  $(\rho, \theta)$  is transformed to a following expression in a toroidal coordinate  $(\xi, \tilde{\theta})$  shown in Fig.3.2.2, where a fixed point  $R_0$  is the center, as

$$\Psi_{e0}(\xi, \tilde{\theta}) = \sum_{n=0} [\tilde{C}_n - r_0 / R_0 \tilde{C}_{n+1} (\xi / 2r_0)^2] (\xi / r_0)^n \cos(n\tilde{\theta}). \quad (25)$$

the relations of coefficients between Eqs.(19) and (25) are given as

$$\tilde{C}_n = C_{0n} + C_{1n} - (n+1)(\Delta/r_0)\{C_{0n+1} + C_{1n+1}\} + (\Delta/4R_0)C_{0n}, \quad (26)$$

to the first order in  $\Delta$ . Where  $\Delta = R_0 - R_p$  and  $\Delta$  is the plasma displacement in the radial direction.

On the other hand, the external field is given by external currents (coils and eddy currents) as

$$\tilde{C}_n = \sum_i \nu_{ni} I_i. \quad (27)$$

Here the sum is over all external current filament, and  $\nu_{ni}$  are coefficients given by geometrical configuration of coils and eddy currents. If coils and eddy current are assumed to be axisymmetric, the coefficients are derived by inverse aspect expansion as same as plasma flux. Or in general, the coefficients are derived by numerical integrations of Biot-Savart's law.

In the next, the self and mutual inductances are expressed. The plasma self-inductance is assumed to be given as

$$L_p = \mu_0 R_p \{ \ln(8R_p/r_p) + 1/2 - 2 \}, \quad (28)$$

and mutual inductance between plasma and an axisymmetric coil is given as

$$M_{pi} = 2\pi \Psi_{p0}(r_i, \tilde{\theta}_i) / I_p. \quad (29)$$

Where  $\Psi_{p0}$  is the plasma flux function of Eq.(18) transformed to the coordinate  $(\xi, \tilde{\theta})$ , and  $(r_i, \tilde{\theta}_i)$  is a position of the coil. In general, the mutual inductance is calculated by the numerical integration of

$$M_{pi} = 1/I_p \int \Psi_{p0} j_{\varphi i} / R \, dv \quad (30)$$

Where  $j_{\varphi i}$  is a component in toroidal direction of current density of  $i$ -th external current and the integration is over the external current distribution. Self and mutual inductances among external currents are derived by inverse aspect expansion or usual numerical integrations.

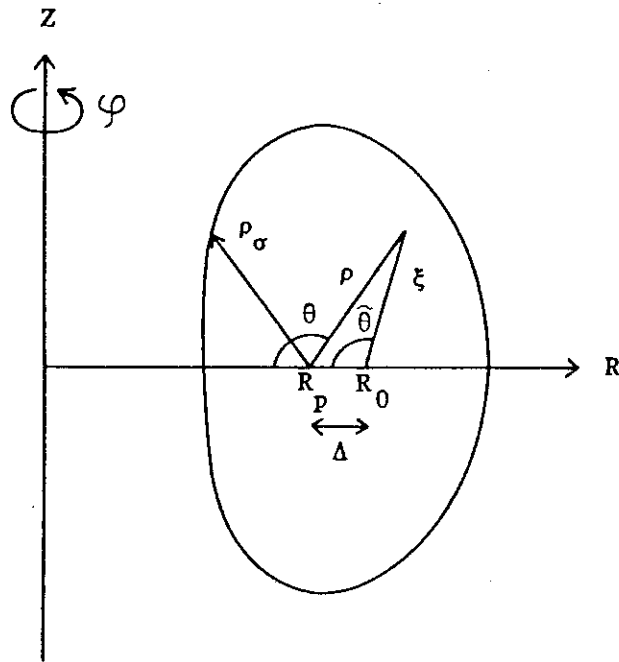


Fig.3.2.2 Coordinate systems.

### 3.2.3 State equations of a plasma, coil and eddy current

State equations of plasma, coil and eddy currents are derived by linearization of the relations shown in the previous section. The procedure to linearize is shown in Sec. 3.2.2. For simplicity, the mean minor radius of a plasma column  $r_p$  and a normalized internal inductance  $l_i$  are assumed to be fixed. We introduce here the shaping parameters  $\delta\epsilon$ , the external currents  $\delta I$ , and the field parameters  $\delta C_0$ ,  $\delta C_1$  and  $\delta\tilde{C}$  as perturbation terms and they are defined as

$$\begin{aligned}\delta\epsilon &= {}^t[\Delta/R_0, \delta\epsilon_{12}, \dots, \delta\epsilon_{1N}], \\ \delta I &= {}^t[\delta I_p, \delta I_1, \dots, \delta I_{NC}], \\ \delta C_0 &= {}^t[\delta C_{02}, \dots, \delta C_{0N}], \\ \delta C_1 &= {}^t[\delta C_{11}, \dots, \delta C_{1N}], \\ \delta\tilde{C} &= {}^t[\delta\tilde{C}_1, \dots, \delta\tilde{C}_N].\end{aligned}\tag{31}$$

Where zero order shape parameters are assumed not to change.  $N$  and  $NC$  are the number of shape parameters to be considered including the radial displacement and the number of external currents, respectively and  $N+1$  must be equal to or less than  $NC$  so that the plasma current and the shape parameters are controllable if no eddy current is included.

The linearized equations correspond to Eqs.(21),(22),(23),(26) and (27) are written in the form

$$\delta C_0 = A_0 \delta\epsilon + B_0 \delta I,\tag{32}$$

$$\delta C_1 = A_1 \delta\epsilon + B_1 \delta I + B_\beta \delta\beta_p,\tag{33}$$

$$\delta\tilde{C} = D\delta C_0 + E\delta C_1 + F\delta\epsilon,\tag{34}$$

and

$$\delta\tilde{C} = F\delta I.\tag{35}$$

Here,  $A_0$ ,  $A_1$ ,  $B_0$ ,  $B_1$ ,  $F$  and  $B_p$  are coefficient matrices and a vector. These coefficients are derived by partial differentiations of the non-linear expressions by the variables and by substituting the values of the reference state. The linearized circuit equations of the plasma current and external currents are written in the matrix form as

$$M\dot{\delta I} + P_\varepsilon \dot{\delta \varepsilon} + P_\beta \dot{\delta \beta}_p + P_a \dot{\delta a}_p + R\delta I = \delta V. \quad (36)$$

Where the matrices  $M$  and  $R$  are the inductance and resistance matrices among plasma current and external currents. And

$$\delta V = {}^t[0, \delta V_1, \dots, \delta V_{NC}], \quad (37)$$

$\delta V_i$  is an applied voltage to  $i$ -th external current. The coefficients  $P_\varepsilon$ ,  $P_\beta$  and  $P$  are derived as same as above.

Finally, from Eqs.(32) to (36), state and output equations are derived in the forms as

$$\dot{\delta I} = S\delta I + T_\beta \dot{\delta \beta}_p + T_a \dot{\delta a}_p + T_v \delta V \quad (38)$$

$$\delta \varepsilon = U\delta I + V_\beta \delta \beta_p. \quad (39)$$

These equations are in the usual form of a linear system. The inputs to the system are applied voltages on the coils, perturbation of plasma poloidal beta and resistance. The outputs are plasma radial displacement and deformations.

#### Reference

- [1] T. Shoji, Plasma equilibrium in axisymmetric hybrid systems, Nucl. Fusion 165 (1976) 829.

### 3.3 Simulation studies on plasma position control for the next generation tokamak machines with up-down asymmetry

#### 3.3.1 Introduction

The control of plasma vertical position is one critical issue in future tokamak reactors with elongated plasmas, favorable for increasing allowable beta limit and probably energy confinement time, since vertically elongated plasmas are inherently unstable in the vertical direction without feedback control. A lot of works on this area have been performed for the next generation tokamak reactors [1 ~ 4, 7]. The accommodation of active coils, the design of highly conductive passive shells, non-circular plasma shape, etc. will provide significant constraints not only on the position control property, but also on the design concept of reactor structure, like a reactor maintenance, bellows resistance and so on.

In those studies, the power required for the plasma position control is evaluated to clear the relation between the reactor design options and the required control power, taking into account the shielding effect that passive structures (vacuum vessel, blanket and shield) and poloidal field coils (Ohmic heating (OH) and equilibrium field (EF) coils) weaken the control field by active coils. However, in those evaluations, an initial vertical displacement of a plasma or an external radial disturbance field is intentionally supplied to a plasma as an initial perturbation. These disturbances are rather artificial and appropriate origins of them are difficult to be identified. It is then not easy to estimate the reasonable required power for vertical position control. On the other hand, in up-down asymmetric plasmas, the vertical displacements are generated by introducing the radial plasma displacements, the origin of which are rather clear, e.g. plasma MHD activities. As a result, the power supply requirements could be evaluated on the reasonable ground.

It is first pointed out that the plasma vertical motion is coupled with the radial motion in an up-down symmetric configuration, and that the radial perturbation on plasma position will force the plasma to move vertically [5]. Some design of the next generation tokamak reactors such as INTOR adopt a single-null divertor configuration, in which the external equilibrium field and reactor structures surrounding plasma are asymmetric with respect to a  $Z=0$  plane. There are two types of couplings

to be considered. One is asymmetric components of eddy currents in passive structures induced by plasma radial displacement, which produce radial perturbation fields. The other is asymmetric external equilibrium fields, which is essentially canceled in an original equilibrium position, but appear when plasmas are displaced radially.

The stable region of plasma parameters for position control, which is more severely limited due to the radial-vertical coupling, and the growth rate are analyzed in some details [5]. In those asymmetric configurations, plasmas are expected to move significantly in the vertical direction and vertical position would result in uncontrollable with a practical level of control power, even by a moderate disturbance of radial motion. In a symmetric option, for such a moderate perturbation, plasmas move in the radial direction and could find a new equilibrium position with accompanying some weak interaction between plasma and first wall, and plasmas could be shut down in a controlled way. On the other hand, the asymmetric feature would induce large vertical displacement, which would yield a strong interaction between plasma and first wall and/or divertor plates on the single-null point side, and finally plasmas would be disrupted violently, although the radial motion may not be so severe.

This paper devotes to detailed analyses on plasma position control in an asymmetric plasma configuration like a single-null divertor concept. Section 2 describes fundamental formulations on plasma position control. Section 3 represents stability analysis. Section 4 shows results of simulation studies on the control of both vertical and radial position in an asymmetric tokamak reactor with respect to a  $Z=0$  plane. The conclusions are summarized in Section 5.

## 3.3.2 Fundamental formulations

Adiabatic compression/decompression is assumed when a plasma moves in the radial direction. However, a plasma shape is assumed not to change at plasma movement (rigid displacement model).

A kinetic equation of plasma radial movement is simply expressed as eq. (1) by using the Shafranov formula [6] which uses circular, high aspect ratio and low beta approximation.

$$M_p \ddot{R}_p = \frac{\mu_0 I_p^2}{2} \{ \ln(8R_p/a_p) + \beta_p + \frac{1}{2}(\ell_1 - 3) \} + F_R \quad (1)$$

Where,  $M_p$  : plasma mass  
 $R_p$  : plasma major radius  
 $a_p$  : plasma minor radius  
 $I_p$  : plasma toroidal current  
 $\beta_p$  : poloidal beta  
 $\ell_1$  : normalized internal inductance  
 $\mu_0$  : permeability  
 $F_R$  : radial force by external field

When a plasma moves in the radial and vertical directions by  $\delta R_p$  and  $\delta Z_p$ , respectively, external vertical field applied to the plasma by equilibrium field coils,  $B_z(R+\delta R_p, Z+\delta Z_p)$ , is expressed by eq. (2).

$$B_z(R+\delta R_p, Z+\delta Z_p) \doteq B_z(R, Z) + \frac{\partial B_z}{\partial R} \delta R_p + \frac{\partial B_z}{\partial Z} \delta Z_p \quad (2)$$

Where,  $B_z(R, Z)$  is an external vertical field in the plasma at an equilibrium position. Multiplying eq. (2) by plasma toroidal current density,  $i_p(R, Z)$ , and integrating it in the plasma region, we obtain the equation of external radial force,  $F_R$ , at plasma displacement as eq. (3).

$$F_R \doteq 2\pi I_p B_{v0}(R_p - n\delta R_p + k\delta Z_p) + 2\pi I_p R_p B_v \quad (3)$$

Here,  $B_{v0}$  is equilibrium vertical field, and  $R_p$ ,  $n$ ,  $k$  and  $B_v$  are defined by the following equations.



$$R_p = \frac{1}{I_p B_{VO}} \iint R \cdot i_p(R, Z) \cdot B_Z(R, Z) dR dZ \quad (4)$$

$$B_{VO} = \frac{1}{I_p} \iint B_Z(R, Z) \cdot i_p(R, Z) dR dZ \quad (5)$$

$$n = - \frac{1}{I_p B_{VO}} \iint R \cdot \frac{\partial B_Z}{\partial R} \cdot i_p(R, Z) dR dZ \quad (6)$$

$$\begin{aligned} k &= - \frac{1}{I_p B_{VO}} \iint R \cdot \frac{\partial B_Z}{\partial Z} \cdot i_p(R, Z) dR dZ \\ &= \frac{1}{I_p B_{VO}} \iint \frac{\partial}{\partial R} \{ R \cdot B_R(R, Z) \} i_p(R, Z) dR dZ \end{aligned} \quad (7)$$

$$B_v = \frac{1}{2\pi I_p R_p} \iiint R \cdot i_p(R, Z) B_{Zd}(R, Z, \Theta) dR dZ d\Theta \quad (8)$$

The  $n$  defined by eq. (6) is a natural extension of the decay index  $n$  value ( $n$ -index)[7]. The  $k$  represents the strength of the interaction between radial and vertical displacements and becomes zero if the external field is completely symmetric with respect to midplane ( $Z=0$  plane). However, if the external field is asymmetric like INTOR plasma, the  $k$  is not zero and affects plasma position dynamics. We call this  $k$  as  $k$ -index in the present paper. The  $B_{Zd}$  represents the vertical fields by active coils, eddy currents, induced current in EF and OH coils and so on.

Linearizing eq. (1), the following equation is obtained for plasma radial movement.

$$\begin{aligned} M_p \ddot{\delta R_p} &= \{ 2\pi B_{VO} (1 - \frac{1}{\Lambda_0} - n) - \frac{\mu_0 I_p}{4R_p} - \frac{7}{6} \mu_0 I_p \frac{\beta_p}{R_p} \} \delta R_p - 2\pi B_{VO} k \delta Z_p \\ &\quad - (2\pi R_p B_{VO} + \mu_0 I_p \beta_p) \frac{\delta I_p}{I_p} + I_p \left( \sum_i \frac{\partial M_{pi}}{\partial R_p} \frac{\delta I_i}{I_p} + \sum_k \frac{\partial M_{pk}}{\partial R_p} \frac{\delta I_k}{I_p} \right) \\ &\quad + \frac{\mu_0 I_p}{2} (\delta \beta_p + \frac{1}{2} \delta \ell_i) + 2\pi R_p B_{vd} \end{aligned} \quad (9)$$

where,  $M_{pi}$  : mutual inductance between plasma and the  $i$ -th coil  
 $M_{pk}$  : mutual inductance between plasma and the  $k$ -th eddy current mode

$I_i$  : the i-th coil current (subscript i represents each poloidal coil)

$I_k$  : eddy current of the k-th mode (subscript k represents each eddy current)

$B_{vd}$  : vertical disturbance field

$\Lambda_0$  in eq. (9) is defined by eq. (10).

$$\Lambda_0 = -4\pi R_p B_{v0} / (\mu_0 I_p) = \ln(8R_p/a_p) + \beta_p + \frac{1}{2}(\ell_1 - 3) \quad (10)$$

The vertical field,  $B_{vm}$ , by active coil and/or induced eddy current in the structures is expressed by the following equation. (Subscript, m, represents each active coil and/or eddy current modes in the structures.)

$$B_{vm} \doteq \frac{1}{2\pi R_p} \frac{\partial M_{pm}}{\partial R_p} \delta I_m \quad (11)$$

The mutual inductances between plasma and eddy current modes are numerically calculated by eddy current analysis code [8].

In deriving eq. (9),  $a_p^2/R_p$  is kept constant (conservation of toroidal flux in a plasma) and  $\beta_p$  scales as  $1/(I_p^2 R_p^{7/3})$  (adiabatic compression/decompression). The  $\delta\beta_p$  in eq. (9) represents the  $\beta_p$  change owing to the change in plasma thermal energy which is not adiabatic.

The linearized equation of plasma vertical movement is represented by eq. (12).

$$\begin{aligned} M_p \ddot{\delta Z_p} = & 2\pi B_{v0} n \delta Z_p - 2\pi B_{v0} k \delta R_p + I_p \left( \sum_i \frac{\partial M_{pi}}{\partial Z_p} \frac{\delta I_i}{I_p} + \sum_k \frac{\partial M_{pk}}{\partial Z_p} \frac{\delta I_k}{I_p} \right) \\ & - 2\pi R_p B_{Rd} \end{aligned} \quad (12)$$

The radial field,  $B_{Rm}$ , by active coil and/or induced eddy current is represented by the following equation.

$$B_{Rm} \doteq - \frac{1}{2\pi R_p} \frac{\partial M_{pm}}{\partial Z_p} \delta I_m \quad (13)$$

The second term in eq. (12) represents the coupling between radial and vertical movements, and  $B_{Rd}$  represents radial disturbance field.

Other equations needed for simulation are circuit equations of plasma current, poloidal coils and eddy currents as expressed by the following equations [7], [9]. Each eddy current mode is normalized so as to compose a circuit with a self-inductance  $\tau_k$  and a unit resistance [8].

$$(\dot{L}_p I_p) + \sum_i (\dot{M}_{pi} I_i) + \sum_k (\dot{M}_{pk} I_k) + r_p I_p = 0 \quad (14)$$

$$L_i \dot{I}_i + (\dot{M}_{pi} I_p) + \sum_j \dot{M}_{ij} I_j + \sum_k \dot{M}_{ik} I_k + r_i I_i = V_i \quad (15)$$

$$\tau_k \dot{I}_k + (\dot{M}_{pk} I_p) + \sum_i \dot{M}_{ik} I_i + I_k = 0 \quad (16)$$

Where,  $L_p$  : plasma self-inductance

$r_p$  : plasma one turn resistance

$L_i$  : self-inductance of the  $i$ -th coil

$M_{ij}$  : mutual inductance between the  $i$ -th coil and the  $j$ -th coil

$M_{ik}$  : mutual inductance between the  $i$ -th coil and the  $k$ -th eddy current mode

$r_i$  : resistance of the  $i$ -th coil

$I_j$  : the  $j$ -th coil current

$\tau_k$  : time constant of the  $k$ -th current mode

Equation (14) can be linearized and written as

$$-(2\pi R_p B_{v0} + \mu_0 I_p \beta_p) \delta R_p + I_p L_p \frac{\delta I_p}{I_p} + \sum_i I_p M_{pi} \frac{\delta I_i}{I_p} + \sum_k I_p \frac{(\dot{M}_{pk} I_k)}{I_p} + r_p \delta I_p = 0 \quad (17)$$

In deriving eq. (17),  $r_p$  is assumed to be constant and the following relations are used together with condition for toroidal flux conservation.

$$\sum_i \frac{\partial M_{pi}}{\partial R_p} I_{i0} = 2\pi R_p B_{v0} \quad \sum_i \frac{\partial M_{pi}}{\partial Z_p} I_{i0} = 0 \quad (18)$$

Here,  $I_{i0}$  represents the  $i$ -th coil current for plasma equilibrium.

$$\dot{\delta I_p} I_p = I_p \left\{ \frac{\partial L_p}{\partial R_p} + \left( \frac{a_p}{2R_p} \right) \frac{\partial L_p}{\partial a_p} \right\} \dot{\delta R_p} = -(4\pi R_p B_{vo} + \mu_0 I_p B_p) \dot{\delta R_p} \quad (19)$$

Differentiating eqs. (9) and (12) with respect to time,  $t$ , and neglecting plasma mass,  $M_p$ , equations (9), (12), (15), (16), (17) are written in the form

$$\dot{\vec{A}}\vec{y} + \vec{R}\vec{y} = \vec{b} \quad (20)$$

Where, the vectors  $\vec{y}$  and  $\vec{b}$ , and the symmetric matrixes  $A$  and  $R$  are expressed as follows.

$$\vec{y} = (\delta Z_p, \delta R_p, \delta I_p/I_p, \dots, \delta I_1/I_p, \dots, \delta I_k/I_p, \dots)^t \quad (21)$$

$$\vec{b} = \left\{ 2\pi R_p B_{Rd}, -\frac{\mu_0 I_p}{2} (\delta \beta_p + \frac{\delta \ell_1}{2}) - 2\pi R_p B_{vd}, \right. \\ \left. , 0, \delta V_1, \dots, \delta V_i, \dots, 0, \dots \right\}^t \quad (22)$$

Here,  $\delta V_i$  represents the voltage change of the  $i$ -th coil from the initial equilibrium conditons.

$$A = \begin{bmatrix} 2\pi B_{vo} n, & -2\pi B_{vo} k, & 0 & , & \dots, & I_p \frac{\partial M_{pi}}{\partial Z_p}, & \dots, & I_p \frac{\partial M_{pk}}{\partial Z_p}, & \dots \\ -2\pi B_{vo} k, & a_{22}, & -(2\pi R_p B_{vo} + \mu_0 I_p \beta_p), & \dots, & I_p \frac{\partial M_{pi}}{\partial R_p}, & \dots, & I_p \frac{\partial M_{pk}}{\partial R_p}, & \dots \\ 0 & , & -(2\pi R_p B_{vo} + \mu_0 I_p \beta_p), & L_p I_p, & \dots, & I_p M_{pi}, & \dots, & I_p M_{pk}, & \dots \\ \vdots & \vdots & \vdots & \ddots & \vdots & \vdots & \vdots & \vdots & \vdots \\ \vdots & \vdots & \vdots & \vdots & \ddots & \vdots & \vdots & \vdots & \vdots \\ I_p \frac{\partial M_{pi}}{\partial Z_p}, & I_p \frac{\partial M_{pi}}{\partial R_p}, & L_p M_{pi}, & \dots, & I_p L_i & & & 0 & \\ \vdots & \vdots & \vdots & \ddots & \vdots & \ddots & \vdots & \vdots & \vdots \\ \vdots & \vdots & \vdots & \vdots & \ddots & \vdots & \ddots & \vdots & \vdots \\ I_p \frac{\partial M_{pk}}{\partial Z_p}, & I_p \frac{\partial M_{pk}}{\partial R_p}, & I_p M_{pk}, & \dots, & 0 & & & I_p \tau_k & \\ \vdots & \vdots & \vdots & \ddots & \vdots & \ddots & \vdots & \vdots & \vdots \\ \vdots & \vdots & \vdots & \vdots & \ddots & \vdots & \ddots & \vdots & \vdots \\ \vdots & \vdots & \vdots & \vdots & \ddots & \vdots & \ddots & \vdots & \vdots \end{bmatrix} \quad (23)$$

$$a_{22} = 2\pi B_{V0} \left(1 - \frac{1}{\Lambda_0} - n\right) - \frac{\mu_0 I_p}{4R_p} - \frac{7}{6} \mu_0 I_p \frac{\beta_p}{R_p} \quad (24)$$

$$R = \begin{bmatrix} 0 & & & & \\ & 0 & & & \\ & & I_p r_p & & \\ & & & \ddots & \\ & & & & I_p r_i \\ & 0 & & & & I_p \\ & & & & & & \ddots \end{bmatrix} \quad (25)$$

In non-circular and high beta plasma, the equilibrium vertical field,  $B_{V0}$ , given by eq. (10) is different from that of numerical equilibrium calculation given by eq. (5). In applying the analytical formulation to non-circular and/or high beta plasmas, the functional dependences of vertical field,  $B_{V0}$ , and plasma self-inductance,  $L_p = \mu_0 R_p \{\ln(8R_p/a_p) + \ell_i/2 - 2\}$ , on  $I_p$ ,  $R_p$ ,  $a_p$ ,  $\beta_p$  and  $\ell_i$  are assumed to be the same as low beta circular plasma. For the analyses of the plasma position control, we use  $B_{V0}$ ,  $\ell_i$  and  $L_p$  numerically obtained by plasma equilibrium calculation, and re-define  $\beta_p$  by eq. (26) to ensure that the analytical formulation provides the same  $B_{V0}$  as numerical one.

$$\beta_p = \Lambda_0 - \frac{L_p}{\mu_0 R_p} - \frac{1}{2} \quad (26)$$

This definition of  $\beta_p$  is different from the usual definition,  $\beta_p = \langle p \rangle / 2\mu_0 \bar{B}_p^2$ , but makes the radial hoop force of the analytical formulation for low beta, circular plasma consistent with the numerical one.

### 3.3.3 Stability analysis

Since there exists the coupling effect between radial and vertical movements described in Section 2, the stability criteria should be somewhat modified. By using Laplace transform of eqs. (9), (12), (16) and (17) and eliminating eddy current,  $\delta I_k$ , the change of plasma

positions and current without feedback control are described by the following equation. Here, the stabilizing effects of poloidal field coils are neglected, and plasma one turn resistance,  $r_p$ , is set to zero.

$$A(s)Y = B \quad (27)$$

Where,  $Y$  and  $B$  are the Laplace transform of eqs. (21) and (22), and  $A(s)$  is defined as eq. (28).

$$A(s) = \begin{pmatrix} A_{11}(s), A_{12}(s), A_{13}(s) \\ A_{21}(s), A_{22}(s), A_{23}(s) \\ A_{13}(s), A_{23}(s), A_{33}(s) \end{pmatrix} \quad (28)$$

$$\text{where, } A_{11}(s) = 2\pi B_{VO}\{n + N_Z(s)\} - 2\pi B_{VO} \frac{M_p}{2\pi B_{VO} I_p} s^2$$

$$A_{12}(s) = -2\pi B_{VO}\{k - K_S(s)\}$$

$$A_{13}(s) = 2\pi B_{VO} B_Z(s) R_p$$

$$A_{22}(s) = 2\pi B_{VO}\{1 - \frac{1}{2\Lambda_0} - n + N_R(s)\} - \frac{7}{6} \mu_0 I_p \frac{\beta_p}{R_p} - 2\pi B_{VO} \frac{M_p}{2\pi B_{VO} I_p} s^2$$

$$A_{23}(s) = -2\pi R_p B_{VO}\{1 - B_R(s)\} - \mu_0 I_p \beta_p$$

$$A_{33}(s) = L_p\{1 - K_p(s)\} I_p$$

$$N_Z(s) = \sum_k \frac{s\tau_k}{1 + s\tau_k} \left\{ - \frac{I_p}{2\pi B_{VO}\tau_k} \left( \frac{\partial M_{pk}}{\partial Z_p} \right)^2 \right\} \quad (29)$$

$$N_R(s) = \sum_k \frac{s\tau_k}{1 + s\tau_k} \left\{ - \frac{I_p}{2\pi B_{VO}\tau_k} \left( \frac{\partial M_{pk}}{\partial R_p} \right)^2 \right\} \quad (30)$$

$$K(s) = \sum_k \frac{s\tau_k}{1 + s\tau_k} \left\{ - \frac{I_p}{2\pi B_{VO}\tau_k} \left( \frac{\partial M_{pk}}{\partial R_p} \right) \left( \frac{\partial M_{pk}}{\partial Z_p} \right) \right\} \quad (31)$$

$$B_R(s) = \sum_k \frac{s\tau_k}{1 + s\tau_k} \left\{ - \frac{I_p M_{pk}}{2\pi R_p B_{VO}\tau_k} \left( \frac{\partial M_{pk}}{\partial R_p} \right) \right\} \quad (32)$$

$$B_Z(s) = \sum_k \frac{s\tau_k}{1 + s\tau_k} \left\{ - \frac{I_p M_{pk}}{2\pi R_p B_{VO}\tau_k} \left( \frac{\partial M_{pk}}{\partial Z_p} \right) \right\} \quad (33)$$

$$K_p(s) = \frac{\sum \frac{s\tau_k}{k^1 + s\tau_k} \frac{M_{pk}^2}{L_p\tau_k}}{\quad} \quad (34)$$

The transfer functions defined by eqs. (29)~(34) represent the shell properties of passive elements [5], [7], [9], [10].

The stability criteria for the movement with the time scale of Alfven velocity can be derived as eq. (35) from the condition that the equation,  $\det A(s) = 0$ , has no positive root at  $s \rightarrow \infty$ .

$$\begin{aligned} \{n - N_{Rs} - 1 - \frac{\Lambda_o}{2\Lambda} \frac{(1 - B_{Rs} - 2\beta_p/\Lambda_o)^2}{1 - K_{ps}} + \frac{1}{2\Lambda_o} - \frac{7}{3} \frac{\beta_p}{\Lambda_o}\} (n + N_{zs} + \frac{\Lambda_o}{2\Lambda} \frac{B_{zs}^2}{1 - K_{ps}}) \\ + (k - K_s - \frac{\Lambda_o}{2\Lambda} \frac{1 - B_{Rs} - 2\beta_p/\Lambda_o}{1 - K_{ps}} B_{zs})^2 < 0 \end{aligned} \quad (35)$$

$$\Lambda = L_p/(\mu_o R_p)$$

Where,  $N_{Rs}$ ,  $N_{zs}$ ,  $K_s$ ,  $B_{Rs}$ ,  $B_{zs}$  and  $K_{ps}$  are the values of the transfer functions at  $s = \infty$  defined by eqs. (29)~(34), i.e.  $N_R(\infty)$ ,  $N_z(\infty)$ ,  $K(\infty)$ ,  $B_R(\infty)$ ,  $B_z(\infty)$  and  $K_p(\infty)$ , respectively.

Plasma positions are stable even though the shell effects are neglected, when plasma parameters satisfies the following conditions [5] which can be derived by setting  $N_{Rs}=N_{zs}=K_s=B_{Rs}=B_{zs}=K_{ps}=0$ .

$$n\{n - 1 - \frac{\Lambda_o}{2\Lambda}(1 - 2\frac{\beta_p}{\Lambda_o})^2 + \frac{1}{2\Lambda_o} - \frac{7}{3} \frac{\beta_p}{\Lambda_o}\} + k^2 < 0 \quad (36)$$

Assuming that  $\ln(8R_p/a_p)$  is large enough, eq. (36) is simplified as eq. (37).

$$n(n - \frac{3}{2}) + k^2 < 0 \quad (37)$$

When the k-index is zero, we can obtain well-known stability criteria " $0 < n < 3/2$ ". Equation (37) shows that the stability of plasma position is deteriorated when there is an interaction between radial and vertical movements.

For unstable cases, the growth rate,  $\gamma_g$ , of plasma movement without feedback control is the root of the equation given by  $\det A(\gamma_g) = 0$ , where,  $A(s)$  is defined as eq. (28).

The simulation studies have been performed for the next step (TNS) tokamak reactor with asymmetric plasma. The main parameters of this tokamak are summarized in Table 3.3.1.

Figure 3.3.1 shows a half sector model of passive elements. The passive elements consist of movable shield, semi-permanent shield and vacuum vessel (similar structures as Fusion Experimental Reactor [11]). The outboard movable shield contains breeding blanket in which saddle type copper conductive shells of 2 cm in thickness are installed (shaded part of Fig. 3.3.1). The width of front part and side part of Cu shell are 1 m and 0.75 m, respectively. The semi-permanent shield is installed inside the vacuum vessel and the movable shield is installed inside the semi-permanent shield. Figure 3.3.1 represents these passive elements separately. In analyzing shell properties of passive elements, plasma toroidal current profile is taken into account based on plasma equilibrium calculations.

Figures 3.3.2 and 3.3.3 show the growth rates of plasma position movement for high beta phase and low beta phase, respectively. In the curve (b), the k-index is neglected. From these figures, it can be seen that the radial-vertical coupling increases the growth rate of position movements. The  $K(s)$  function defined by eq. (31) represents the interaction between radial and vertical directions through eddy currents in the structures. If passive structures and plasma are perfectly symmetric with respect to  $Z=0$  plane,  $K(s)$  becomes zero. The  $K(s)$  functions of our TNS tokamak are shown in Fig. 3.3.4 for both high beta phase and low beta phase. The absolute values of these  $K(s)$  functions are small as compared with the corresponding k-index. So the asymmetry of the passive elements does not significantly affect the coupling between plasma radial and vertical movements.

#### 3.3.4 Simulations of radial and vertical position control

Radial position of plasma is moved by changes of the plasma current distribution and the plasma thermal energy during MHD activities such as fishbone, minor or major disruptions. This radial movement generates vertical movement of plasma through the mechanisms mentioned above. Then, for realistic analyses and clear issue identification on radial and vertical position control of an asymmetric plasma, it is appropriate procedures to give, as the initial perturbation, a change which directly



causes radial movement of the plasma.

Simulation analyses have been carried out for the following initial perturbations:

- a) A change of plasma current distribution ( $\ell_i$  change).
- b) Changes of plasma thermal energy ( $\beta_p$  change) and plasma current distribution.

(1) Plasma Position Control at  $\ell_i$  Reduction

In order to show the difference of control property between up-down symmetric and asymmetric systems, we simply assume a change of  $\ell_i$  by 0.1 with a time constant of 1 msec. That is,  $\delta\ell_i(t)$  is given by the following equation.

$$\delta\ell_i(t) = -\delta\ell_{i0}(1 - e^{-t/\tau_\ell}) \quad (38)$$

$$\delta\ell_{i0} = 0.1, \quad \tau_\ell = 1 \text{ msec}$$

The locations of active coils and other poloidal field coils are shown in Fig. 3.3.5. The outer active coils are used for this simulation. Other poloidal field coils provide both OH and EF components (hybrid poloidal coil system), and shield the magnetic field generated by active coils. The magnitude of this magnetic shield effect depends strongly on active coil positions. The position of outer active coils are selected so as to minimize this magnetic shielding effect. Proportional control is used in feedback control simulations for simplicity.

Simulation results of plasma position control for  $\ell_i$  perturbation are shown in Figs. 3.3.6 to 3.3.8. The same voltage limit is applied to both upper and lower active coils for position control. The maximum loop voltage on a plasma for plasma current control is assumed to be 10 V. The power supply capacity for both vertical and radial position control,  $P_{SRV}$ , is 38 MVA in high beta/outer active coil case as shown in Fig. 3.3.6. In Fig. 3.3.7, the k-index is set to zero to simulate the position control of up-down symmetric plasma. By comparing the vertical displacements shown in Figs. 3.3.6 and 3.3.7, it can be seen that the vertical displacements is generated mainly by the asymmetric external equilibrium field and the effect of the asymmetry of passive structures is small in our TNS tokamak reactor. It can be also seen from Figs. 3.3.6 and 3.3.8 that shielding property of poloidal coils against the magnetic fields by active coils increases the power supply requirement by more than ~150%.

(2) Plasma Displacements at Large Changes in  $\beta_p$  and  $\ell_i$ 

As for abnormal losses of the plasma thermal energy, we assume that the thermal energy (poloidal beta  $\beta_p$ ) be lost by 40% with a time constant of 5 msec at disruptions for our TNS tokamak. Furthermore the normalized plasma internal inductance,  $\ell_i$ , is assumed to decrease by approximately 40% (from 0.8 to 0.5) with the same time constant in order to simulate the plasma current flattening. Then the temporal changes of  $\beta_p$  and  $\ell_i$ ,  $\delta\beta_p(t)$  and  $\delta\ell_i(t)$ , are given by the following equations.

$$\delta\beta_p(t) = -\delta\beta_{p0}(1 - e^{-t/\tau_d}) \quad (39)$$

$$\delta\ell_i(t) = -\delta\ell_{i0}(1 - e^{-t/\tau_d}) \quad (40)$$

$$\tau_d = 5 \text{ msec}$$

Figure 3.3.9 presents simulation results, which are all for high  $\beta_p$  operations. The calculation is carried out up to 50 msec. The active coils are assumed to be located inside the TF coils to increase controllability. The results with copper shells installed inside the blanket are shown by curve (a), and those without copper shells by the curve (b). It is observed that the plasma shrinks mainly radially in the first stage of disruption, and next moves downward. Both radial and vertical displacements increase to  $\sim 30$  cm in 50 msec after disruption initiation in case of curve (a). Thus the asymmetry of the plasma causes vertical movements of the plasma in addition to radial displacements. Because of the active coil voltage limitation of  $\pm 200$  V ( $\pm 50$  V for one turn plasma voltage), the radial and vertical displacements,  $\delta R_p$  and  $\delta Z_p$ , have turned out to be fairly large values (plasma positions are practically uncontrollable by a realistic control power) as shown in Fig. 3.3.9. The vertical displacement in the case without Cu shell is approximately 2.5 times of that with Cu shells, while the difference of the radial displacement between the cases with and without Cu shell is only  $\sim 5$  cm at 50 msec after disruption.

The simulation results with the k-index set to be zero are shown by the curve (c). In this case, the vertical displacement is less than 1/10 of that obtained in the curve (a). The reason why vertical movements are yielded even with the k-index assumed to be zero is attributed to asymmetry of the reactor structures surrounding the plasma.

However, it is observed, through comparison between the curves (a) and (c), that the effects of the asymmetry of structures is minor (Ref. Section 3).

### 3.3.5 Summary

The basic formulation has been derived for the position control system having the strong coupling effect between radial and vertical movements. The plasma position control has been numerically studied for the next generation tokamak reactor like INTOR. The following conclusions are obtained.

1) The vertical and radial plasma displacements are mutually coupled in an up-down asymmetric system, which has two types for the asymmetry: asymmetric external fields by equilibrium field coils and asymmetric eddy currents induced in asymmetric reactor structures. The governing cause is the former effect and the effect of asymmetric eddy currents is minor in the asymmetric tokamak reactor with single-null plasma, unless the  $k$ -index is much less than  $\sim 0.5$ .

2) The effect of asymmetric equilibrium field is characterized by the  $k$ -index defined by the equation (7) in section 2. This coupling effect makes a plasma position control more difficult. It increases a growth rate of plasma vertical instability. The stability criteria of the asymmetric plasma on an Alfvén time scale instability is slightly modified as shown by eqs. (35)~(37) in Section 3.

3) The disturbances for plasma vertical position are naturally generated by the radial displacements, probably due to large MHD activities in tokamak plasmas. The estimation of control power to be prepared can therefore have a reasonable ground, compared with the past works with assumptions of artificial vertical displacements.

4) The simulations show that plasma moves largely in the vertical direction (toward divertor plates) as well as toward inboard first wall at plasma disruptions in asymmetric tokamak plasma systems.

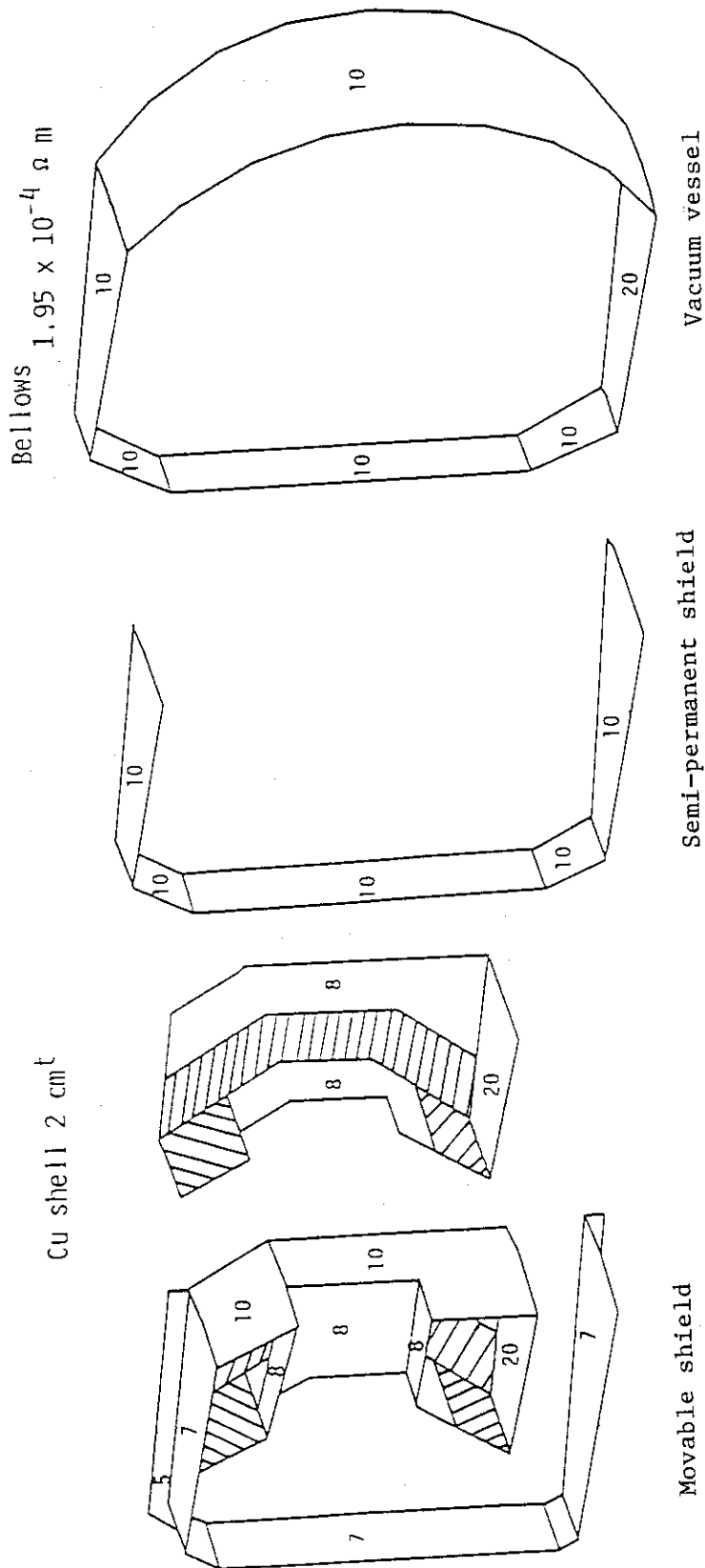
5) Poloidal field coils shield the magnetic field produced by active control coils to some extent. This effect increases significantly the power supply requirement for position control. The active coil location should be carefully selected so that outer active coils do not interact strongly with poloidal field coils.

# References

- [1] R. Albanse, E. Coccoresse, R. Martone, H. Rubinecci and E. Salpietro, European Contribution to INTOR Workshop Phase 2A (part 2) Session X Group C, 15-26 October 1984.
- [2] M. Kasai, K. Ueda, S. Niikura, A. Kameari, H. Iida, et al., Japanese Contribution to INTOR Workshop Phase 2A (part 2) Session X Group C, 15-26 October 1984.
- [3] R.J. Thom, R.D. Pillsbury, W.R. Mann, G. Bateman, A.M. Fuller, et al., USA Contribution to INTOR Workshop Phase 2A (part 2) Session X Group C, 15-26 October 1984.
- [4] A.L. Kostenko, R.N. Lintovsky, A.M. Astapkovich, V. Beijakov, Ju. Batakov, et al., USSR Contribution to INTOR Workshop Phase 2A (part 2) Session X Group C, 15-26 October 1984.
- [5] M. Kasai, A. Kameari, F. Matsuoka, Y. Imamura, H. Iida and N. Fujisawa, Parametric Studies on Plasma Position Control, INTOR Workshop Phase 2A (part 2) Session XI Group C, 15 April - 3 May 1985.
- [6] V.S. Mukhovatov and V.D. Shafranov, Nucl. Fusion 11 (1971) 605.
- [7] A. Kameari, S. Niikura and N. Fujisawa, Control of Plasma Vertical Position in Tokamak Reactors, Nuclear Engineering and Design/Fusion 2 (1985) 365-375.
- [8] A. Kameari, Transient Eddy Current Analysis on Thin Conductors with Arbitrary Connections and Shapes, J. Comput. Phys., Vol.42, PP.124-140, 1981.
- [9] H. Ninomiya, T. Ozeki, H. Yoshida and S. Seki, JAERI-M 84-028, 1984 (in Japanese).
- [10] S. Seki, H. Ninomiya and H. Yoshida, JAERI-M 83-165, 1983 (in Japanese).
- [11] FER design team, JAERI-M 86-134, 1986 (in Japanese).

Table 3.3.1 Main parameters of TNS tokamak plasma used for parametric studies on plasma position control

Major Radius (m)	5.0
Minor Radius (m)	1.2
Plasma Current (MA)	
flat-top phase	7.5
re-charging phase	5.7
Poloidal Beta	
flat-top phase	1.3
re-charging phase	0.1
n-index	
flat-top phase	-1.35
re-charging phase	-1.956
k-index	
flat-top phase	0.574
re-charging phase	1.0
Vertical Field (T)	
flat-top phase	-0.474
re-charging phase	-0.255



\* The numbers in the figure are the thickness (cm) of stainless steel.  
Resistivities of copper and stainless steel are  $2 \mu\Omega$  cm and  $75 \mu\Omega$  cm, respectively.

Fig. 3.3.1 Half sector model of passive elements.

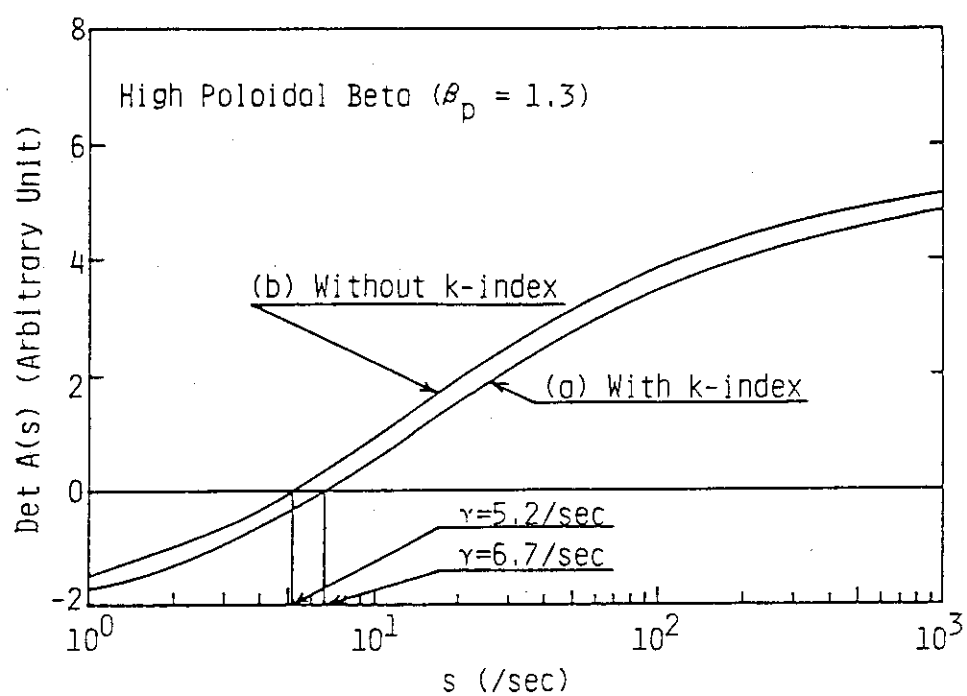


Fig. 3.3.2 Growth rates of plasma position movements at high beta phase with and without k-index.

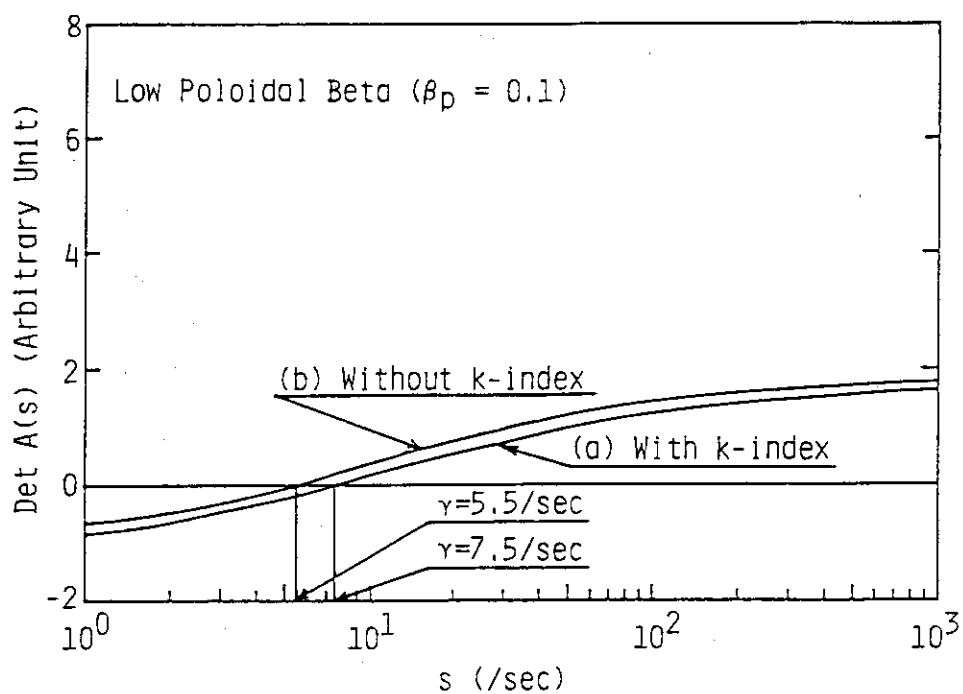


Fig. 3.3.3 Growth rates of plasma position movements at low beta phase with and without k-index.

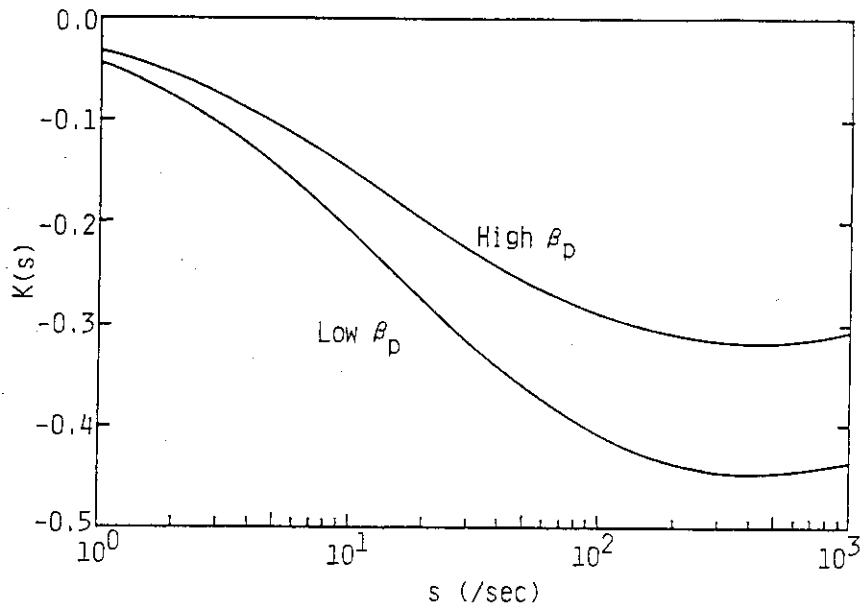
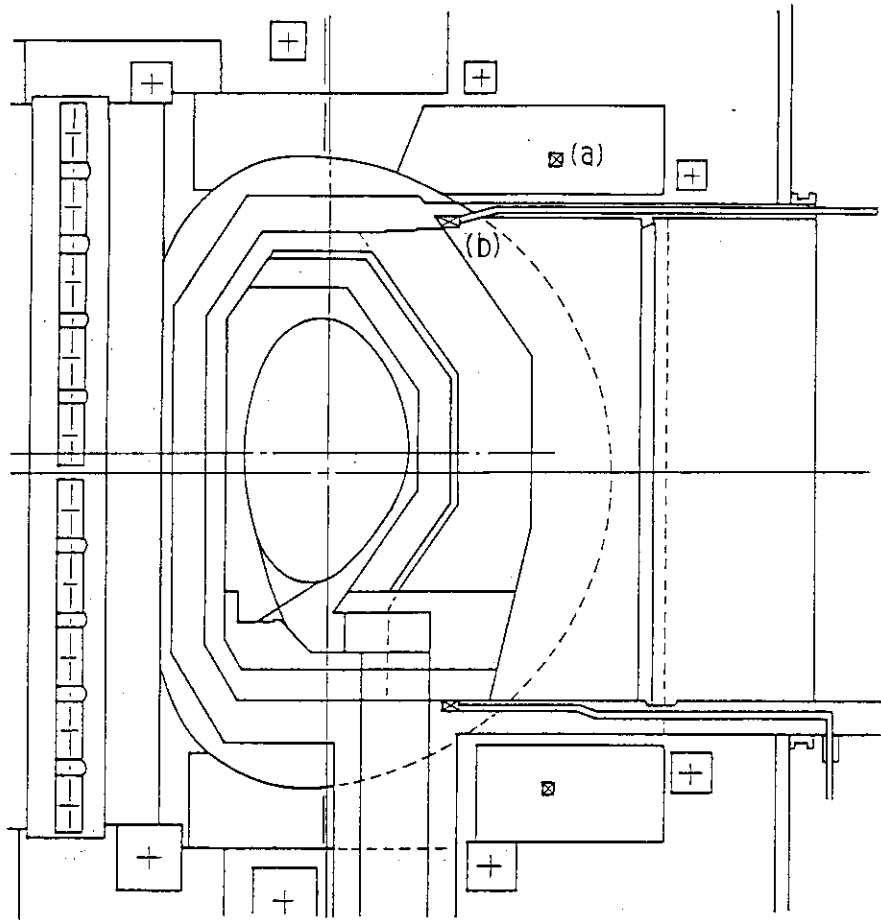


Fig. 3.3.4 Coupling functions,  $K(s)$ , between radial and vertical movements in high beta and low beta phases.



(a) Outer Active Coil Location (8.2m,  $\pm 4.2$ m)

(b) Inner Active Coil Location (7.0m,  $\pm 3.6$ m)

Fig. 3.3.5 Locations of poloidal field coils.



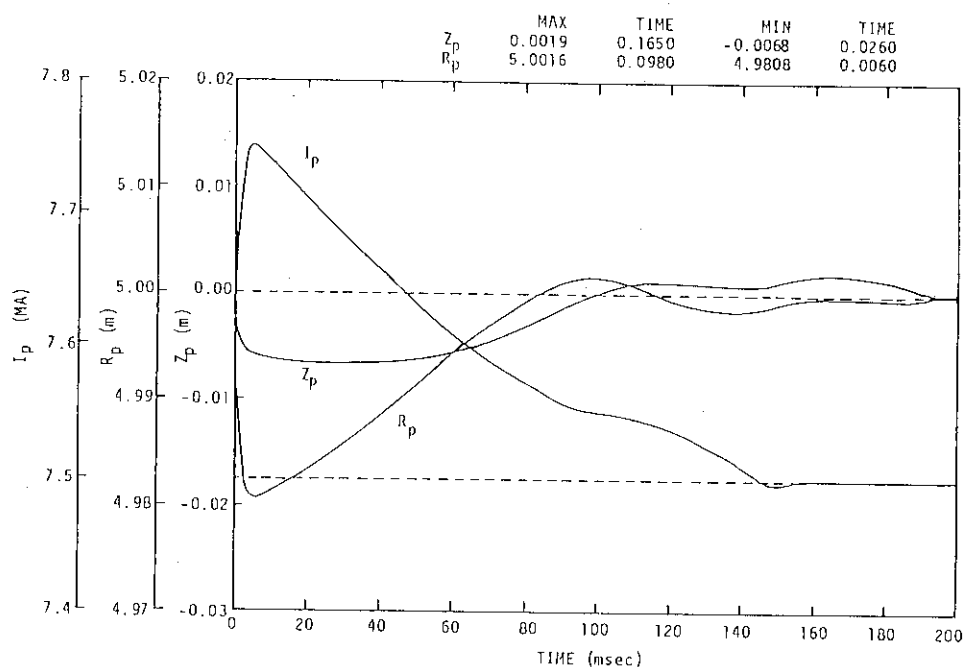


Fig. 3.3.6 Simulation result of plasma position control by outer active coils in high beta phase. The shielding effect of PF coils is neglected. Active coil voltage is limited to  $\pm 110$  V.  $\delta Z_{pMax}$  : 6.8 mm,  $\delta R_{pMax}$  : 19.2 mm,  $I_{Max}$  : 175 kA, Power supply requirement : 38 MVA.

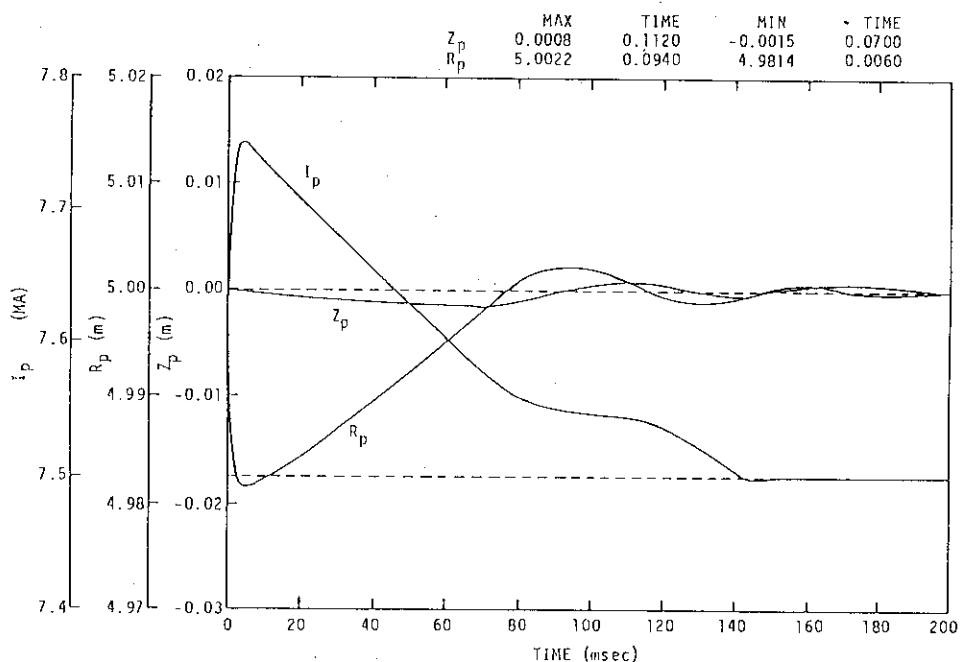


Fig. 3.3.7 Simulation result of plasma position control by outer active coils in high beta phase. The k-index is set to be zero in this simulation. The shielding effect of PF coils is neglected. Active coil voltage is limited to  $\pm 110$  V.  $\delta Z_{pMax}$  : 1.5 mm,  $\delta R_{pMax}$  : 18.4 mm,  $I_{Max}$  : 145 kA, Power supply requirement : 32 MVA.

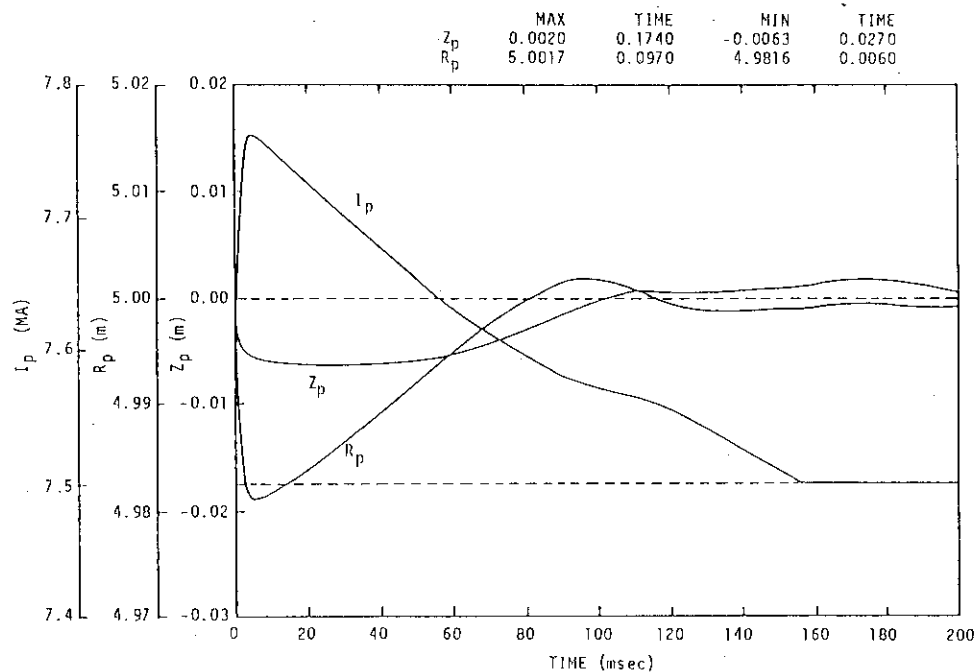


Fig. 3.3.8 Simulation result of plasma position control by outer active coils in high beta phase. Active coil voltage is limited to  $\pm 150V$ .  $\delta Z_{pMax}$  : 6.3 mm,  $\delta R_{pMax}$  : 18.7 mm,  $I_{Max}$  : 295 kA, Power supply requirement : 88 MVA.

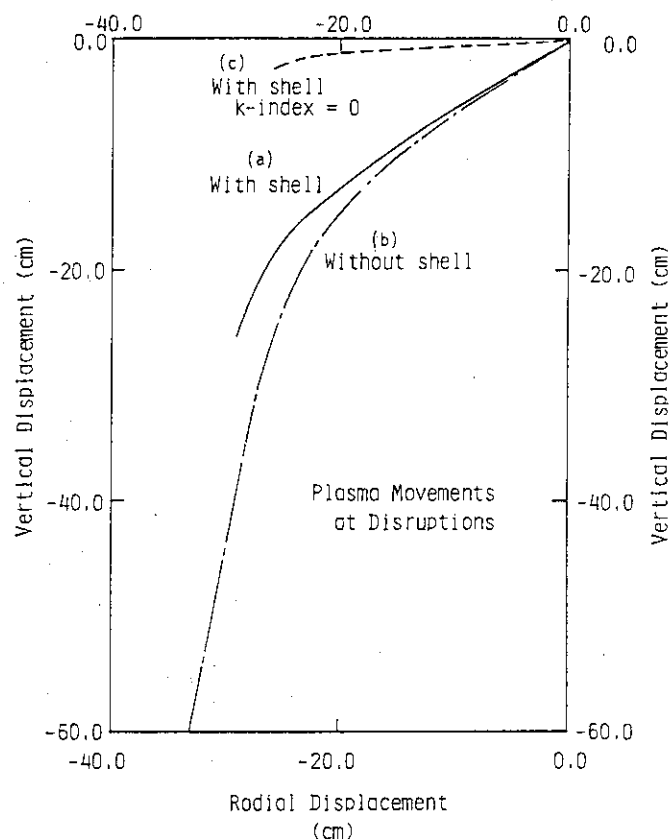


Fig. 3.3.9 Plasma movements at plasma disruption in 50 msec after disruption initiation.

### 3.4 Estimation of AC losses in cryogenic structures generated with plasma vertical position control

AC losses in cryogenic structures (SC coil can and shear panels) caused by plasma vertical position control are calculated for the next generation tokamak reactor of INTOR class with an FEM eddy current analysis code, 'EDDYCUFF' [1]. Figure 3.4.1 shows the half sector model of passive elements which is a 1/24 part of whole structures. The passive elements consist of movable shield, semi-permanent shield, vacuum vessel and cryogenic structures. The outboard part of the movable shield contains breeding blanket in which copper conductive shells of 2 cm in thickness are installed to reduce the growth rate of plasma vertical position instability [1]. The width of toroidal bar and side wall of Cu shell are 1 m and 0.75 m, respectively. The semi-permanent shield is installed inside the vacuum vessel and the movable shield is installed inside the semi-permanent shield. Each shear panel is assumed to be electrically insulated at the middle part of the panel for toroidal one turn break.

The locations of active coils are shown in Fig. 3.4.2. Two locations are considered, i.e. (1) outside TF coils (outer active coil case) and (2) between TF coils and shield (inner active coil case). The current patterns of active coils are assumed to oscillate with sine curves, corresponding with the movement of plasma vertical position. The phase difference is  $180^\circ$  between upper and lower active coils to produce radial magnetic field. When the plasma is displaced by 1 cm in the vertical direction, the radial magnetic field of approximately 10 Gauss is required to return the plasma vertical position to the original point. Then, the peak active coil current is defined so as to generate radial magnetic field of 10 Gauss in the plasma, taking account of the shielding effect by passive structures (FWBS/VV) against the magnetic field by active coils.

Figure 3.4.3 shows the typical example of simulation on plasma vertical position control [1]. The pulse length of active coil currents is approximately 150 msec, which corresponds with a half cycle of sine wave. Then, the frequency,  $f$ , of the active coil current pattern is defined as  $f = 1/T = 1/0.2\text{sec} = 5/\text{sec}$  for the standard case to overestimate AC losses.

Figure 3.4.4 shows the time behavior of total AC losses in the half

sector of cryogenic structures for one pulse oscillation. Figure 3.4.5 illustrates the flow pattern of eddy currents and the distribution of Joule heating rate for the outer active coil (Fig. 3.4.5a) and inner active coil (Fig. 3.4.5b) cases. Most of the AC losses in the cryogenic structures are induced in the shear panels. The AC losses in these two figures are calculated with the peak active coil current of 100 kA (normalized AC losses). The peak currents of the outer and inner active coils are defined as  $\sim 110$  kA and  $\sim 75$  kA, respectively, to generate the radial field of 10 Gauss, taking into account the magnetic shielding effect by the FWBS/VV. Then, the averaged Joule heating rates/the Joule heating energy deposition in the whole cryogenic structures during one pulse of oscillation are approximately 150 kW/15 kJ and 15 kW/1.5 kJ for the outer and inner active coil cases, respectively. The peak Joule heating rates are  $\sim 3$  kW/m<sup>2</sup> (outer active coil case) and  $\sim 0.8$  kW/m<sup>2</sup> (inner active coil case). The total AC losses in the inner active coil case is approximately 1/10 of those in the outer active coil case at the frequency of 5 /sec.

It is hard to assume that plasma vertical position moves cyclically all the time with the amplitude of 1 cm and the frequency of 5 /sec assumed in this calculation, since plasma vertical displacements seem to be significantly lesser than 1 cm in the current tokamak machines. Then, the factor something like duty factor should be considered to estimate the averaged Joule heating rate for the duration of a few seconds. As an example, if plasma vertical position is displaced with the coupling between radial and vertical position movements [1] at sawtooth oscillations, the averaged Joule heating rates during a few seconds are estimated as  $\sim 10$  kW and  $\sim 1$  kW in the outer and inner active coil cases, respectively, since the duration between sawteeth is estimated as 3 $\sim$ 4 sec in FER (Fusion Experimental Reactor) at JAERI.

Figure 3.4.6 shows the dependency of the AC losses on the frequency of the active coil current change (or plasma vertical position change) in the case of inner active coils. The solid circles in this figure represent the AC losses for the outer active coil case. The AC losses in this figure are also the values when the peak current of active coils is set to 100 kA (normalized AC losses). By using this figure and the peak active coil current obtained with the simulation of plasma vertical position control, the AC losses in the cryogenic structures can be roughly estimated. The normalized AC losses does not strongly depend

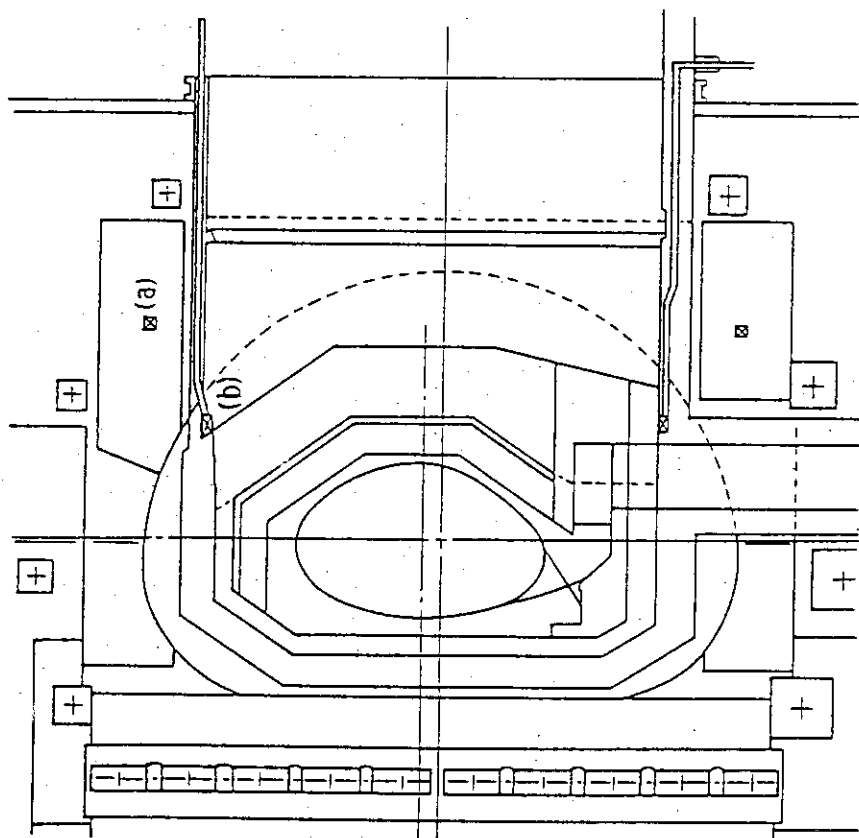
on the frequency of active coil currents, since the eddy current are directly induced in the cryogenic structures with the active coil currents. On the other hand, the normalized AC losses decrease with the increase in the frequency ( $>4/\text{sec}$ ) in the inner active coil case, since the magnetic fields by the active coils are shielded more and more with the frequency by the vacuum vessel which is installed between the active coils and the cryogenic structures. However, the radial magnetic field generated in a plasma by the active coils is also shielded more and more with the FWBS/VV and then the required active coil currents increase with the frequency increment to generate the required radial field in a plasma. Taking into account both effects mentioned above, the averaged Joule heating rate and the Joule heating energy deposition during one pulse oscillation are roughly estimated from the FER '83 design [2] as  $15\sim 20\text{ kW}$  and  $0.75\sim 1.0\text{ kJ}$  at the frequency of  $10/\text{sec}$ , respectively, in the inner active coil case. The sensitivity of Joule heating rate during a pulse of oscillation dose not seem to be large in the frequency range of  $5\sim 10/\text{sec}$  in the inner active coil case.

Main conclusions of this work are as follows.

- (1) The AC losses in cryogenic structures are approximately ten times higher in the outer active coil case than that in the inner active coil case when the active coil currents/plasma vertical position change cyclically with the frequency of  $5/\text{sec}$ .
- (2) The averaged heating rates/total energy depositions during one pulse of oscillation are estimated as approximately  $150\text{ kW}/15\text{ kJ}$  and  $15\text{ kW}/1.5\text{ kJ}$  for the outer and inner active coil cases, respectively. Assuming that plasma is displaced by  $\sim 1\text{ cm}$  in the vertical direction at sawteeth because of the radial-vertical coupling, the averaged Joule heating rates during a few seconds are roughly estimated as  $\sim 10\text{ kW}$  (outer active coil case) and  $\sim 1\text{ kW}$  (inner active coil case).
- (3) The sensitivity of the AC loss rate during a pulse of plasma vertical position oscillation dose not seem to be large within the frequency of  $5\sim 10/\text{sec}$  in the case of inner active coils. Further work is required to clear the dependence of the AC losses on the frequency in wider frequency range, consisting with the magnetic shield effect of passive structures (FWBS/VV) and the simulations of plasma vertical position control.

Rererences

- [1] A. Kameari, "Transient Eddy Current Analysis on Thin Conductors with Arbitrary Connections and Shapes", J. Comput. Phys., Vol.42, PP.124-140, 1981.
- [2] M. Kasai, A. Kameari, F. Matsuoka, Y. Imamura, H. Iida and N. Fujisawa, "Parametric Studies on Plasma Position Control", INTOR Workshop Phase 2A (Part 2) Session XI Group C, April 15 - May 3, 1985.
- [3] M. Kasai, K. Ueda, S. Niikura, A. Kameari, et al., JAERI-M 85-077 1985.



(a) Outer Active Coil Location ( $8.2\text{m}, \pm 4.2\text{m}$ )  
 (b) Inner Active Coil Location ( $7.0\text{m}, \pm 3.6\text{m}$ )

Fig. 3.4.2 Active Coil Locations.

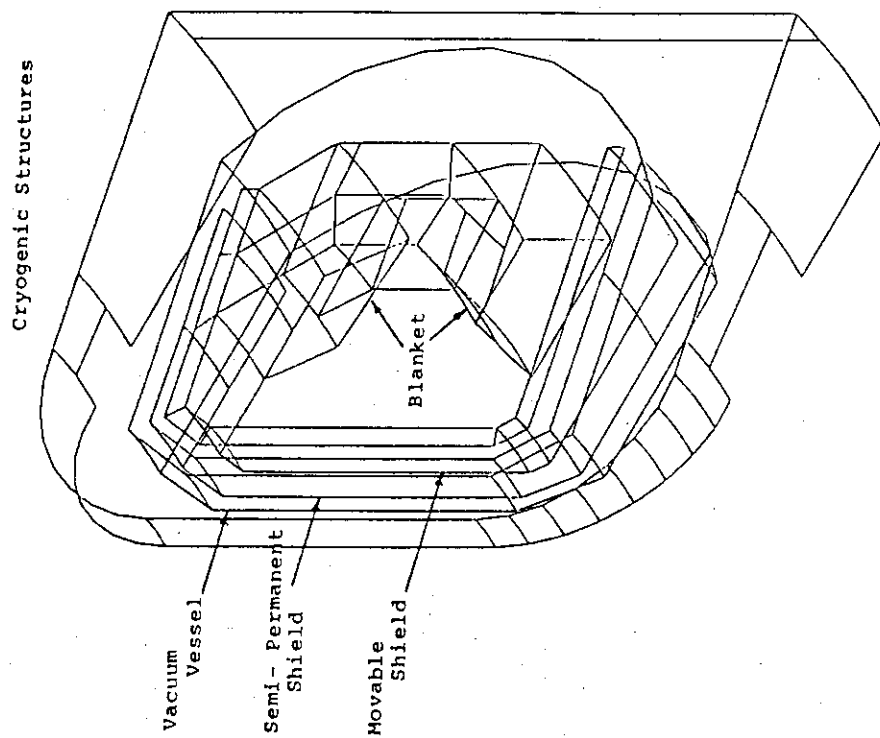


Fig. 3.4.1 Half Sector Model of Passive Elements.

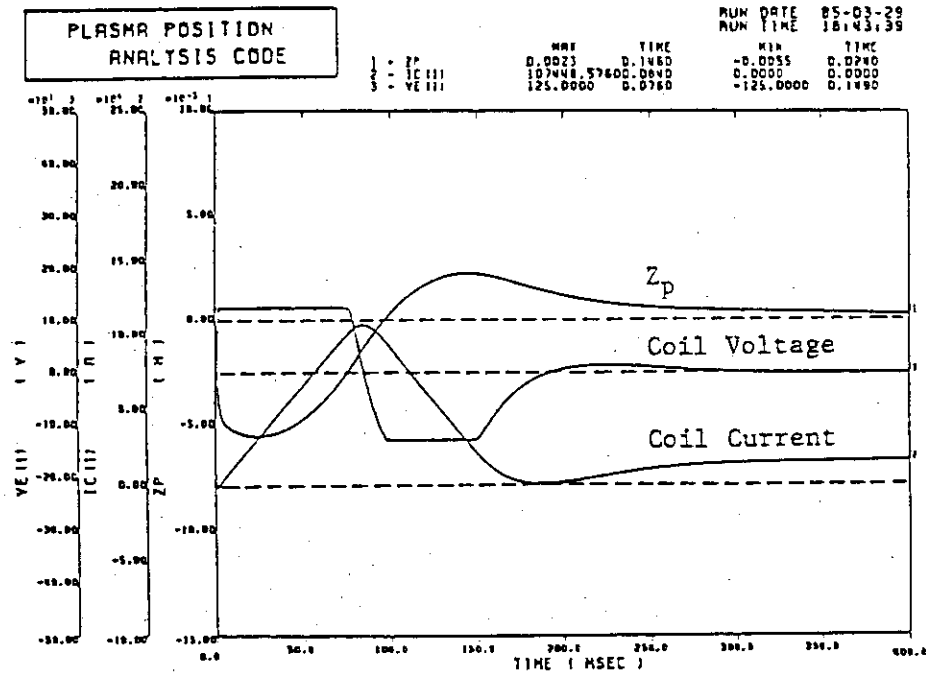


Fig. 3.4.3 Example of Simulation on Plasma Vertical Position Control [2].

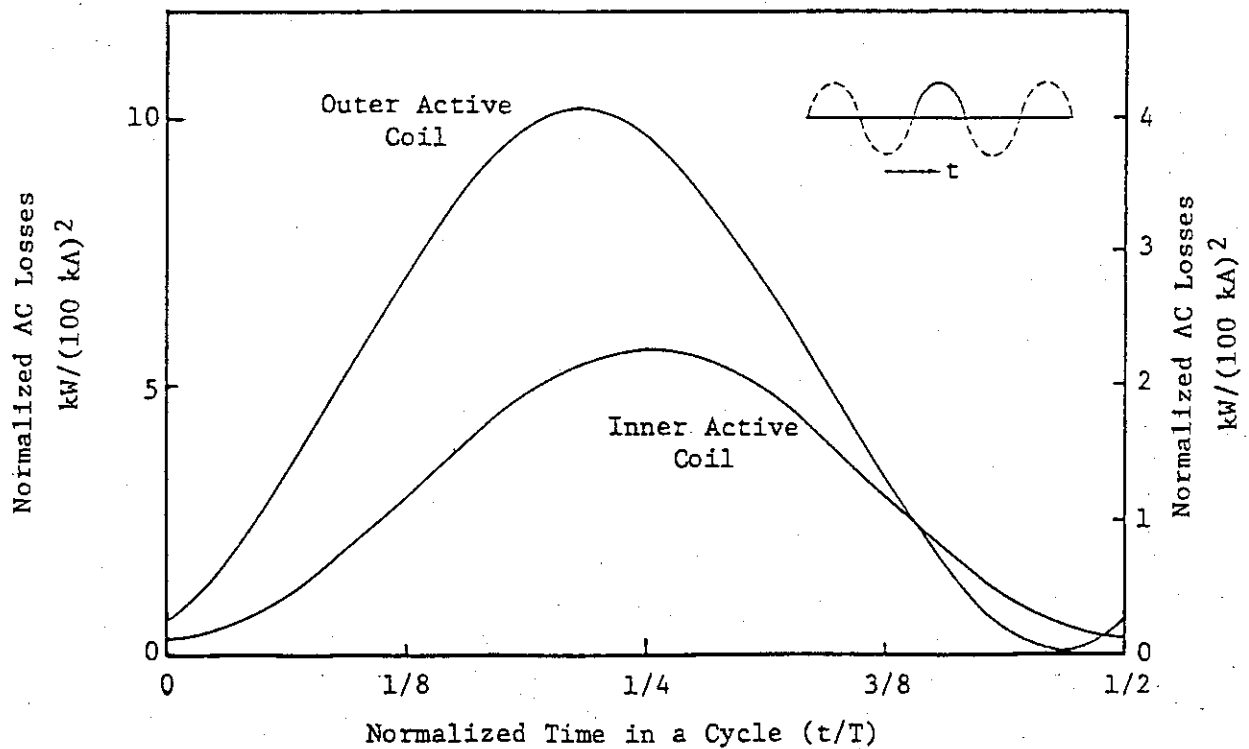


Fig. 3.4.4 Time Behavior of Total AC Loss in Half Sector. Peak Active Coil Currents are 100 kA.



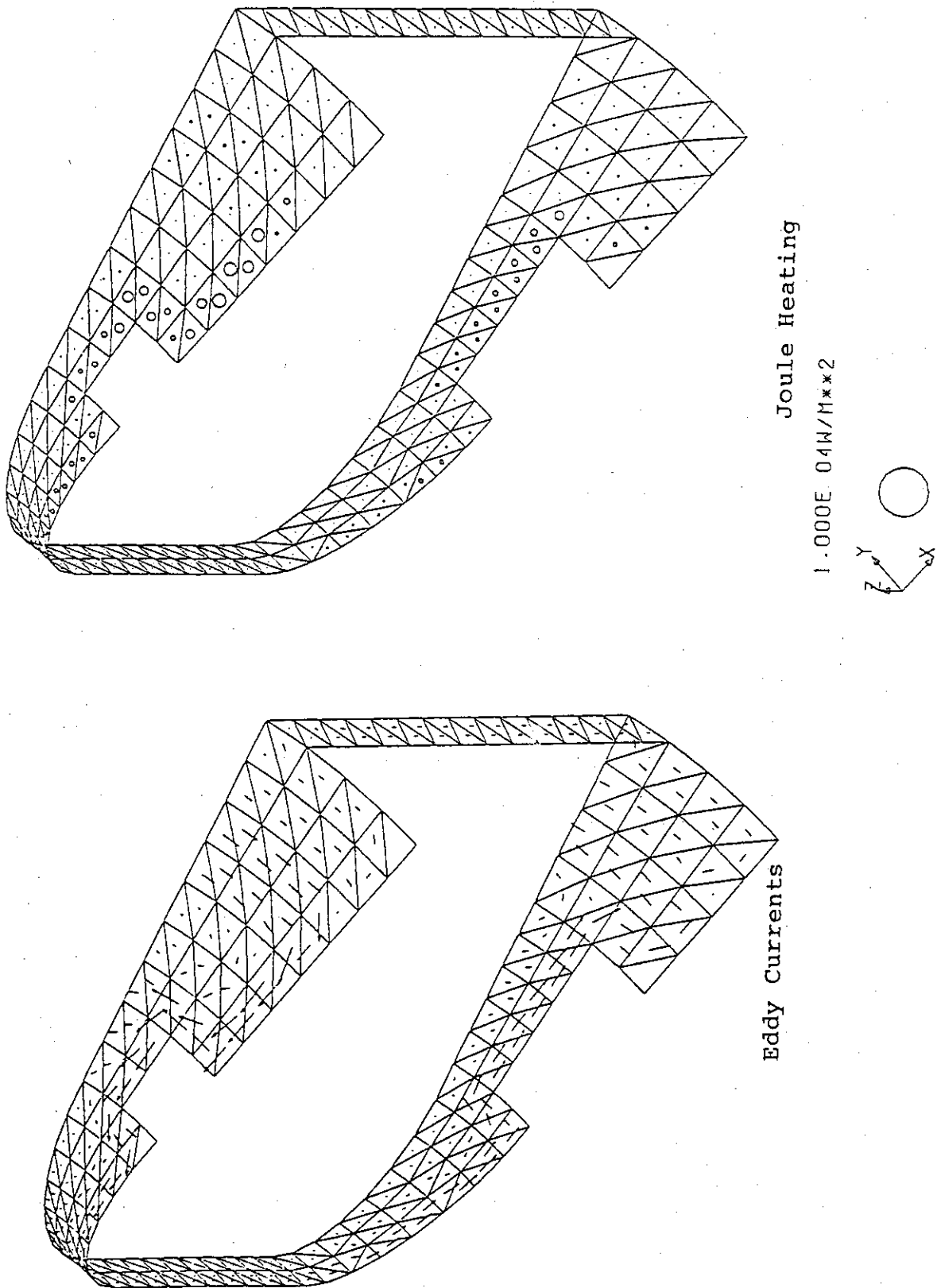


Fig. 3.4.5a Eddy Currents Flow Pattern and Joule Heating Distribution.  
(Outer Active Coil Case)

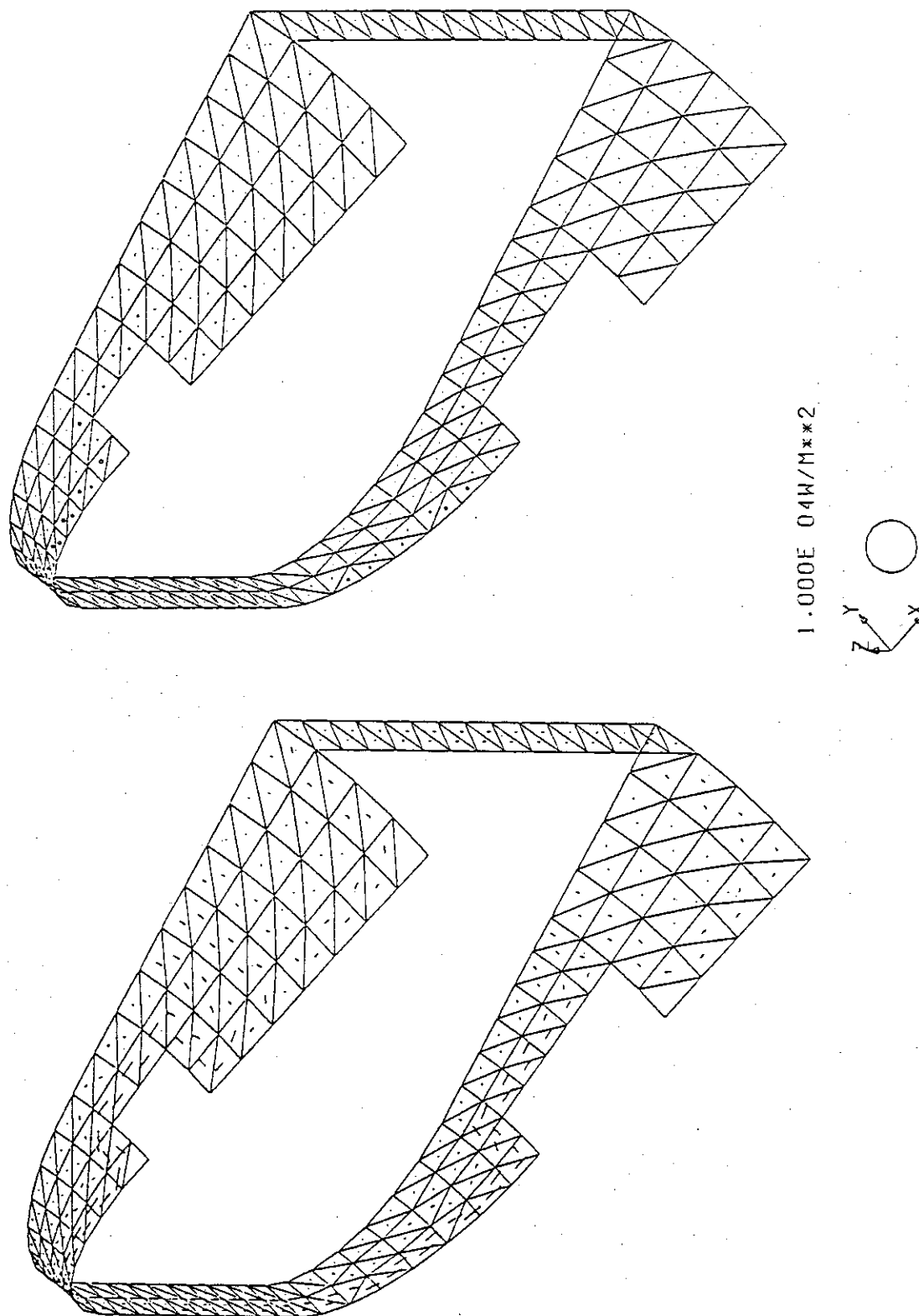


Fig. 3.4.5b Eddy Current Flow Pattern and Joule Heating Distribution.  
(Inner Active Coil Case)

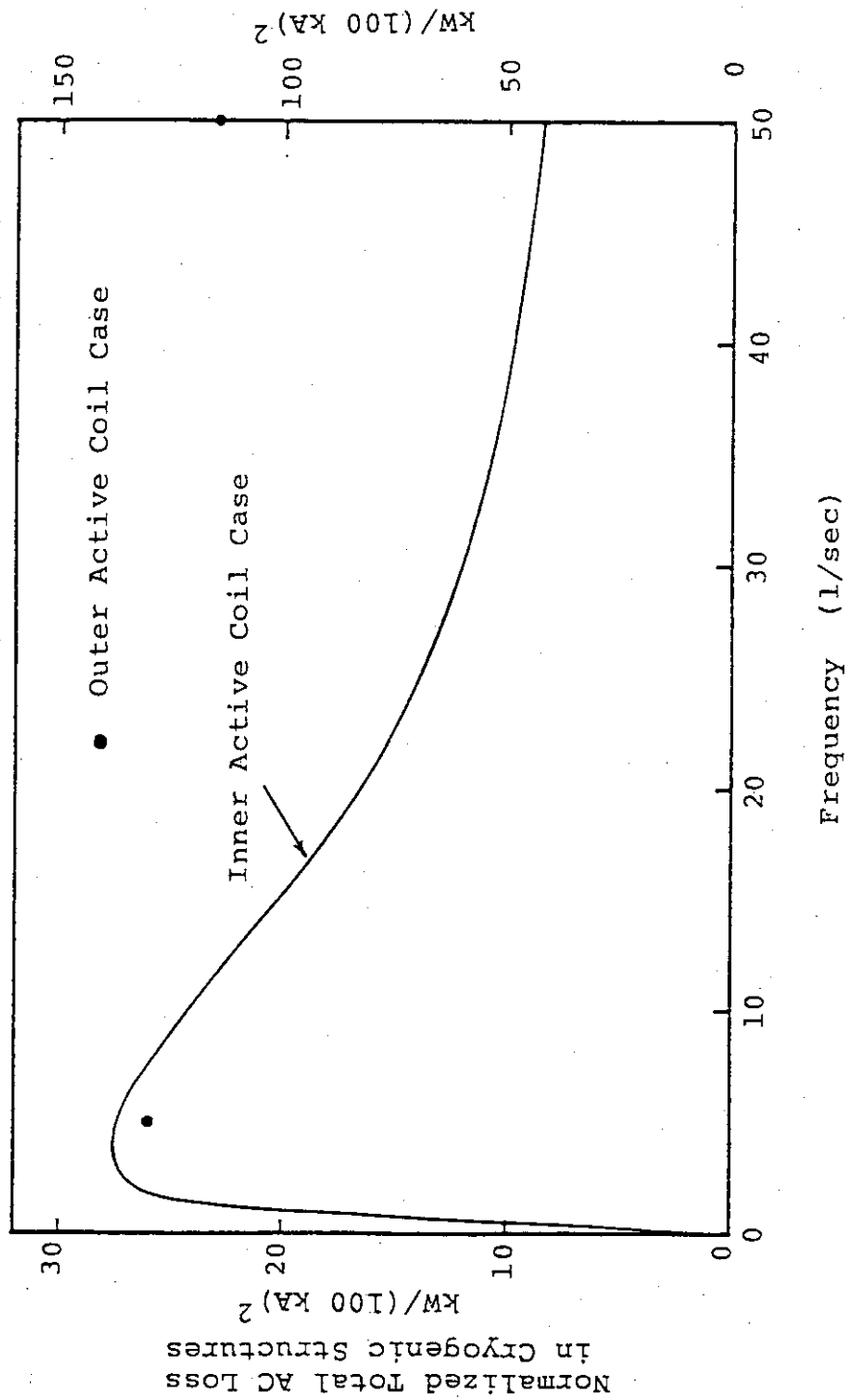


Fig. 3.4.6 Dependence of AC Losses on the Frequency of Active Coil Currents/Plasma Vertical Position Oscillation.  
Peak Active Coil Currents are 100 kA in This Calculation.

### 3.5 Effect of ferromagnetic steel on plasma position control

Ferromagnetic martensitic steel like HT-9 is an candidate material of first wall/blanket of commercial fusion reactor because of expected long life time [1]. Major concern in this paper is the difference of characteristics on plasma position control between ferromagnetic steel and non-magnetic conductive material like stainless steel. Shielding effect to applied external field and stabilizing/destabilizing effect on the plasma position movements are estimated by simple cylinder model. Relative magnetic permeability to poloidal field in high DC toroidal field  $B_0$  is approximated by  $\mu_s = (B_0 + B_{sat})/B_0$ , here  $B_{sat}$  is the intrinsic saturation induction [1]. The saturation induction of HT-9 is less than 1.5T and when  $B_0 = 5T$ ,  $\mu_s$  is less than 1.3.

When an uniform field  $B_{ex} \exp(st)$  is applied perpendicularly to a cylinder with inner radius  $b$ , outer radius  $c$  and thickness  $d=c-b$ , as shown in Fig. 3.5.1, the ratio of the penetrated field  $B_{in} \exp(st)$  to applied field is given by [2],

$$T(s) = \frac{B_{in}}{B_{ex}} = - \frac{8\mu_s}{(\mu_s+1)^2 \lambda^2 b^2 D} \quad , \quad (1)$$

$$\text{here, } \lambda = \sqrt{\sigma \mu_s \mu_0 s} \quad , \quad \kappa_s = \frac{\mu_s - 1}{\mu_s + 1}$$

$$\Delta_{ij} = I_i(\lambda b) K_j(\lambda c) - I_j(\lambda c) K_i(\lambda b)$$

$$D = \Delta_{20} - \kappa_s (\Delta_{00} + \Delta_{22}) + \kappa_s^2 \Delta_{02}$$

$I_i, K_i$  : i-th first and second modified Bessel functions

The stabilizing/destabilizing property of ferromagnetic wall is estimated by  $N(s)$ -function [3] which represents magnitude of induced field in the cylinder when plasma column shifts to the cylinder wall.  $N(s)$  is given by  $G(s)n_s$ , where  $n_s$  is  $2R_p^2/\lambda b^2$  [2].  $R_p$  is plasma major radius and  $\lambda = \ln(8R_p/a_p) + (l_i - 3)/2 + \beta_p$ , here  $a_p$ ,  $l_i$  and  $\beta_p$  are plasma minor radius, normalized internal inductance and poloidal beta, respectively. The ratio  $G(s)$  is given by,

$$G(s) = \frac{\Delta_{00} - \kappa_s (\Delta_{20} + \Delta_{02}) + \kappa_s^2 \Delta_{22}}{D} \quad . \quad (2)$$

The shielding function  $S(s) = 1 - T(s)$  and the stabilizing function  $G(s)$  are shown in Fig. 3.5.2 and Fig. 3.5.3, respectively. Here,  $\mu_s = 1.0$  (non-magnetic material),  $\mu_s = 1.3$  (HT-9 in 5T toroidal field) and  $\mu_s = 2.0$  (exaggerated case), and  $d/b = 0.5$  and  $\tau_s$  is penetration time of uniform field into thin non-magnetic cylinder given by  $\mu_0 \sigma b d / 2$ . The magnetic material has higher shielding and destabilizing effect than non-magnetic material, but the differences between  $\mu_s = 1.0$  and 1.3 are small even in case of very thick wall ( $d/b = 0.5$ ). When  $d/b \ll 1$ , the functions are approximated by

$$T(s) \doteq \frac{1}{1 + s\tau_s + \frac{(\mu_s - 1)^2}{2\mu_s} \cdot \frac{d}{b}}, \quad (3)$$

$$G(s) \doteq \frac{s\tau_s - \frac{(\mu_s^2 - 1)}{2\mu_s} \cdot \frac{d}{b}}{1 + s\tau_s + \frac{(\mu_s - 1)^2}{2\mu_s} \cdot \frac{d}{b}}. \quad (4)$$

The additional terms owing to the magnetization are small if  $\mu_s$  and  $d/b$  are less than 1.3 and 0.5, respectively. Since the position control characteristics is determined by these functions [3], it is concluded that the control characteristics in ferromagnetic structures is nearly same as in usual non-magnetic conductive structures and ferromagnetic steel is allowable as first wall/blanket material in view point of plasma position control.

#### References

- [1] J.M. Rawls, W.K. Chen, E.T. Cheng, et al., "Assessment of martensitic steel as structural materials in magnetic fusion devices", GA-A15749 (1980)
- [2] A. Fukuyama, S. Seki, H. Momota and R. Itatani, "Position Instability in a tokamak with a resistive shell", Japanese Journal of Applied Physics, 14 (1975) 871-877
- [3] A. Kameari, S. Niikura and N. Fujisawa, "Control of plasma vertical position in tokamak reactors", Nuclear Engineering and Design/Fusion 2 (1985) 365-373

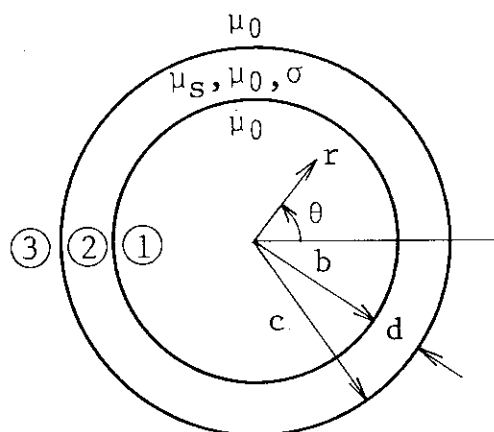


Fig. 3.5.1 Cylinder model

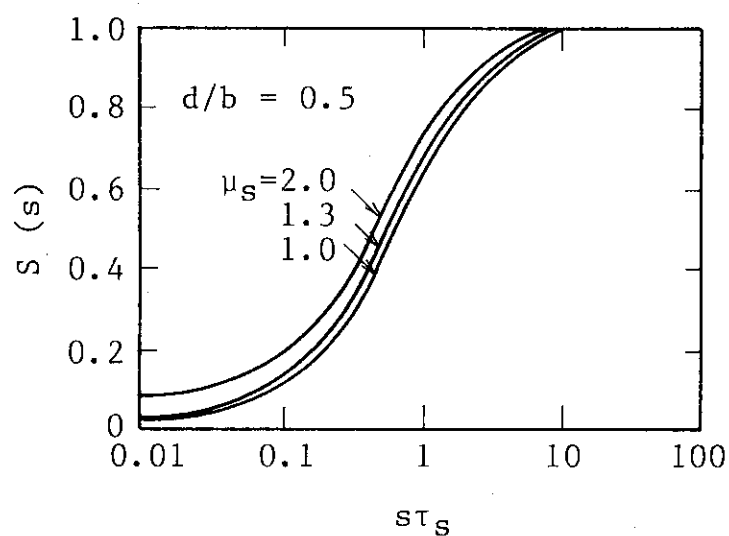


Fig. 3.5.2 Shielding functions

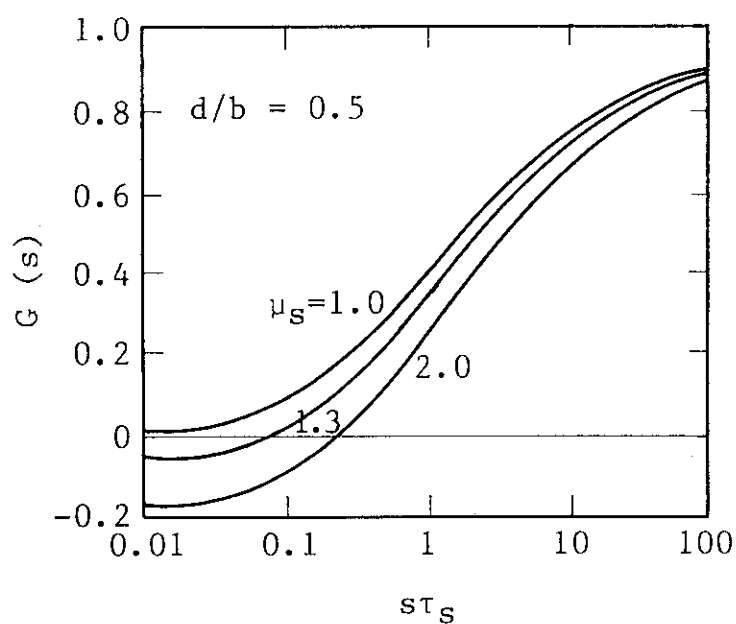


Fig. 3.5.3 Stabilizing functions

### 3.6 Review of control experimental results

#### 3.6.1 JFT-2M Tokamak

In the JFT-2M tokamak ( $R_p=1.31\text{m}$ ,  $a_p=0.35\text{m}$ ,  $I_p\leq 550\text{kA}$ ), the experiments of wide range of elongation  $1.0\sim 1.7$  and triangularity  $0\sim 0.7$  have been performed as shown in Fig. 3.6.1 [1,2]. The measured growth rates with various  $\xi = -R_0^2 B_{z0} n / \mu_0 R_p I_p$  ( $R_0$ : major radius of the geometrical center of vacuum vessel,  $B_{z0}$ : vertical equilibrium field,  $n$ : n-index) is plotted in Fig. 3.6.3 and their values are in the range of  $10\sim 500/\text{sec}$ . The growth rates are in a good agreement with calculation based on the filament current model taking account of non-axisymmetric effect of the vacuum vessel. The stability  $\tilde{G}$  (open loop gain)- $\xi$  diagram of the feedback control are obtained and the results are in a good agreement with the theoretical prediction as shown in Fig. 3.6.3. The discrepancy of upper limit of  $\xi$  seems to come from the sampling and holding character of the thyristor. The step response of vertical position also agrees well with the theoretical prediction as shown in Fig. 3.6.4.

#### 3.6.2 JT-60 Tokamak

Experimental and analytical study of the plasma current, position and shape control is presented in Appendix A. In the JT-60 tokamak,  $I_p$  (plasma current),  $\Delta_R$  (radial shift),  $\Delta_z$  (vertical shift),  $\delta_{30}$  (minimum clearance between the separatrix surface and toroidal limiter,  $\delta_t$  (clearance between separatrix surface and main divertor coil) and  $X_p$  (location of separatrix line of divertor plate) are controlled by closed feedback loops. Control coils are OH-coil (OH transformer coil), V-coil (vertical field coil), H-coil (horizontal field coil), Q-coil (quadrupole field coil) and M-coil (divertor coil). The separatrix line on the divertor plate was swung to reduce the heat flux and was precisely controlled. The experimental results are in a good agreement with estimations by the regression analysis, the matrix transfer function analysis and the simulation study. The regression analysis to determine the relations between controlled variables and measurement values is performed and is useful for the sensor algorithm of plasma shape and location of separatrix lines in the feedback system. Although the

plasma is vertically stable in JT-60, the success of control of separatrix surface is meaningful in design of control system in INTOR class tokamak reactor.

#### References

- [1] I. Yanagisawa, M. Mori, T. Shoji and N. Suzuki, Measurements and analysis of vertical instability in the JFT-2M tokamak, Proc. of 11th Symp. on Fusion Engineering, (1985) pp.571-575
- [2] M. Mori, N. Suzuki, T. Shoji, et al., Stability limit of feedback control for vertical instability in the JFT-2M tokamak, to be published in Nuclear Fusion.



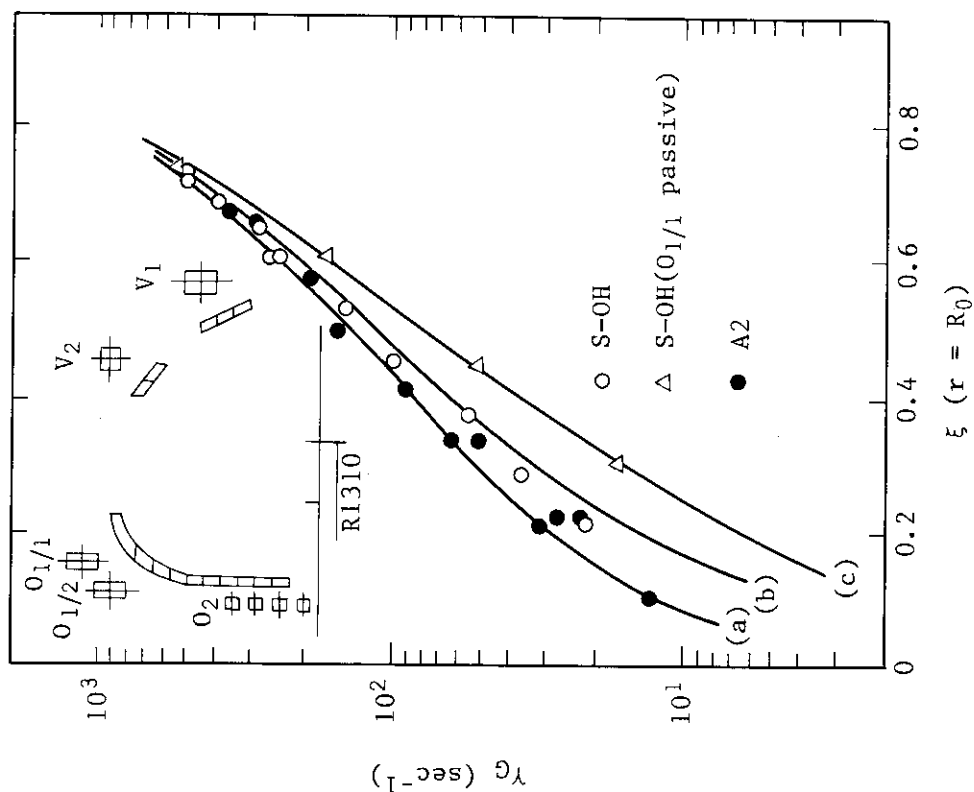


Fig. 3.6.2 Relation between the growth rate ( $\gamma_G$ ) of the vertical instability and  $\xi$ -parameter. Solid lines show the calculated growth rate.

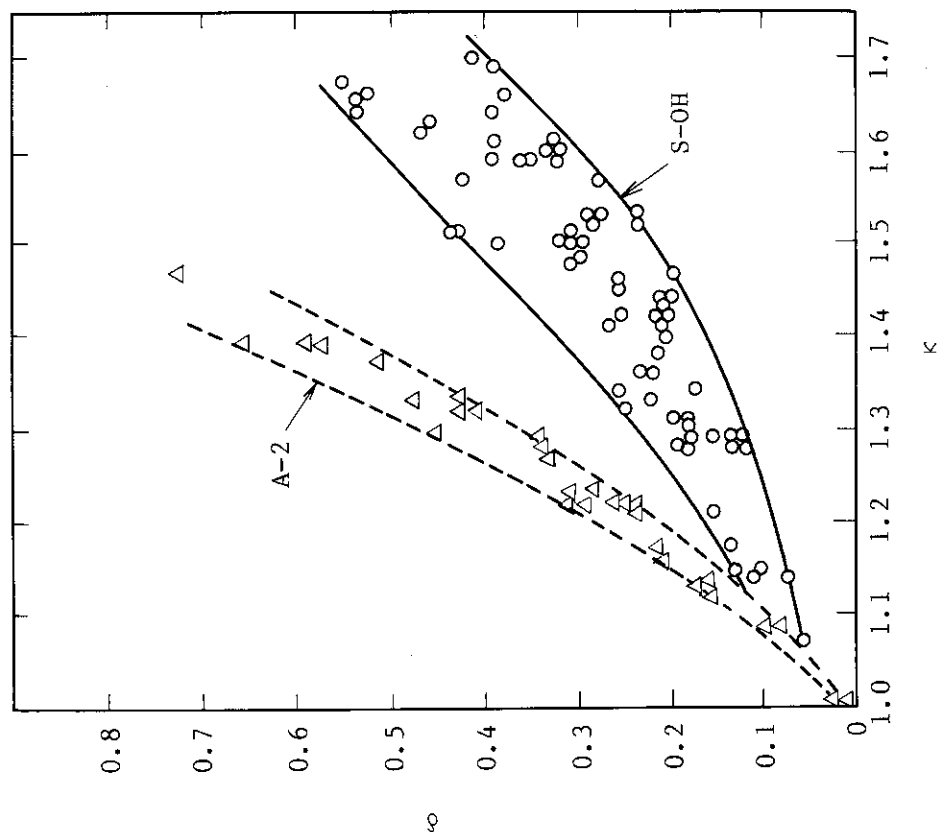


Fig. 3.6.1 Operation range of triangularity ( $\delta$ ) and ellipticity ( $\kappa$ ) in the JFT-2M tokamak

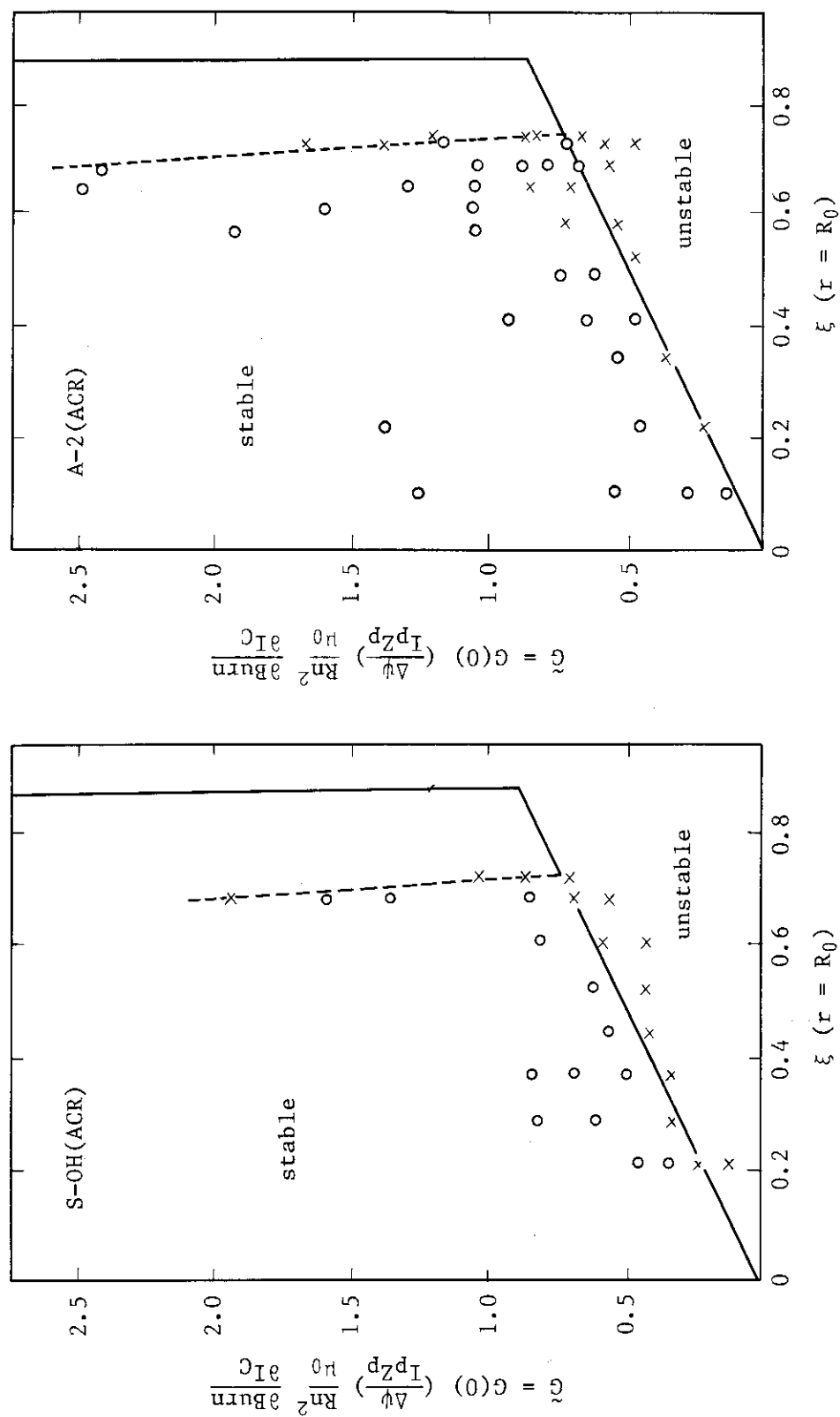


Fig. 3.6.3 Stability  $\tilde{G}$  (open loop gain) -  $\xi$  diagrams of vertical feedback control. Open circle and cross indicate experimental data correspond to stable and unstable discharge, respectively. Solid line shows theoretical prediction.

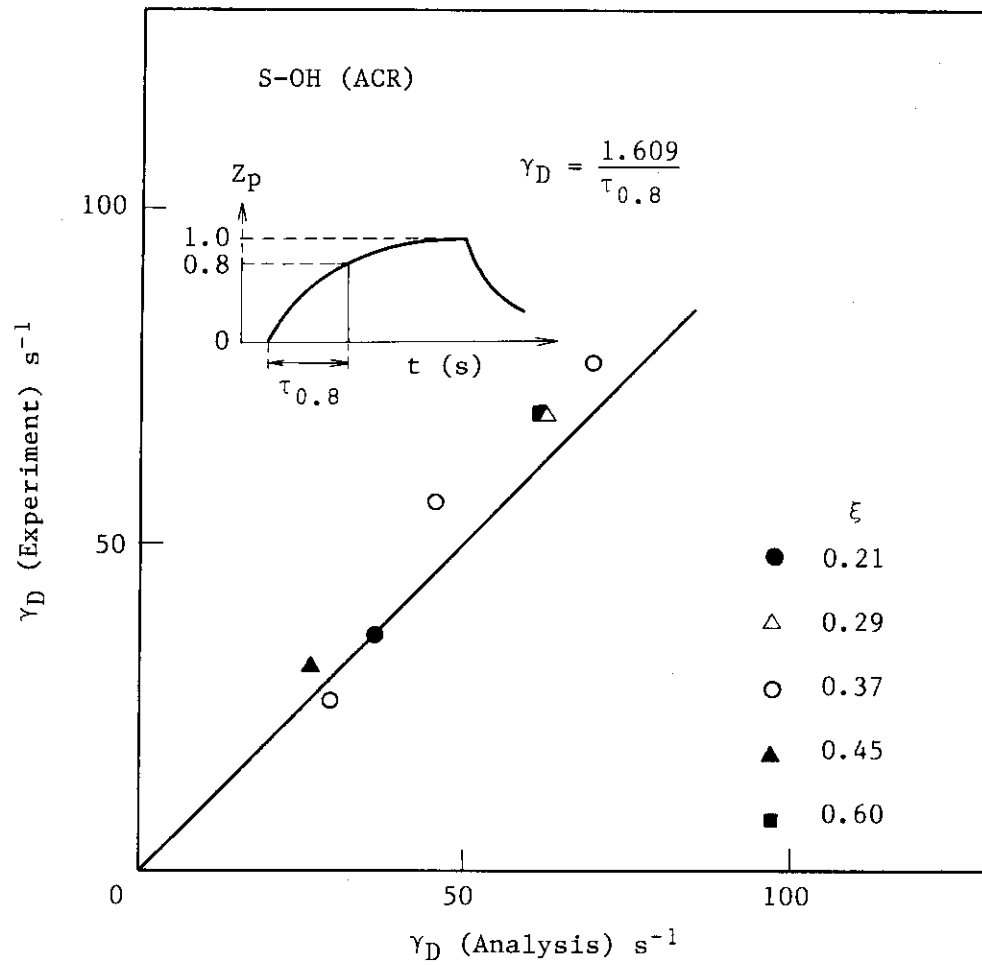


Fig. 3.6.4 Measured and calculated step response of vertical position control

### 3.7 Electromagnetic measurements of plasma

#### 1) Basic parameters of plasma for controlled operation

- plasma current
- plasma column position
- plasma shape

These parameters are usually measured electromagnetically by the Rogowski coil and magnetic probes.

#### 2) Problems on application of these method to INTOR

- long term operation of flat-top
- usage in the field of hard radiation of neutron and  $\gamma$ -ray

It is difficult to integrate the output of Rogowski coil during the long flat-top term.

Neutron causes deterioration of the electrical property of the organic insulator.

These coils have to be cooled, in order to remove both nuclear heating in the coils and heat load by the radiation from the plasma.

#### 3) Rogowski coil

The plasma current is determined by integrating the output signals of the Rogowski coil. Integration is done analogically by an electrical circuit or numerically by a digital computer. On application to INTOR, it is difficult to integrate accurately during the flat-top longer than 100 sec. Because in the case of use of the passive electrical circuit, integration needs a circuit with the time constant about ten times the observation term. If the signals are integrated by an operational amplifier, we need to develop an operational amplifier which is able to integrate for the steady state without noise.

Increasing and decreasing the plasma current in INTOR is done slowly, respectively, in comparison with the time constant of the vacuum vessel for the magnetic diffusion. Therefore, we can set the coil outside the shield. We can make both heat load of the coil and damage to the insulator small.

## 4) Magnetic probe

The motion of the plasma is from fast like disruption to slow like small perturbation at the flat-top. It is thought that the speed of the former becomes to faster than 10 m/s, and another slower than 0.001 m/s. It is very difficult to measure the plasma motion with such large region of speed by a magnetic probe. Because in the case of the slow motion, the coil must have large numbers of turn in order to obtain sure output signals of the probe. While, it must not wind numerously in the fast motion to respond quickly. Therefore, we propose that we choose different probes in measurement to suit the fast and slow motions. We assume that it critical speed is approximately 0.1 m/s. We can design a probe which is located outside the first wall for slow motion. We can reduce heat load and neutron damage of the probe. The fast probe must be set in the front of the first wall as aim at quick response. This probe is exposed to high neutron flux and hard  $\gamma$ -ray radiation. Then this probe must be cooled. We can not employ the organic matter as the electrical insulator. We suggest to use as the insulator ceramic which is sintered. We use gold which is deposited on the ceramic as the conductor.

## 5) Alternatives

## • Plasma current

We can consider application of a DC-CT (Direct Current Current Transformer) for measurement of the plasma current. This method has advantage that we can obtain the plasma current without integration (Fig. 3.7.1). But, there are some problems in this method. For example, an iron core is used, that occurs the error field near the plasma.

## • Plasma column position and shape

On measurement of the magnetic field, there is a method used the property of the light, the plane of polarization of the light rotates, when the light passes through the magnetic optical element ( $\text{Bi}_{12}\text{GeO}_{20}$  etc.), as shown in Fig. 3.7.2. But there are some problems, that is, these elements are unsatisfactory in the high neutron flux environment.

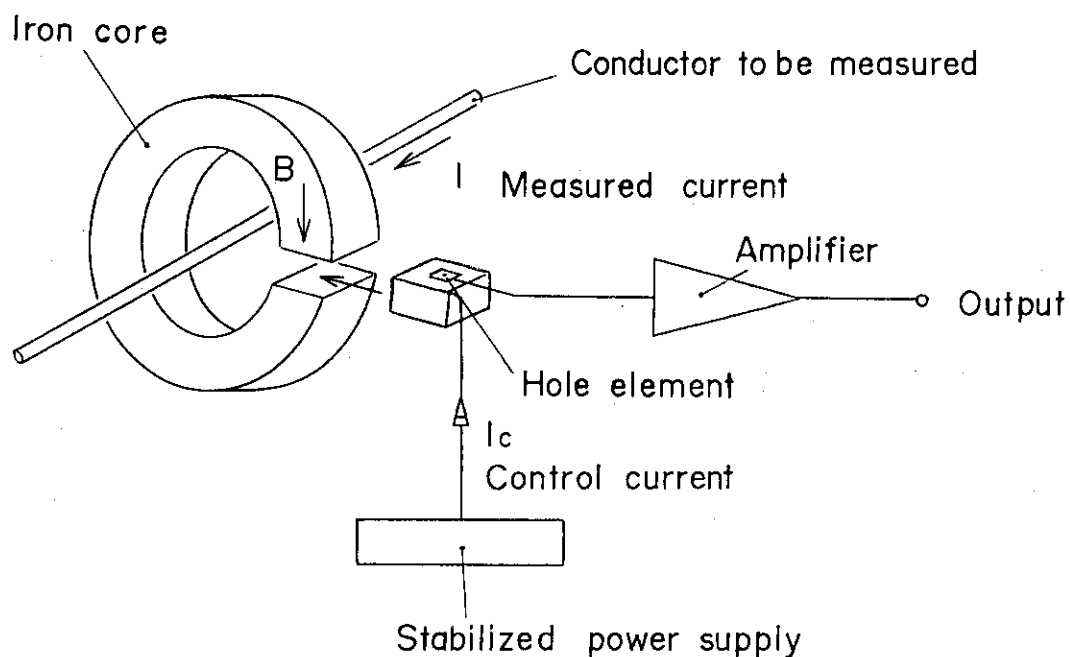


Fig. 3.7.1 Schematic view of a hole CT (Current Transformer).

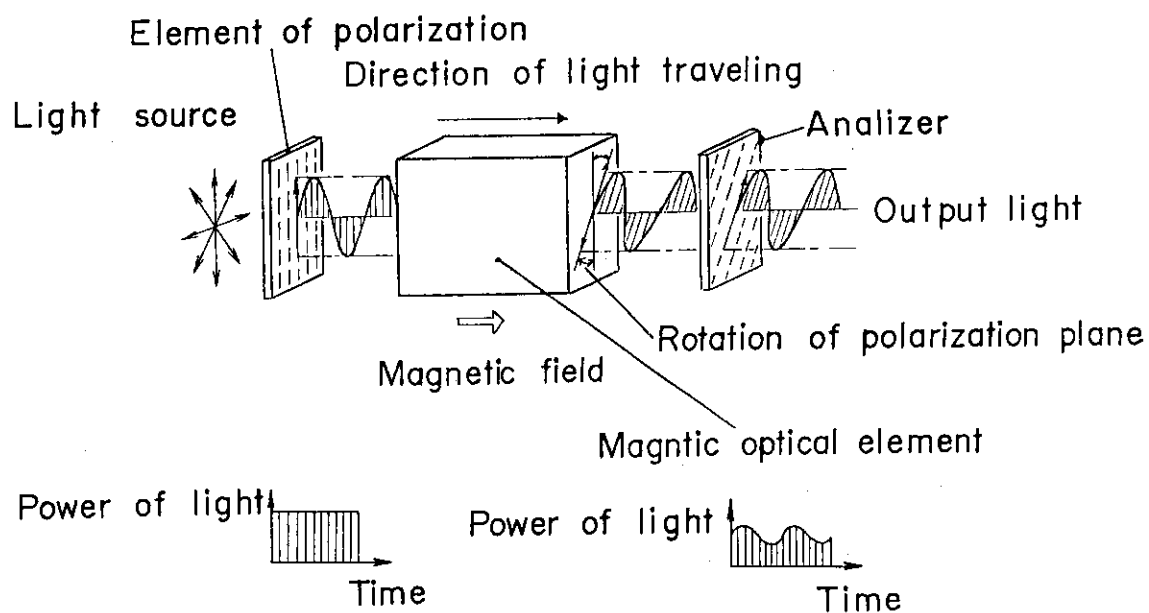


Fig. 3.7.2 Measurement principle of the magnetic field by using a magnetic optical element.

#### 4. Plasma Disruptions

##### 4.1 Analyses of the loop voltages on PF coil induced at plasma disruptions

The induced loop voltages on PF coils at plasma disruptions are calculated for the INTOR class tokamak reactor as a function of plasma current quench time,  $\tau_d$ . The shielding effect of passive structures against the induced electric field (voltage shielding effect) is also clarified. The results are summarized in Table 4.1.1. The plasma current is assumed to decay linearly within a time of  $\tau_d$ . The toroidal one turn resistance of the vacuum vessel is set to 0.2 m $\Omega$  in these calculations. The term "Direct Loop Voltage" represents the induced loop voltage on PF coil by direct interaction in the case without passive structures (or in the case of neglecting the electric shielding effect of passive structures). The voltage shielding effect is defined as "(Direct Loop Voltage - Real Loop Voltage)/Direct Loop Voltage" in this work.

The loop voltages on PF coils are order of several tens to several hundreds volts and the reduction of PF coil voltage due to the voltage shielding effect ranges from approximately 0.5 to 0.8 in case of  $\tau_d = 20$  msec. The PF coil locations used in these calculations are illustrated in Fig. 4.1.1. The loop voltage and the voltage shielding effect on the PF coils with larger bore radius are higher than that with smaller bore radius. Figure 4.1.2 shows the time behavior of the induced loop voltage and the voltage shielding effect for No. 1 (small bore radius) and No. 9 (large bore radius) PF coils.

These results are on the safety side since the voltages on PF coils are largely reduced when PF coils are electrically closed.

Table 4.1.1 Summary of induced loop voltages on PF coils

Coil No.	Current Quench Time	$\tau_d=10$ msec	$\tau_d=20$ msec	$\tau_d=50$ msec
	Induced Voltage (V)			
1	Real Loop Voltage	252 V	169 V	85 V
	Direct Loop Voltage	485 V	243 V	97 V
	Voltage Shielding Effect	0.480	0.304	0.124
2	Real Loop Voltage	241 V	162 V	81 V
	Direct Loop Voltage	449 V	224 V	90 V
	Voltage Shielding Effect	0.463	0.279	0.098
3	Real Loop Voltage	207 V	139 V	69 V
	Direct Loop Voltage	365 V	182 V	73 V
	Voltage Shielding Effect	0.432	0.235	0.049
4	Real Loop Voltage	155 V	105 V	53 V
	Direct Loop Voltage	273 V	137 V	54 V
	Voltage Shielding Effect	0.433	0.229	0.033
5	Real Loop Voltage	116 V	80 V	41 V
	Direct Loop Voltage	222 V	111 V	44 V
	Voltage Shielding Effect	0.477	0.277	0.070
6	Real Loop Voltage	267 V	189 V	100 V
	Direct Loop Voltage	573 V	287 V	115 V
	Voltage Shielding Effect	0.534	0.342	0.127
7	Real Loop Voltage	512 V	375 V	211 V
	Direct Loop Voltage	1340 V	670 V	268 V
	Voltage Shielding Effect	0.618	0.439	0.214
8	Real Loop Voltage	819 V	634 V	376 V
	Direct Loop Voltage	2557 V	1278 V	511 V
	Voltage Shielding Effect	0.680	0.504	0.265
9	Real Loop Voltage	902 V	738 V	460 V
	Direct Loop Voltage	3226 V	1613 V	645 V
	Voltage Shielding Effect	0.720	0.543	0.286
10	Real Loop Voltage	238 V	160 V	80 V
	Direct Loop Voltage	449 V	224 V	90 V
	Voltage Shielding Effect	0.469	0.289	0.109
11	Real Loop Voltage	207 V	139 V	69 V
	Direct Loop Voltage	365 V	182 V	73 V
	Voltage Shielding Effect	0.433	0.238	0.053
12	Real Loop Voltage	165 V	112 V	55 V
	Direct Loop Voltage	273 V	137 V	55 V
	Voltage Shielding Effect	0.396	0.178	0.0
13	Real Loop Voltage	116 V	81 V	40 V
	Direct Loop Voltage	197 V	99 V	40 V
	Voltage Shielding Effect	0.411	0.179	0.0
14	Real Loop Voltage	83 V	60 V	32 V
	Direct Loop Voltage	159 V	80 V	32 V
	Voltage Shielding Effect	0.477	0.249	0.0
15	Real Loop Voltage	185 V	137 V	76 V
	Direct Loop Voltage	413 V	207 V	83 V
	Voltage Shielding Effect	0.552	0.336	0.084
16	Real Loop Voltage	340 V	266 V	158 V
	Direct Loop Voltage	989 V	495 V	198 V
	Voltage Shielding Effect	0.656	0.462	0.203
17	Real Loop Voltage	558 V	467 V	297 V
	Direct Loop Voltage	1999 V	999 V	400 V
	Voltage Shielding Effect	0.721	0.533	0.258
18	Real Loop Voltage	712 V	611 V	401 V
	Direct Loop Voltage	2793 V	1397 V	559 V
	Voltage Shielding Effect	0.745	0.562	0.282



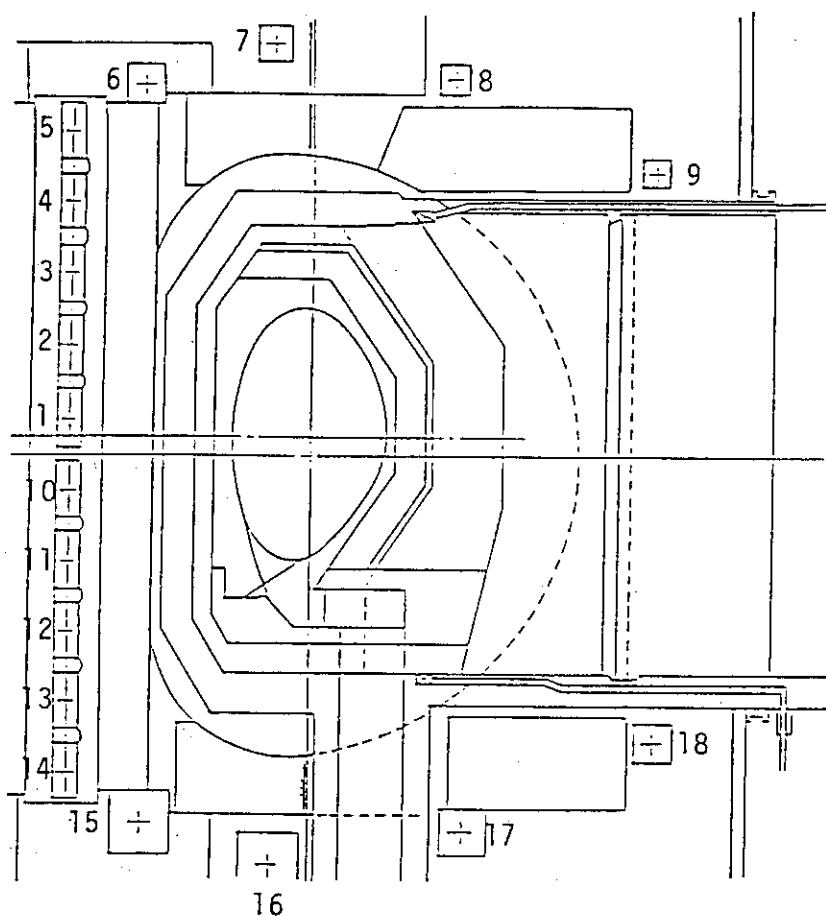


Fig. 4.1.1 PF coil locations.

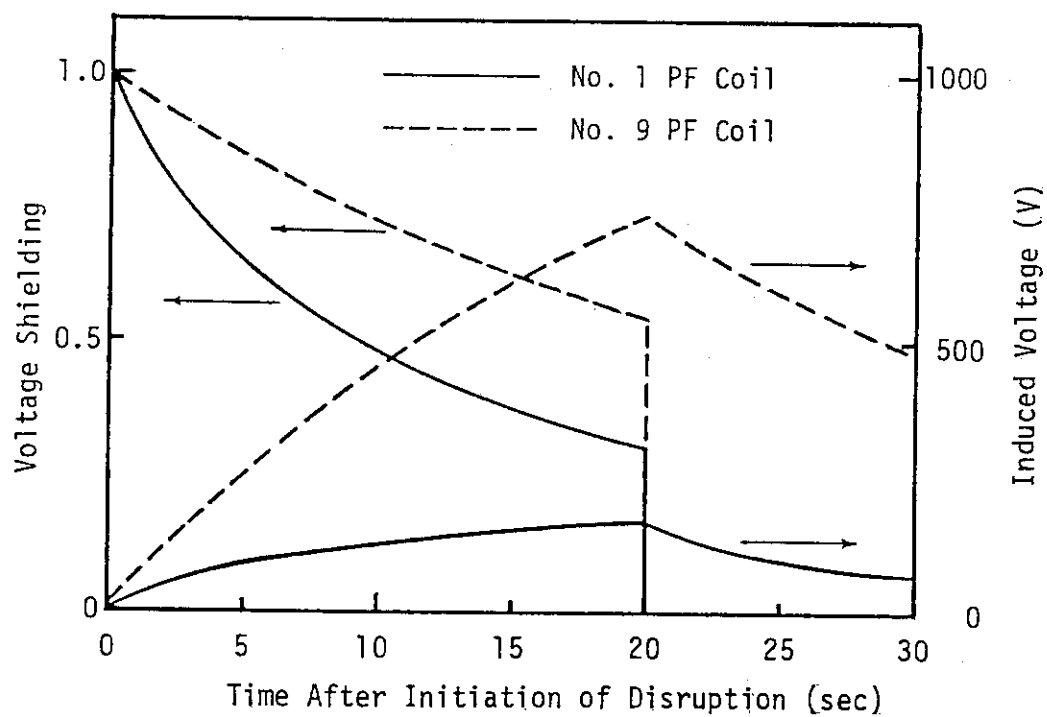


Fig. 4.1.2 Time behavior of induced loop voltages and voltage shielding effects on PF coils.

## 4.2 Analyses of a coil quench (PF and TF) triggered by plasma disruption

### Introduction

The design of next large tokamak has been studied for this several years. (Fig. 4.2.1) Some of the designed parameters are based on the normal operation plasma, though the more rigorous restriction is required for the disruptive plasma. The plasma in FER tokamak will be controlled in so well-tuned conditions that the current disruption will hardly occur. However, it is necessary to consider the worst situation from the view point of a machine design. In this paper especially the quench of superconducting coils (PF and TF) triggered by the plasma disruption is examined.

### Procedure

A large one turn loop voltage (generally larger than several ten volts) is induced during the current disruption and it changes the coil currents. Although the power supplies are still apt to regulate the coil currents, it is not enough to cancel the induced voltage since the maximum voltage of the power supply is at most 10 V/turn. Therefore there is a possibility that the increase in the coil current and the AC loss due to the change in magnetic field trigger the quench of the superconductor. Then two cases were examined, one was that all the power supplies were shorted during the disruption and the currents were not regulated at all, and the other was that the power supplies worked to regulate as much as possible. Since the possible disruption time of FER plasma current is about 20 ms and the toroidal current decay time of FER vacuum vessel is about 300 ms, it may be considered that the plasma current is replaced by the vacuum vessel one within 20 ms and it decays with 300 ms e-folding time. (Fig. 4.2.2) Considering the mutual coupling of each coil, the changes in coil currents during the disruption were obtained solving the L-R's circuits equation (Fig. 4.2.3). Using the values of these coil current the time dependences of magnetic field strength at each coil position were calculated. For the purpose of estimating the AC loss and the stability margin of the superconductor, the rate of change of magnetic field ( $\dot{B}$ ) and the temperature margin ( $\Delta T$ ) was calculated. (The temperature margin is defined in Appendix.) The recommended values for these parameters are given as  $\dot{B} \leq 10$  T/s and  $\Delta T \geq 2^\circ\text{K}$

in the FER design.

### Results

Evolutions of the coil currents, magnetic field strength at each coil position and the temperature margin of super conducting coil with and without current regulation are shown in Figs. 4.2.4, 5 and 6. The starting time of disruption was assumed to be  $t=120$  s. The number of the coil corresponds to that in Fig. 4.2.1. The lowest value of temperature margin of 7.4 K and the largest value of  $\dot{B}$  of 3.4 T/s were observed at No. 3 and No. 6 coil without current regulation, respectively. When the current regulation worked, these values moved in the more relaxed direction.  $\dot{B}$  at the toroidal coil position was 4 T/s and was also lower than 10 T/s. These analyses were also made for the case that the disruption starts at  $t=920$  s. In this case more relaxed values were obtained for  $\dot{B}$  and  $\Delta T$  than in former ones. Therefore the coil quench triggered by the disruption will not occur in the FER Tokamak.

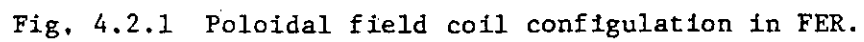
From these analyses we can estimate the case that the vacuum vessel has shorter toroidal current decay times as pulsed operation Tokamak. In such a case the temperature margin does not change and  $\dot{B}$  is multiplied by  $\tau_v^{FER}/\tau_v$ , where  $\tau_v$  is the time constant of the vacuum vessel and  $\tau_v^{FER}=300$  ms. For the case of  $\tau_v=50$  ms,  $\dot{B}$  at the toroidal coil position is about 24 T/s and becomes larger than 10 T/s. Therefore it is required to pay attention in such a case, though the skin time of the toroidal coil case is about 80 ms and a little relaxation of this value can be expected.

APPENDIX

The temperature margin is defined as follows,

$$\begin{aligned}\Delta T = T_{cs} - T_b &= \left(1 - \frac{I_{op}}{I_c}\right) (T_c - T_b) \\ &= \left(1 - \frac{I_{op}}{I_c}\right) \left\{ T_{co} \left(1 - \frac{B}{B_{co}}\right)^{1/2} - T_b \right\}\end{aligned}$$

$T_{cs}$ :	Current shearing temperature	(K)
$T_b$ :	Helium temperature	(5 K)
$I_{op}$ :	Operation current	(A)
$I_c$ :	Critical current	(A)
$T_c$ :	Critical temperature at magnetic field BT	(K)
$T_{co}$ :	Critical temperature at magnetic field OT	(18.3 K)
$B$ :	Magnetic field	(Tesla)
$B_{co}$ :	Critical magnetic field	(24.5 Tesla)



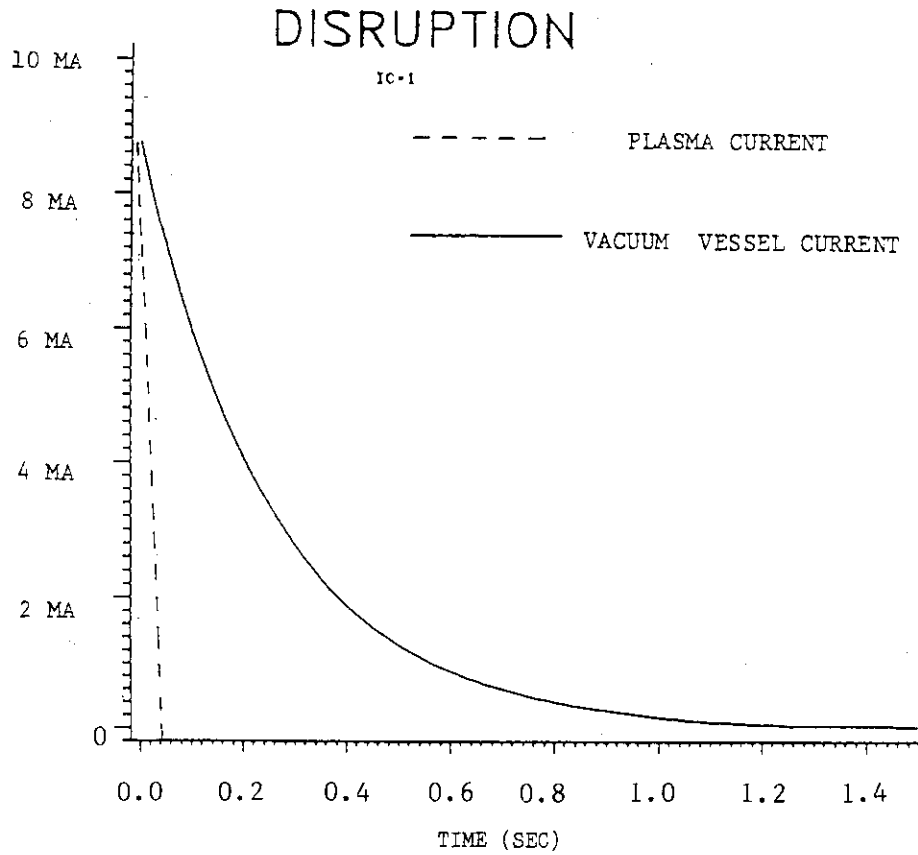


Fig. 4.2.2 Evolutions of plasma current and vacuum vessel current at the disruption.

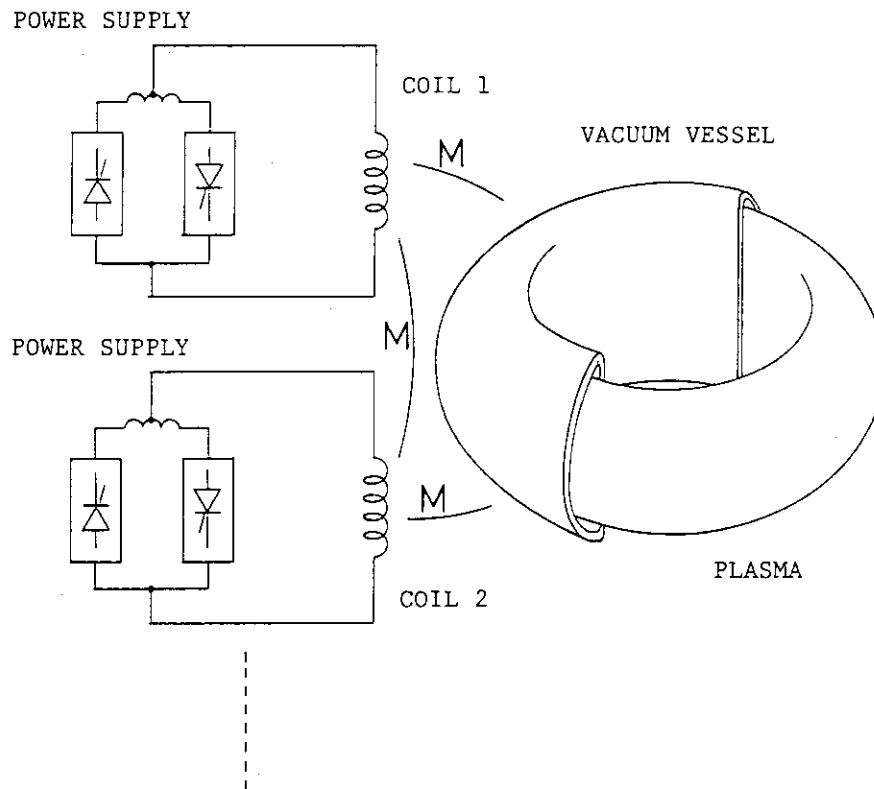


Fig. 4.2.3 Schematic drawing of plasma and coil.

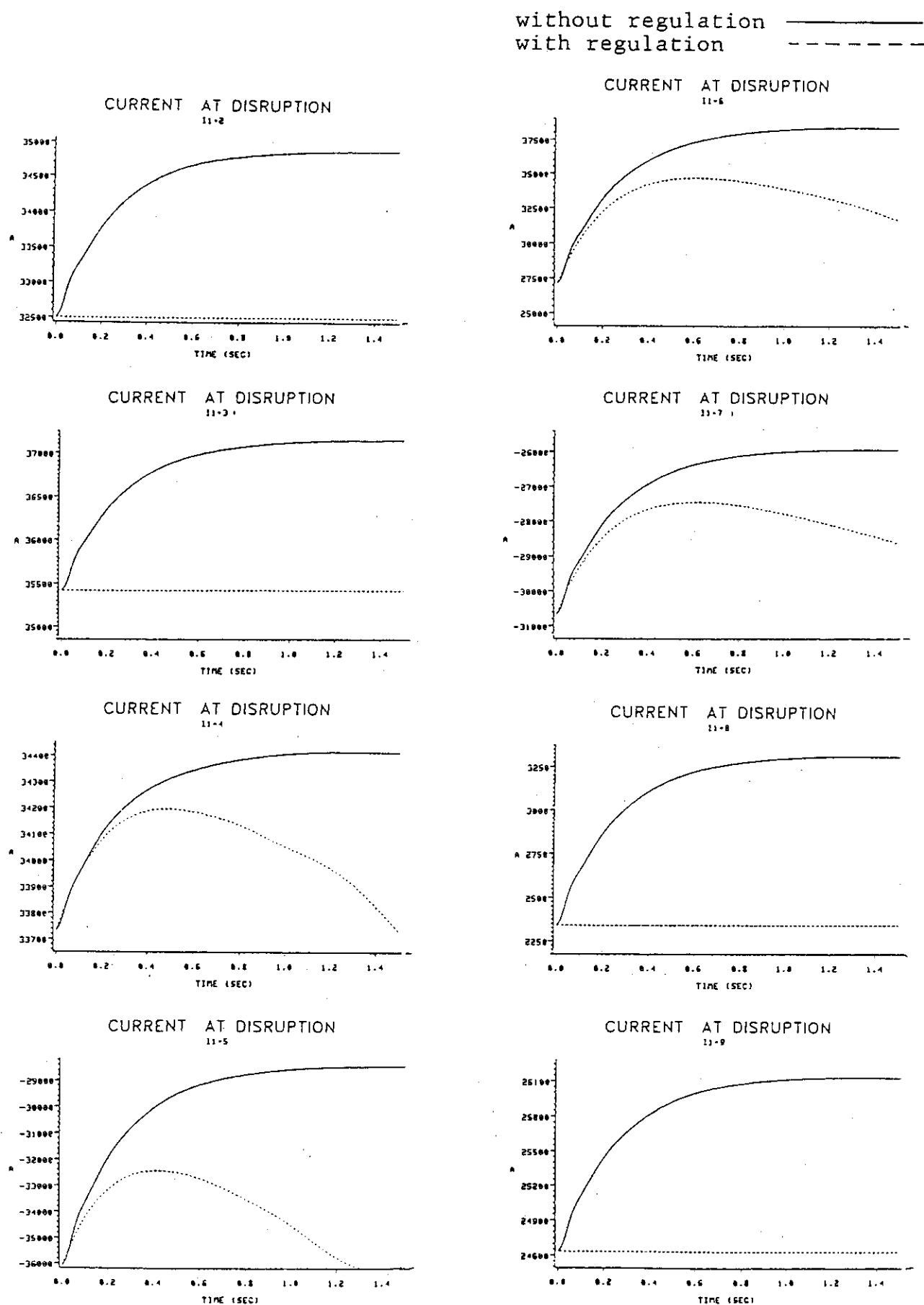
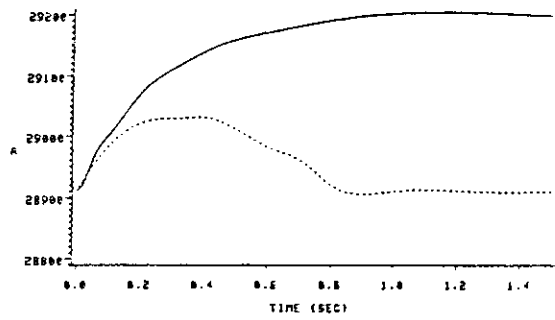


Fig. 4.2.4 Evolution of coil current with and without current regulation.

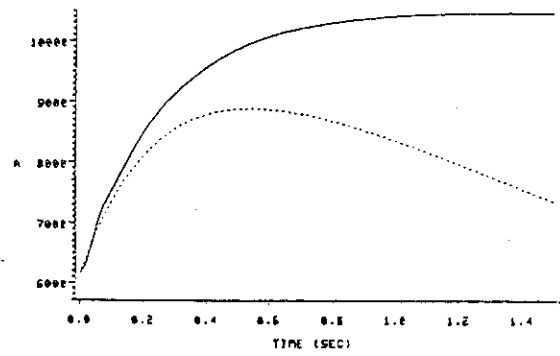
CURRENT AT DISRUPTION

11-10



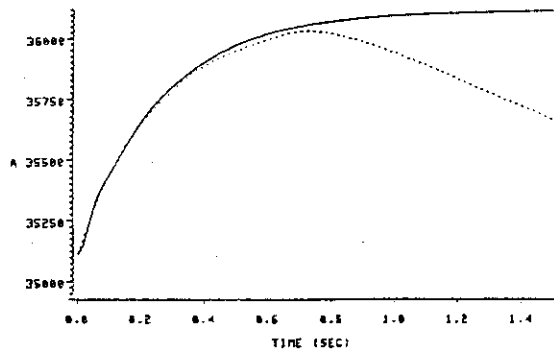
CURRENT AT DISRUPTION

11-14



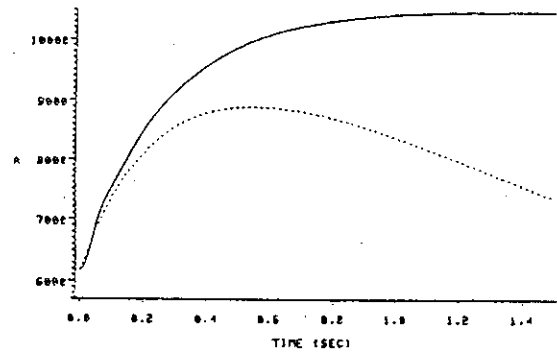
CURRENT AT DISRUPTION

11-11



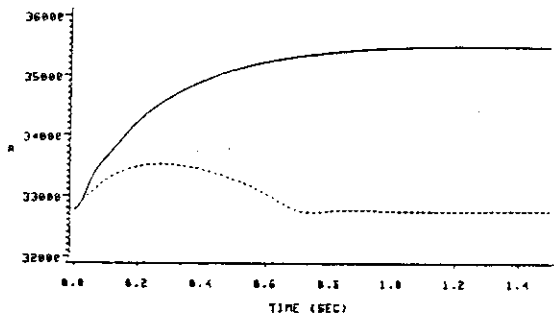
CURRENT AT DISRUPTION

11-15



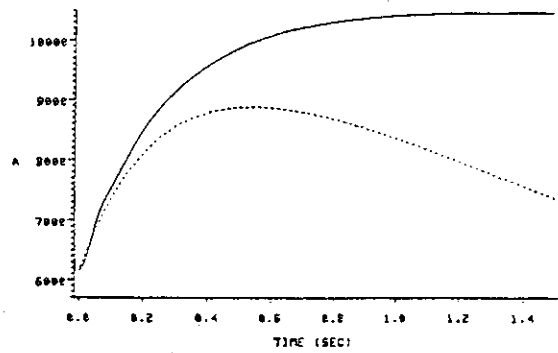
CURRENT AT DISRUPTION

11-12



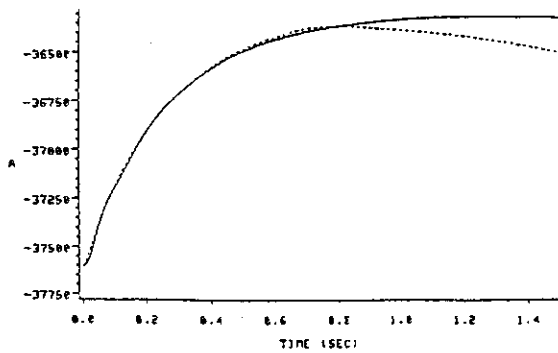
CURRENT AT DISRUPTION

11-16



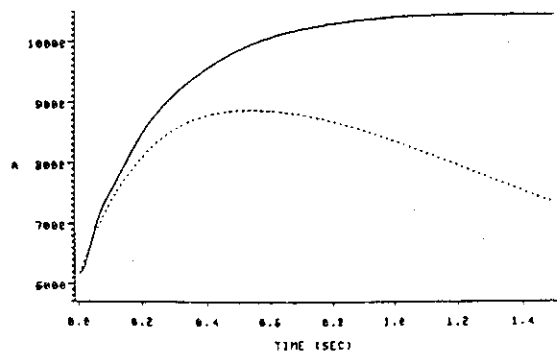
CURRENT AT DISRUPTION

11-13



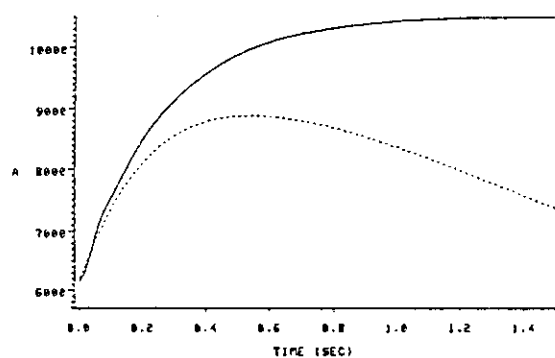
CURRENT AT DISRUPTION

11-17

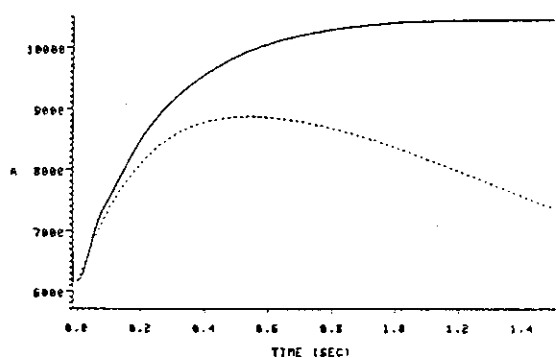




CURRENT AT DISRUPTION  
11-18



CURRENT AT DISRUPTION  
11-19



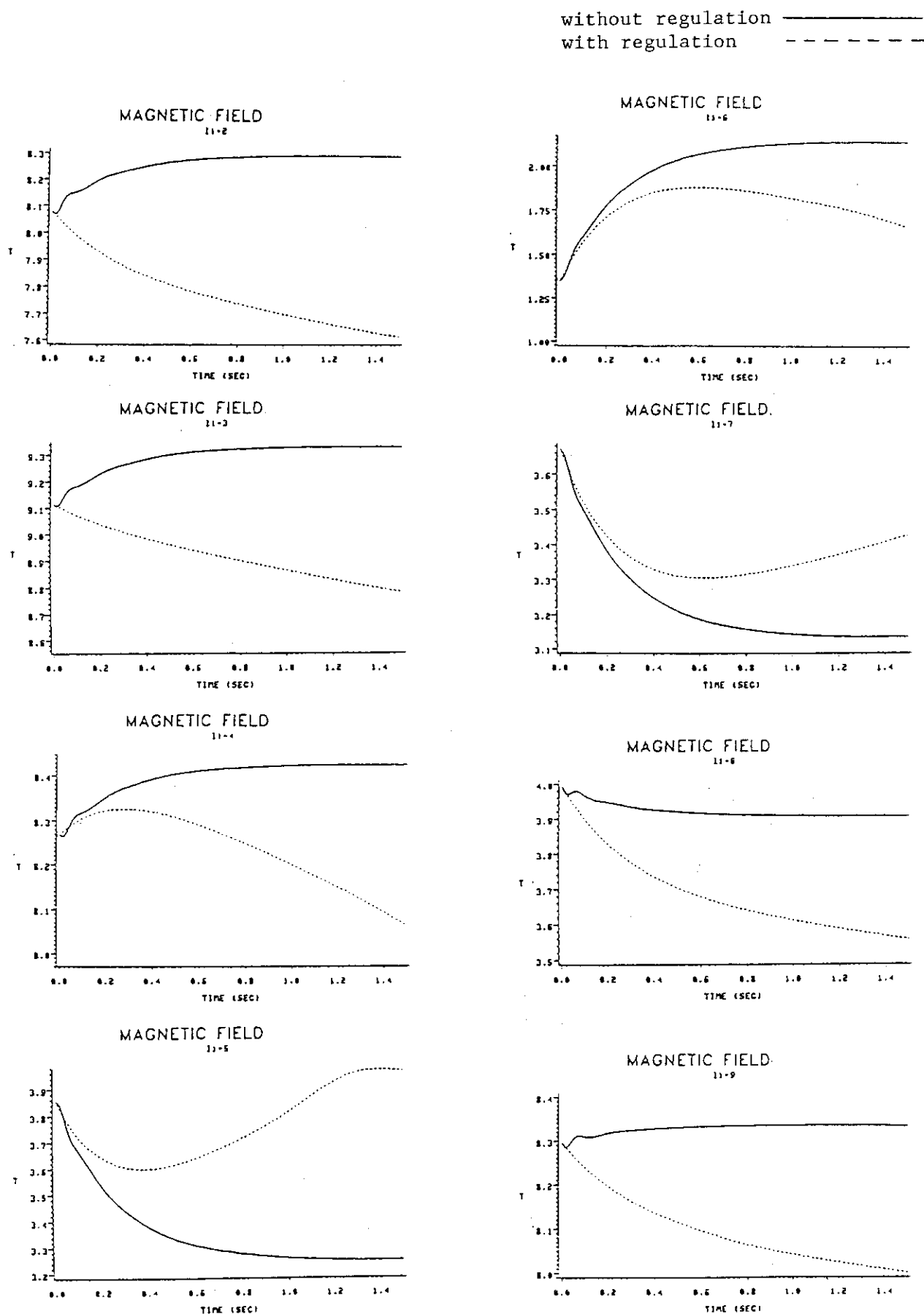
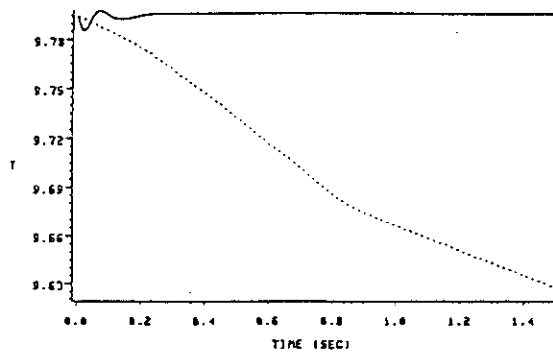


Fig. 4.2.5 Evolution of magnetic field at coil position with and without current regulation.

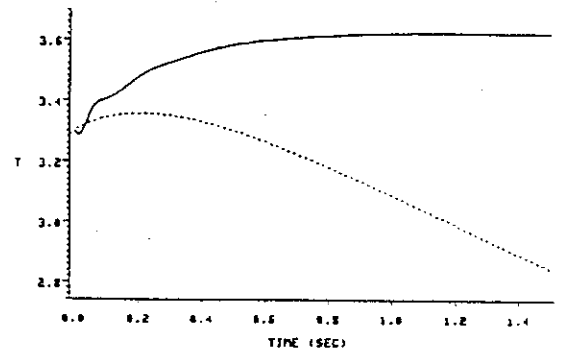
MAGNETIC FIELD

11-10



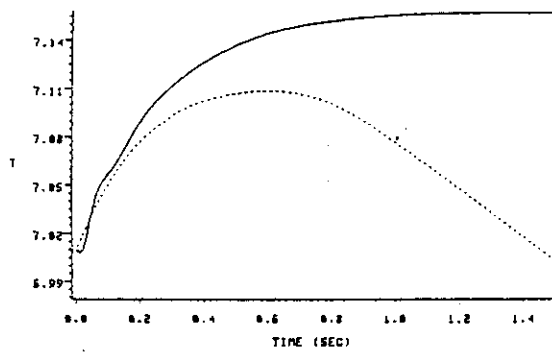
MAGNETIC FIELD

11-14



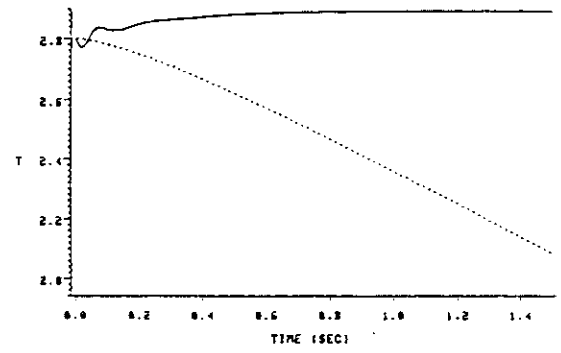
MAGNETIC FIELD

11-11



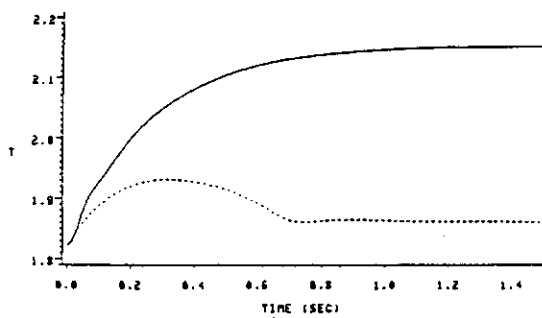
MAGNETIC FIELD

11-15



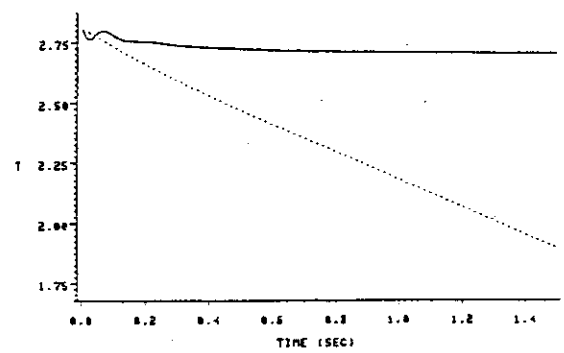
MAGNETIC FIELD

11-12



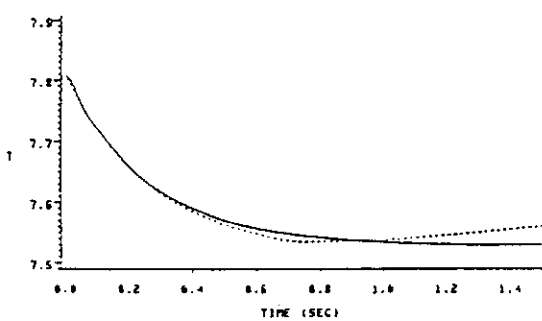
MAGNETIC FIELD

11-16



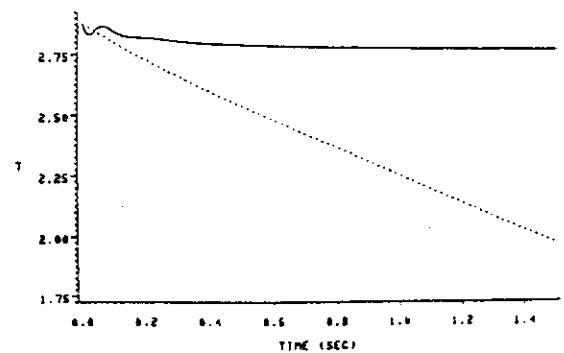
MAGNETIC FIELD

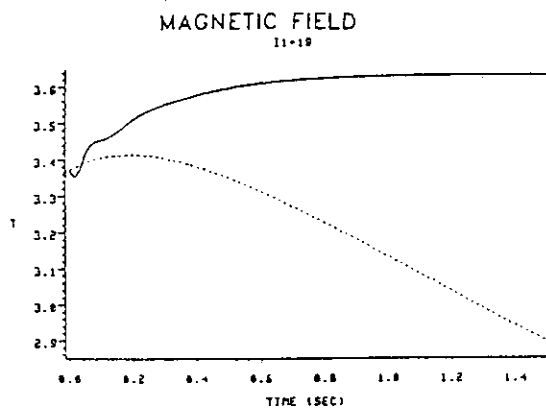
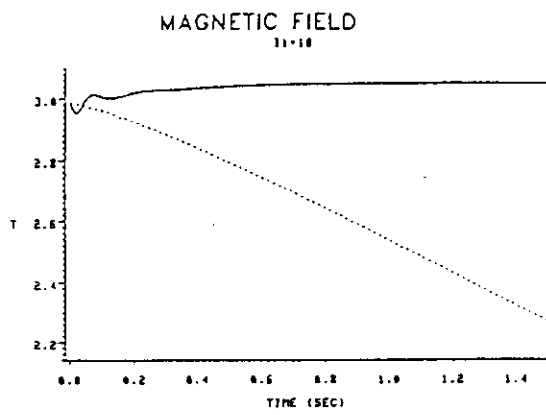
11-13



MAGNETIC FIELD

11-17





without regulation ———  
with regulation - - - - -

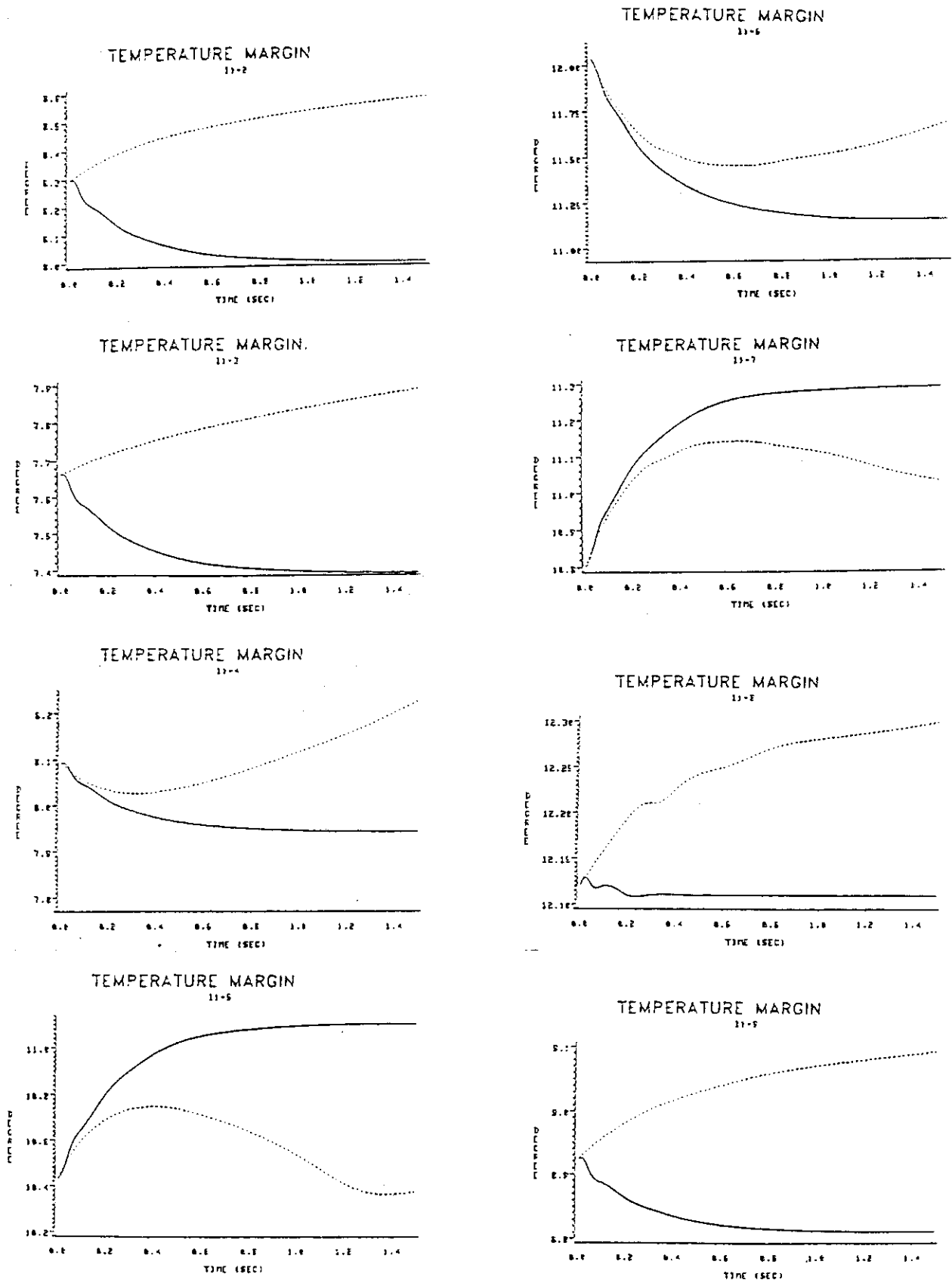
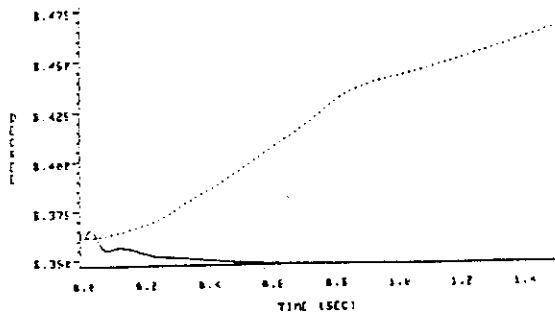
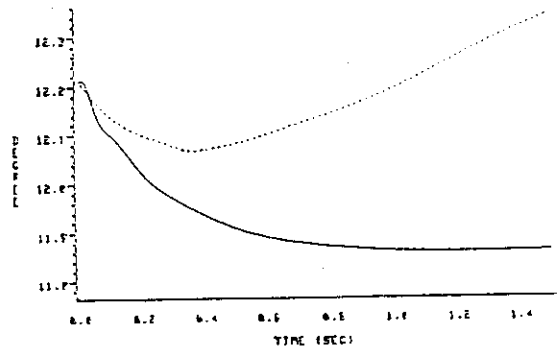


Fig. 4.2.6 Evolution of temperature margin with and without current regulation.

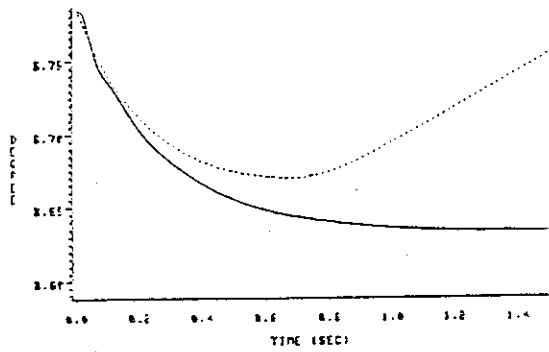
TEMPERATURE MARGIN  
11-10



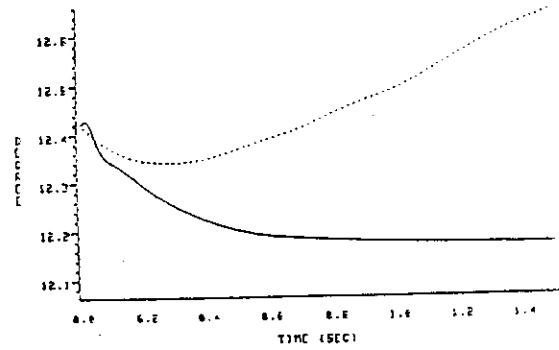
TEMPERATURE MARGIN  
11-14



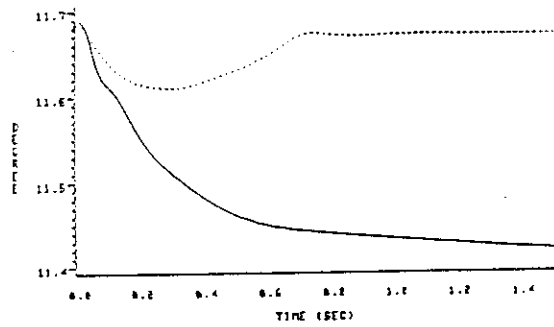
TEMPERATURE MARGIN  
11-11



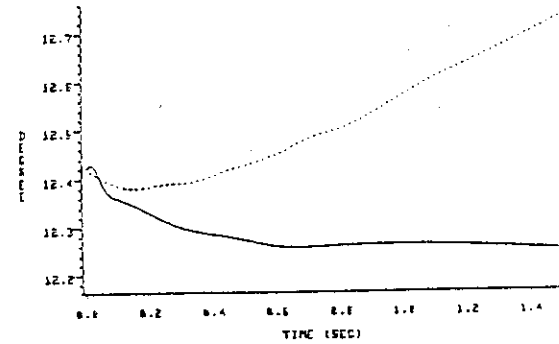
TEMPERATURE MARGIN  
11-15



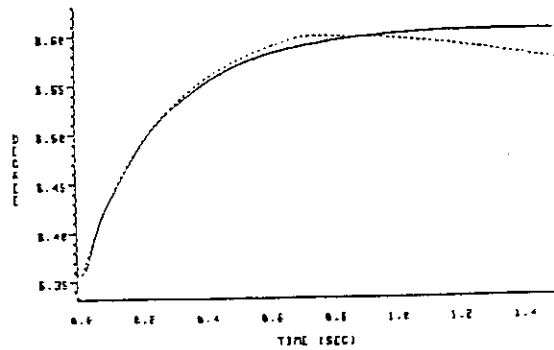
TEMPERATURE MARGIN  
11-12



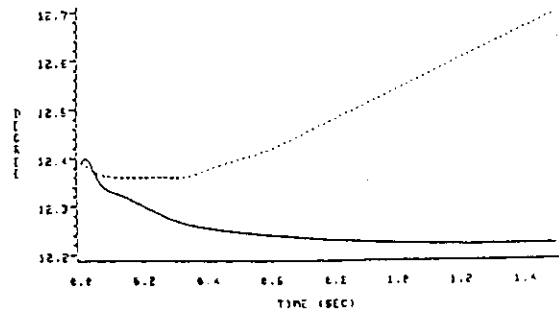
TEMPERATURE MARGIN  
11-16

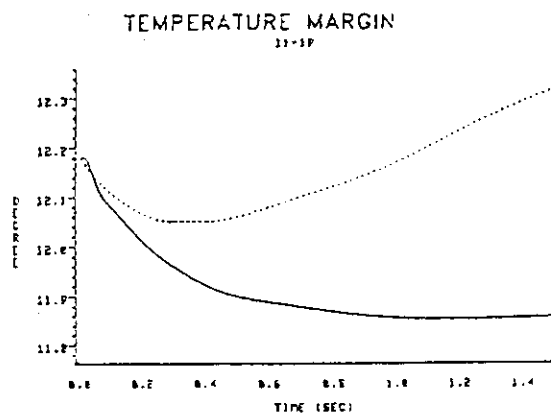
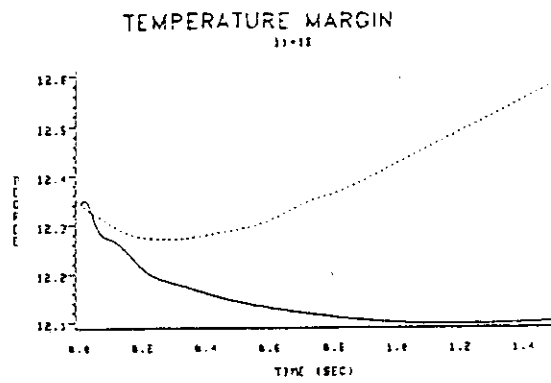


TEMPERATURE MARGIN  
11-13



TEMPERATURE MARGIN  
11-17





#### 4.3 Protection by shunt resistor for JFT-2M vacuum vessel against disruptions

Shunt resistor (bypass resistor) had been developed for the JFT-2M vacuum vessel for preventing arcing across insulated gaps and protecting PF coil/PF coil power supply at disruptions. The detail of the shunt resistor is described in Appendix E (DEVELOPMENT OF SEMICONDUCTOR SHUNT RESISTOR). The JFT-2M vacuum vessel is electrically broken with insulation at two positions in the toroidal direction. It was feared that the electrically insulated parts would be damaged with arcing across the flanges at plasma disruptions. More than 100 of shunt resistors are installed at these insulated flanges of the vacuum vessel (see Fig. 4.3.1). Induced currents flow from one side of the flange (left side for example) to another side of the flange through the shunt resistor, bolt and the tapered washer. Another important role of the JFT-2M shunt resistor is to fasten tightly the joints of the flanges to obtain high vacuum. The composite ceramic of Si and SiC is selected as resistance material, since this ceramic has high mechanical strength and high thermal conductivity, and is a varistor (variable resistor) which resistance decreases rapidly with the increase of applied voltage. The one turn toroidal resistance is high enough to break down plasma and rise plasma current, since the applied voltage is not so high. On the other hand, at plasma disruptions, one turn resistance is reduced and the induced voltage across the insulated gaps decreases enough to stop arc generation.

Several shunt resistors were found damaged at the first and the second vents, and damaged shunt resistors were replaced with new ones. After that, we found no damaged shunt resistor. There has been no trace of arcing at the flanges of the JFT-2M vacuum vessel.

#### Reference

- [1] M. Yamada, M. Kasai, T. Uchikawa and H. Kawai : Proc. 10th Symposium on Fusion Engineering, Vol.2, 973 (1983).



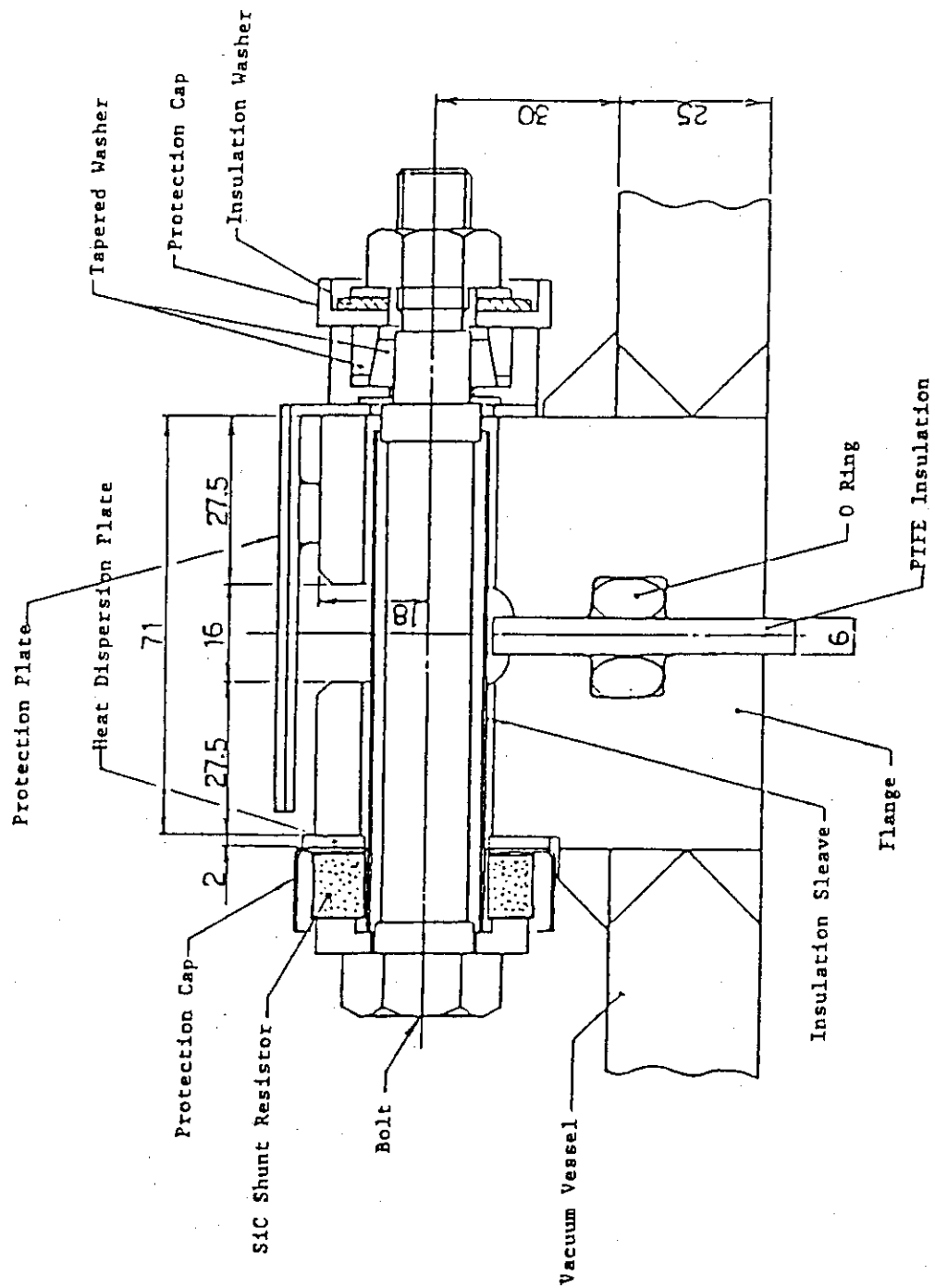


Fig. 4.3.1 Cross-section view of SiC shunt resistor

## II. INNOVATIONS

## 1. High Current Density and High Field for Toroidal Field Coil

To define general guidelines for INTOR TF coil design, the following conditions are set.

- i) This study has been focused on a cable-in-conduit conductor (CICC) with copper stabilized  $(\text{NbTi})_3\text{Sn}$ .
- ii) Based on the manufacturing experiences of cable-in-conduit superconductor, optimum conditions are as follows.
  - a) Cross section of a conductor is square. This configuration is desirable on manufacturing process.
  - b) Helium void fraction in conduit (1-fco) is 0.4. This is a minimum fraction to avoid the severe critical current degradation during manufacturing.
  - c) Strand diameter is from 0.5 mm to 1.0 mm. The smaller value is effective to cryogenic stabilization, but increases pressure drop. And a minimum limit due to strand manufacturing is considered to be 0.5 mm.
- iii) Fraction of copper in the conductor strands (f) is varied from 0.5 to 0.67 to obtain a higher current density.

## 1.1 General guidelines for INTOR TF coil design

## (1) Quench voltage

Quench voltage is limited by magnet insulation. Maximum operating voltage of 20 kV is acceptable with high voltage insulation technology.

## (2) Peak conductor temperature

Peak conductor temperature ( $T_m$ ) during a quench is ordinarily limited to the value of 100 K in order to reduce the thermal stress to the negligible order. In this study, we propose to raise the allowable peak conductor temperature to higher level in order to satisfy the current density requirement of INTOR innovations. But the peak conductor temperature ( $T_m$ ) must be under 220 K to keep the thermal expansion less than 0.2% even at the end of current dumping (Fig. 1.1.1).

This condition gives the limit of current density in copper stabilizer.

$$U_m = \int_{T_b}^{T_m} \frac{\gamma C(T)}{\rho(T)} dT = \int_0^{\infty} J^2(t) dt = \frac{1}{2} J_0^2 \tau_0$$

$T_m$  : Peak conductor temperature (220 k)

$T_b$  : Initial temperature at the beginning of temperature rise

$\tau_0$  : Current dumping time constant (sec)

$J_0$  : Current density in copper stabilizer (A/m<sup>2</sup>)

On the other hand, a relation between current, voltage and stored energy is

$$\tau_0 = \frac{2Q}{VI}$$

$Q$  : Stored energy (2.5 × 10<sup>9</sup> J)

$V$  : Quench voltage (20,000 V)

$I$  : Conductor current (A)

$$\therefore J_0^2 = \frac{UmV}{Q} I = 8 \times 10^{-6} UmI \quad (A^2/m^4)$$

The value of  $U_m$  is given in Fig. 1.1.2, and the relation between  $J_0$  and  $I$  is shown in Fig. 1.1.3. A relation between current density in copper stabilizer ( $I_0$ ), current density inside conduit ( $J$ ), and current density of conductor ( $J_{total}$ ) is given by

$$J = fco \cdot f \cdot j_0 = (0.3 \sim 0.4) J_0$$

$$J_{total} = \frac{A_{cable}}{A_{total}} J = 0.54 J$$

where  $fco$  : Strand area ratio in the conduit (0.6)

$f$  : Stabilizer area ratio in strands (0.5 ~ 0.67)

$$= \frac{n}{n+1}$$

$n$  :  $A_{Cu}/A_{Sc} = 1 \sim 2$

## (3) Maximum conductor current

When a current density is given, a conductor current is defined from a conductor size. The limit of conductor size comes from a maximum strain of superconductor and minimum winding radius.

The allowable strain of  $(\text{NbTi})_3\text{Sn}$  cable-in-conduit conductor (CICC) is about 0.8%. Suppose the maximum allowable strain is 0.8% and strain by the electromagnetic force is 0.2%, the allowable winding strain becomes the value of 0.6%. The maximum conductor current ( $I_m$ ) is calculated by the minimum winding radius ( $R_m$ ) as follows;

$$I_m = J (2 \varepsilon R_m)^2$$

$J$  : Current density inside the conduit ( $\text{A}/\text{mm}^2$ )

$\varepsilon$  : Allowable winding strain ( $6 \times 10^{-3}$ )

$R_m$  : Minimum winding radius (mm)

The  $I_m$ - $R_m$  curves are shown in Fig. 1.1.4. Maximum conductor current is 43 kA under the condition of  $R_m=2\text{m}$  and  $J=75 \text{ A}/\text{mm}^2$ .

On the other hand, minimum conductor current is decided from stored energy ( $Q$ ), quench voltage ( $E$ ) and current density in copper stabilizer ( $J_0$ ). The minimum value is 26 kA in the case of  $Q = 2.5 \text{ GJ}$ ,  $V = 20 \text{ kV}$  and  $J = 75 \text{ A}/\text{mm}^2$  ( $J_0 = J / (f_{co} \cdot f) = 188 \text{ A}/\text{mm}^2$ ). In Fig. 1.1.5, the current density inside the conduit is shown plotted against conductor current under the winding strain limit and quench protection limit. Allowable conductor currents are from 26 to 43 kA for the current density inside the conduit of  $75 \text{ A}/\text{mm}^2$ . Maximum current density inside the conduit is  $125 \text{ A}/\text{mm}^2$ .

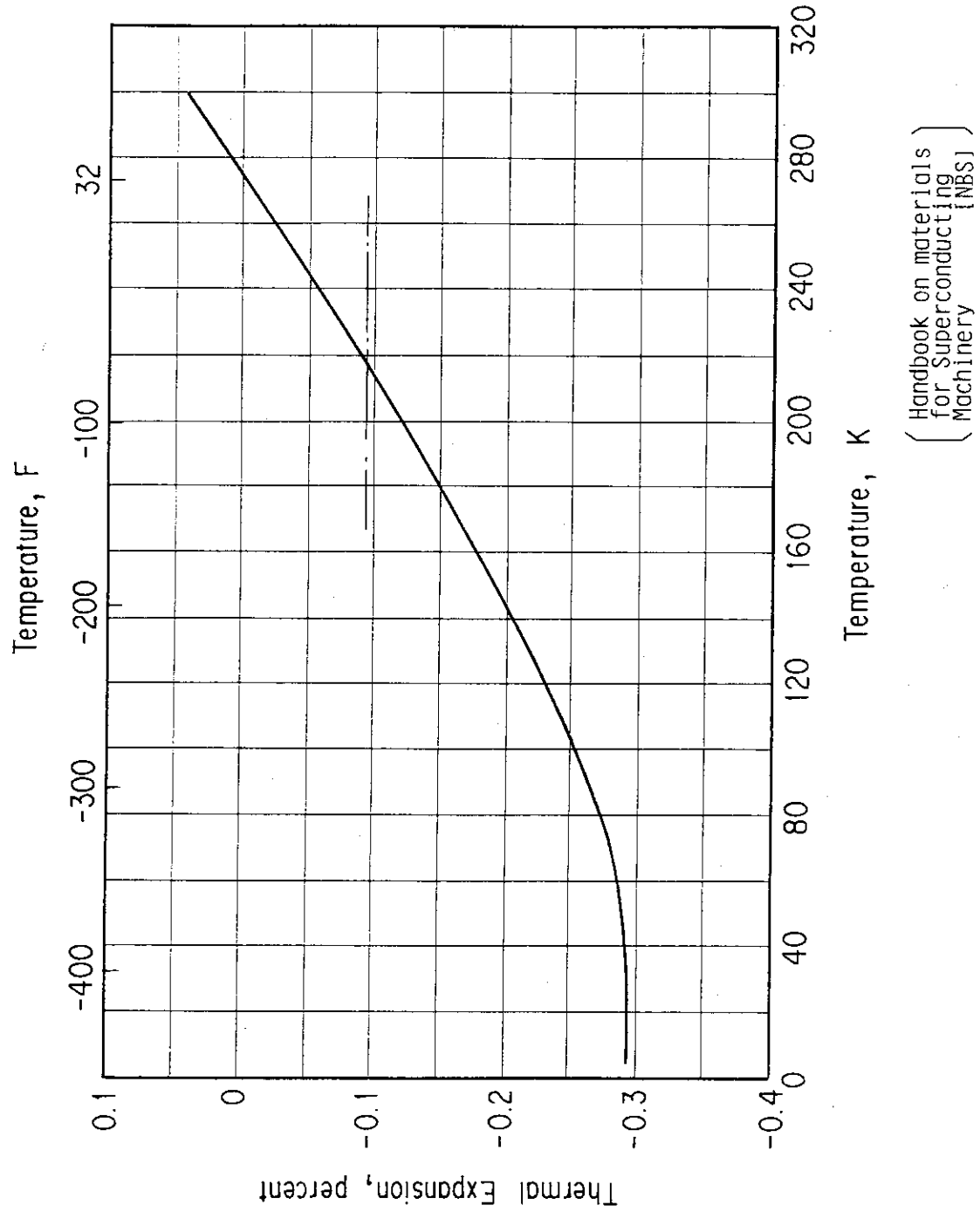


Fig. 1.1.1.1 Thermal expansion versus temperature for copper.

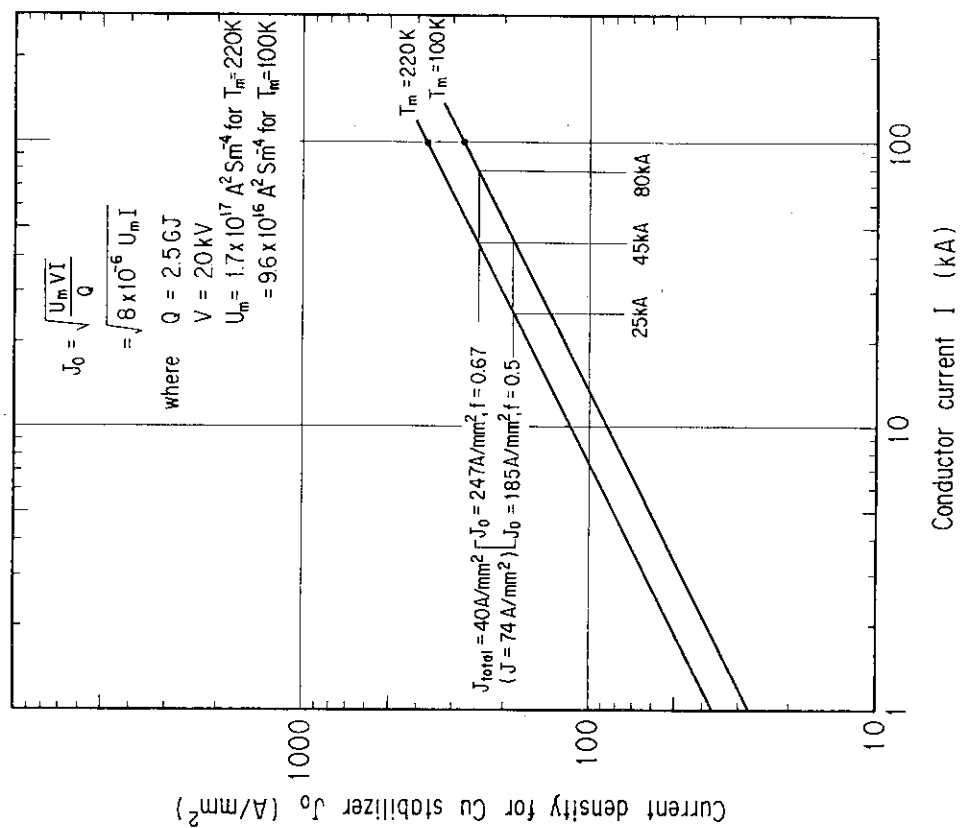
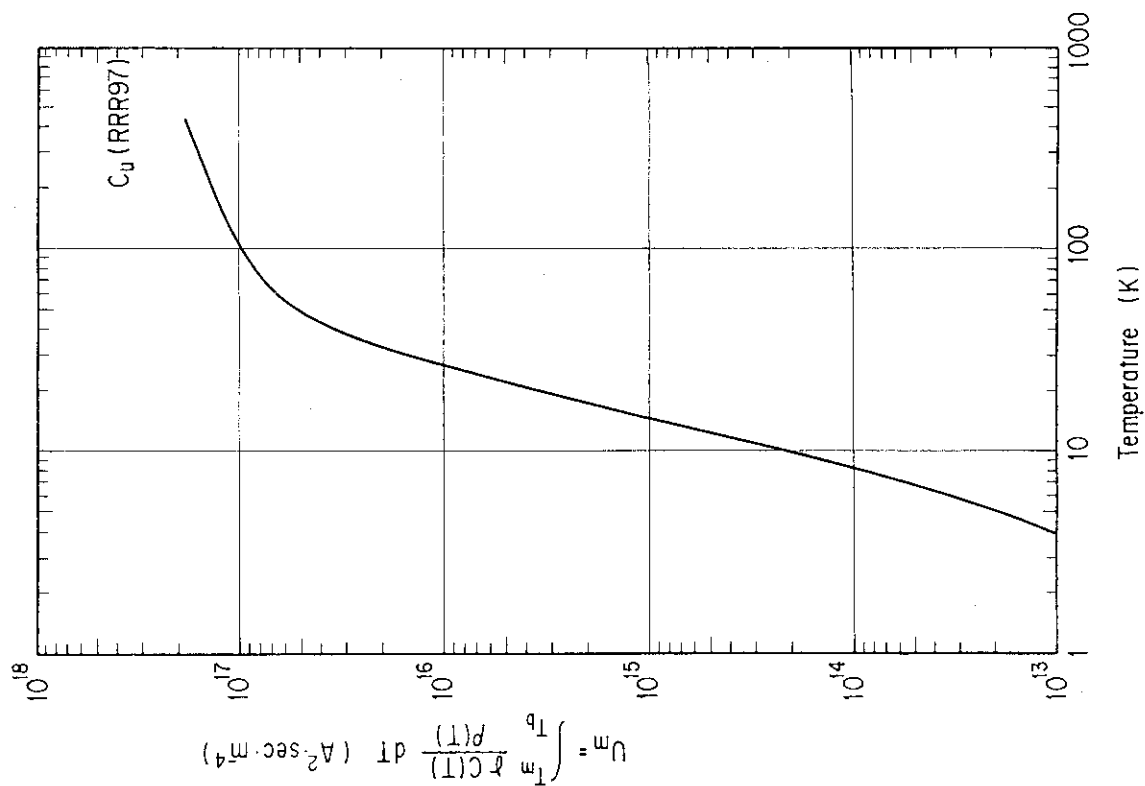


Fig. 1.1.3 Current density for Cu stabilizer VS conductor current.

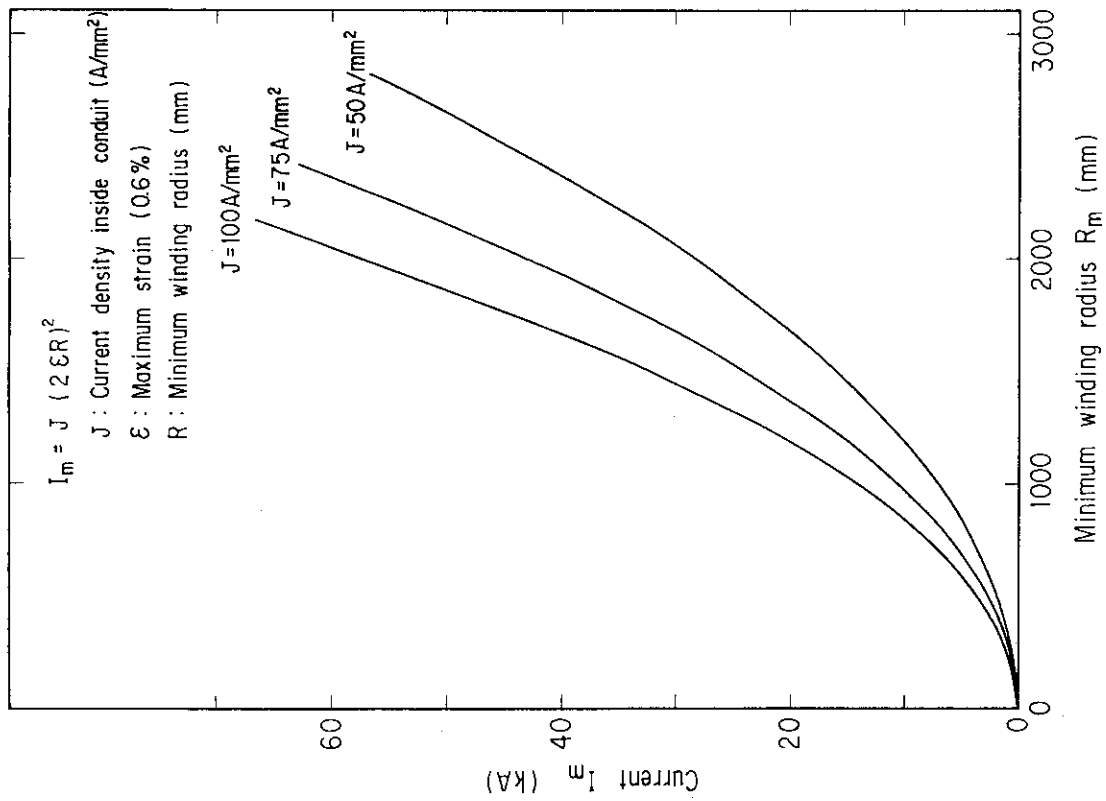


Fig. 1.1.4 Maximum current  $I_m$  vs minimum winding radius  $R_m$ .

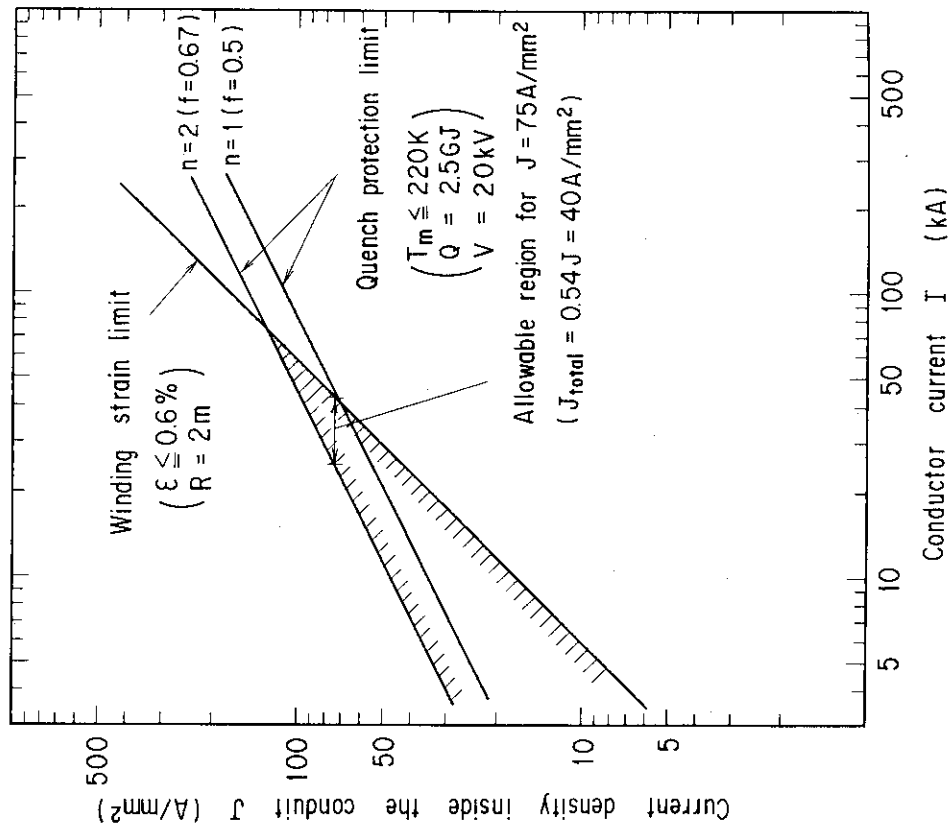


Fig. 1.1.5 Current density inside the conduit based on the winding strain limit and quench protection limit.

## 1.2 Generalized graph to select current density

(1) Operation current density ( $J_{op}$ ) inside the conduit

Operation current is limited from temperature margin ( $T_{cs}-T_b$ ).

$$\begin{aligned} T_{cs}-T_b &= \left(1 - \frac{I_{op}}{I_c}\right)(T_c-T_b) \\ &= \left(1 - \frac{I_{op}}{I_c}\right)\left\{T_{co}\left(1 - \frac{B}{B_{co}}\right)^{1/2} - T_b\right\} \end{aligned}$$

$T_{cs}$ :	Current shearing temperature	(k)
$T_b$ :	Helium temperature	(5 k)
$I_{op}$ :	Operation current	(A)
$I_c$ :	Critical current	(A)
$T_c$ :	Critical temperature at magnetic field BT	(K)
$T_{co}$ :	Critical temperature at magnetic field OT	(18.3 K)
$B$ :	Magnetic field	(Tesla)
$B_{co}$ :	Critical magnetic field	(24.5 Tesla)

$$\therefore \frac{I_{op}}{I_c} = 1 - \frac{T_{cs} - T_b}{T_{co}\left(1 - \frac{B}{B_{co}}\right)^{1/2} - T_b}$$

$$\begin{aligned} J_{op} &= J_c \cdot f_{co} \cdot (1-f) \left(\frac{I_{op}}{I_c}\right) \\ &= J_c \cdot f_{co} \cdot (1-f) \left\{1 - \frac{T_{cs} - T_b}{T_{co}\left(1 - \frac{B}{B_{co}}\right)^{1/2} - T_b}\right\} \end{aligned}$$

$f_{co}$  : Strand area ratio in the conduit (0.6)

$f$  : Stabilizer area ratio in strands =  $\frac{n}{n+1}$

$n$  :  $A_{cu}/A_{sc} = 1 \sim 2$

$J_c$  : Critical current density of non copper area in strands

If the temperature margine ( $T_{cs} - T_b$ ) assume 2 deg, the above equation becomes

$$J_{op} = 0.3 J_c \left\{1 - \frac{2}{18.3\left(1 - \frac{B}{24.5}\right)^{1/2} - 5}\right\}$$

where temperature rise of 0.5 deg caused by the nuclear heating 1 mW/cc



is assumed. And the temperature margin of 2 K includes the decrease of temperature margin caused by  $I_c$  degradation.

(2) Limiting current density ( $J_B$ ) inside the conduit

Limiting current density ( $J_B$ ) is shown as follows;

$$J_B = \frac{0.86 \times 10^5}{d} \cdot \left( \frac{f \cdot f_{co}^3}{1 - f_{co}} \right)^{1/2} \left( \frac{T_c - T_b}{6.65 - 4.2} \right)^{1/2} \left( \frac{\rho_1}{\rho_2} \right)^{1/2}$$

$$T_c - T_b = T_{co} \left( 1 - \frac{B}{B_{co}} \right)^{1/2} - T_b$$

$\rho_1$  : Resistivity of stabilizer at 6T ( $3.9 \times 10^{-10} \Omega \cdot m$ )

$\rho_2$  : Resistivity of stabilizer at magnetic field B(T) ( $\Omega \cdot m$ )

$$\rho_2 \sim (0.63 + 0.48B) \times 10^{-10} \Omega \cdot m$$

$$\therefore J_B = 118.4 \left( \frac{18.3 \left( 1 - \frac{B}{24.5} \right)^{1/2} - 5}{0.63 + 0.48B} \right)^{1/2}$$

(3) Current density ( $J_Q$ ) inside the conduit limited from guidelines

Combining the equation of current density in copper stabilizer ( $J_O$ ) and maximum conductor current ( $I_m$ ), we obtain another equation of current density limit.

$$J_O^2 = \frac{U_m V}{Q} I = \frac{U_m V}{Q} J_Q \quad (2 \in R_m)^2$$

$$J_Q = f_{co} \cdot f \cdot J_O$$

$$Q = 2.0 \times 10^7 B^2$$

$$\therefore J_Q = 8.8 \times 10^9 \frac{f^2 R_m^2}{B^2} (A/m^2) = 8.8 \times 10^3 \frac{f^2 R_m^2}{B^2} (A/mm^2)$$

(4) Current density selection

The current densities ( $J_{Op}$ ,  $J_B$  and  $J_Q$ ) inside the conduit as a function of magnetic field are shown in Table 1.2.1 and Fig. 1.2.1. In Fig. 1.2.1,  $J_{Op}$  and  $J_B$  are shown by solid lines, and  $J_Q$  is shown by dotted lines. The parameter in this figure is Cu/SC area ratio. The tolerable current density for each magnetic field has to be determined from a minimum value of  $J_{Op}$ ,  $J_B$  and  $J_Q$ . The winding current density

$J_{\text{total}}$  is defined as 0.54 times of current density inside the conduit.

From Fig. 1.2.1, we can design the INTOR TFC conductor at the value of  $B = 12$  T and  $J_{\text{total}} = 40$  A/mm<sup>2</sup>, but the point of  $B = 16$  T and  $J_{\text{total}} = 25$  A/mm<sup>2</sup> is critical and the minimum winding radius of conductor must be larger than the value of 2.2 m.

Table 1.2.1 Current density and magnetic field

B(T)	$J_c$ (A/mm <sup>2</sup> )	$J_{op}$ (A/mm <sup>2</sup> )	$J_B$ (A/mm <sup>2</sup> )
10	900	210.5	153.1
12	630	142.2	133.1
14	440	94.2	115.4
16	280	54.9	98.7
18	165	27.1	81.8

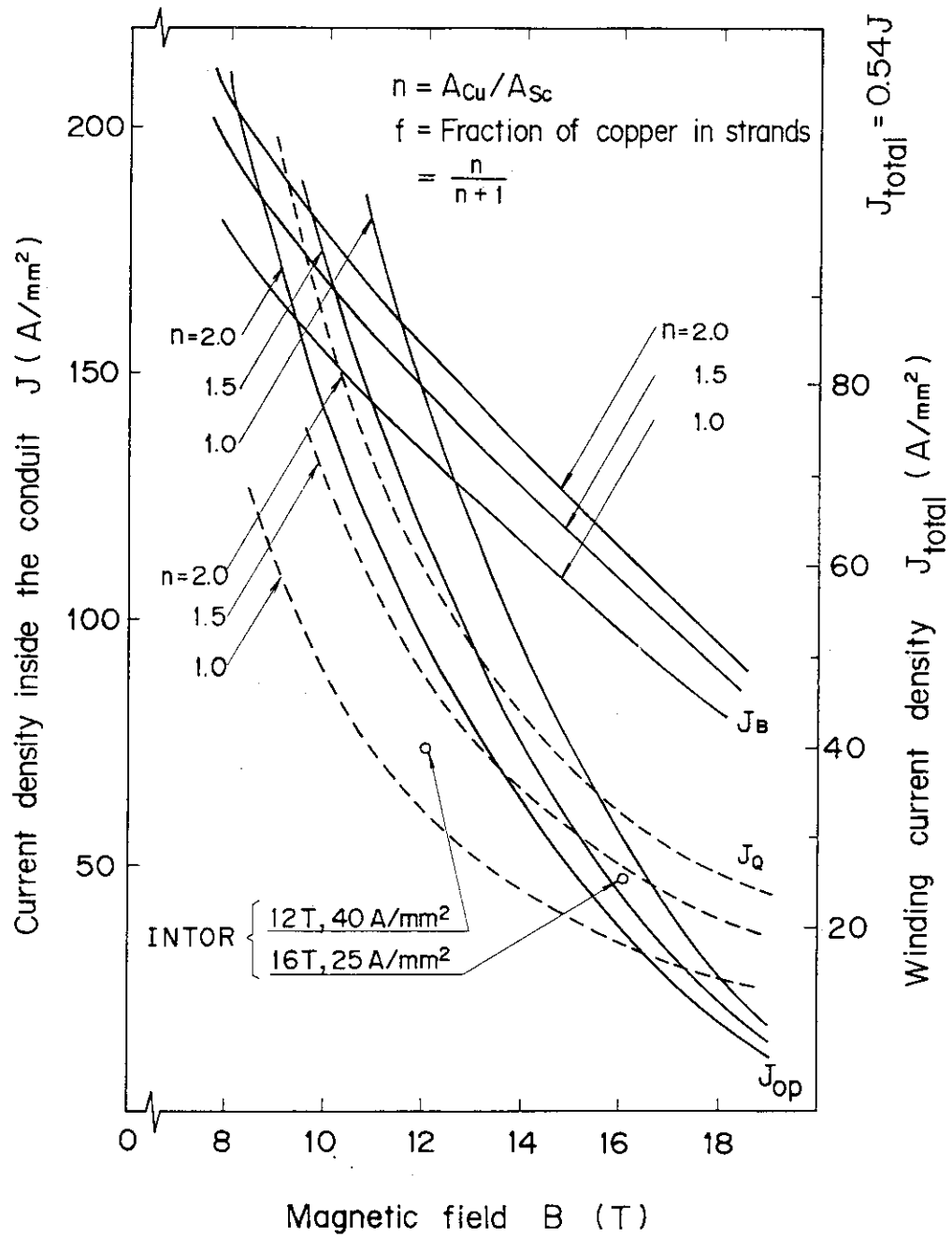


Fig. 1.2.1 Current density inside the conduit versus magnetic field.

### 1.3 Conductor and coil manufacturing

It is necessary to use  $Nb_3Sn$  for the achievement of high current densities and high fields. Since  $Nb_3Sn$  is very sensitive to strain, the wind-and-react method must be used for small bending radius coils.

The manufacturing process of internally cooled cable-in-conduit superconductor of  $Nb_3Sn$  using wind-and-react method is as follows.

1. Conduit material in the form of thin plate is bent and wraps a twisted cabled conductor.
2. The conduit is welded and swaged to the final conductor shape.
3. The conductor is wound into a coil while being wrapped with a cross fiber to reinforce the insulation.
4. The coil is heated up to the temperature of about  $700^\circ C$  where  $Nb_3Sn$  precipitates, and held at that temperature for 100 to 200 hours.
5. The coil is cooled down to the room temperature, and impregnated with resin.

In react-and-wind method the 3rd and 4th stages in the above processes are changed.

There are some additional requirements in the wind-and-react manufacturing processes compared with the react-and-wind method;

- (a) the conductor temperature over the large coil need to be well controlled in the heat treatment process,
- (b) the reduction of strength in the conduit material and reinforcing fiber for insulation must be little even after heat treatments.

The problem (b) has been almost solved by the development of new materials. The problem (a) still remains for large size coils such as TF coils.

We are using following criterion for the  $Nb_3Sn$  coil design. The maximum allowable strain is 0.8 %, which is the sum of the winding strain of 0.6 % and the strain caused by electromagnetic force of 0.2 %.

On the basis of this criterion, TF coils can be manufactured with the react-and-wind method because the minimum bending radius of the coil is more than 2 m.

On the other hand, OH coils which have a minimum bending radius less than one meter must be manufactured using wind-and-react method. But those coils are rather small and it is easy to controll the heat treatment temperature.

#### 1.4 Analysis of quench protection

It is difficult to analyse the fault condition in the event that the quench protection system doesn't work well, especially to estimate the safety of personnel and the prevention of a catastrophic failure of the facility. Such a catastrophic failure depends on the design of the whole facility, for example the design of coils, coil support structure, vacuum vessel, etc. We should better to improve the interlock system to avoid such an accident that the quench protection system doesn't work well. Here, it seems better to consider the analysis of quench protection with greater precision.

We must analyse constraints that the temperature at any point of cable-in-conduit type conductor and the pressure inside the conduit must not exceed some safe value in the event of a quench. These coil protection requirements constrain the current density in the conductor.

##### (1) Peak conductor temperature

Peak conductor temperature ( $T_m$ ) is ordinarily set less than 100 K in order to avoid damage to insulation by severe thermal stress. Characteristics of TF coil conductor are shown in table 1.4.1. The cable-space current density is constrained by maximum hot-spot temperature according to a relation of the form which includes not only copper heat capacity but also non copper (superconducting material) and helium heat capacity.

$$J \leq \left\{ \frac{V_D \cdot I_{op}}{Q} [(1 - f_{co})f_{co} \cdot f U_1 + f^2 \cdot f_{co}^2 U_2 + (1 - f)f \cdot f_{co}^2 U_3] \right\}^{\frac{1}{2}}$$

where  $J$  : Operating current density inside the conduit of a CICC (A/mm<sup>2</sup>)  
 $V_D$  : Terminal voltage resulting from a dump at full field (V)  
 $I_{op}$  : Operation current at full field (A)  
 $Q$  : Stored energy at full field (J)  
 $f_{co}$  : Fraction of conductor inside the conduit of the CICC (=0.6)  
 $f$  : Fraction of stabilizing copper in the superconductor composite strands (=0.6)

$$U_1 = \int_{T_b}^{T_m} \frac{\gamma_{He} \cdot C_{V \cdot He}}{\rho_{cu}} dT$$

$$U_2 = \int_{T_b}^{T_m} \frac{\gamma_{cu} \cdot C_{cu}}{\rho_{cu}} dT$$

$$U_3 = \int_{T_b}^{T_m} \frac{\gamma_{core} \cdot C_{core}}{\rho_{cu}} dT$$

$T_b$  : Bulk fluid temperature of the internal helium of a CICC (K)

$T_m$  : Maximum conductor temperature (K)

$\gamma_{He}$  : Density of internal He in a CICC at the initial operating temperature and pressure, i.e., before a quench ( $\text{kg/m}^3$ )

$\gamma_{cu}$  : Density of copper ( $\text{Kg/m}^3$ )

$\gamma_{core}$  : Density of noncopper fraction of the composite superconductor ( $\text{Kg/m}^3$ )

$C_{V,He}$  : Specific heat at constant volume for He ( $\text{J/Kg}\cdot\text{K}$ )

$C_{cu}$  : Specific heat of copper ( $\text{J/Kg}\cdot\text{k}$ )

$C_{core}$  : Specific heat of noncopper fraction of the composite superconductor ( $\text{J/Kg}\cdot\text{K}$ )

$\rho_{cu}(B)$  : Resistivity of the stabilizing copper at operating field ( $\Omega\cdot\text{m}$ )

$U_1$ ,  $U_2$ ,  $U_3$  curves are shown in Fig. 1.4.1 which means that He is most effective until 25 K, but noncopper fraction of the superconductor becomes effective above 25 K.

Using Fig. 1.4.1, we can calculate the relation between the cable space current density and maximum hot-spot temperature which is shown in Fig. 1.4.2. The cable space current density in our design is  $J=75 \text{ A/mm}^2$ , therefore if we use a dumping voltage of 20 kV which is severe for the insulator, we can show the maximum hot-spot temperature ( $T_m$ ) less than 100 K by using improved hot-spot model. Figure 1.4.3 shows the relation between dumping time constant and maximum hot-spot temperature. This means that we should select dump resistivity to keep dumping time constant less than  $\tau=8 \text{ sec}$ .

## (2) Peak pressure

The maximum allowable pressure in the event of a quench also constraints the cable-space current density according to Miller's equation.

$$J \leq \frac{8.71 (P_{\max})^{0.694} (1 - f_{\text{co}})^{3/4} f_{\text{co}}^{1/4} f^{1/2} D_W^{1/4}}{\rho_{\text{cu}}^{1/2} \ell^{3/4}}$$

where

$P_{\max}$  : Maximum allowable, absolute pressure during a quench of the CICC (Pa)

$D_W$  : Diameter of a superconductor composite strand in the CICC (m)

$\ell$  : Length of CICC between helium flow-connections (m)

Fig. 1.4.4 shows the relation between current density (J) and allowable maximum pressure in conduit. If we take allowable maximum pressure in conduit more than 35 MPa, we can use current density  $J=75.6 \text{ A/mm}^2$ . But this pressure is severe for a ceramic breaks in the coil. We should pay more attention to the possibility that the maximum allowable pressure will be constrained by a ceramic break rather than cable conduit.

Table 1.4.1 Characteristics of the superconductor for TFC

No.	Item	sign	unit	12T conductor
1.	Superconducting material		—	(NbTi) <sub>3</sub> Sn
2.	Strand diameter	$D_W$	$\phi$ mm	0.79
3.	Filament diameter (Number of filaments)		$\phi$ $\mu$ m	5 (2852)
4.	Bronze ratio		—	2.5
5.	Copper ratio		—	1.5
6.	No. of strands	n	—	$3^4 \times 7 = 567$
7.	Superconducting material area of strands	$A_{SC}$	mm <sup>2</sup>	111.1
8.	Copper area of strands	$A_{Cu}$	mm <sup>2</sup>	166.7
9.	Total area of strands	$A_{Co}$	mm <sup>2</sup>	277.8
10.	Operation current	$I_d$	KA	32.7
11.	Critical current at 12T, 5K ( $J_c = 540$ A/mm <sup>2</sup> )	$I_c$	KA	60.0
12.	S.S. Conduit outer dimensions	a	mm	$28.6 \times 28.6$
13.	S.S. Conduit inner dimensions	b	mm	$21.6 \times 21.6$
14.	S.S. Conduit area	$A_{SUS}$	mm <sup>2</sup>	328.7
15.	Insulation thickness	t <sub>ins</sub>	mm	0.7
16.	Helium area	$A_{He}$	mm <sup>2</sup>	185.2
17.	Volume fraction of copper in strands	$f = A_{Cu}/A_{Co}$	—	0.6
18.	Volume fraction of metal in the cable space	$f_{Co} = A_{Co}/(A_{Co} + A_{He})$	—	0.6
19.	Cable space area $A = A_{Co} + A_{He}$	A	mm <sup>2</sup>	463
20.	Void fraction $f_{He} = 1 - f_{Co}$	$f_{He}$	—	0.4
21.	Limiting current	$I_B$	KA	42.7
22.	Stability margin	$\Delta H$	J/cc	1.45



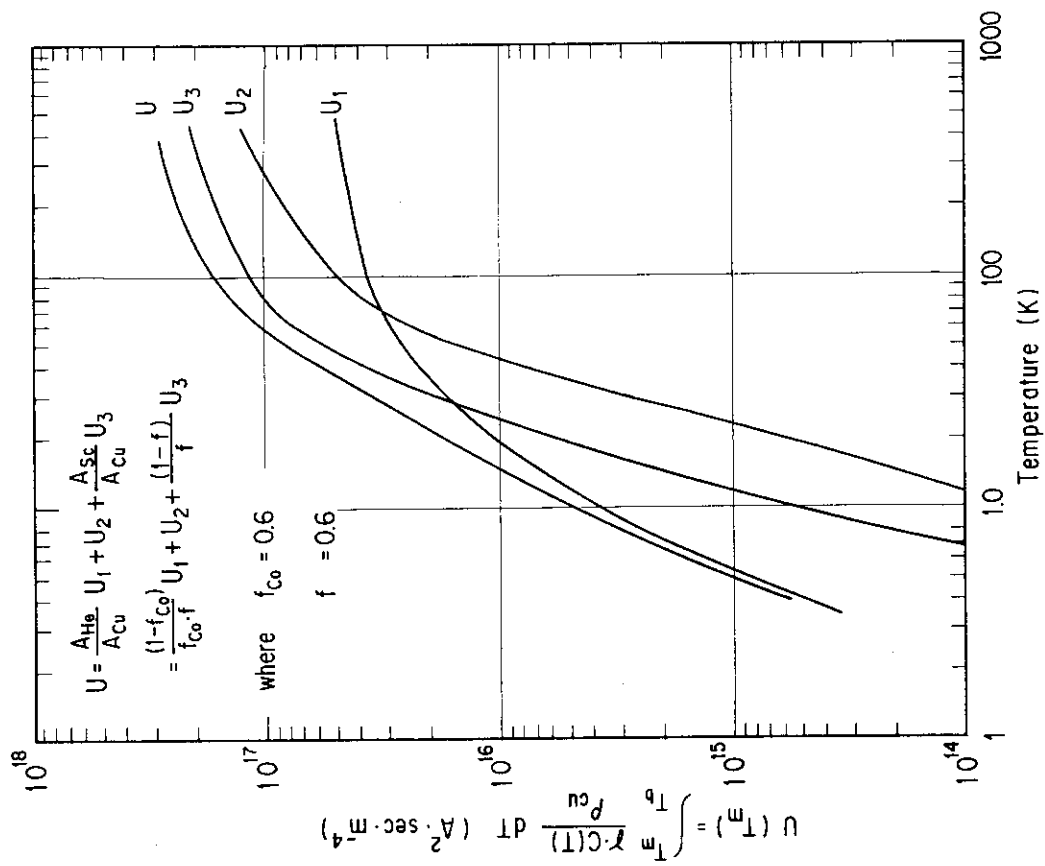


Fig. 1.4.1 Temperature -  $U(T_m)$  curve.

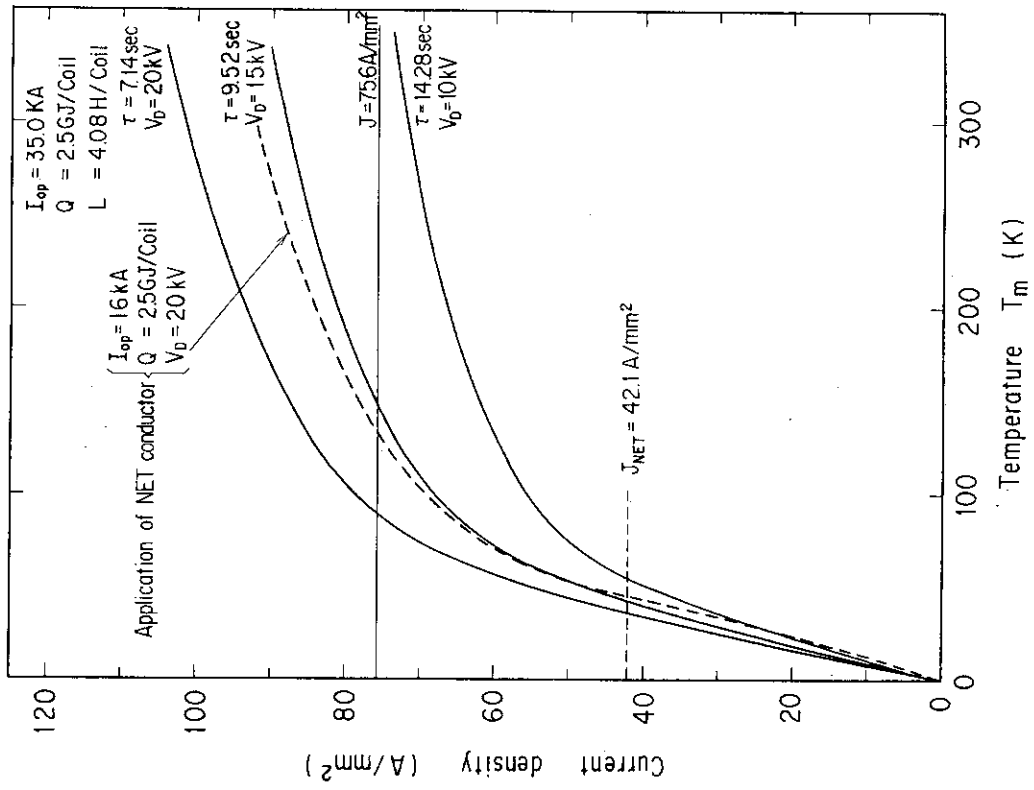


Fig. 1.4.2 Current density -  $T_m$  curve.

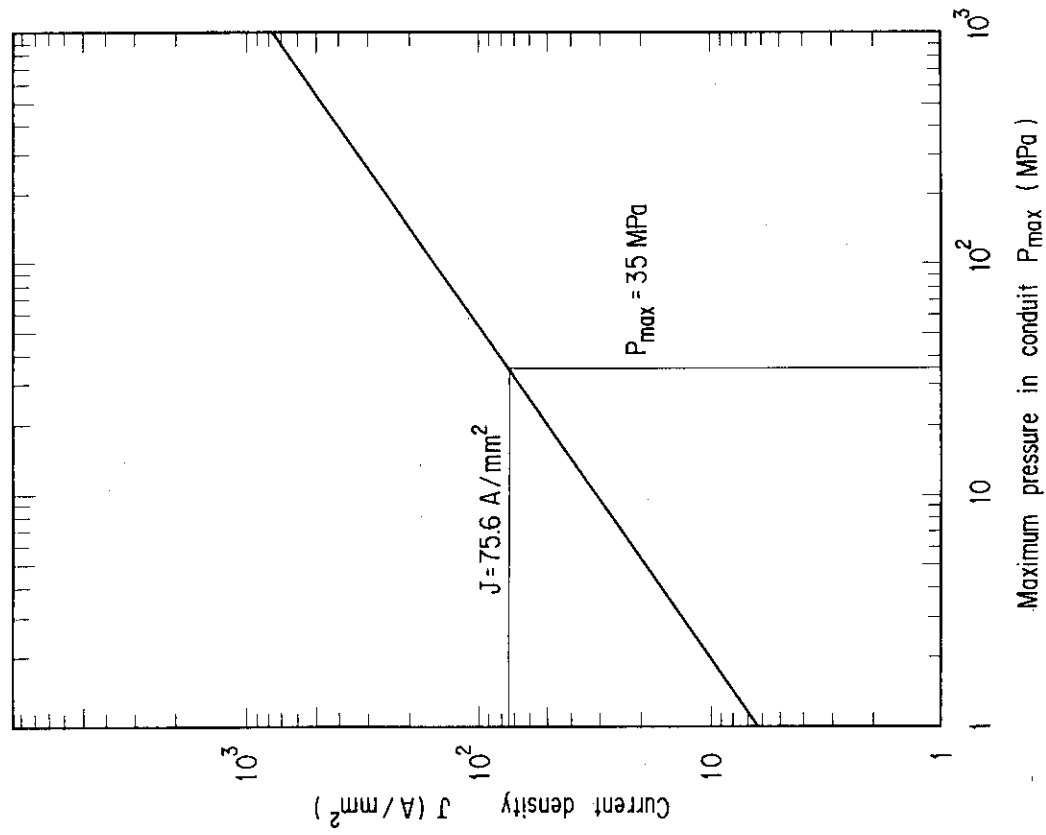


Fig. 1.4.4 Current density vs. maximum pressure in conduit.

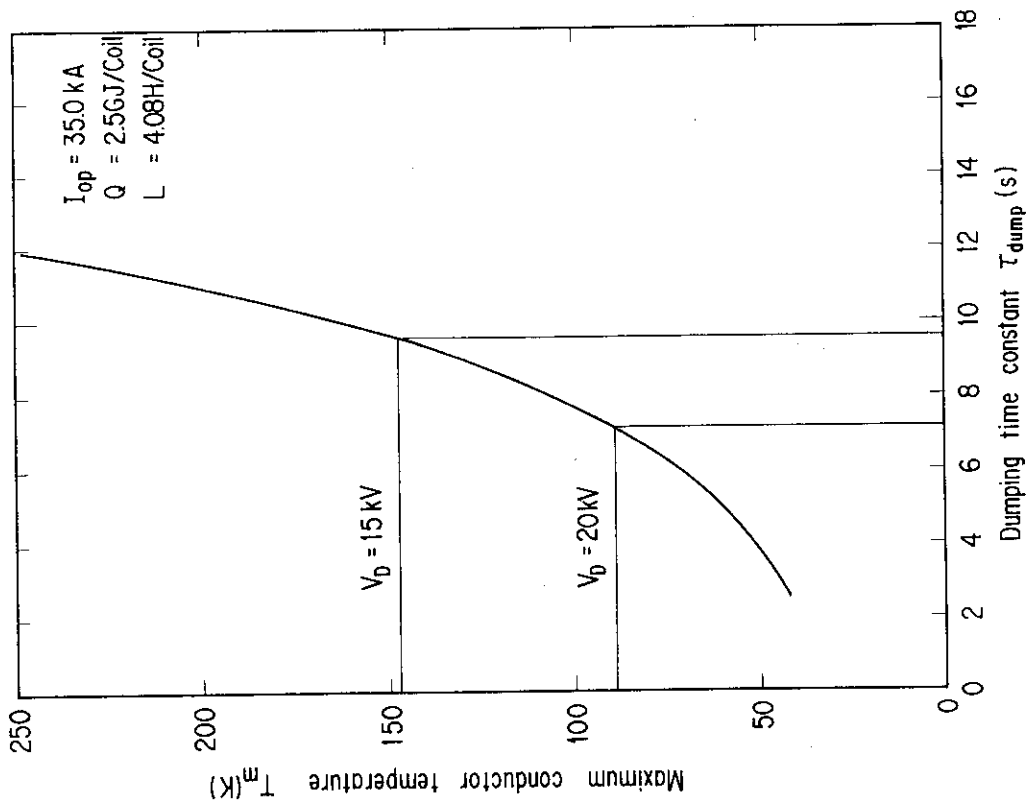


Fig. 1.4.3 Maximum conductor temperature vs. dumping time constant.

## 2. The Use of Nb<sub>3</sub>Sn for PF Coils

### 2.1 Basic conditions for design of central solenoid (OH) coils

- (1) A cable-in-conduit superconductor has been investigated on defining field and current in the central solenoid. Parametric study has been done in the range of maximum magnetic fields of 8 to 16 T. Candidate coolant temperatures are 4.5 K and 3.5 K. Allowable current densities have been decided based on both superconductor design and stress analysis in conduit.
- (2) It is reasonable to consider that a slip does not occur between strands and conduit. The sum of bending strain ( $\sim 1\%$ ) and the strain ( $\sim 0.3\%$ ) due to magnetic force is in the irreversible region of Ekin's experiments<sup>1)</sup>. According to his paper, the degradation of critical current caused by cyclic magnetic force (fatigue effect) is more than 40 %. Therefore we have to manufacture OH coils by using wind and react method.
- (3) Problems of the wind and react method are decrease of strength of conduit material and insulation effect at heat treatment. However the stainless steel, of which strength does not decrease at heat treatment, was already developed and the development of refractory insulating materials has started. Therefore there is no problem in the use of wind and react method.
- (4) The critical current density used in the design is 80 % of the value of single wire considering the strain effect caused by cooldown and magnetic force.
- (5) In the design of OH coils, allowable stress of the conduit material (SS304LN) is 530 MPa, two thirds of the yield strength.

### 2.2 Conductor design

Table 2.2.1 shows design parameters of a conductor. Operating current  $I_{op} = 40$  kA and  $Cu/SC = 1.5$  are selected in order to maintain the temperature rise of the conductor below 100 K and the damp voltage below 20 kV at coil quench. Here values of 100 K and 20 kV is adopted because

of the possibility of an increase of specific resistivity of copper caused by inserting barrier material in order to decrease AC losses. Helium void fraction of 40 % is in the region of small reduction of critical current due to cooldown. Strand diameter is more than about 0.5 mm required to manufacture. The number of strand  $3^6 = 729$  is decided to satisfy the requirement of limiting current in all case considered.

Table 2.2.2 shows design criteria of a conductor. These values are also used in the design of FER.

Ti added  $\text{Nb}_3\text{Sn}$  by the bronze method is selected as a superconducting material in order to reduce AC losses. Table 2.2.3 shows the dependence of critical current density of  $(\text{Nb Ti})_3\text{Sn}$  on magnetic field and temperature. The critical current density used in the design is 80 % of the value in the table considering the strain effect caused by cooldown and magnetic force.

Characteristics of designed conductor are summarized in Table 2.2.4. Criteria of Table 2.2.2 are all satisfied. To evaluate  $J_B$ ,  $\Delta T$  and  $\Delta H$ , 4.8 K is used as a helium temperature considering temperature rise caused by AC losses.

Table 2.2.1 Design parameters

Operating current $I_{op}$	40 kA
Cu/SC	1.5
He void fraction	0.4
Strand diameter	$\geq 0.5$ mm
Strand number	$3^6=729$

Table 2.2.2 Criteria of conductor design

Critical current	$I_c$	$>1.5 \times I_{op}$
Limiting current	$I_B$	$>I_{op}$
Stability margin	$\Delta H$	$>300$ mJ/cc strand
Temperature margin	$\Delta T = T_{cs} - T_b$	$>1$ K(*)

(\*) This is the value considering the critical current degradation already.

Table 2.2.3 Critical current density and critical temperature of  $(NbTi)_3Sn$ 

	Magnetic field (T)				
	8	10	12	14	16
$J_c$ (A/mm <sup>2</sup> ) at 4.5 K	1260	880	615	415	265
$J_c$ (A/mm <sup>2</sup> ) at 3.5 K	1335	950	670	465	310
$T_c$ (K)	15.0	14.1	13.1	12.0	10.8

Table 2.2.4 Characteristics of conductor

T(K)	B(T)	d(mm)	A <sub>sc</sub>	A <sub>co</sub>	A <sub>co</sub> +A <sub>He</sub>	w <sub>o</sub> (mm)	I <sub>B</sub> (kA)	ΔT	ΔH
4.5	8	0.511	59.8	149.5	249.2	15.8	57	3.4	610
	10	0.611	85.5	213.7	356.2	18.9	59	3.1	590
	12	0.732	122.7	306.7	511.3	22.6	62	2.8	550
	14	0.889	181.0	452.5	754.2	27.5	66	2.4	510
	16	1.112	283.2	708.0	1180.0	34.5	71	2.3	500
3.5	8	0.496	56.3	140.9	234.8	15.3	58	3.7	770
	10	0.587	78.9	197.3	323.8	18.1	60	3.4	730
	12	0.699	111.9	279.8	466.3	21.6	62	3.1	680
	14	0.840	161.6	404.0	673.2	26.0	66	2.7	610
	16	1.024	240.1	600.4	1000.6	31.6	70	2.6	600

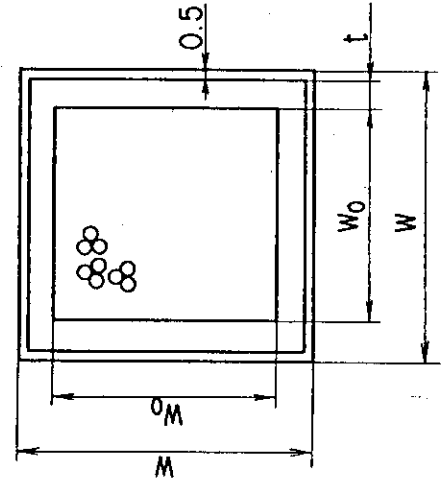
I<sub>c</sub> ; Critical current (60 kA)

d ; Strand diameter (mm)

A<sub>sc</sub> ; Superconducting material area of strands (mm<sup>2</sup>)A<sub>co</sub> ; Total area of strands (mm<sup>2</sup>)A<sub>He</sub> ; Helium area of a conductor (mm<sup>2</sup>)I<sub>B</sub> ; Limiting current (kA)

ΔT ; Temperature margin (K)

ΔH ; Stability margin (mJ/cc-strand)



## 2.3 OH coil design

OH coils are designed using following formulas;

$$\Delta\phi = 2\pi B_{OH} (R_o^2 - R_o \cdot D + \frac{D^2}{3}) = 112 \text{ V}\cdot\text{s}$$

$$B_{max} = \frac{\alpha}{\epsilon} B_{OH} = \frac{\alpha \cdot \beta \cdot \gamma}{\epsilon} \mu_0 \cdot j \cdot D$$

$$\sigma = \frac{B_{max} \cdot j \cdot R_i}{f}$$

$$f = \frac{\text{Conduit Area}}{\text{Conductor Area}}$$

$\alpha$  ; Field ripple factor (= 1.055)

$\beta$  ; Space factor (= 0.85)

$\gamma$  ;  $B_{L=\infty}/B_{L=L_0}$  (= 0.96)

$\epsilon$  ; Effect of  $I_p$  and  $B_{EF}$  (= 0.8)

In the above equation, the maximum stress of conduit ( $\sigma$ ) is assumed to cause at inner-radius of the coil.

Calculated results are summarized in Table 2.3.1, Fig. 2.3.1 and Fig. 2.3.2.

Table 2.3.1 Characteristics of coil

T(K)	B(T)	Ass	t(mm)	w(mm)	R <sub>O</sub> (m)	R <sub>I</sub> (m)	D(m)	J (A/mm <sup>2</sup> )
4.5	8	976.6	9.61	36.02	1.809	1.617	0.192	30.9
	10	1052.0	9.32	38.54	1.668	1.394	0.274	26.9
	12	1094.5	8.73	41.06	1.582	1.208	0.374	23.7
	14	1095.6	7.77	44.04	1.539	1.037	0.502	20.6
	16	1030.6	6.31	48.12	1.538	0.853	0.685	17.3
3.5	8	977.3	9.75	35.80	1.808	1.619	0.189	31.2
	10	1054.1	9.54	38.18	1.666	1.397	0.269	27.5
	12	1098.8	8.98	40.56	1.578	1.213	0.365	24.3
	14	1106.0	8.11	43.22	1.530	1.047	0.483	21.4
	16	1062.5	6.90	46.40	1.517	0.880	0.637	18.6

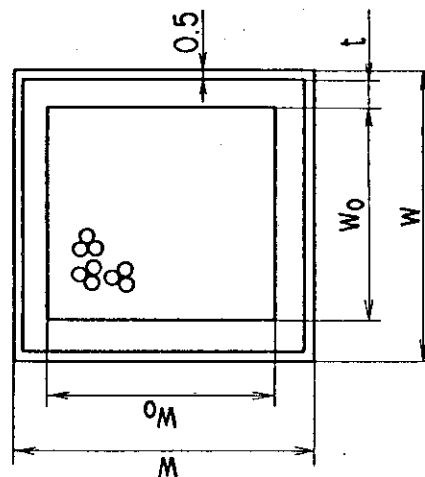
Ass ; Conduit area of a conductor (mm<sup>2</sup>)

t ; Conduit thickness (mm)

w ; Conductor width (mm)

R<sub>O</sub> ; Coil outer-radius (m)R<sub>I</sub> ; Coil inner-radius (m)

D ; Coil thickness (m)

J ; Coil current density (A/mm<sup>2</sup>)



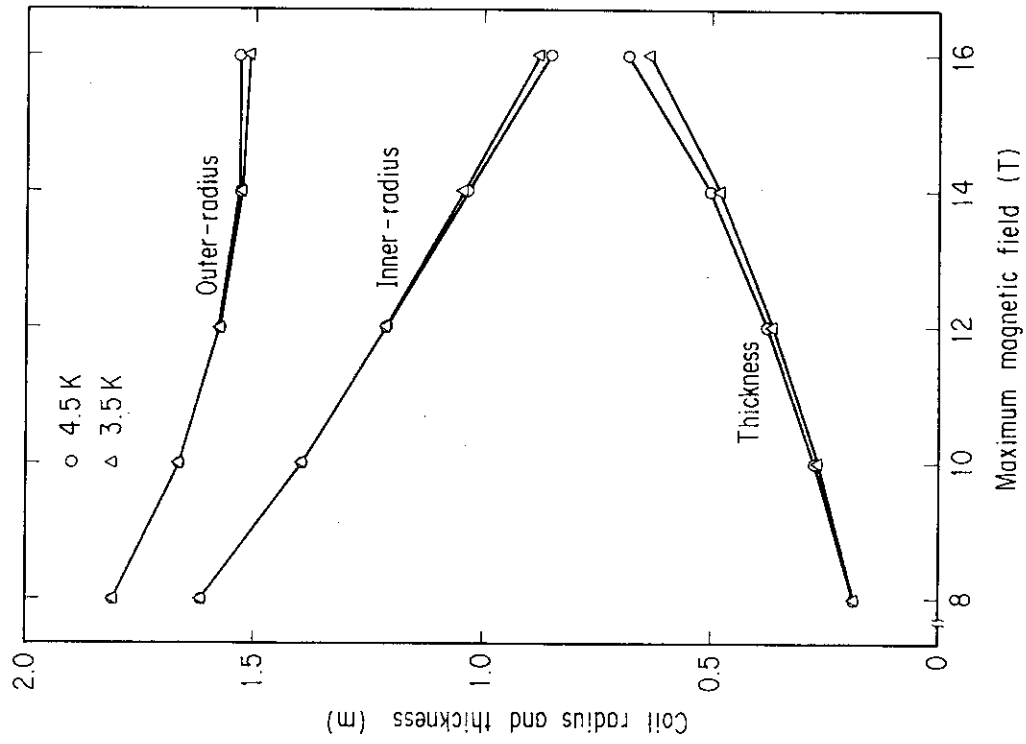


Fig. 2.3.2 Coil radius and thickness.

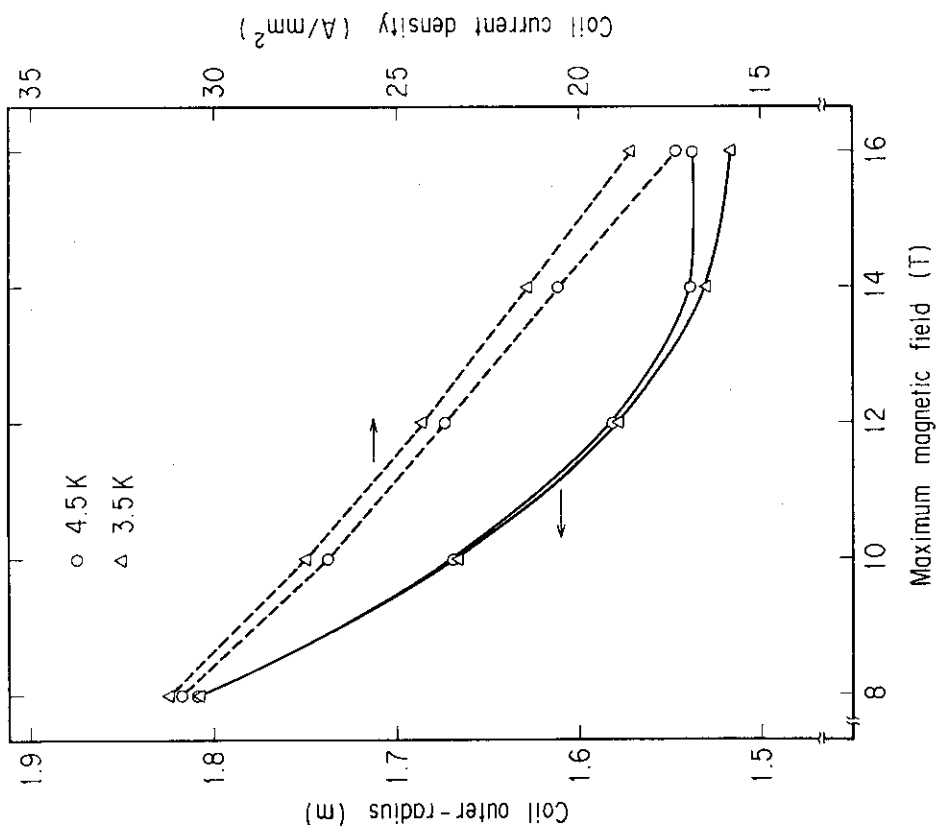


Fig. 2.3.1 Coil outer-radius and current density.

## 2.4 OH coil design criteria

Figure 2.3.2 shows the use of helium subcooling have little merit in the aim of outer-radius reduction. Stability margin in the case of 4.5 K cooling shown in Table 2.2.4 is more than 300 mJ/cc.

In the coil design described above, discrete effect of the conductor turn is neglected. In the case of 4.5 K, 10 T, for example, the calculated number of conductor layers is 7.1 turns. The necessary number is 8 turns.

Therefore we propose following criteria in the OH coil design.

25 A/mm<sup>2</sup> at 10 T, 4.5 K  
or  
20 A/mm<sup>2</sup> at 12 T, 4.5 K

## Reference

- [1] J.W. Ekin, Adv. Cryo. Eng. 24 (1978) 306

### 3. Forced Flow Subcooled HeII Superconducting Coils (FFSSC)

As part of innovation studies for INTOR, one target has been set for high field and high current density in order to achieve a more compact tokamak fusion reactor. The possible range of innovation discussed in previous INTOR specialists' meeting is as follows.

- (1) As priority I, current density of 40 A/mm<sup>2</sup> at 12 T for TF coil
- (2) As priority II, current density of 25 A/mm<sup>2</sup> at 16 T for TF coil
- (3) Current density of 30 A/mm<sup>2</sup> at 12 ~ 14 T for PF coil

There are two options for achieving a high field and high current density coil. One is the development of superconducting materials for high field and high current density. The other is the improvement of critical current density ( $J_c$ ) in the high field region by reducing the coolant temperature. Forced flow cooling by pressurized superfluid HeII is one method of reducing the coolant temperature.

In this paper, we discuss the possibility of the coil cooled by forced flow subcooled HeII for a future tokamak fusion reactor.

#### 3.1 Non-copper critical current density

A NbTi-alloy conductor and a (NbTi)<sub>3</sub>Sn conductor are considered to be applicable to the winding of large scale coils at present. These superconductors are used to study the forced flow subcooled HeII superconducting coils.

Figure 3.1.1 shows non-copper critical current density ( $J_c$ ) versus magnetic field (B) for the NbTi-alloy superconductors. The  $J_c$  of NbTi conductor is 400 A/mm<sup>2</sup> ~ 500 A/mm<sup>2</sup> in a magnetic field of 10 T at 4.2 K. Reduced temperature operation at 1.8 K yields a higher  $J_c$  of 800 A/mm<sup>2</sup> ~ 1000 A/mm<sup>2</sup> in the NbTi conductor even at 12 T field. This implies that the application of HeII cooling to NbTi conductor is an possible approach for the high field coils, which operate at a magnetic field of 12 T.

In the A-15 compound type superconductors, on the other hand, the low temperature enhancement of  $J_c$  is small at less than 20 T field. Figure 3.1.2 shows the non-copper critical current density versus magnetic

field for the A-15 compound type superconductors. The  $J_c$  of a  $(\text{NbTi})_3\text{Sn}$  conductor made by bronze process is  $400 \text{ A/mm}^2$  in the high field region of 16 T at 1.8 K. The increase of  $J_c$  due to the low temperature operation at 1.8 K is only 40% comparing with the  $J_c$  at 4.2 K.

Meanwhile, new technological developments in the  $(\text{NbTi})_3\text{Sn}$  conductor have been achieved which have higher critical current density than the above-mentioned  $J_c$  at 1.8 K. As shown in Fig. 3.1.2, the  $J_c$  of the  $(\text{NbTi})_3\text{Sn}$  conductor made by Nb tube method is  $500 \text{ A/mm}^2$  in 16 T field at 4.2 K. As a result, it is considered that the application of HeII cooling to A-15 compound type superconductors has a little advantage at magnetic field below 20 T. Also, as shown in Fig. 3.1.1 and Fig. 3.1.2, the  $J_c$  of the NbTiTa conductor at 1.8 K is larger than that of the  $(\text{NbTi})_3\text{Sn}$  conductor at 4.2 K only at fields less than 12 T.

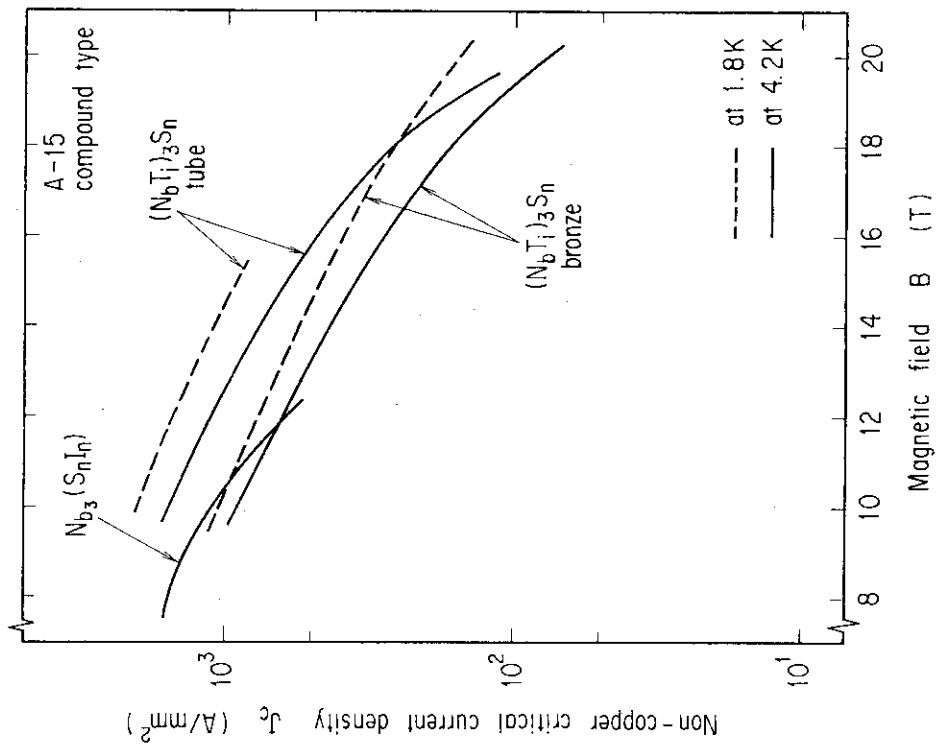


Fig. 3.1.2 Non-copper critical current density for the A-15 compound type superconductors versus magnetic field at 1.8 K and 4.2 K.

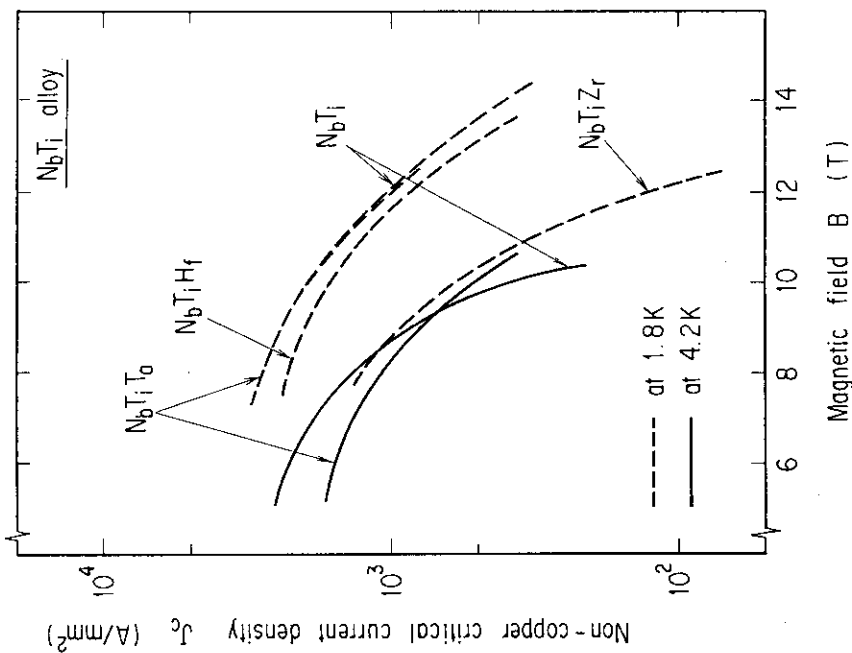


Fig. 3.1.1 Non-copper critical current density for the NbTi alloy superconductors versus magnetic field at 1.8 K and 4.2 K.

### 3.2 Conductor design

In the present study, we estimate the possible current densities inside the conduit for the NbTiTa and (NbTi)<sub>3</sub>Sn conductors. Their estimates are based on the limiting current ( $J_{lim}$ ) and the stability margin ( $\Delta H$ ) of superconductor. Applied coolant conditions are the supercritical HeI at 10 atm, 4.5 K, and the superfluid HeII at 1 atm, 1.8 K.

The following parameters are used in all calculations.

$d$  : Strand diameter (0.5 mm)

$f_{He}$  : Helium void fraction =  $A_{He}/A$  (0.4)

$f_{co}$  : Strand area ratio in the conduit =  $1 - f_{He}$  (0.6)

$n$  : Copper ratio =  $A_{cu}/A_{cs}$  (1.5 at 4.5 K)

Copper ratio at 1.8 K is calculated from the same temperature rise during a quench at 4.5 K.

(1) Operation current density ( $J_a$ ) inside the conduit.

This value is limited from temperature margin ( $T_{cs} - T_b$ ).

$$T_{cs} - T_b = \left(1 - \frac{I_{op}}{I_c}\right)(T_c - T_b)$$

$$I_c = J_c A_{sc}$$

$$I_{op} = J_a (A_{He} + A_{co})$$

$$\therefore J_a = \frac{3}{5(n+1)} \cdot J_c \cdot \left(1 - \frac{T_{cs} - T_b}{T_c - T_b}\right)$$

$$= \frac{3}{5(n+1)} \cdot J_c \cdot \left\{1 - \frac{T_{cs} - T_b}{T_{co}(1 - B/B_{co})^{1/2} - T_b}\right\} \quad (A/mm^2)$$

$T_{cs}$  : Current shearing temperature (K)

$T_b$  : Helium temperature (1.8 K or 4.5 K)

$T_c$  : Critical temperature at magnetic field BT (K)

$I_{op}$  : Operation current (A)

$I_c$  : Critical current (A)

$T_{co}$  : Critical temperature at magnetic field OT (K)

$B$  : Magnetic field (T)

$B_{co}$  : Critical magnetic field (T)

- (2) Limiting current density ( $J_{lim}$ ) inside the conduit.

Limiting current density is shown as follows:

$$J_{lim} = \frac{0.86 \times 10^5}{d} \left( \frac{f \cdot f_{co}^3}{1 - f_{co}} \right)^{\frac{1}{2}} \left( \frac{T_c - T_b}{6.65 - 4.2} \right)^{\frac{1}{2}} \left( \frac{\rho_1}{\rho_2} \right)^{\frac{1}{2}} \quad (\text{kA/m}^2)$$

$\rho_1$  : Resistivity of stabilizer at 6 T ( $3.9 \times 10^{-10} \Omega \cdot \text{m}$ )

$\rho_2$  : Resistivity of stabilizer at magnetic field BT ( $\Omega \cdot \text{m}$ )

$$\rho_2 \sim (0.63 + 0.48B) \times 10^{-10} \Omega \cdot \text{m}$$

$$\therefore J_{lim} = 167 \left( \frac{n}{n+1} \right)^{\frac{1}{2}} \left\{ \frac{T_{co}(1 - B/B_{co})^{\frac{1}{2}} - T_b}{0.63 + 0.48B} \right\}^{\frac{1}{2}} \quad (\text{A/mm}^2)$$

- (3) Stability margin.

$$\Delta H = S_{He} \cdot (T_{cs} - T_b) \cdot (A_{He}/A_{co})$$

$$= S_{He} \cdot (T_{cs} - T_b) \cdot \frac{2}{3}$$

$S_{He}$  : Volumetric heat capacity of the helium

$$= 0.434 \text{ J/cc} \cdot \text{K at 1 atm, 1.8 K}$$

$$= 0.476 \text{ J/cc} \cdot \text{K at 10 atm, 4.5 K}$$

Figure 3.2.1 show the limiting current density inside the conduit and operating current density with the stability margin of about 250 mJ/cc. The shadowed region shown in Fig. 3.2.1 indicates the minimum value between the limiting current density and operating current density for the given magnetic field. This shadowed region shows the safety operating region for the superconductor.

In comparison with the safety operating region for  $(\text{NbTi})_3\text{Sn}$  conductor at 4.5 K, the region for NbTiTa conductor at 1.8 K is lower and more narrow for the same stability margin.

Figure 3.2.2 and Fig. 3.2.3 show the limiting current density inside the conduit and the operating current density with the temperature margin of 0.5 K and 1.0 K, respectively. The temperature margin of 0.5 K provides the stability margin of about 120 mJ/cc at 4.5 K and 250 mJ/cc at 1.8 K, respectively, which is larger than the stability margin of 100 mJ/cc in TORE SUPRA coil. It should be noted that the

operating current density of  $(\text{NbTi})_3\text{Sn}$  conductor is estimated based on the total temperature margin  $\Delta T=1.5\text{K}$  and  $2.0\text{K}$  including the margin of  $1\text{K}$  due to  $I_c$  degradation.

For each temperature margin, the safety operating region for NbTiTa conductor at  $1.8\text{K}$  is lower than that for  $(\text{NbTi})_3\text{Sn}$  conductor at  $4.5\text{K}$ , at the field more than  $10\text{T}$ .

The forced flow cooling of NbTiTa conductor with HeII has no merit in terms of the stability margin and safety operationg current.



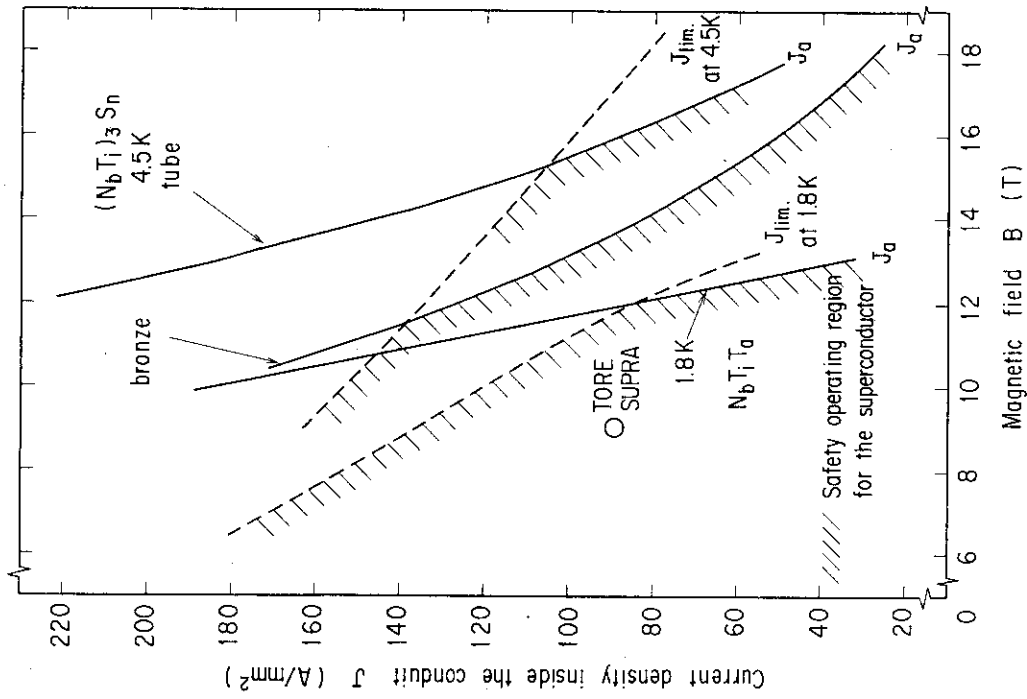


Fig. 3.2.2 Limiting current density inside the conduit and operating current density with the temperature margin of 0.5 K. ( $\Delta H \approx 120$  mJ/cc at 4.5 K,  $\Delta H \approx 250$  mJ/cc at 1.8 K)

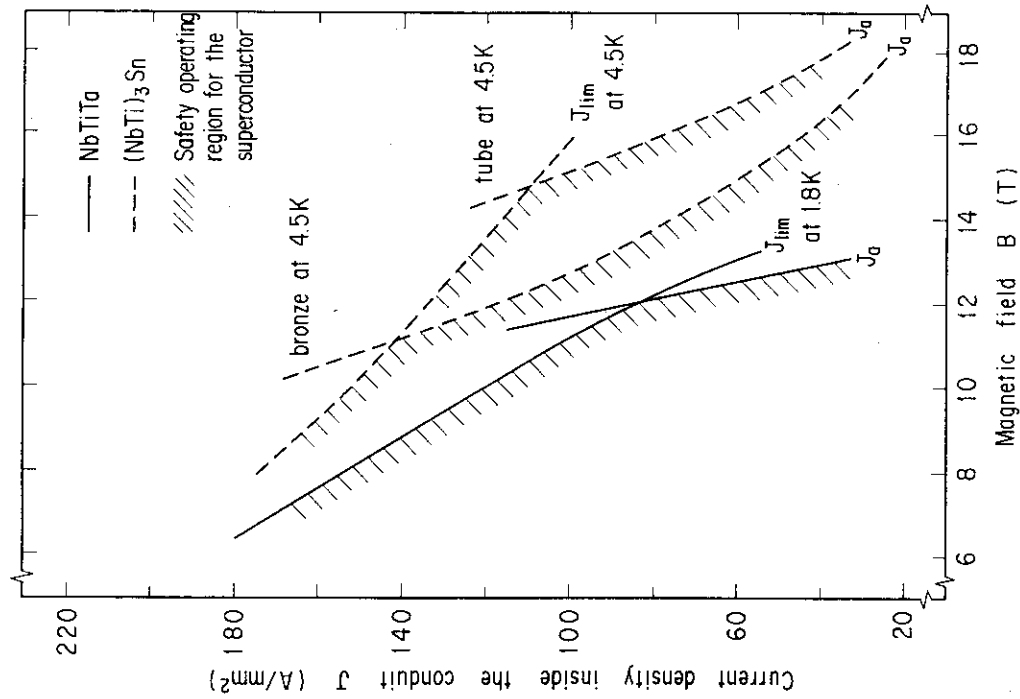


Fig. 3.2.1 Limiting current density inside the conduit and operating current density with the stability margin or about 250 mJ/cc.

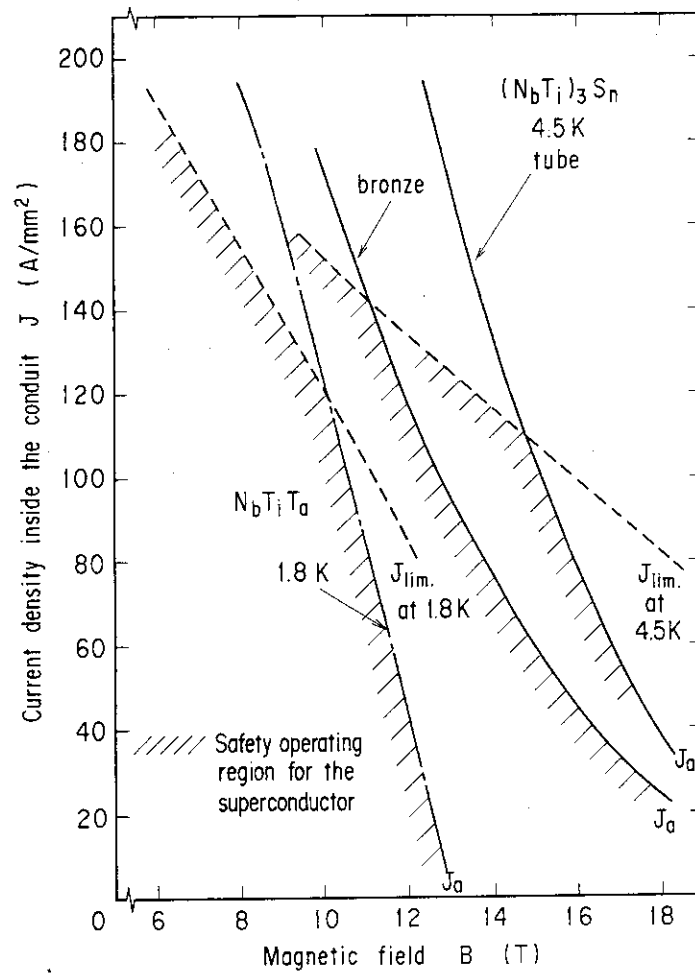


Fig. 3.2.3 Limiting current density inside the conduit and operating current density with the temperature margin of 1.0 K. ( $\Delta H \approx 240$  mJ/cc at 4.5 K,  $\Delta H \approx 350$  mJ/cc at 1.8 K)

### 3.3 Comparison of cooling system

The critical current density and the operating current density inside the conduit have been discussed for the two cooling methods, namely the forced flow supercritical HeI cooling and the forced flow subcooled HeII cooling. Figure 3.3.1 shows the allowable set of operating current density and magnetic field in the use of each cooling method.

The greatest merit of forced flow subcooled HeII cooling is that the NbTi alloy superconductor can be used in the high field of 12 T. But demerits are (1) large weakness against large continuous heat disturbance such as nuclear heating, (2) high cost, unreliable and complicated cooling system.

Furthermore, the obtained current density of NbTiTa conductor at 1.8 K is lower than that of  $(\text{NbTi})_3\text{Sn}$  conductor at 4.5 K at the same order of the stability margin  $\Delta H \approx 250 \text{ mJ/cc}$ .

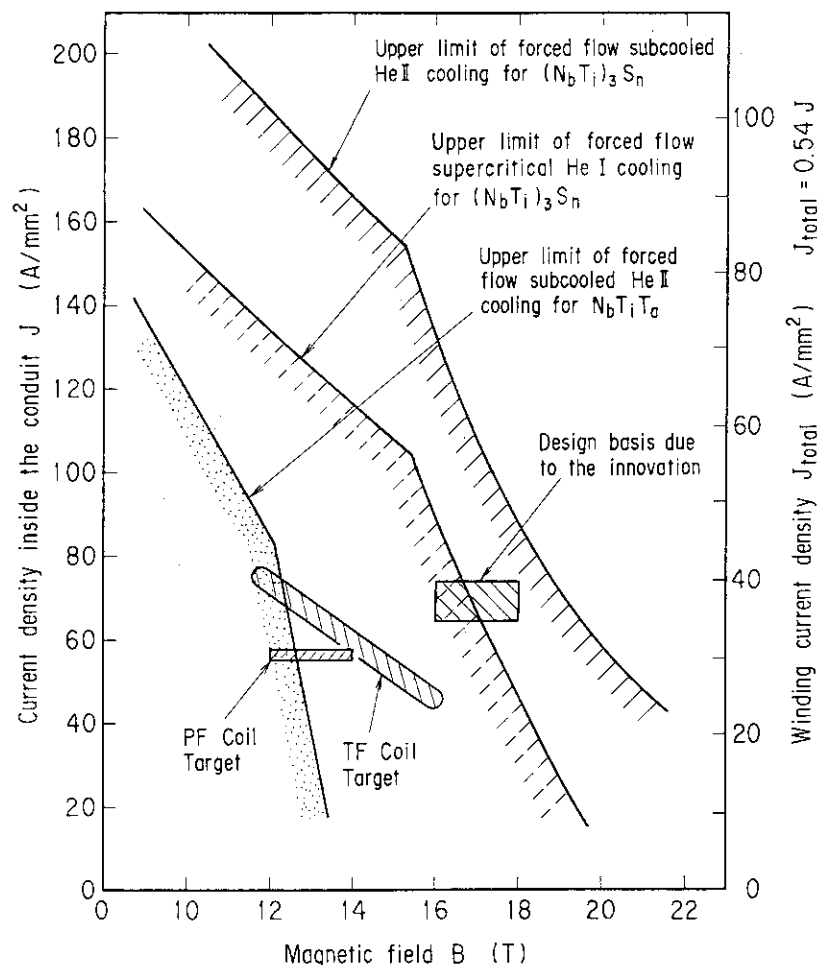


Fig. 3.3.1 Allowable set of operating current density and magnetic field in the use of each cooling method.

### 3.4 Conclusions

Two cooling methods have been discussed about superconducting materials, conductor design, and cooling system: (1) forced flow supercritical HeI cooling. (2) forced flow subcooled HeII cooling.

In a future tokamak fusion reactor, we propose as follows.

- (1)  $B \leq 20 \text{ T}$  : forced flow supercritical HeI cooling
- (2)  $20 \text{ T} < B$  : forced flow subcooled HeII cooling

### Reference

1. Furuto, Y. Adv. Cryog. Eng. (1984) 30 721.
2. Imaizumi, M., Wakata, M., Yoshizaki, K., Fujiwara, F. and Hashimoto, Y. Adv. Cryog. Eng. (1984) 30 779.
3. Suenaga, M., Tsuchiya, K., Higuchi, N. and Tachikawa, K. Cryogenics (1985) 25 123.
4. Murase, S., Shiraki, H., Tanaka, M., Koizumi, M., Maeda, H. and Takano, I., IEEE Trans. Magn. (1985) 21 316.
5. Miller, J. R. Cryogenics (1985) 25 552.
6. Dresner, L. Cryogenics (1984) 24 283.
7. Miller, J. R. Adv. Cryog. Eng. (1982) 27 207.
8. Tsuji, H., Shimamoto, S., Ulbricht, A., Komarek, P., Katheder, H., Wüchner, F. and Zahn, G. Cryogenics (1985) 25 539.
9. Claudet, G., Bon Mardion, G., Jager, B. and Gistau, G. Cryogenics (1986) 26 443.
10. Riband, P., Aymar, R., Bessette, D., et al., SOFT (1986) HP13
11. Wake, M., et al., Applied Superconductivity Conference, (1982).

#### 4. Design Guidelines of Toroidal Field Coil Sizing

A superconducting toroidal field (TF) coil with high current density reduces the reactor size in Tokamak. Internally cooled conductors composed of superconducting materials such as niobium tin composite have a great potential in high current density. Therefore, the guidelines for current density of winding pack were described in the previous section.

In this section, generalized formulations of average current density, maximum magnetic field and size of TF coil are pointed out based on the stress guideline, comparing between wedging and bucking cylinder (B.C.).

##### 4.1 Formulation of TF coil

###### 1) Supporting models for electromagnetic forces

Models and symbols for two supporting method of TF coil, i.e. wedging and B.C., are shown in Fig. 4.1.1 and 4.1.2 each other. Since we assume that a TF coil is D-shaped, and radius ratio of outer leg ( $R_2$ ) to inner one ( $R_1$ ) is about 4 as usual tokamak reactor design, centering force and z-direction force of coils are mostly dependent on magnetic field strength of inner legs.

###### 2) Formulation of the two types of supports

###### a) Wedging support

According to models in Fig. 4.1.1, average stress intensity is described as equation (4.1-1).

$$\begin{aligned}\sigma_W &= \sigma_t + \sigma_c \\ &= \frac{\mu_0 J_{cav} NI}{8\pi} \cdot \ln \frac{R_2}{R_1} + p_1 \frac{2R_{1i}^2}{R_{1i}^2 - R_i^2} \\ &= \frac{(B_T^m)^2}{2\mu_0} \cdot \frac{1}{1 - (R_i/R_{1i})^2} \cdot \left( \ln \frac{R_2}{R_1} + 2 \right) \quad (4.1-1)\end{aligned}$$

$$= \frac{1}{4} J_{cav} B_T^m R_{1i} \left( \ln \frac{R_2}{R_1} + 2 \right) \quad (4.1-2)$$

where

$\sigma_t$  : average tensile stress in gross cross section

$\sigma_c$  : maximum compressive stress in thick cylinder model of homogeneous media

NI : total ampereturns of TF coils  $[(2\pi/\mu_0)B_T^m R_{1f}]$

$B_T^m$  : mean maximum field in TF coil leg  $[R_p B_{T0} = R_{1f} B_T^m]$

$P_1$  : magnetic pressure  $[B_T^{m2}/(2\mu_0)]$

$J_{cav}$  : average current density in gross cross section of TF coil leg

$R_{1f}, R_i, R_2, R_1$  : (refer to Fig. 4.1.1)

When we adopt a design stress criteria  $\sigma_D$  of structural material as half of ultimate strength  $[(1/2)\sigma_u]$  and coil average stress design guideline as  $f_W \sigma_D$ , the following equation is obtained.

$$\begin{aligned} f_W \sigma_D &= \sigma_W \\ &= \frac{(B_T^m)^2}{2} \cdot \frac{1}{1 - (R_i/R_{1f})^2} \cdot \left( \ln \frac{R_2}{R_1} + 2 \right) \end{aligned}$$

where

$$\sigma_D = \frac{1}{2} \sigma_u \quad (4.1-3)$$

$$(0 < f_W < 1.0)$$

A factor of ' $f_W$ ' what is called 'stress design guideline factor', means a ratio of average stress to the allowable limit of peak stress ( $\sigma_D$ ) obtained by the detailed design.

Eq. (4.1-3) shows that mean maximum toroidal field ( $B_T^m$ ) is only a function of normalized coil inner radius ( $\alpha_W = R_i/R_{1f}$ ) with parameter of mechanical stress criteria  $f_W \sigma_D$ , since a ratio of  $R/R$  is nearly constant value ( $\sim 4.0$ ).

Using the value of stress design criteria for stainless steel as  $\sigma_D = 600$  MPa, relations between  $B_T^m$  and  $\sigma_W$  are shown in Fig. 4.1.3 with parameter of stress design guideline factor ( $f_W$ ), which give the values of maximum attainable fields  $B_T^m$  due to the limit to compressive stress.

#### b) B.C. support

By the same manner, average stress intensity of coil cavity and

B.C. are described in case of B.C. support as Eqs. (4.1-4) and (4.1-5).

i) Coil cavity

$$\begin{aligned}\sigma_B^C &= \sigma_t + \sigma_c \\ &= \frac{(B_T^m)^2}{2\mu_0} \left[ \frac{1}{1 - (R_i/R_{1i})^2} \cdot \ln \frac{R_2}{R_1} + \frac{R_{1i}}{R_i} \right]\end{aligned}\quad (4.1-4)$$

where

1st term : average tensile stress

2nd term : compressive stress due to reaction force from B.C.

ii) B.C.

(thick cylinder cavity model)

$$\sigma_B^B = \frac{(B_T^m)^2}{2\mu_0} \cdot \frac{1}{(R_i/R_{1i})} \cdot \frac{2}{1 - (R_c/R_i)^2} \quad (4.1-5)$$

A criteria for coil average stress and cylinder stress are as follows,

$$\begin{aligned}f_B \sigma_D &= \sigma_B^C \\ &= \frac{(B_T^m)^2}{2\mu_0} \left[ \frac{1}{1 - (R_i/R_{1i})^2} \cdot \ln \frac{R_2}{R_1} + \frac{R_{1i}}{R_i} \right]\end{aligned}\quad (4.1-6)$$

$$\begin{aligned}\sigma_D &= \sigma_B^B \\ &= \frac{(B_T^m)^2}{2\mu_0} \cdot \frac{1}{(R_i/R_{1i})} \cdot \frac{2}{1 - (R_c/R_i)^2} \\ &= \frac{(B_T^m)^2}{2\mu_0} \cdot \frac{1}{(R_i/R_{1i})} \cdot \frac{2}{1 - (R_c/R_{1i} \cdot R_{1i}/R_i)^2}\end{aligned}\quad (4.1-7)$$

where

$\sigma_D = 600$  MPa for stainless steel

Eqs. (4.1-6) and (4.1-7) are functions of normalized radii  $R_i/R_{1i}$  ( $\equiv \alpha_B$ ) and  $R_c/R_{1i}$  ( $\equiv (\alpha\beta)_B$ ).

Fig. 4.1.4 shows dependency of normalized coil inner radius required ( $\alpha_B$ ) and B.C. inner radius ( $(\alpha\beta)_B$ ) on mean maximum toroidal field ( $f_B$ ) with parameters of stress design guideline factor ( $f_B$ ) in case of B.C. support. In this figure, curves are different from the wedge support ones and two solutions of  $\alpha_B$  and  $(\alpha\beta)_B$  for a certain  $B_T^m$  exist. Larger ones of  $\alpha_B$  and  $(\alpha\beta)_B$  are smaller ones by the compressive stress limit of B.C.

- 3) Formation of mean maximum toroidal field ( $B_T^m$ ) and average current density

Using stress guideline factors of  $f_W$  and  $f_B$ , we can obtain the relations between mean maximum toroidal field ( $B_T^m$ ) and average current density as following Eqs. (4.1-8)~(4.1-11).

- i) Wedge support

$$J_{cav} \cdot R_{li} = \left( \frac{4 f_W \sigma_D}{\ln \frac{R_2}{R_1} + 2} \right) \cdot \frac{1}{B_T^m} \quad (4.1-8)$$

- ii) B.C. support  
for coil part

$$J_{coil} \cdot R_{li} = \frac{2}{\mu_0} \cdot \frac{1}{1 - (R_i/R_{li})^2} \cdot B_T^m \quad (4.1-9)$$

for total cross section (including B.C.)

$$J_{total} \cdot R_{li} = \frac{2}{\mu_0} \cdot \frac{1}{1 - (R_c/R_{li})^2} \cdot B_T^m \quad (4.1-10)$$

$$= \frac{2}{\mu_0} \cdot \frac{1}{1 - (R_i/R_{li} \cdot R_c/R_i)^2} \cdot B_T^m \quad (4.1-11)$$

where

$$B_T^m = B_T^m(f_B \sigma_D, R_i/R_{li}, R_c/R_{li})$$

$R_{li}$  : independent of  $f_B \sigma_D$ ,  $R_i/R_{li}$  and  $R_c/R_{li}$

In these equations,  $R_{li}$  is independent of normalized radii as  $R_i/R_{li}$ ,  $R_c/R_{li}$ , and  $B_T^m$  has maximum value for each stress guideline factor ( $f_W$ ) or ( $f_B$ ) as shown in Figs. 4.1.3 and 4.1.4. Figs. 4.1.5~4.1.7 show the



relations between  $B_T^m$  and various average current density.

4) Designed parameters on the obtained formulations

Designed parameters of TF coils are summarized in Table 4.1.1, and are plotted in Figs. 4.1.5~4.1.7. Since the curves along the same value of factors ( $f_W$ ) and ( $f_B$ ), show the same coil design philosophy, INTOR specification is rather advanced than that of FER '85 and TFCX-S.

5) Limitation of factions  $R_C/R_{1i}$ ,  $R_i/R_{1i}$  and  $R_t/R_{1i}$

Some detailed discussion on the parameters,  $\alpha$  and  $\beta$ , is given in consideration of the inner structure of TF coils, that is, packing factor,  $f_W$ , and the winding part as a reinforcement. The packing factor,  $f_W$ , may be fixed on the basis of attainable current density of super-conductor and the strength of the TF coils against the overturning force besides the resultant stress generated by the hoop and centering forces.

The following equations are obtained by modification of Eqs. (4.1-3), (4.1-6) and (4.1-7):

B.C.

$$\sigma_D < \frac{(B_T^m)^2}{2\mu_0} \left\{ \frac{1}{1-\beta^2} \ln\left(\frac{R_2}{R_1}\right) \frac{1-f}{1-(1-k)f} + \frac{1}{\beta} \right\}, \quad (4.1-12)$$

$$\sigma_D < \frac{(B_T^m)^2}{2\mu_0} \frac{2\beta}{\beta^2-\alpha^2}, \quad (4.1-13)$$

Wedging

$$\sigma_D < \frac{(B_T^m)^2}{2\mu_0} \left\{ \frac{1}{1-\alpha^2} \frac{1}{1-(1-k)f} \ln\left(\frac{R_2}{R_1}\right) + \frac{2\beta^2 p}{\beta^2-\alpha^2} \right\}, \quad (4.1-14)$$

where  $\alpha=R_C/R_{1i}$ ,  $\beta=R_i/R_{1i}$  or  $R_t/R_{1i}$ ,  $k_t=k_c=E_W/E_S$ ,

$$P_t = \left( \frac{2}{1-\beta^2} \right) / [k(1-\nu_S) + 1 + \nu_W + 2\left\{ \frac{\alpha^2 k}{\beta^2-\alpha^2} + \frac{\beta^2}{1-\beta^2} \right\}],$$

$R_{1i}$ ,  $R_C$ ,  $R_i$ ,  $R_t$  : (refer to Figs. 4.1.8),

$E_{S,W}$  : Young's modulus,  $\nu_{S,W}$  : Poisson's ratio.

Additionally, the parameters,  $\alpha$  and  $\beta$ , must satisfy the following relations from geometrical restriction.

$$0 < \alpha < \beta < 1 \quad (4.1-15)$$

$$\beta^2 < f_c \alpha^2 + (1-f_c) \quad (4.1-16)$$

The reasonable region of the parameters,  $\alpha$  and  $\beta$ , are given by these equations when the values of  $\sigma_D$ ,  $B_T$ ,  $R_2/R_1$ ,  $f_c$ ,  $k_t$ ,  $k_c$ ,  $v_S$ , and  $v_W$  are fixed.

The value of  $\alpha R_{1i}$  indicates the outer radius of OH coils when a value of  $R_{1i}$  is fixed. Figs. 4.1.9 and 4.1.10 show reasonable regions of  $\alpha^2$  and  $\beta^2$  in a bucking cylinder support and wedging support, respectively. The values of FER and NET are plotted in the figures.

Equations (4.1-12) ~ (4.1-16) do not included all restrictions of  $\alpha$  and  $\beta$ . Then the other restrictions left behind must be made clear. For example, the restriction imposed by attainable current density of superconductor also has to be considered.

#### 6) Summary

From the view point of average stress guidelines, a generalized formulation for average current density, mean maximum toroidal field and coil sizing are made in case of wedge support and B.C. support. This formulation could be related with coil winding pack current density  $J_{wdg}$ , required OH flux swing (Volt Second) and reactor plasma parameters, using simple stress guideline factor. Overall magnet design guideline are discussed in the task of Engineering Group.

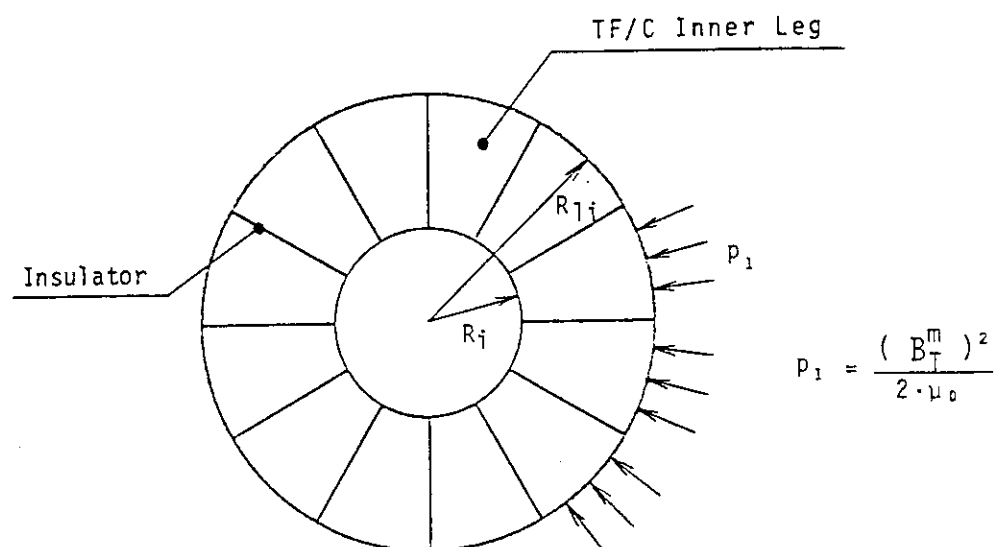
Table 4.1.1 Designed parameters of TF coil

## (a) Wedge support

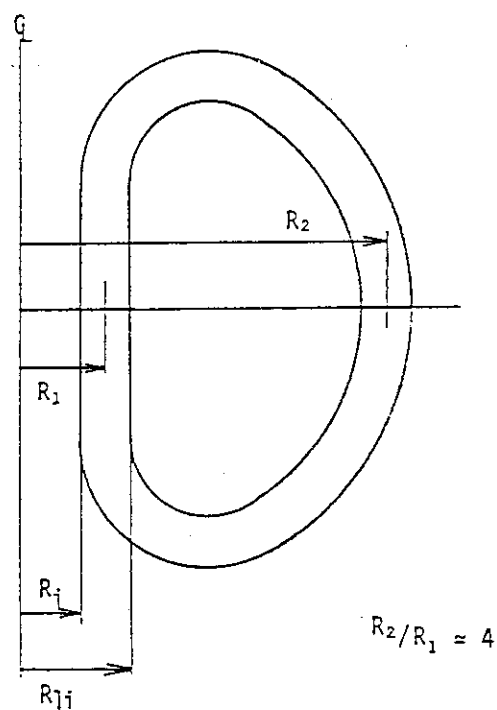
Design	$R_p, B_{T0}$ (m) (T)	$R_p \cdot B_{T0}$ $= B_T^m \cdot R_{li}$ (m · T)	$R_{li}$ (m)	$B_T^m$ (T)	$R_i$ (m)	$a_w$	$J_{cav}$ (A/mm <sup>2</sup> )	$J_{cav} \cdot R_{li}$ (A/mm <sup>2</sup> · m)
NET/DN	5.18 , 5.0	25.9	2.48	10.4	1.78	0.718	13.8 SC-9.37m <sup>2</sup>	34.2
NET/SN	5.79 , 5.8	33.582	(2.895)	11.6				

## (b) Bucking cylinder support

Design	$R_p, B_{T0}$ (m) (T)	$R_p \cdot B_{T0}$ $= B_T^m \cdot R_{li}$ (m · T)	$R_{li}$ (m)	$B_T^m$ (T)	$R_i$ (m)	$R_C$ (m) ( $\Delta C$ )	$a_s$ ( $a\beta$ ) <sub>s</sub>	$J_{coil}$ (A/mm <sup>2</sup> )	$J_{total}$ (A/mm <sup>2</sup> )	$J_{coil} \cdot R_{li}$ (A/mm <sup>2</sup> · m)	$J_{total} \cdot R_{li}$ (A/mm <sup>2</sup> · m)
INTOR (RED BOOK)	5.0, 5.5	27.5	2.65	10.38	1.98	1.70 (0.28)	0.747 0.642	14.1 SC-9.75m <sup>2</sup>	10.6	37.37	28.09
FER'85	5.2, 5.3	27.56	2.86 (-0.098)	9.64 (9.98)	2.03	1.73 (0.3)	0.71 0.605	10.8 SC-12.75m <sup>2</sup>	8.46 (8.28 ~8.5)	30.89	24.19
TFCX-S	3.61 , 4.23	15.27	1.6 (-0.04)	9.54 (9.57)	1.147	1.047 (0.1)	0.717 0.654	19.5 SC-3.91m <sup>2</sup>	16.6	31.2	26.56

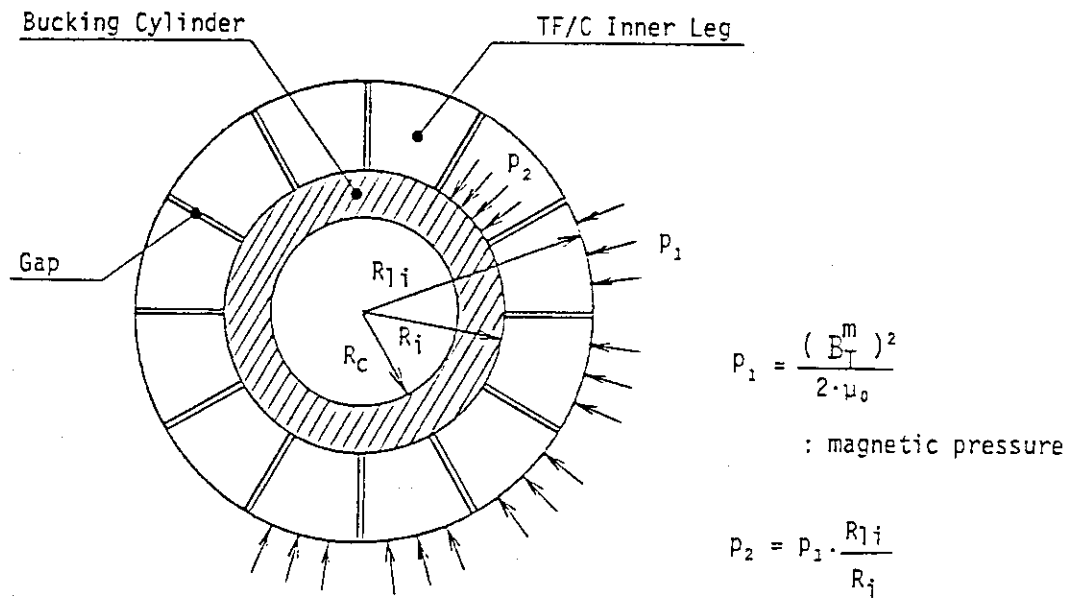


(a) Horizontal cross section of TF coil inner legs

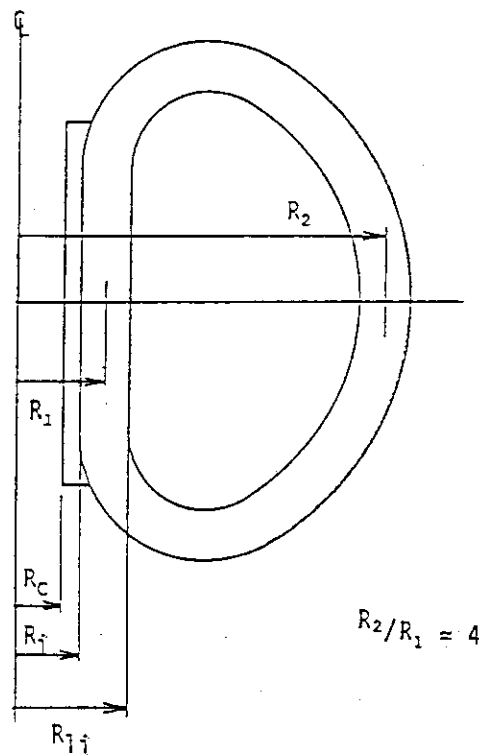


(b) Vertical cross section of TF coil

Fig. 4.1.1 Model for wedge support type of TF coil.



(a) Horizontal cross section of TF coil inner legs



(b) Vertical cross section of TF coil

Fig. 4.1.2 Model for bucking cylinder support type of TF coil.

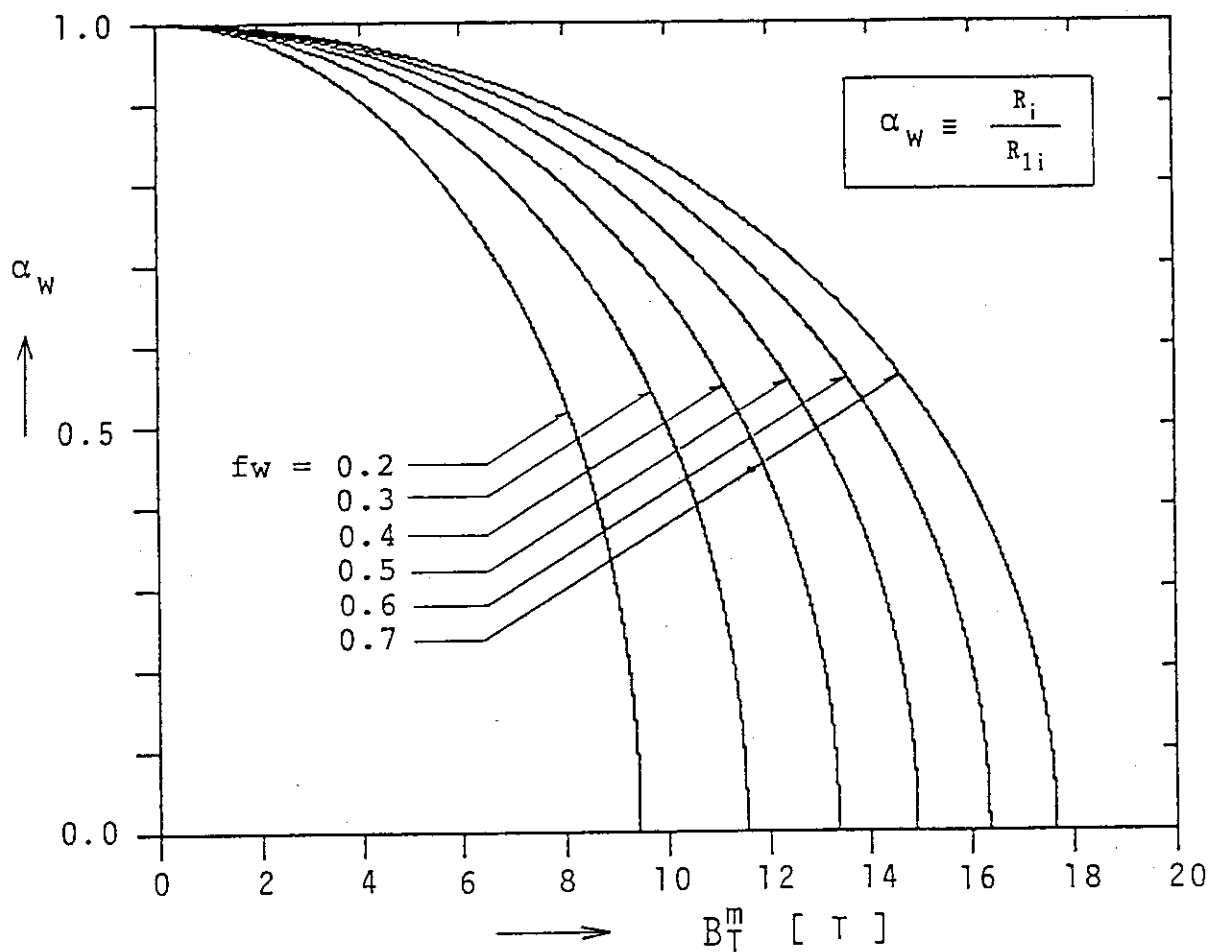


Fig. 4.1.3 Dependency of normalized required coil inner radius ( $\alpha_w$ ) on mean maximum toroidal field ( $B_T^m$ ) with parameters of stress design guideline factor ( $f_w$ ) in case of wedge support.  
 $(1-\alpha_w)$  : normalized required coil thickness

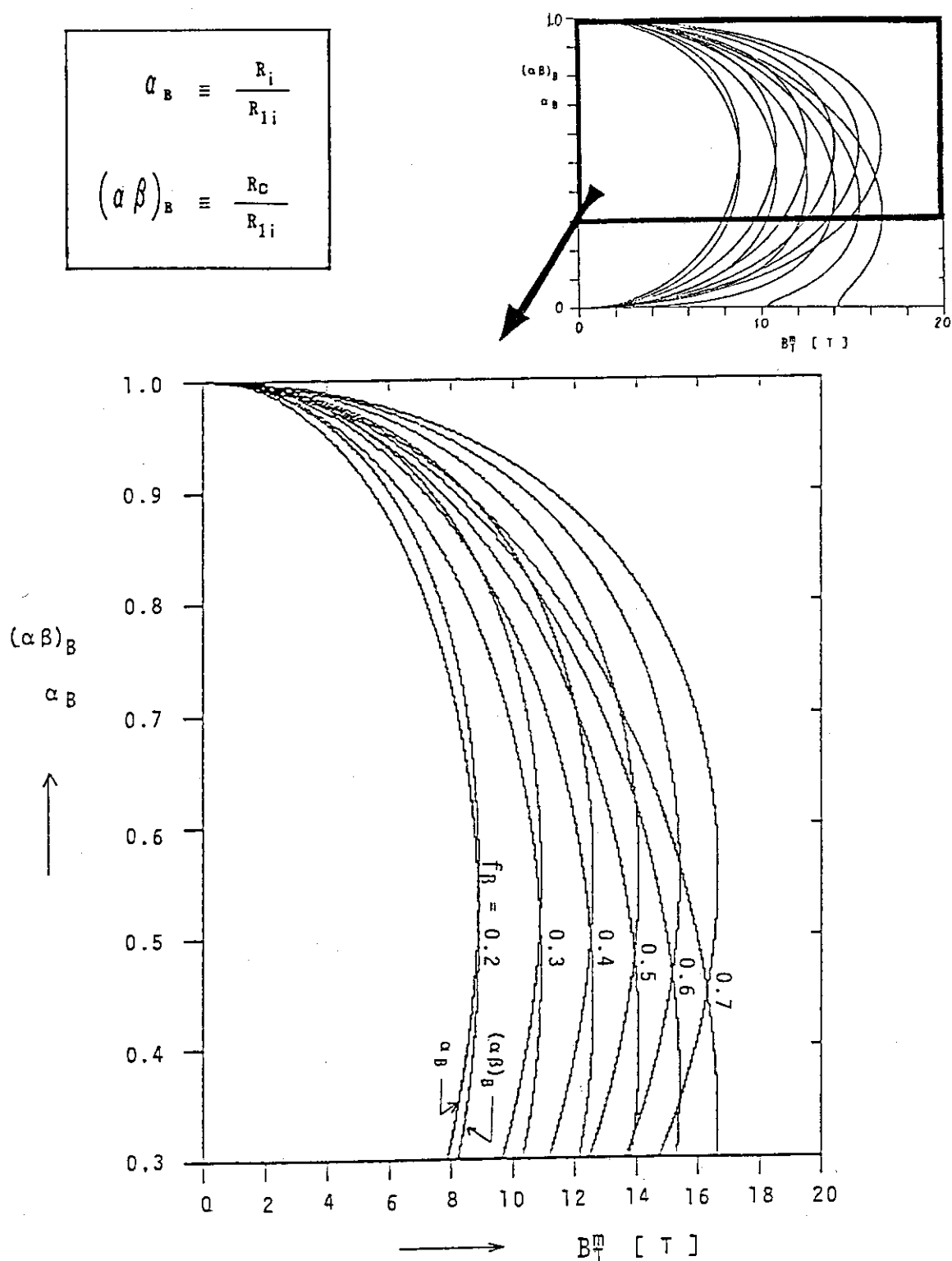


Fig. 4.1.4 Dependency of normalized coil inner radius required ( $\alpha_B$ ) and bucking cylinder inner radius ( $(\alpha\beta)_B$ ) on mean maximum toroidal field ( $B_T^m$ ) with parameters of stress design guideline factor ( $f_B$ ) in case of bucking cylinder support.

1- $\alpha_B$  : normalized coil thickness required

1- $(\alpha\beta)_B$  : normalized total thickness including bucking cylinder

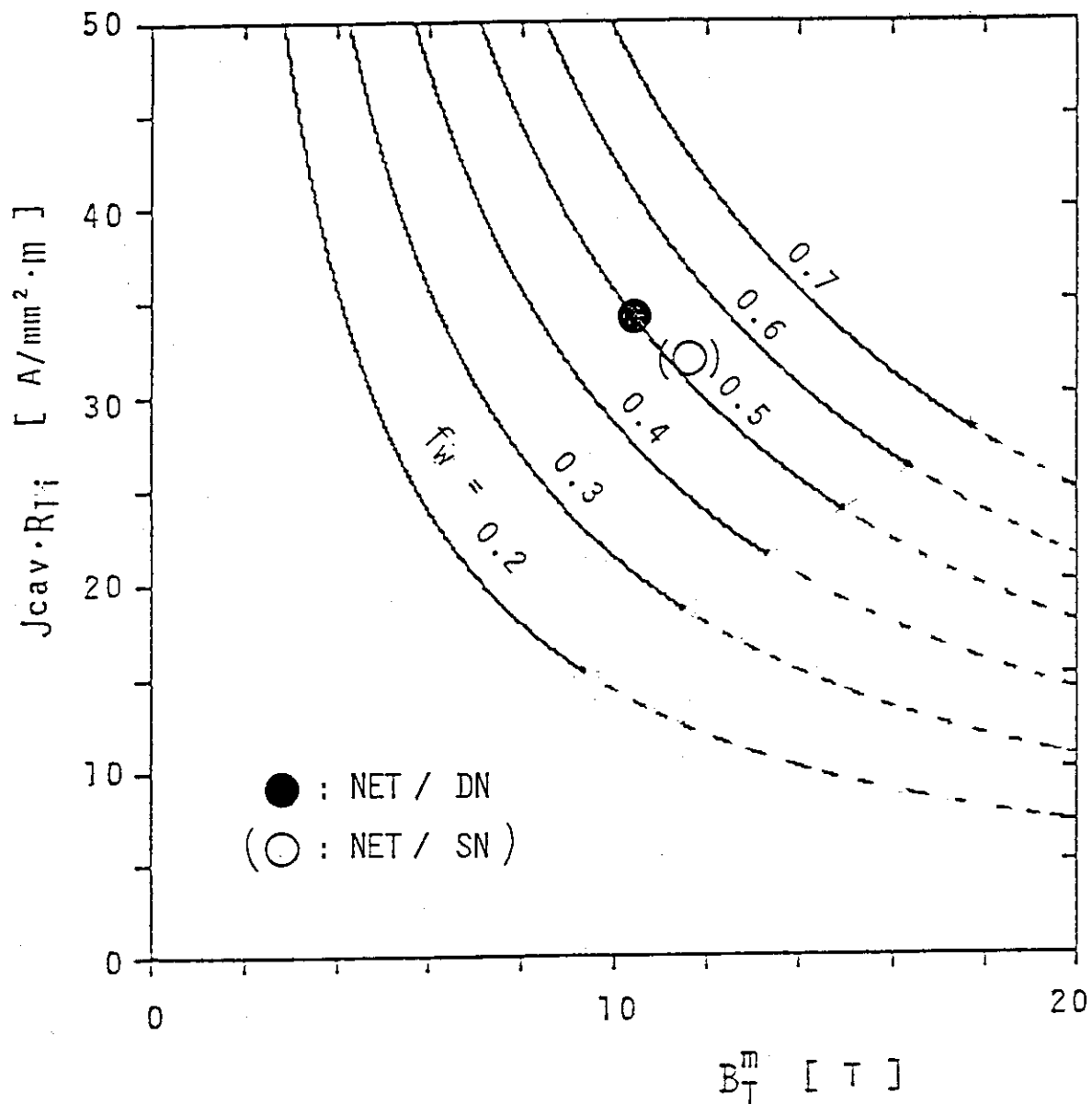


Fig. 4.1.5 Dependency of average coil cavity current density ( $J_{cav}$ ) times coil outer radius ( $R_{1i}$ ) on mean maximum toroidal field ( $B_T^m$ ) with parameters of stress design guideline factor ( $f_B$ ) in case of wedge support.



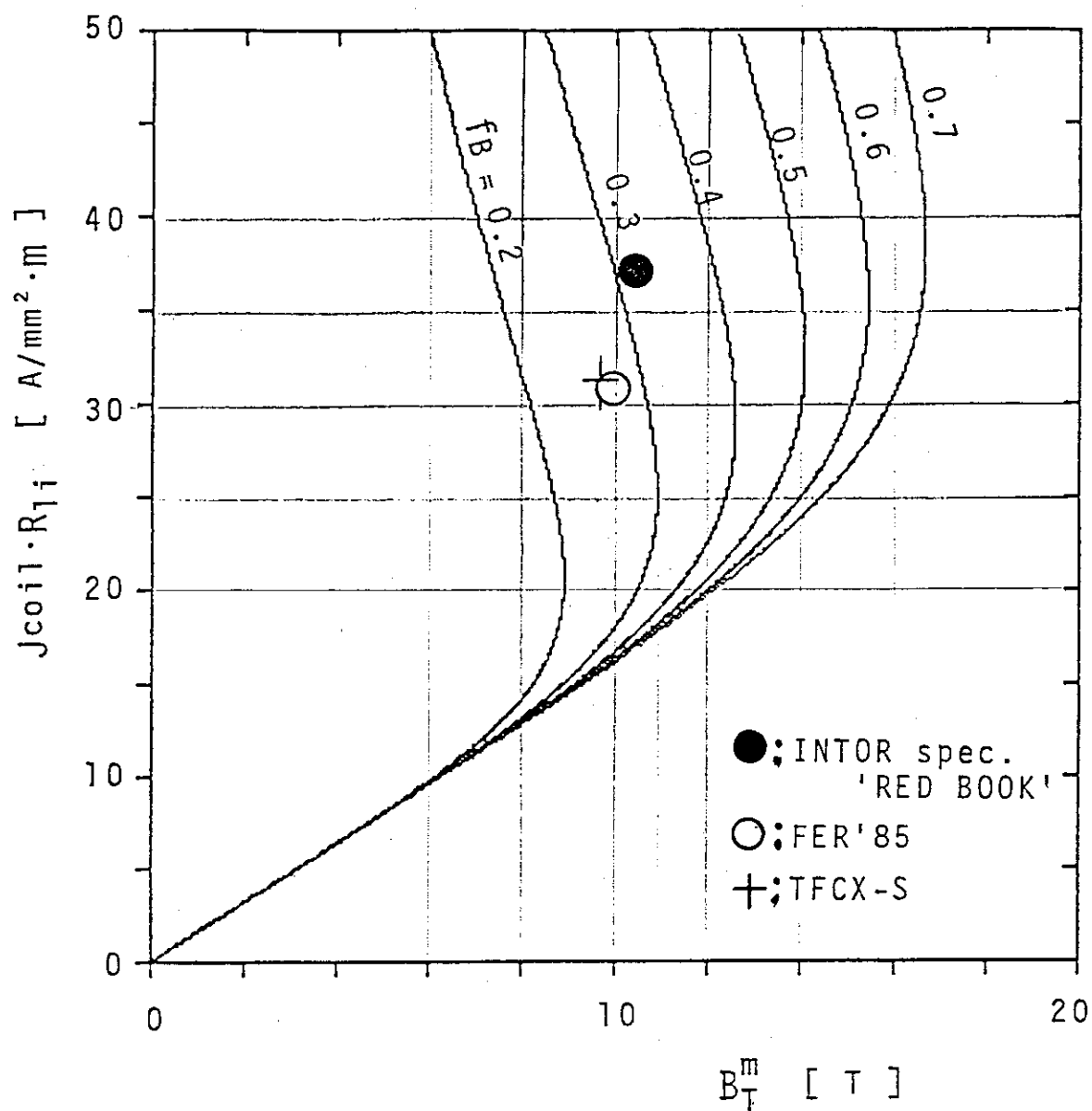


Fig. 4.1.6 Dependency of average coil cavity current density ( $J_{coil}$ ) times coil outer radius ( $R_{1i}$ ) on mean maximum toroidal field ( $B_T^m$ ) with parameters of stress design guideline factor ( $f_B$ ) in case of bucking cylinder support.

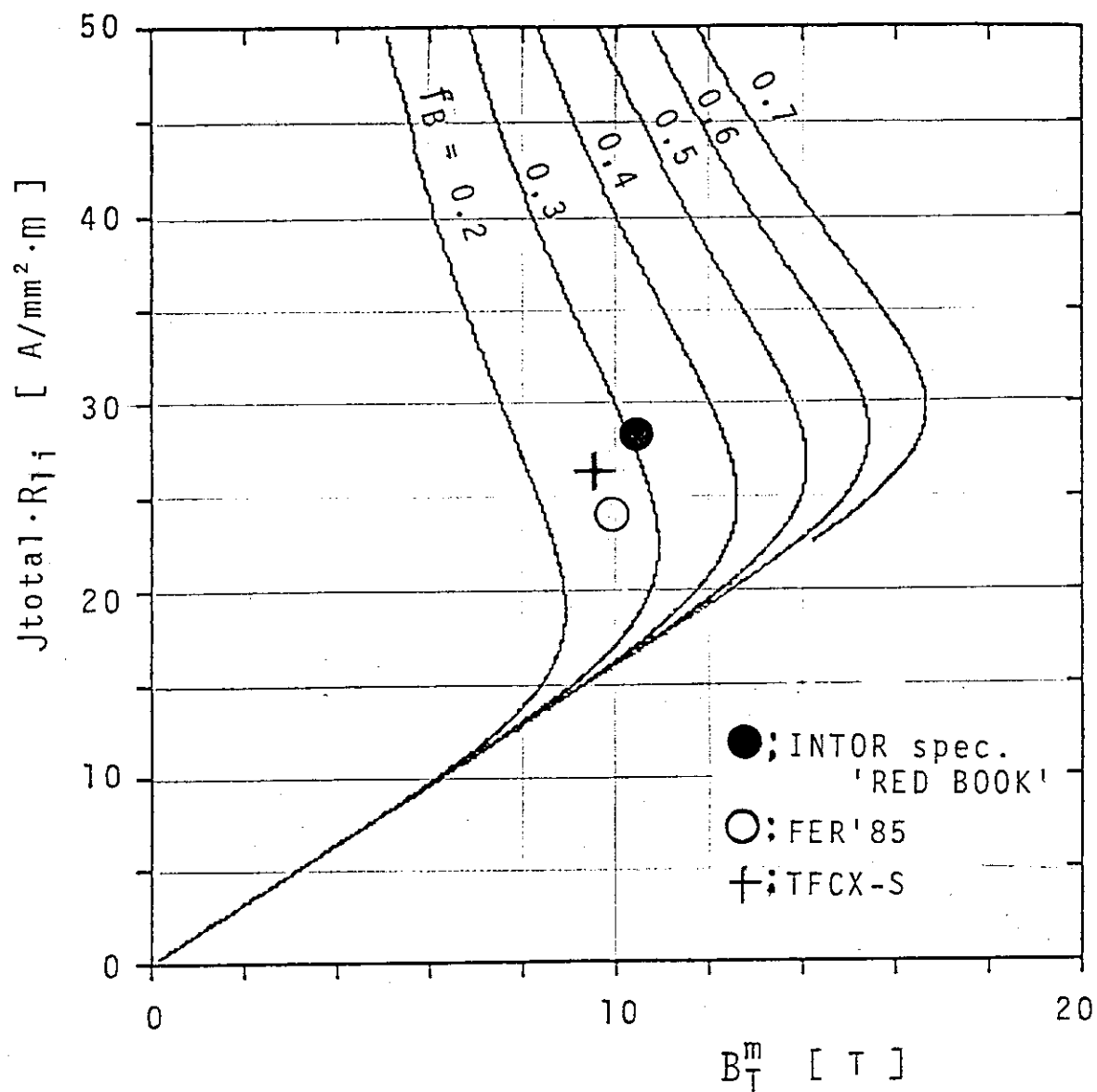
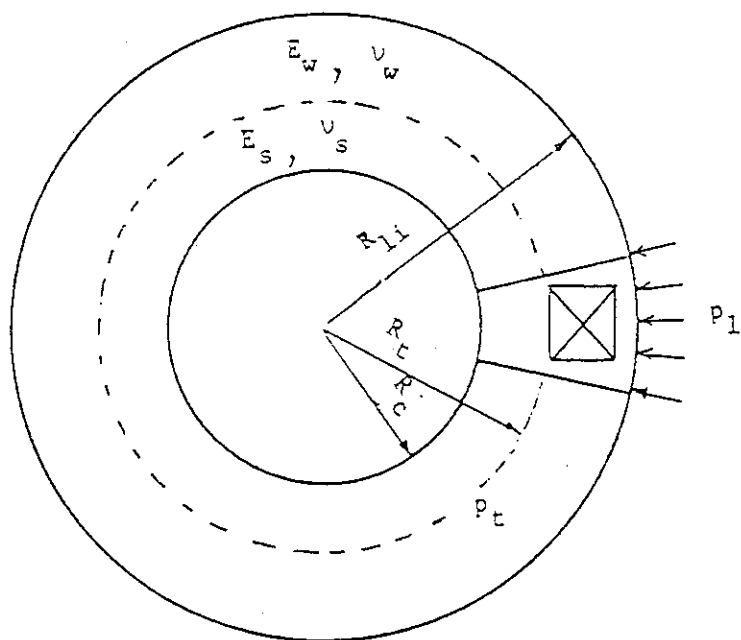
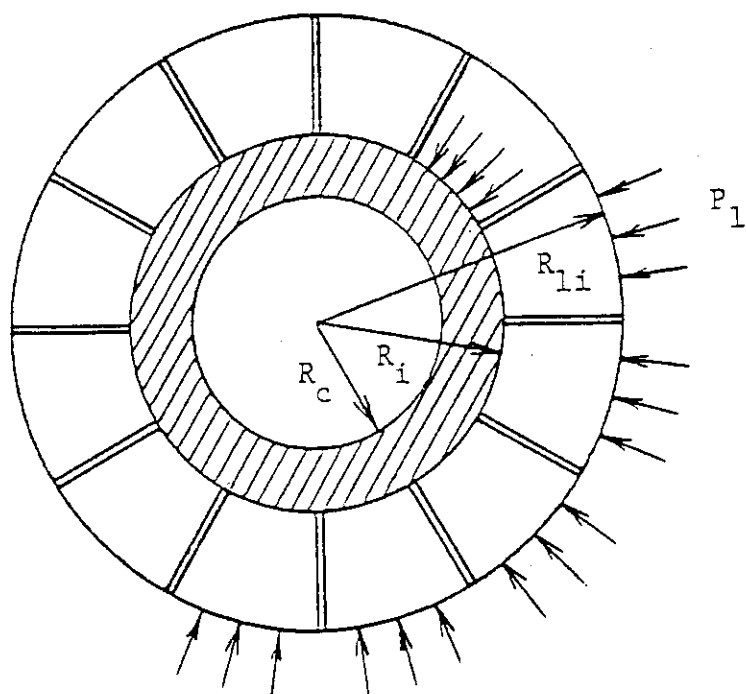


Fig. 4.1.7 Dependency of total average current density ( $J_{total}$ ) times coil outer radius ( $R_{li}$ ) on mean maximum toroidal field ( $B_T^m$ ) with parameters of stress design guideline factor ( $f_B$ ) in case of bucking cylinder support.



$$P_1 = \frac{(\bar{B}_T^m)^2}{2 \cdot \mu_0}$$

Wedge Support



B. C. Support

Fig. 4.1.8 Models of TF coil.

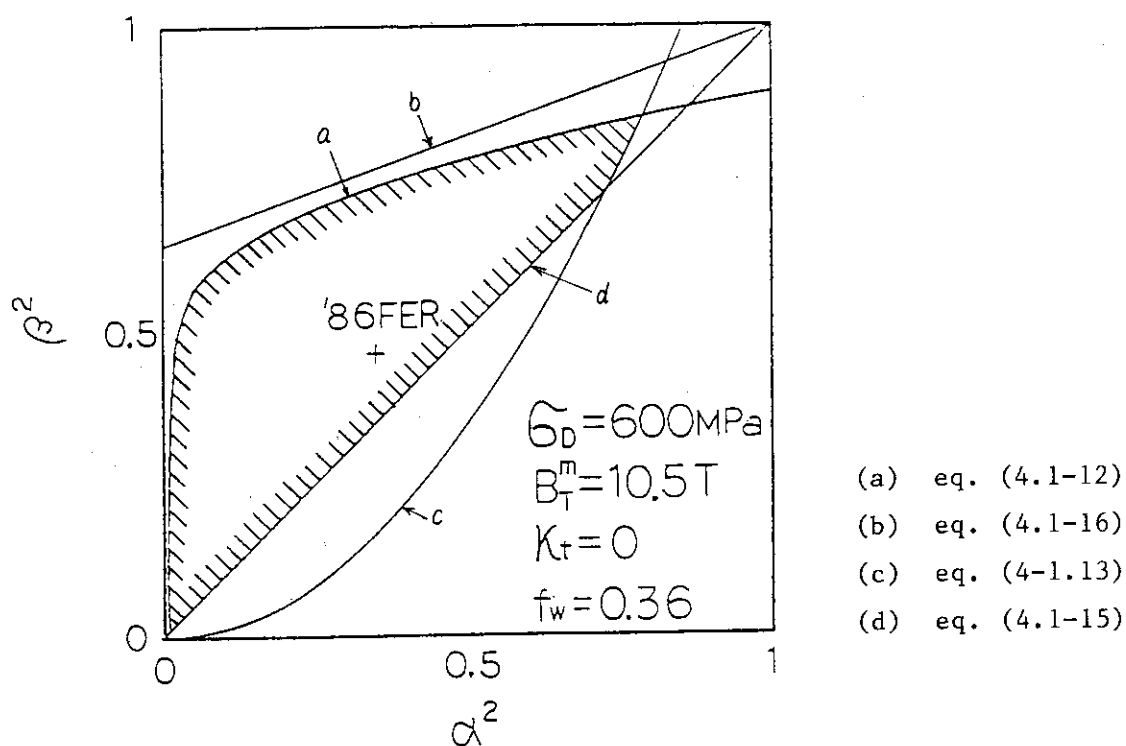


Fig. 4.1.9 Reasonable region of  $\alpha^2$  and  $\beta^2$ .  
(B.C. support)

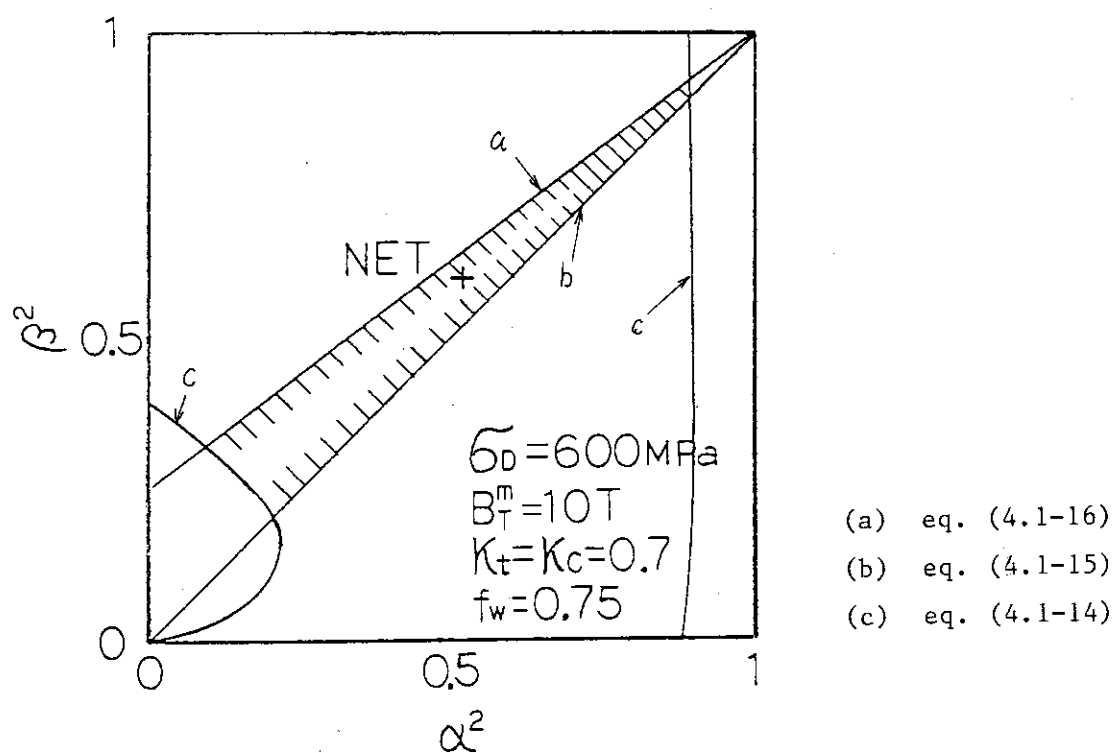


Fig. 4.1.10 Reasonable region of  $\alpha^2$  and  $\beta^2$ .  
(Wedge support)

## 4.2 Feasibility study of the wedging support TF coil

Design of the high-current density and high field TF coil is a critical issue of the INTOR innovation. The supporting methods of these coils, which are subjected to large electromagnetic forces, is major design issue. Two types of forces act on TF coils.

These forces are:

- (1) In-plane forces
  - a) tensional force
  - b) centering force
- (2) Out-of-plane force
  - a) overturning force

As pointed out in previous INTOR studies [1], some designs employed a bucking cylinder and other designs used wedging in order to support the centering force of TF coil. The supporting method of centering force have much effect on the radial build and the current density in gross cross section. This study seeks for the possibility of wedging support of TF coil by means of surveying the effect of rigidities both of a vault and of a winding pack on an axial stress in the vault.

### ANALYSIS MODEL

Fig. 4.2.1 shows the model of TF coil inner legs for wedging support. The assumptions are:

- (1) Slip at the side between coil cases, coil case and winding pack, and conductors does not occur in this model.
- (2) Inner legs are modeled by double thick-walled cylinders subjected to the uniform pressure which is the model of centering force. Inner and outer cylinders correspond to vaults and coil winding packs, which include a part of coil cases, respectively.
- (3) Young's modulus of the outer cylinder is given by an equivalent value less than that of the vault.

Outer radius  $R_{1i}$  and current density in gross cross section  $J_{cav}$  of TF coil are determined by Eq. (1) and (2) respectively.

$$R_{1i} = \frac{R_i}{\sqrt{1 - \frac{(B_p^m)^2}{2\mu_0} \frac{1}{\sigma_d} \{\ln(R_2/R_1) + 2\}}} \quad (1)$$

$$J_{cav} = \frac{4 \sigma_d}{B_p^m R_{ii} [\ln(R_2/R_1) + 2]} \quad (2)$$

where, inner radius  $R_i$  is determined from both outer radius of OH solenoid and gap, the stress criterion  $\sigma_d$  is an allowable stress of coil case which is given as a sum of tensile stress (over case and winding pack) and maximum compressive stress (in vault),  $R_2/R_1$  is the ratio of the center radius of an outer leg to that of an inner leg,  $\mu_0$  is the magnetic permeability of vacuum and  $B_p^m$  is maximum self field (average) of TF coil.

The maximum axial stress (compressive stress)  $\sigma_{\theta max}$  in the inner cylinder is calculated by Eq. (3).

$$\sigma_{\theta max} = \frac{2 L l^2}{L l^2 - R_i^2} P_m \quad (3)$$

$$\begin{aligned} \text{where} \\ P_m = \frac{2 \left\{ \frac{P}{E_{eq}} \frac{R_{ii}^2}{(R_{ii}^2 - L l^2)} \right\}}{\left\{ \frac{m_{sus} - 1}{m_{sus} E_{sus}} + \frac{m_{eq} + 1}{m_{eq} E_{eq}} \right\} + 2 \left\{ \frac{1}{E_{sus}} \frac{R_i^2}{(L l^2 - R_i^2)} + \frac{1}{E_{eq}} \frac{L l^2}{(R_{ii}^2 - L l^2)} \right\}} \\ P = \frac{(B_p^m)^2}{2 \mu_0} \\ (R_i \leq L l \leq R_{ii}) \end{aligned}$$

$P_m$  is a uniform pressure on the contact surface between inner and outer cylinders.  $P$  is a uniform pressure, the model of centering force. Small letters  $m_{sus}$  and  $m_{eq}$  are Poisson's ratios of inner and outer cylinders respectively. Capital letters  $E_{sus}$  and  $E_{eq}$  are Young's moduli of both cylinders in the same manner.

## CONCLUSIONS

Six cases of TF coil were investigated, including NET DN case. Parameters used for calculation and results are summarized in Tables 4.2.1-4.2.3 and Figs. 4.2.2-4.2.6. In Tables, the data  $R_{OH}$ ,  $B_p^m$ ,  $B_p^{max}$ , and  $J_{cav}$  of NET DN case were quoted from references [2] and [3], on the other hand,  $R_i$  and  $R_{ii}$  were calculated from total ampereturns,  $B_p^m$ , and  $J_{cav}$ . In Fig. 4.2.2, curve A shows that centering forces act on the inner cylinder surface directly.

Main results are described as follows.

- (1) As an equivalent Young's modulus  $E_{eq}$  of winding pack increases, maximum axial stress  $\sigma_{max}$  at a vault length decreases. But we suppose that the reasonable level of a winding pack Young's modulus, which depends on conductor design, is less than several fractions of that of stainless steel at most. So, there is a minimum vault length corresponding to an  $E_{eq}$ . A small  $E_{eq}$  and a low stress criterion require long vault length.
- (2) Owing to the support of winding pack and its fabrication, it is limited in packing factor. So, the maximum vault length exists corresponding to a current density  $J_{wnd}$  of winding pack. A large packing factor and a high  $J_{wnd}$  require long vault length.
- (3) For the above reason, there are minimum and maximum vault length at a given stress criterion and a given current density of winding pack.

These results were derived, assuming that coil winding packs and coil cases are regarded as an integrated rigid body. Therefore, several problems mentioned below must be solved to ensure high rigidities of a vault and a winding pack.

- (1) Preventing slip at the side between coil cases, coil case and winding pack, and conductors.
- (2) Transmitting the centering force to the axial direction of winding pack.
- (3) Designing and fabricating a high Young's modulus conductor.
- (4) Winding conductors without deteriorating a Young's modulus of conductor and increasing an equivalent Young's modulus of winding pack up to several fractions of that of vault.

#### REFERENCES

- [1] INTOR GROUP, International Tokamak Reactor: Phase Two A Part 2 (Rep. Int. Tokamak Reactor Workshop Vienna, 1984-85), International Atomic Agency, Vienna (1986).
- [2] MALAVASI, G., MITCHELL, N., SALPIETRO, E., Proc. 14th SOFT, Avignon, 1986.
- [3] NET Status Report, NET Team, Report No. 51, Dec. 1985.

Table 4.2.1 Mechanical properties of structural materials

Poisson's ratio of vault (SUS 304) at 4.2K	$\frac{1}{m_{sus}}$	0.275
Poisson's ratio of winding pack	$\frac{1}{m_{eq}}$	0.3
Young's modulus of vault (SUS 304) at 4.2K	$E_{sus}$	$2.1 \times 10^4 \text{ kg/mm}^2$

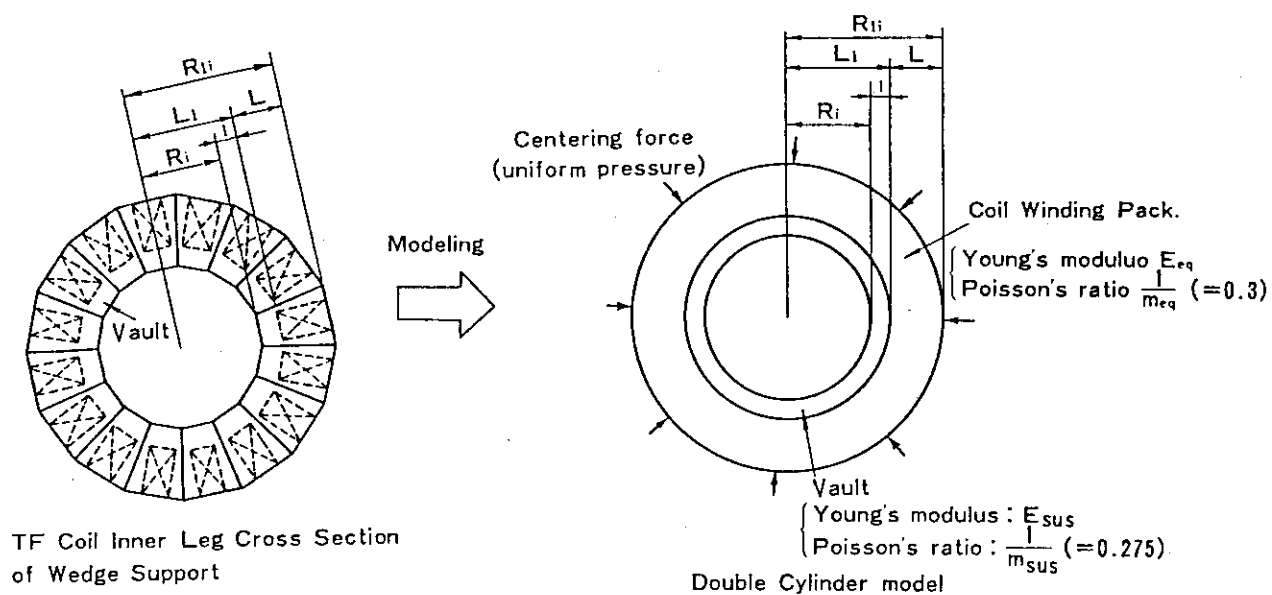


Fig. 4.2.1 Model of TF coil inner legs for wedging support.



Table 4.2.2 Parameters for calculation

	SIGN UNIT	Case					NET DN
		1	2	3	4	5	
OH solenoid parameters	$B_p^{\max}$ (T)	10	12	14	12	12	1.75
	$J_{cav(OH)}(A/mm^2)$	30	25	25	25	30	
	$R_{OH}$ (m)	1.47	1.40	1.34	1.58	1.54	
Gap	$\Delta$ (m)	0.05					0.03
TF coil Parameters	$B_p^{\max}$ (T)	12	12	12	12	12	11.4
	$B_p^m$ (T)	10.5	10.5	10.5	10.5	10.5	10.4
	$R_i$ (m)	1.52	1.45	1.39	1.63	1.59	1.80
Comment	$\alpha$	1			1.055		~4.15
	$\beta$	1			0.85		
	$\gamma$	1			0.96		
	$\varepsilon$	1			0.8		
	$R_2/R_1$	4.0			4.0		
	$\sigma_d$ (MPa)	300			300		
	$\Delta\Phi_{OH}$ (VS)	112			112		181

Table 4.2.3 Calculation results of TF coil

SIGN UNIT	Case					NET DN
	1	2	3	4	5	
$R_{ii}$ (m)	2.14	2.04	1.96	2.29	2.24	2.50
$R_{ii}-R_i$ (m)	0.62	0.59	0.57	0.66	0.65	0.70
$J_{cav}$ (A/mm <sup>2</sup> )	15.8	16.5	17.3	14.8	15.0	13.7
$J_{cav} * R_{ii}$ (10 <sup>6</sup> A/m)	33.8	33.7	33.9	33.9	33.6	34.3

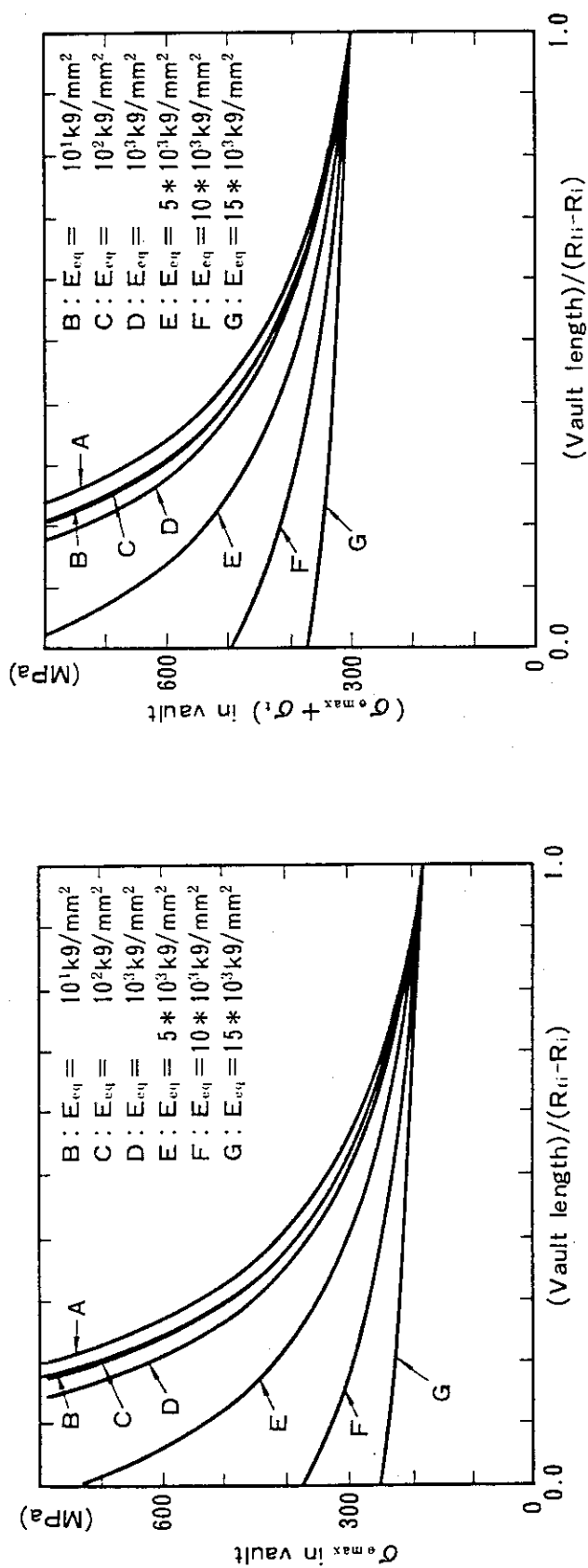


Fig. 4.2.2 Maximum axial stress and stress intensity in vault versus reduced vault length for various Young's modulus of winding pack.

CASE 1 :  $R_{1i}-R_i=0.52 \text{ m}$   
CASE 2 :  $R_{1i}-R_i=0.59 \text{ m}$   
CASE 3 :  $R_{1i}-R_i=0.57 \text{ m}$   
CASE 4 :  $R_{1i}-R_i=0.66 \text{ m}$   
CASE 5 :  $R_{1i}-R_i=0.65 \text{ m}$   
NET DN CASE :  $R_{1i}-R_i=0.70 \text{ m}$

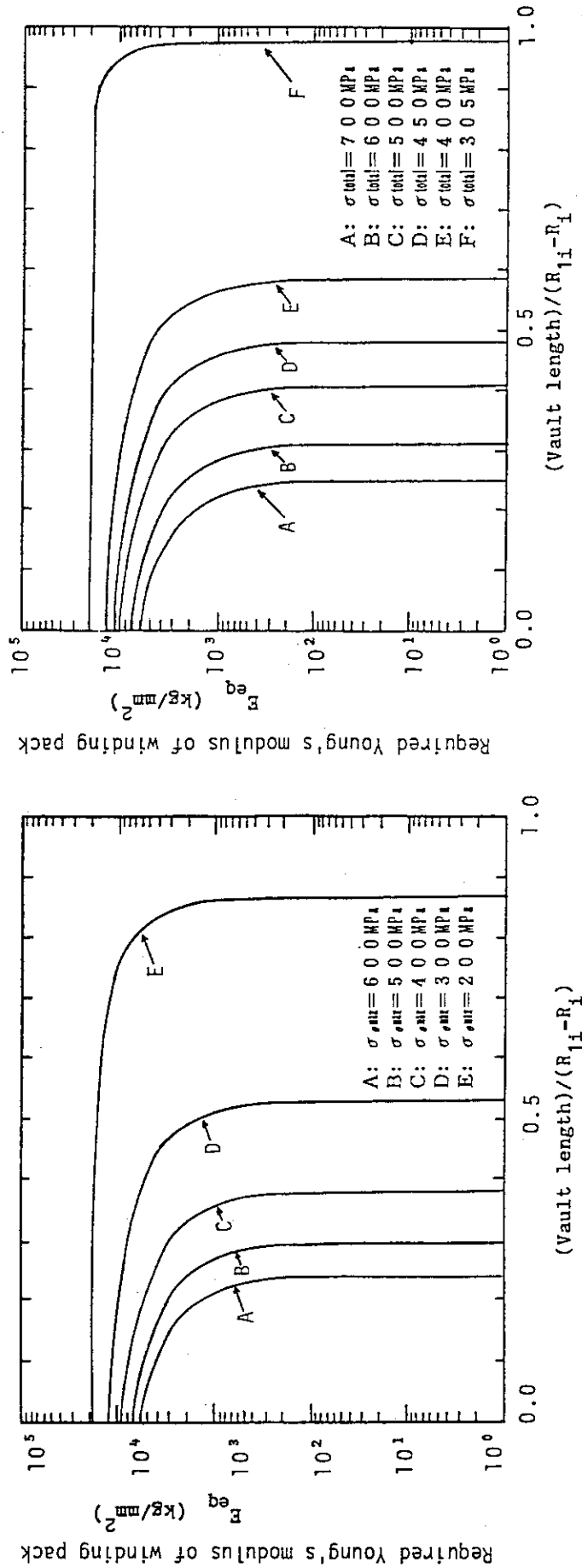


Fig. 4.2.3 Required Young's modulus of winding pack versus reduced vault length for various maximum axial stress and stress intensity. (Tensile stress over case and winding pack is used.)

CASE 1 :  $R_{1i} - R_1 = 0.52 \text{ m}$   
CASE 2 :  $R_{1i} - R_1 = 0.59 \text{ m}$   
CASE 3 :  $R_{1i} - R_1 = 0.57 \text{ m}$   
CASE 4 :  $R_{1i} - R_1 = 0.66 \text{ m}$   
CASE 5 :  $R_{1i} - R_1 = 0.65 \text{ m}$   
NET DN CASE :  $R_{1i} - R_1 = 0.70 \text{ m}$

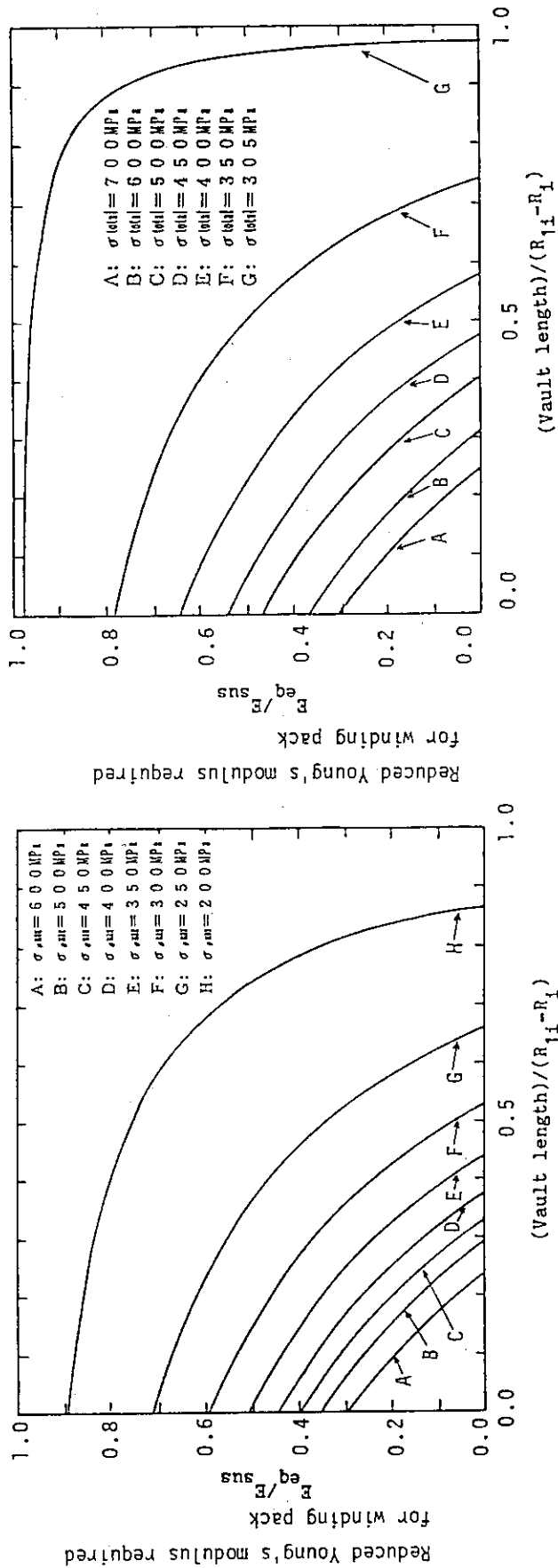


Fig. 4.2.4 Reduced Young's modulus required for winding pack versus reduced vault length for various maximum axial stress and stress intensity. (Tensile stress over case and winding pack is used.)

CASE 1 :  $R_{1i} - R_{1f} = 0.52 \text{ m}$   
CASE 2 :  $R_{1i} - R_{1f} = 0.59 \text{ m}$   
CASE 3 :  $R_{1i} - R_{1f} = 0.57 \text{ m}$   
CASE 4 :  $R_{1i} - R_{1f} = 0.66 \text{ m}$   
CASE 5 :  $R_{1i} - R_{1f} = 0.65 \text{ m}$   
NET DN CASE :  $R_{1i} - R_{1f} = 0.70 \text{ m}$

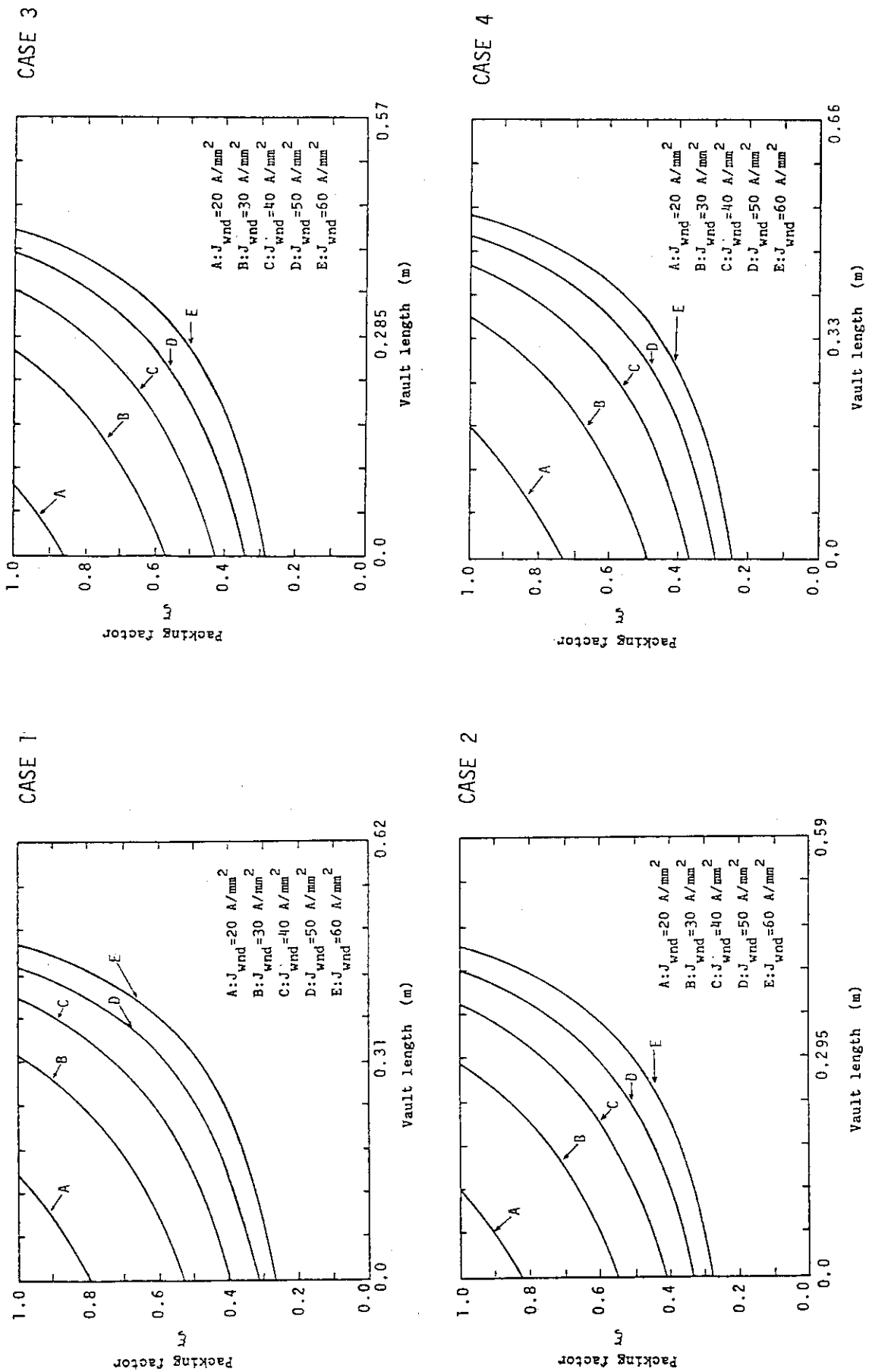


Fig. 4.2.5 Packing factor versus vault length for various current density of winding pack (Packing factor is defined as a ratio of winding area to that of outer cylinder).

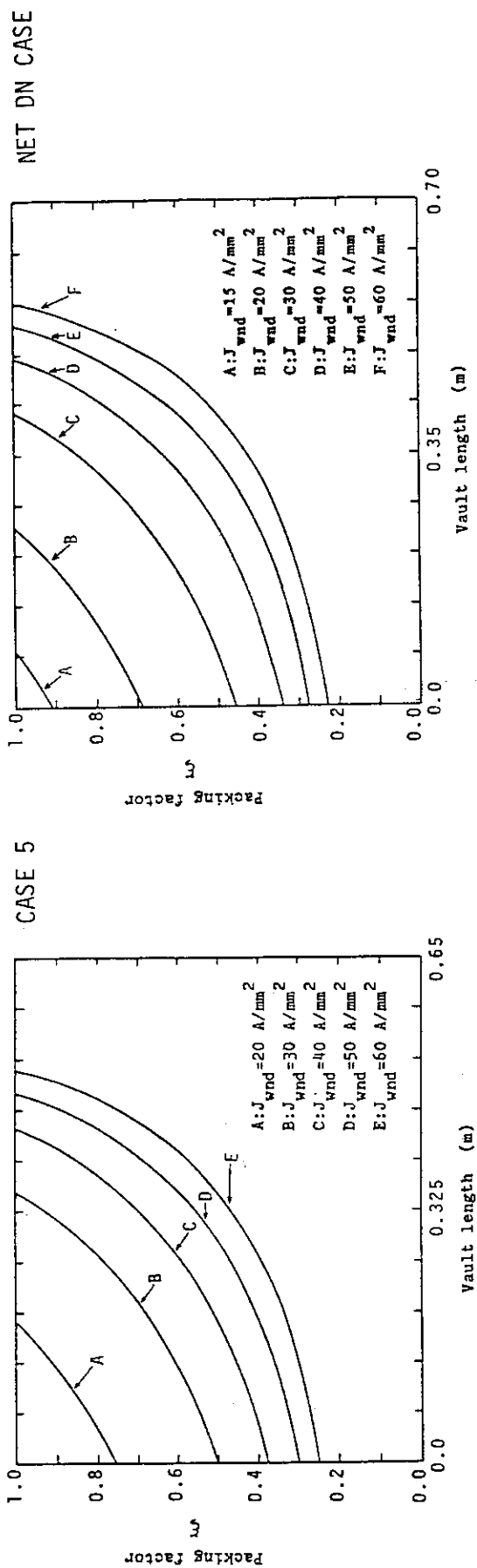


Fig. 4.2.6 Packing factor versus vault length for various current density of winding pack (Packing factor is defined as a ratio of winding area to that of outer cylinder).

### 4.3 Design guidelines for TF coil sizing

#### (1) Winding-pack current density

This study has been focused on a forced flow cooled superconductor with copper stabilized  $(\text{NbTi})_3\text{Sn}$ . To define general guidelines for INTOR TF coil design, the following items were estimated until now.

- A. Quench voltage
- B. Peak conductor temperature
- C. Maximum conductor current
- D. Operating current density

Based on these study, a generalized graph to select the winding-pack current density has been proposed, as shown in Fig. 4.3.1. Figure 4.3.1 shows that it is possible to obtain the winding-pack current density of  $40 \text{ A/mm}^2$  at 12 T. However, the winding-pack current density of  $25 \text{ A/mm}^2$  is critical at 16 T. It is considered that the reasonable current density is below  $20 \text{ A/mm}^2$  at 16 T.

#### (2) Current density limit in gross cross section

Cross section of the TF coil inner leg can be classified into the winding-pack area and the structural material area. The current density in gross cross section is given by following equation.

$$j_{\text{cav}} = \frac{NI}{A_s + A_w} = \frac{1}{A_s/NI + A_w/NI} = \frac{1}{1/j_s + 1/j_w}$$

where  $NI$  : Total ampere turns of TF coils  
 $j_s$  : Current density over the structural material  
 $j_w$  : Current density over the cable space of the conductor  
 (see Fig. 4.3.1)

$$j_s = \frac{4 \sigma_D}{B_T^m R_{1i} (\ln \frac{R_2}{R_1} + 2)} = \frac{8\pi \sigma_D}{\mu NI (\ln \frac{R_2}{R_1} + 2)}$$

where  $\sigma_D$  : Allowable stress of structural material (600 MPa)

The current density over the structural material in gross cross

section of TF coil is shown in Fig. 4.3.2. The current density limit in gross cross section of TF coil has been plotted in Fig. 4.3.3. The current density shown in Fig. 4.3.3 gives the minimum gross area of TF coils, in which the average stress of the structure is limited within the allowable stress. In the practical structure of inner TF coil leg, however, the stress of structure is not distributed uniformly. Therefore, the safety margin should be taken for the inhomogeneity of stress. The safety margin used in this discussion is 1.3. Based on this margin, we propose the following criteria in the TF coil design.

$$j_{\text{cav}} \leq 12 \text{ A/mm}^2 \text{ at } 12 \text{ T}$$

$$j_{\text{cav}} \leq 7.5 \text{ A/mm}^2 \text{ at } 16 \text{ T}$$

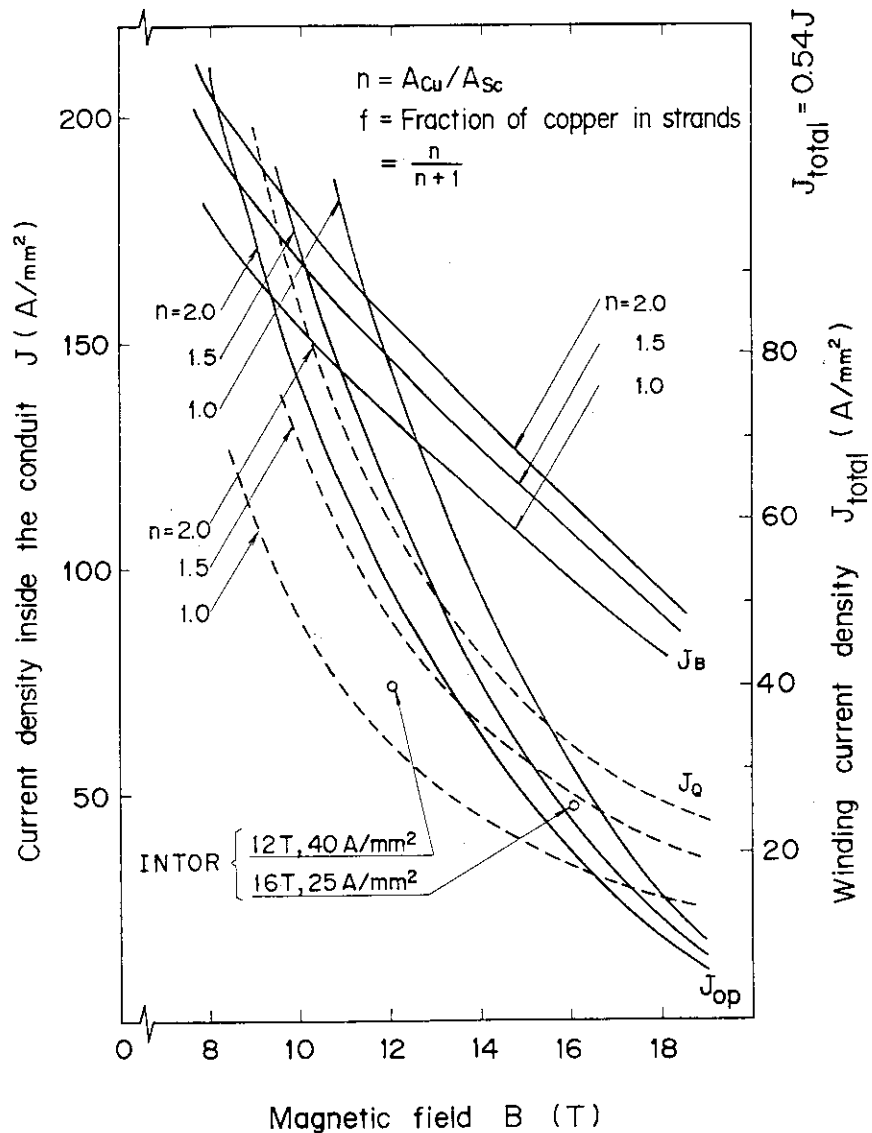


Fig. 4.3.1 Current density inside the conduit versus magnetic field.



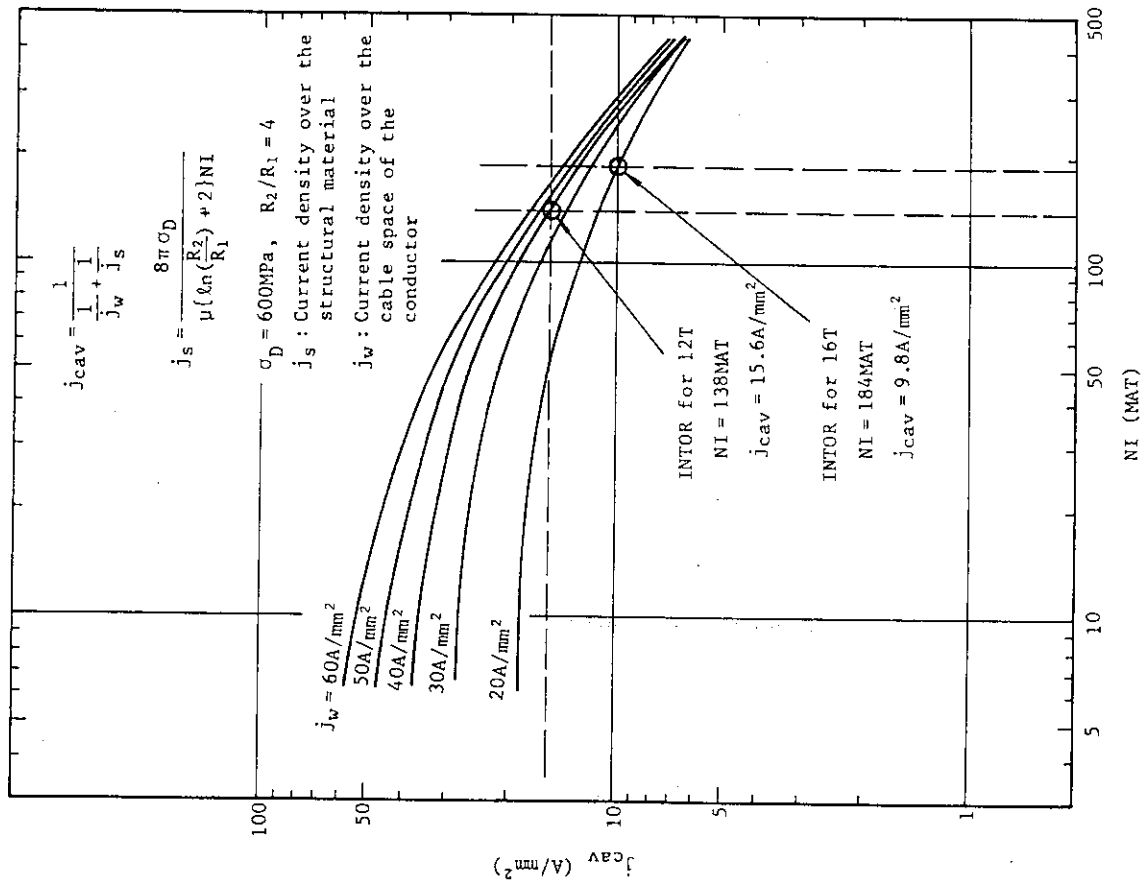


Fig. 4.3.3 Current density limit in gross cross section of TF coil.

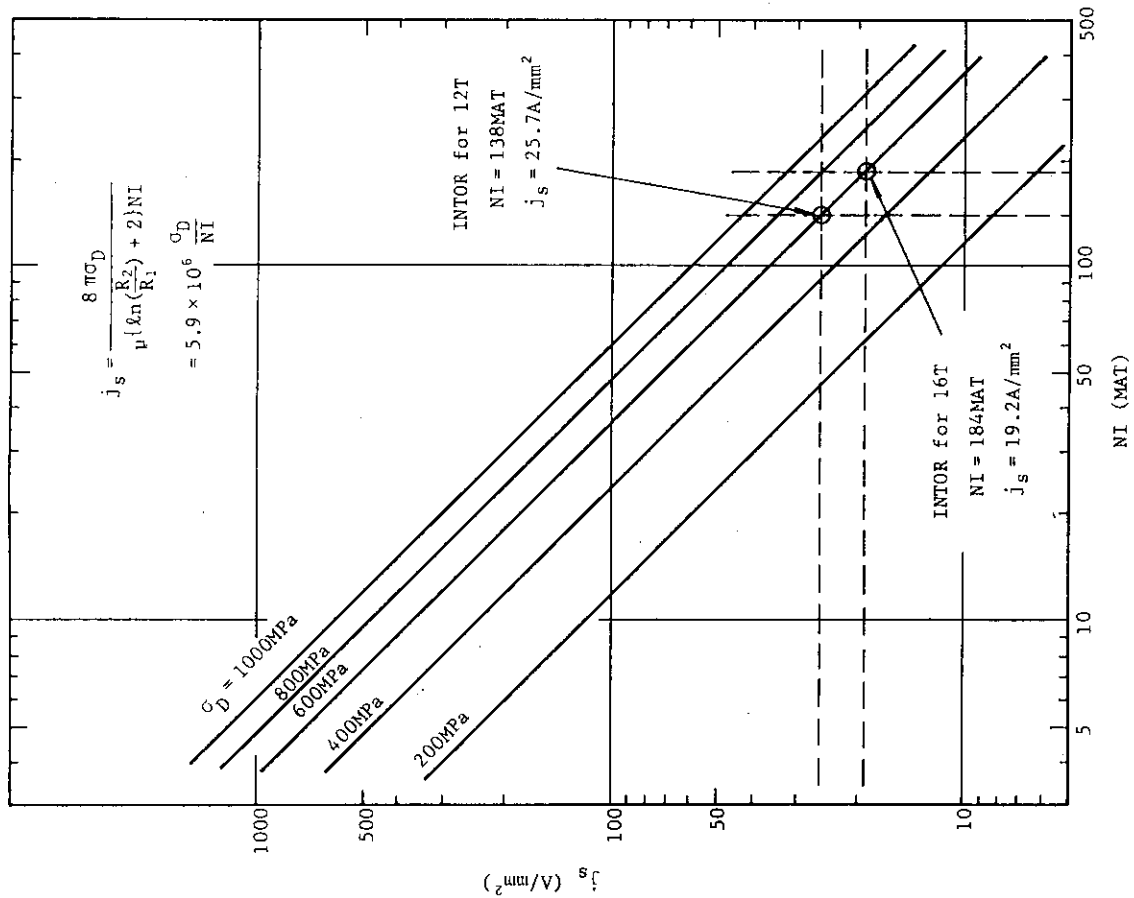


Fig. 4.3.2 Current density over the structural material in gross cross section of TF coil.

## 5. Allowable Stresses in the Structural Material of the Magnetic System

### (1) Type of alloy and material status.

Table 5-1<sup>(1)</sup> shows the chemical compositions of the Japanese Cryogenic Steels (JCS). These steels were developed by JAERI.

Almost all of these steels' characteristics are in the JAERI-box (yield strength of more than 1200 MPa, fracture toughness of more than 200 MPa√m).

Figure 5.1<sup>(1)</sup> shows the fracture toughness and yield strength for thick plate of each JCS at 4K. In addition, tensile tests for thin plate were also conducted for application to conduit materials. Not only the mechanical properties of base metals, but also the efficiency of welding, cold work and heat treatment were measured.<sup>(1)</sup>

Table 5.2 shows the minimum structural material properties of case and conduit.

### (2) Loading conditions and design guideline.

The static criteria for allowable stress intensity is given by

$$S_m = \text{Min} (2\sigma_y/3, \sigma_u/2)$$

where  $\sigma_y$  ; yield strength  
 $\sigma_u$  ; tensile strength

The percent of tensile strength is taken to be higher than that recommended in ASME Code to take advantage of high yield strengths of JCS materials.

Loading conditions are as follows.

#### (i) TF coil case and conduit.

- ① In-plane force due to toroidal field
- ② Out-of-plane force due to poloidal field
- ③ Quench pressure.

#### (ii) PF coil conduit

- ① Radial and vertical force due to poloidal field
- ② Bending moment due to toroidal field ripple
- ③ Quench pressure.

Allowable limits of stress intensity due to these force are shown for each stress category in Table 5.3. Table 5.4 shows the design guideline.

## (3) Fatigue limit and allowable initial flaw size

A relation between the flaw size and the tensile stress is given by

$$K = 1.1 \cdot \sigma \sqrt{\pi a}$$

where  $a$  : flaw size

$\sigma$  : tensile stress

Figure 5.2 shows the flaw size and tensile stress when  $K=K_{IC}/2$  ( $=100 \text{ MPa} \sqrt{\text{m}}$ ). If  $\sigma=1200 \text{ MPa}$ , the critical flaw size  $a=1.83 \text{ mm}$ .

To evaluate the fatigue life and allowable initial flaw size, Paris' equation, Walker's equation and Forman's equation are applicable.

Paris' eq.:  $da/dN = C \Delta K^m$

Walker's eq.:  $da/dN = C (\Delta K_{\text{eff}})^m$

$$\Delta K_{\text{eff}} = \Delta K / (1-R)^{0.5}$$

Forman's eq.:  $da/dN = \frac{C' \Delta K^m}{(1-R)K_{IC} - \Delta K}$

where  $a$  : minor half-diameter for embedded flaw, or flaw depth for surface flaw

$N$  : number of cycles

$C, C', m$  : material constants

$$K : 1.1 \Delta \sigma \sqrt{\pi a}$$

$$\Delta \sigma : \sigma_{\text{max}} - \sigma_{\text{min}}$$

$$R : \sigma_{\text{min}} / \sigma_{\text{max}}$$

Paris' equation can be applied for the cycle ratio  $R=0$  ( $\sigma_{\text{min}}=0$ ). Figure 5.3 shows the fatigue crack growth rate at  $R=0, 0.5, 0.7$  represented by Walker's equation and Forman's equation. For estimating  $C'$  in the Forman's equation, it is assumed that the Paris and Forman curves are coincident in the region of the threshold  $\Delta K_{\text{th}} = 10 \text{ MPa} \sqrt{\text{m}}$  (assumed).

Figure 5.4 shows the allowable initial flaw size of the TF coil case using Walker's equation when  $\sigma_{\text{max}}=400 \text{ MPa}$ . If  $\Delta \sigma=300 \text{ MPa}$ , initial flaw size is  $1.2 \text{ mm}$  and if  $\Delta \sigma=100 \text{ MPa}$ , initial flaw size is  $12 \text{ mm}$ .

Figure 5.5 shows the initial flaw size and maximum tensile stress when  $\Delta \sigma = 100 \text{ MPa}, 200 \text{ MPa}$  and  $300 \text{ MPa}$ .

Figure 5.6 shows the fatigue life of PF coil sheath. The main load of PF coil sheath is radial and vertical force due to poloidal

field. Therefore  $R$  is approximately 0 ( $\sigma_{\min} \div 0$ ). There is no crack growth under  $\Delta K \leq K_{th}$  (assumed to be  $10 \text{ MPa}\sqrt{\text{m}}$ ) that is shown as the constant region of allowable initial flaw size in Fig. 5.6. The allowable values are set up based on these datum. Table 5.5 shows the allowable values against the fatigue limit.

The allowable tensile stress  $\sigma_{\max}$  of TF coil case and PF coil sheath against the fatigue limit is less than  $S_m$ . To use the high strength steels effectively, a high accurate technique for crack detection is needed by all means. The allowable initial flaw size shown in Table 5.5 may be aggressive, and R&D program for determination of minimum detectable crack length will be necessary.

#### Reference

- (1) H. Nakajima, K. Yoshida, M. Oshikiri, Y. Takahashi, K. Koizumi, S. Shimamoto, M. Shimada, S. Tone, S. Sakamoto, K. Suemune, K. Nohara, Tensile properties of new cryogenic steels as conduit materials of forced flow superconductors at 4 K, to be presented to 1987 International Cryogenic Material Conference.

Table 5.1 Chemical Compositions of the Japanese Cryogenic Steels (JCS)

CSUS - JJ1	:	12Cr-12Ni-10Mn-5Mo-0.2N	( 6 tons heats)
CSUS - JN1	:	25Cr-15Ni-4Mn-0.35N	(50 tons heats)
CSUS - JKA1	:	20Cr-14Ni-Mn-Mo-V-0.3N	( 5 tons heats)
CSUS - JK2	:	22Mn-13Cr-5Ni-0.2N	(15 tons heats)
CSUS - JN2	:	25Mn-15Cr-1Ni-Cu-0.2N	(50 tons heats)
CSUS - JKA2	:	9Mn-21Cr-7Ni-0.3N	( 5 tons heats)
CSUS - JK1	:	17Cr-12Ni-2Mo-1Mn-Nb-0.2N	

Table 5.2 Minimum Structural material properties

	Case material	Conduit material <sup>(a)</sup>
Yield stress (MPa)	1200	1100
Ultimate stress (MPa)	1600	1500
Elongation (%)	10	10
Toughness, $K_{IC}$ (MPa $\sqrt{m}$ )	200	200 <sup>(b)</sup>

(a) CSUS-JK1 with both cold work and heat treatment

(b) The plane stress fracture toughness ( $K_{IC}$ ) for a thin conduit reaches a higher level than  $K_{IC} = 200 \text{ MPa } \sqrt{m}$

Table 5.3 Stress Category and Allowable Limits of Stress Intensity

Stress Category	Allowable Limits of Stress Intensities
Primary Membrane (General) Stress Intensity	$S_m$
Primary Membrane (Local) Stress Intensity	$1.5 S_m$
Primary Membrane (Local) and Bending Stress Intensity	$1.5 S_m$
Primary + Secondary Stress Intensity	$3 S_m$

Table 5.4 Design guideline

Criteria	Value
$P_m \leq S_m$	Case; 800 MPa , conduit; 733 MPa
$P_L + P_b \leq 1.5 S_m$	Case; 1200 MPa , conduit; 1100 MPa
$K \leq K_{IC}/2$	$100 \text{ MPa } \sqrt{m}$
$N \leq N_f/4$	$2 \times 10^4 \text{ cycle}$

where  $P_m$  ; primary membrane(general) stress intensity

$P_L$  ; primary membrane(local) stress intensity

$P_b$  ; bending stress intensity

$K$  ; design fracture toughness

$K_{IC}$ ; plane strain fracture toughness

$N$  ; design number of cycles

$N_f$  ; critical number of cycles

Table 5.5 Allowable values against fatigue limit

	TF coil case	TF coil sheath	PF coil sheath
Operating cycles	$2 \times 10^4$	$2 \times 10^4$	$2 \times 10^4$
Allowable initial flaw size $a_i$ (mm) <sup>(1)</sup>	2.0	0.2	0.2
Allowable tensile stress $\Delta\sigma/\sigma_{\max}$ (MPa)	200/450    250/400    300/320	200/1100    250/1000    300/800	500/500

(1) Flaw size

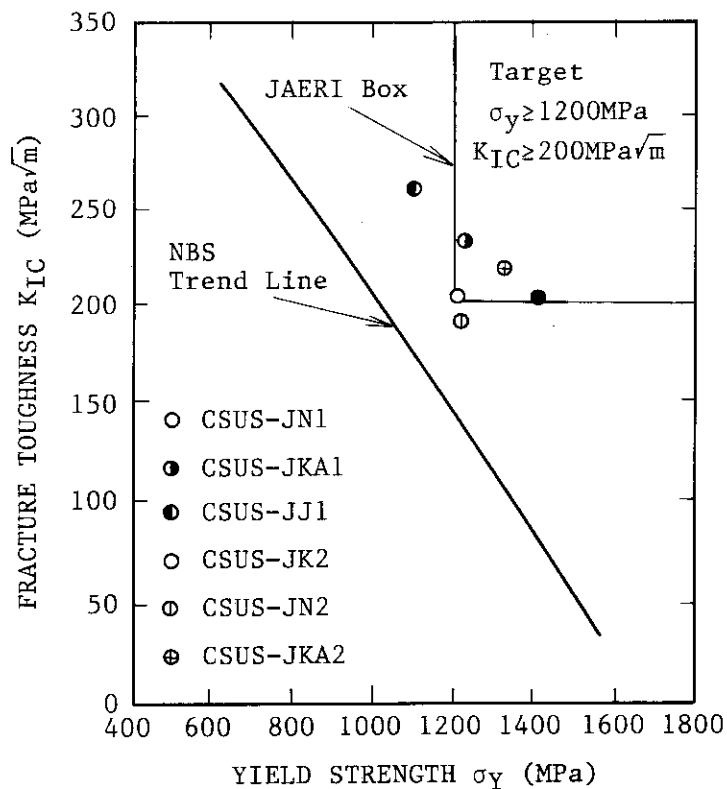
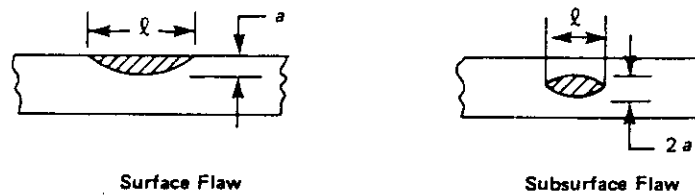


Fig. 5.1 Characteristics of fracture toughness and yield strength of the JCS at 4 K

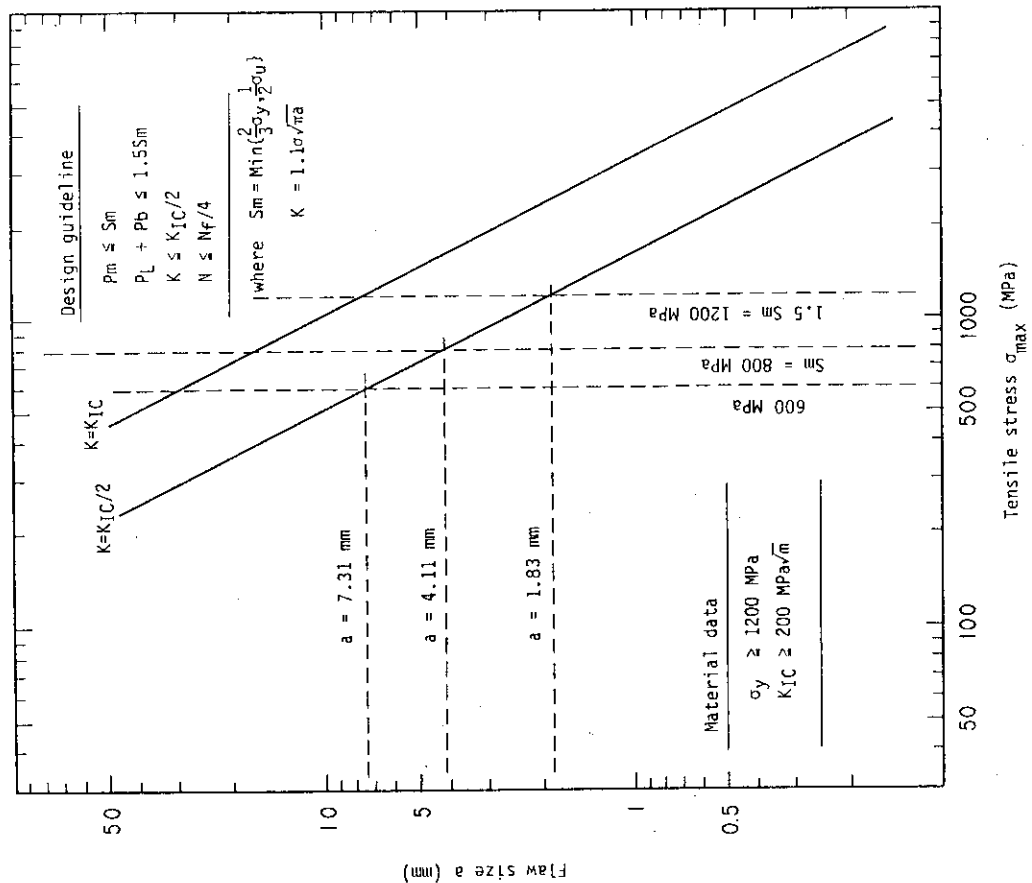


Fig. 5.2 Allowable flaw size based on the fracture toughness

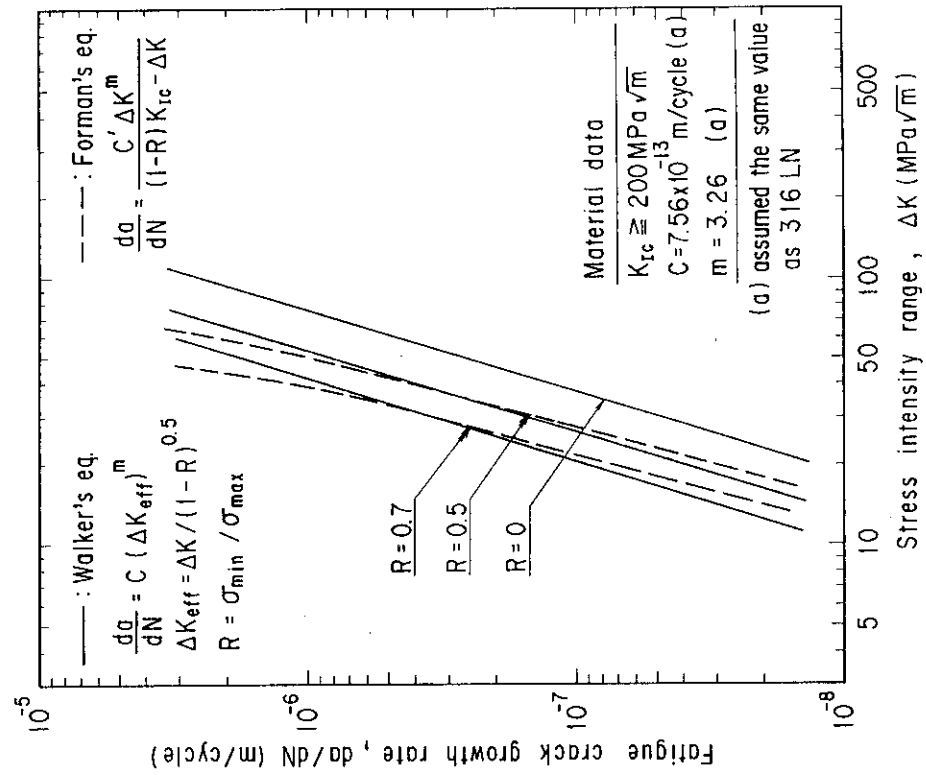


Fig. 5.3 Fatigue crack growth rate for structural material



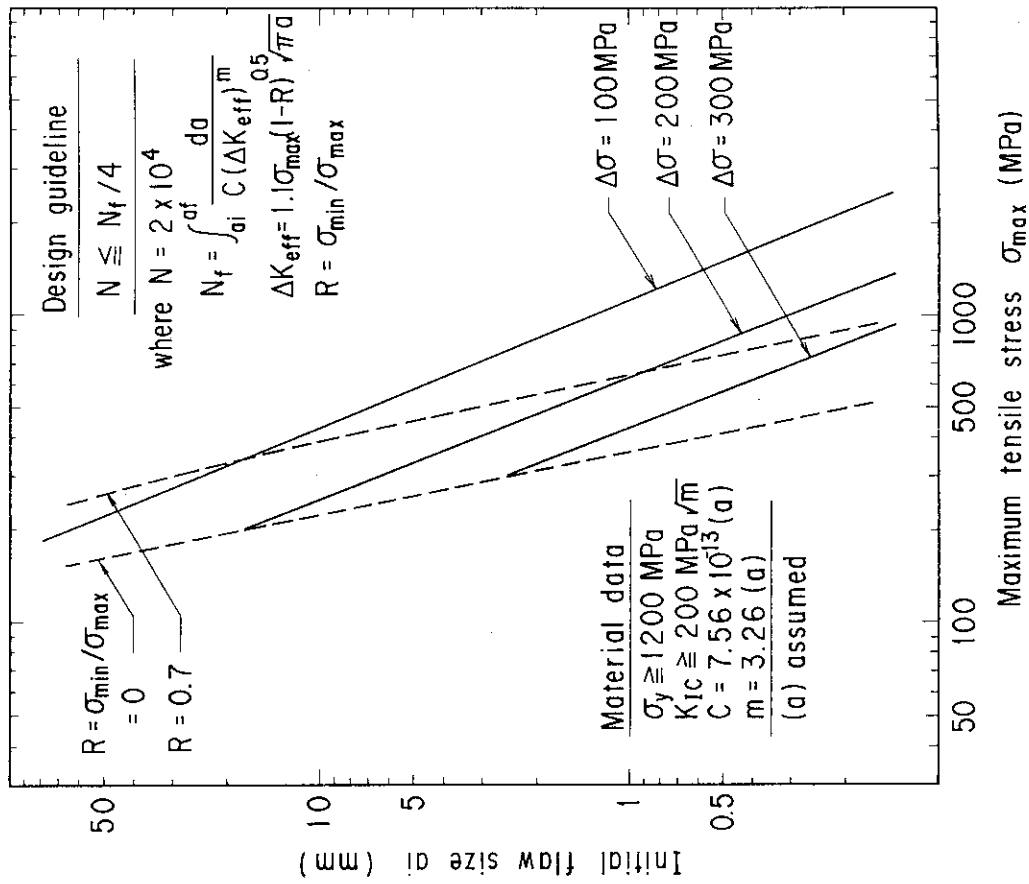


Fig. 5.5 Allowable initial flaw size of the TF coil case for the fatigue life,  $N = 2 \times 10^4$  cycles

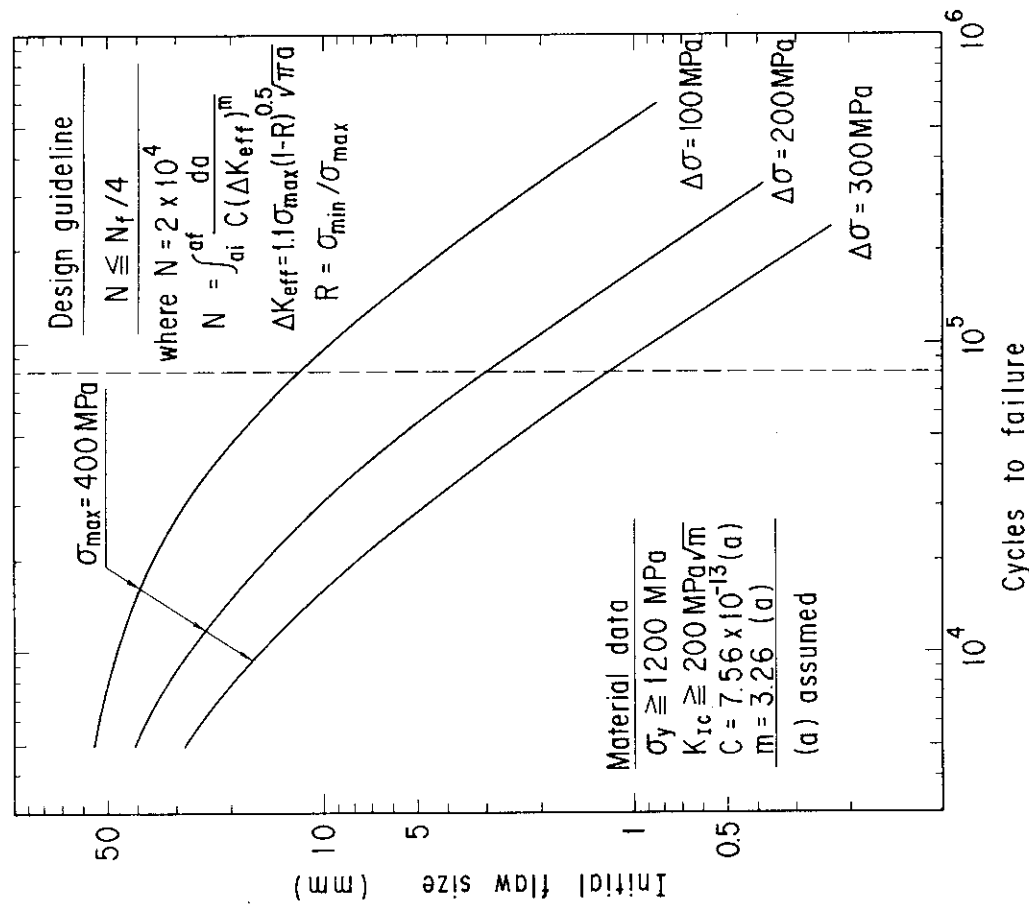


Fig. 5.4 Allowable initial flaw size of the TF coil case based on the fatigue crack growth

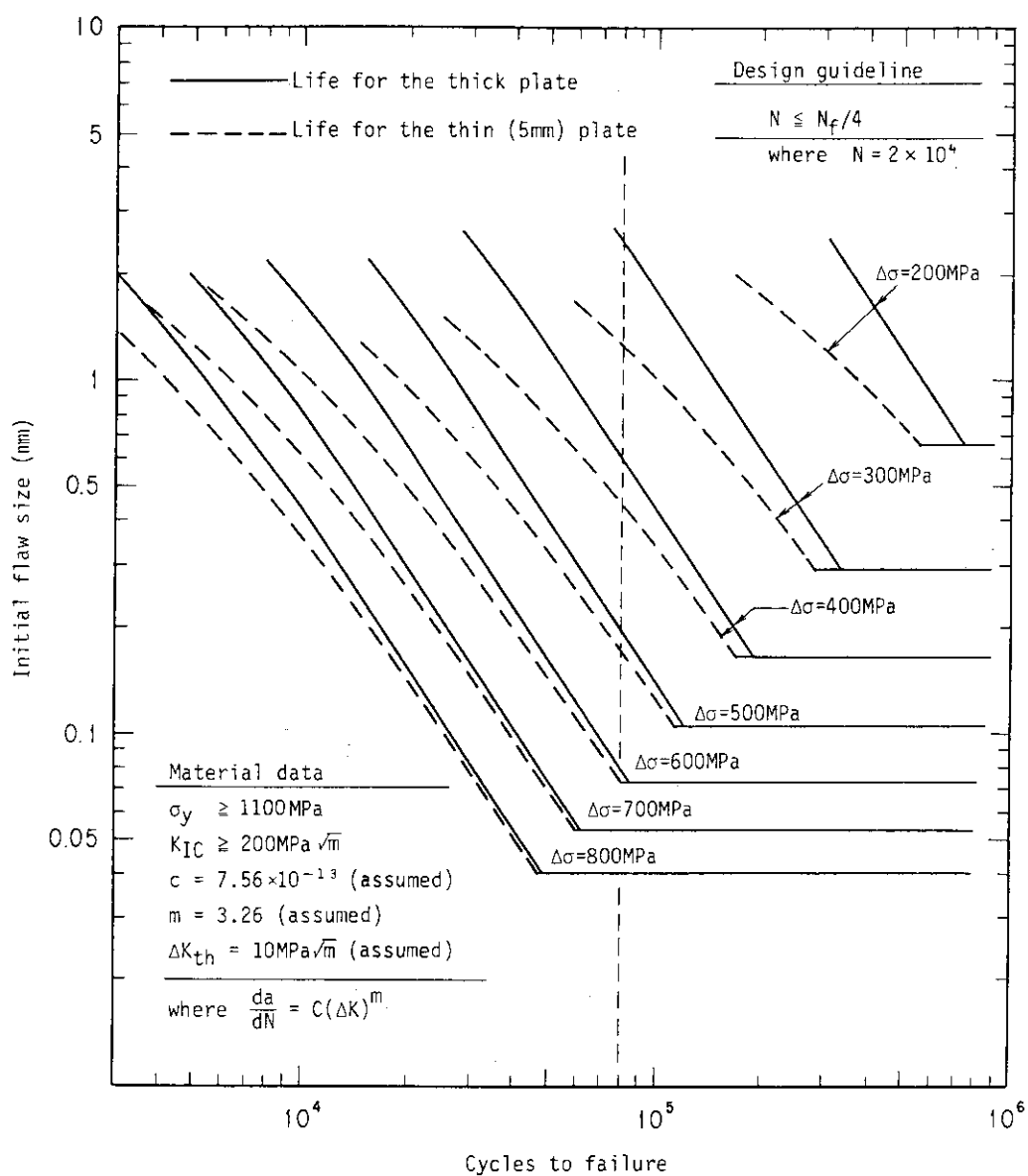


Fig.5.6 Allowable initial flaw size of the PF coil sheath  
based on the fatigue crack growth

$$(R = \sigma_{\min} / \sigma_{\max} = 0)$$

## 6. Non-metallic Structural materials

### 6.1 Study of the application of non-metallic structural materials in the magnet systems

In the magnet systems, non-metallic structural materials such as FRP are used as insulator (ex.: between conduits, between shear panels, slit of the bucking cylinder for reduction in eddy current losses). In addition to these applications, non-metallic structural materials may be used for the bucking cylinder, shear panel and PF coil support. In this study the latter applications are discussed first. Although Young's moduli of FRP materials vary as the kind of contained fiber, in this study Young's moduli of GFRP and CFRP shown in Table 6.1.1 are used.

#### (1) Bucking cylinder

Compressive stress ( $\sigma_c$ ) is generated at the bucking cylinder by centering force. The value of this stress must be equal to or lower than the allowable stress intensity ( $S_m$ ) and allowable buckling stress ( $\sigma_{ck}$ ). The allowable buckling stress is expressed by

$$\sigma_{ck} = \frac{P_{cr}}{S} \times \frac{R}{t}$$

$$P_{cr} = \frac{3 E t^3}{12(1 - \nu^2) R^3}$$

where  $P_{cr}$  : Limit buckling pressure  
 $S$  : Safety factor (=3)  
 $t$  : Thickness of buckling cylinder plate  
 $E$  : Young's modulus  
 $\nu$  : Poisson's ratio

Table 6.1.2 shows the compared result between SS304LN and two kinds of FRP in the application to buckling cylinder. It may be considered that INTOR is same as FER from the point of view of field and demension of the buckling cylinder.

As mentioned above, Young's modulus of FRP is approximately 1/5 ~ 2/5 of steel. Therefore, a buckling cylinder made of FRP must be thick. This application may cause a problem of layout of OH coil, etc.

## (2) Shear panel

The shear panel, which connects each TF coil, is designed to resist overturning force and therefore requires vertical flexural rigidity.

Figure 6.1.1 shows the shape of the shear panel in FER. The shear panel is vertically 1360 mm high.

To keep constant deformation, the flexural rigidity  $EI$  is considered to be kept at a constant value.

The required height of the FRP shear panel is approximately 2700 mm (GFRP) and 2200 mm (CFRP), when the shear panel has the same thickness as that made of stainless steel (max. 200 mm).

Therefore, the height of TF coil is occupied to large extent, which brings a great difficulty in layout of PF coils and access.

## (3) PF coils case

In FER, the ring coil of PF coils is reinforced with a stainless steel coil case against vertical force. The section of the maximum length of the ring coil is given in Figure 6.1.2.

When this case is made of FRP, the height of GFRP case is approximately 950 mm, CFRP case is approximately 850 mm, if its vertical flexural rigidity is kept constant.

Table 6.1.1 Young's modulus and breaking stress obtained in four point flexural test at RT, LNT and LHeT. The values in parenthesis present the standard deviation. The numerics presented suffixally are the number of tested specimen.

	T(K)	GFRP	CFRP	SFRP	ALFRP
Young's	300	36.5(0.35)/2/	79.5(0.1)/2/	79.6(0.6)/2/	82.6(0)/2/
Modulus	77	40.1(0.75)/2/	79.8(1.45)/2/	81.3(3.7)/2/	86.6(0.35)/2/
(GPa)	4.2	42.2(1.27)/3/	81.2(0.1)/2/	84.9(1.6)/2/	95.6(0.45)/2/
Breaking	300	1.07(0.02)/2/	1.14(0.015)/2/	1.33(0.02)/2/	1.30(0.02)/2/
Stress	77	2.28(0.045)/2/	1.68(0.07)/2/	2.38(0.01)/2/	2.23(0.035)/2/
(GPa)	4.2	2.32(0.116)/3/	1.64(0.08)/2/	2.21(0.11)/2/	2.37(0.095)/2/

Table 6.1.2 Comparison of bucking cylinders in terms of materials

material	SS304LN	GFRP	CFRP
$\sigma_y$ (MPa)	765		
$\sigma_u$ (MPa)	1648	1600	
E (MPa)	$2.06 \times 10^5$	$4.22 \times 10^4$	$8.12 \times 10^4$
$\nu$	0.3	0.21	
outer radius (m)	2.03	2.03	2.03
thickness (m)	0.30	0.50	0.40
$\sigma_c$	370	224	278
$S_m$	510		
$\sigma_{ck}$	480	290	338

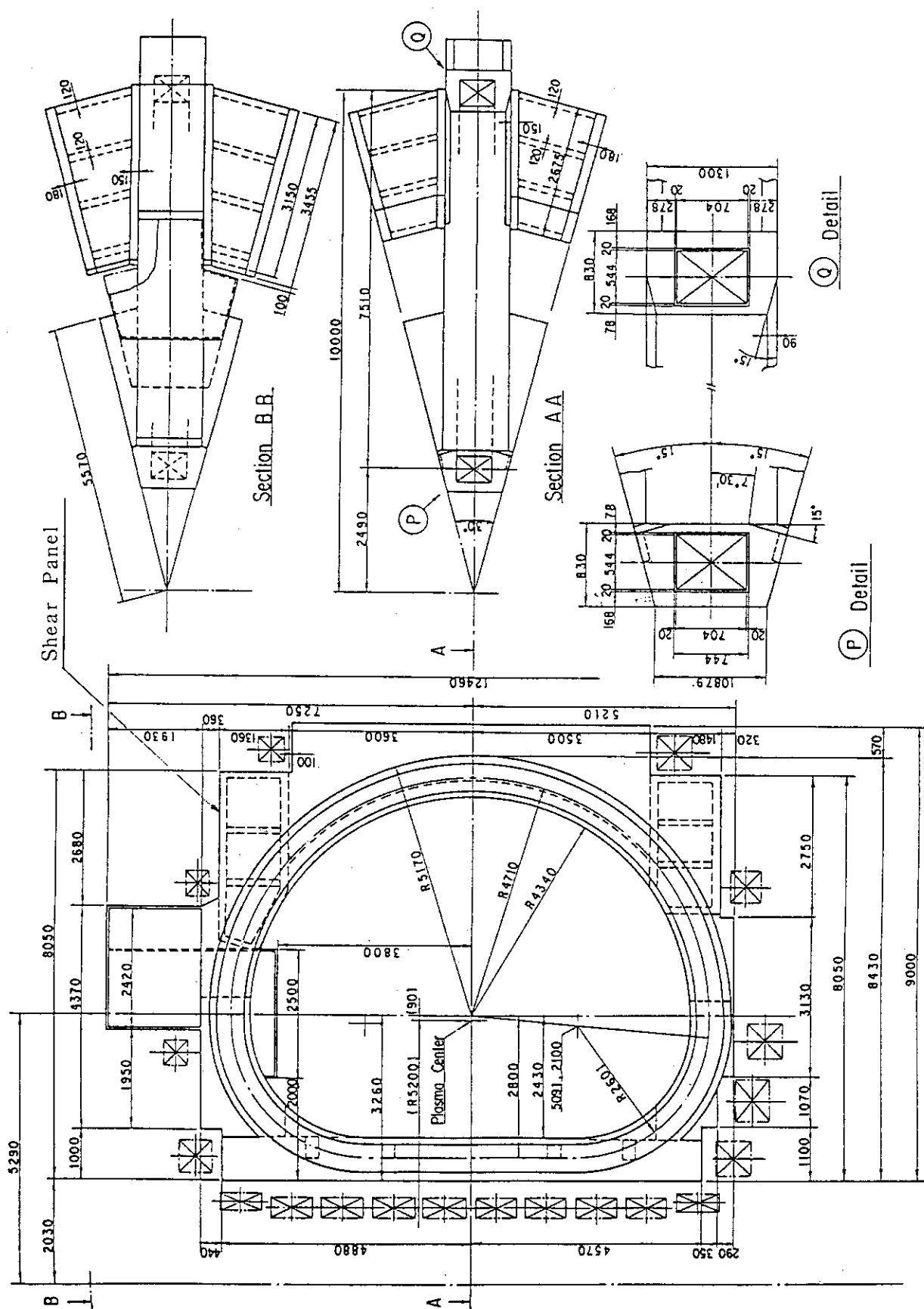


Fig. 6.1.1 Structure of TF coil and Shear Panel

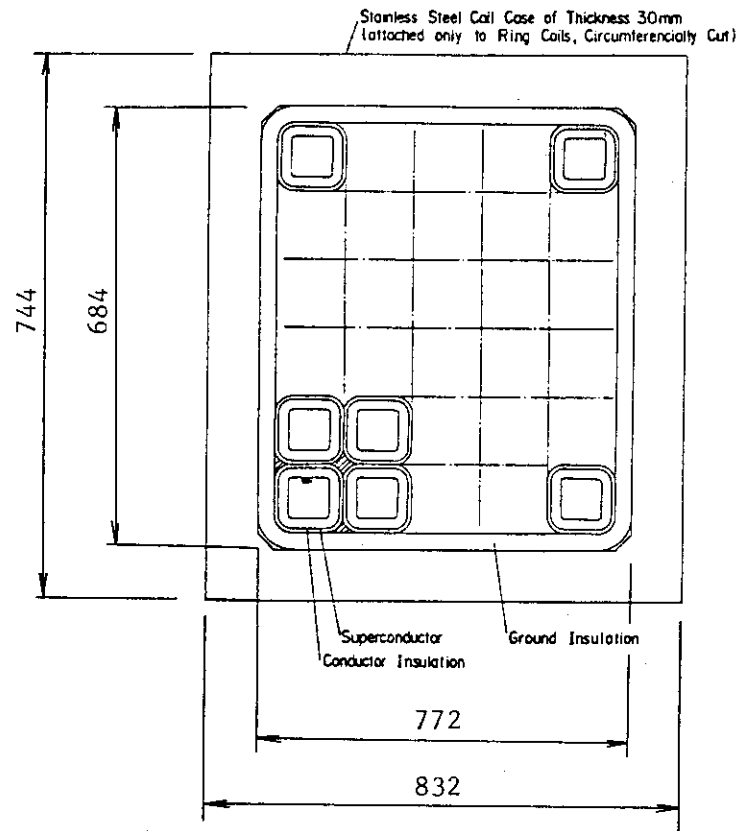


Fig. 6.1.2 Cross section of maximum PF coil

## 6.2 Proposal of composites with required properties

Requirements for non-metallic structural materials are low loss, high strength and high rigidity. In view of low loss, ordinary FRP has good characteristics. But FRP has not enough performance in strength, rigidity and fracture toughness. Furthermore, FRP has poor rigidity as structural material. As already mentioned in 6.1, rigidity is the biggest disadvantage in application of non-metallic materials to the magnetic system. The rigidity of FRP derives from the strength of a fiber material. To improve the rigidity of FRP, a new type of FRP using a modified fiber material (what is called "advanced composite materials") has been proposed recently.

For the reasons mentioned above, description will be centered around the advanced composite materials.

### (1) Summary of the existing data base for design

The advanced composite materials which are reinforced by carbon (CFRP), silicon carbide (SFRP) alumina (ALFRP) fiber, and so on have a Young's modulus twice or more than GFRP.

It is not long since researches on these composite materials started on a full scale. Data from the researches will build up day by day. The following data on the advanced composite materials will be presented. (Refs.; 1, 2)

- Property of fiber (Table 6.2.1)
- Strength of composite materials (Fig. 6.2.1, 6.2.2)
- Young's modulus and shearing stress of composite materials (Table 6.1.1, Fig. 6.2.3, 6.2.4)
- Load-displacement curve of composite materials (Fig. 6.2.5)
- Thermal conductivity of composite materials (Fig. 6.2.6, 6.2.7, 6.2.8)
- Thermal contraction of composite materials (Fig. 6.2.9, 6.2.10, 6.2.11)

As to the other properties, property of the composite originating from the matrix property in particular, these remains no remarkable difference with well-known GFRP.

### (2) Required R & D

The required items of R & D are as given below.

- Improvement of rigidity: It will be possible to develop higher-rigidity composite materials by changing sorts and content volume of carbon, silicon carbide, alumina fibers and so on. As a result, a

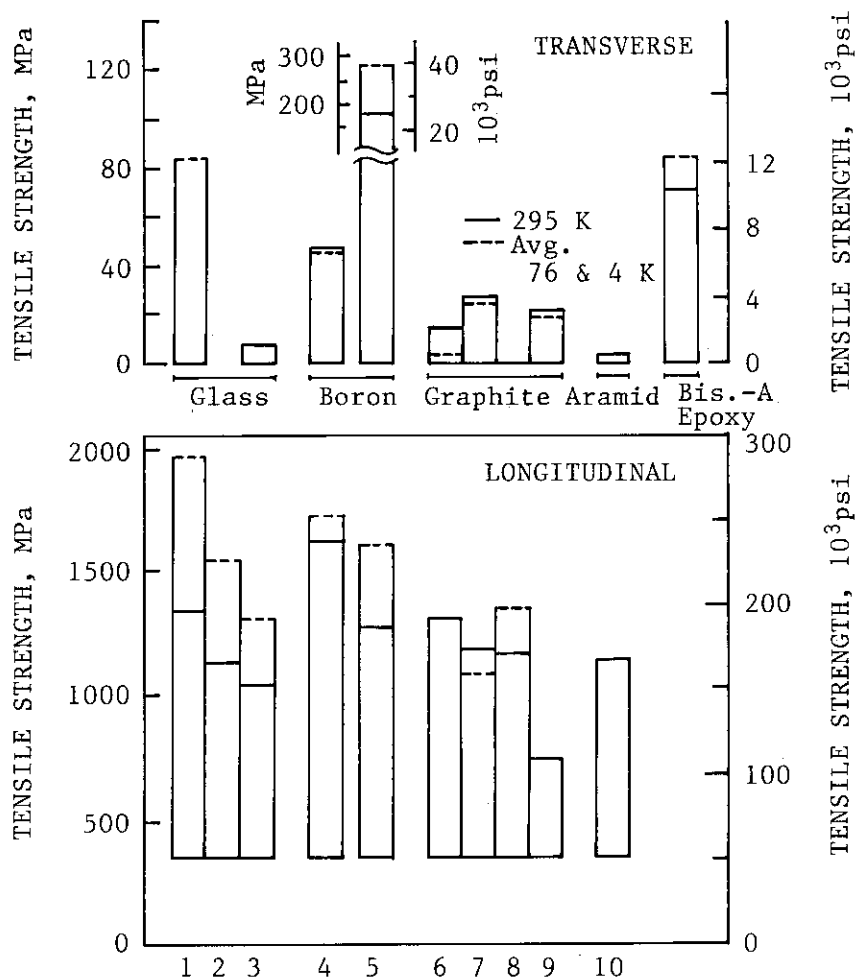


wider range of applications will be obtained for non-metallic structural materials. In this regard, data now available to us is extremely limited. At least 4 or 5 more years of researches will be needed.

- Verification of irradiation-proof performance: If FRP is submitted to irradiation of gamma rays, its matrix will degrade, which reduces interlaminar shearing strength with fiber and fatigue limit (see Fig. 6.2.12). Therefore, it is essential to have a sufficient buildup of data on degradation in irradiation. In addition, points where FRP is used must be shielded.
- Standardization of evaluation methods: As known from Fig. 6.2.13 data obtained differs with FRP test methods, which results in difficulty of screening of materials. The evaluation methods must be standardized among researchers.

Table 6.2.1 Properties of each reinforcement from their catalog

Fiber	Young's Modulus (GPa)	Tensile Strength (GPa)	Density (g/cc)	Fiber Diameter ( $\mu\text{m}$ )
Glass	75.5	2.45	2.5	9
Carbon	235	2.74	1.7	8
Silicon Carbide	176	2.45	2.5	10
Alumina	206	1.76	3.2	17



## Glass Reinforcement

- 1-S-901/Resin 2, 66 vol.%(1)
- 2-R/bisphenol A, 63 vol.%(2)
- 3-E/bisphenol A, 50.6 vol.%(2)

## Boron Reinforcement

- 4-140 $\mu$ m (5.6 mil) B/2387 epoxy, 52 vol.%(1)
- 5-140 $\mu$ m (5.6 mil) B/6061 aluminum, 47 vol.%(1)

## Graphite Reinforcement

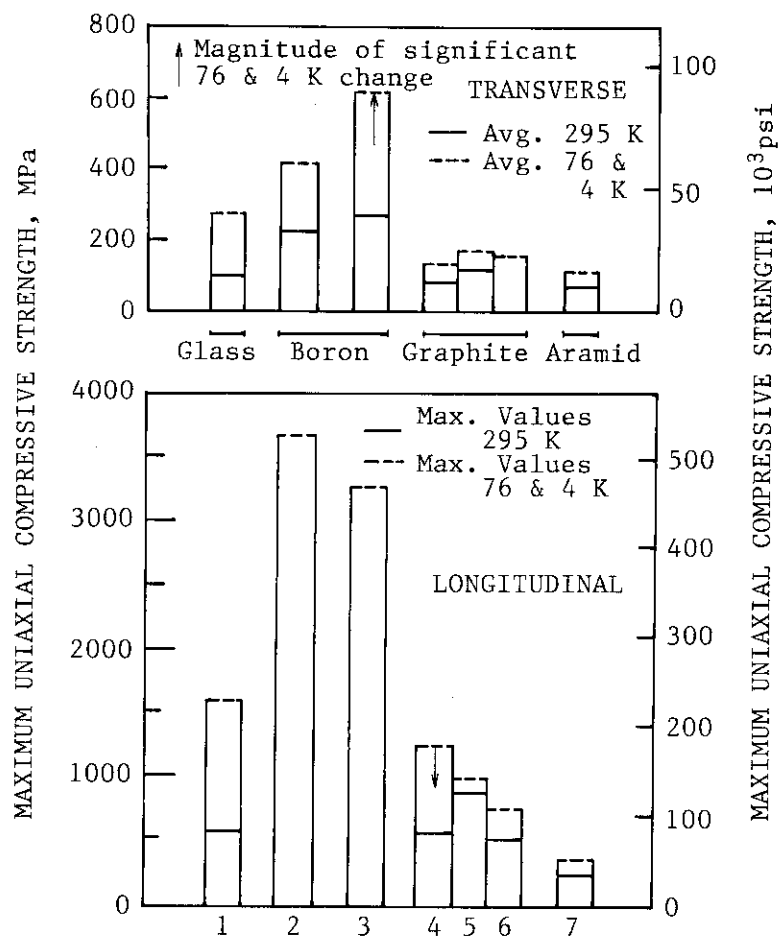
- 6-AS/Resin 2, 64 vol.%(1)
- 7-HM-S/934, 62 vol.%(3)
- 8-HM-S/bisphenol A, 55 vol.%(2)
- 9-GY-70/934, 65 vol.%(3)

## Aramid Reinforcement

- 10-Kevlar 49/934, 67 vol.%(3)

Vol.% = fiber volume fraction. Refs.: (1) Schramm and Kasen (1977a); (2) Dahlerup-Petersen and Perrot (1979); (3) Kasen, Schramm, and Beck (1980). Bisphenol A epoxy: CY 205 (2).

Fig. 6.2.1 Temperature dependence of the uniaxial longitudinal and transverse tensile strengths of glass-, boron-, graphite-, and aramid-reinforced epoxy laminates



## Glass Reinforcement

1-S-901/Resin 2, 66 vol.%(1)

## Boron Reinforcement

2-140 $\mu$ m (5.6 mil) B/2387

epoxy, 52 vol.%(1)

3-140 $\mu$ m (5.6 mil) B/6061

aluminum, 47 vol.%(1)

## Graphite Reinforcement

4-AS/Resin 2, 64 vol.%(1)

5-HM-S/934, 62 vol.%(1)

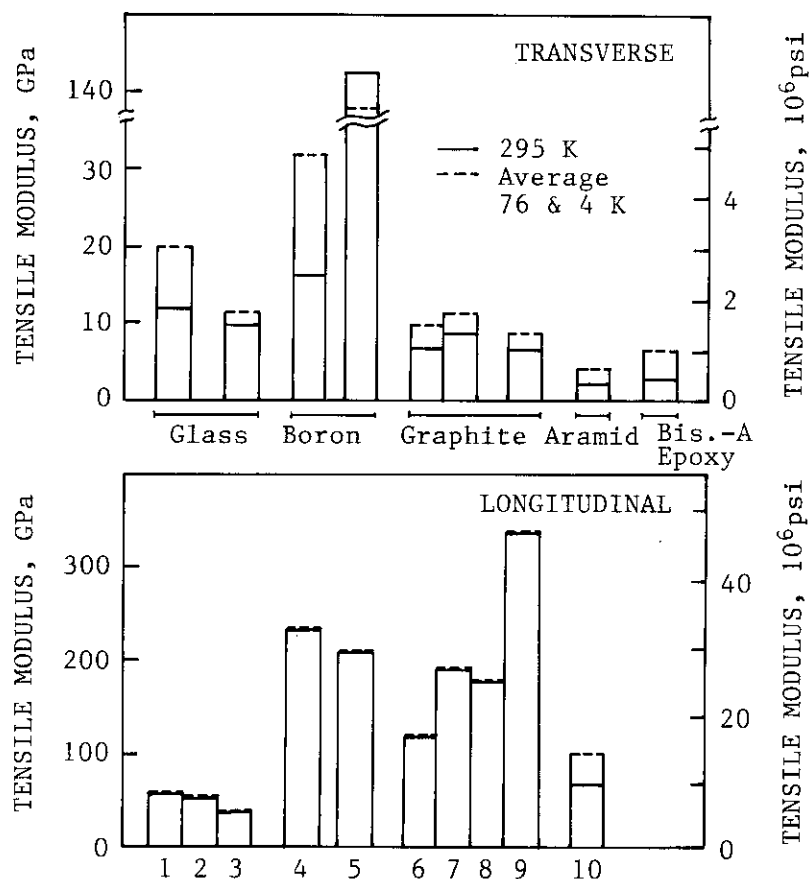
6-GY-70/934, 65 vol.%(2)

## Aramid Reinforcement

7-Kevlar 49/934, 67 vol.%(2)

Plotted values are maximum values for the longitudinal direction and average values for the transverse direction. Vol.% = fiber folume fraction. Refs.: (1) Schramm and Kasen (1977a); (2) Kasen, Schramm, and Beck (1980).

Fig. 6.2.2 Temperature dependence of the uniaxial longitudinal and transverse compressive strengths of glass-, boron-, graphite-, and aramid-reinforced laminates.



## Glass Reinforcement

1-S-901/Resin 2, 66 vol.%(1)

2-R/bisphenol A, 63 vol.%(2)

3-E/bisphenol A, 50.6 vol.%(2)

## Boron Reinforcement

4-140 $\mu$ m (5.6 mil) B/2387  
epoxy, 52 vol.%(1)5-140 $\mu$ m (5.6 mil) B/6061  
aluminum, 47 vol.%(1)

## Graphite Reinforcement

6-AS/Resin 2, 64 vol.%(1)

7-HM-S/934, 62 vol.%(3)

8-HM-S/bisphenol A, 55 vol.%(2)

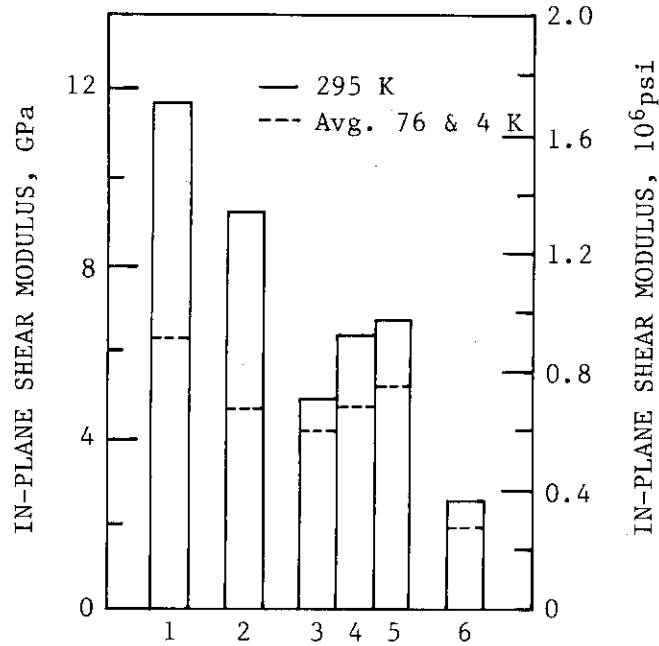
9-GY-70/934, 65 vol.%(3)

## Aramid Reinforcement

10-Kevlar 49.934, 67 vol.%(3)

Vol.% = fiber volume fraction. Refs.: (1) Schramm and Kasen (1977a); (2) Dahlerup-Petersen and Perrot (1979); (3) Kasen, Schramm, and Beck (1980).

Fig. 6.2.3 Temperature dependence of uniaxial longitudinal and transverse tensile moduli of glass-, boron-, graphite-, and aramid-reinforced laminates



1-S-901/Resin 2, 66 vol.%(1)  
 2-140 $\mu$ m (5.6 mil) boron/2387 epoxy, 52 vol.%(1)  
 3-AS graphite/Resin 2, 64 vol.%(1)  
 4-HM-S graphite/934 epoxy, 62 vol.%(2)  
 5-GY-70 graphite/934 epoxy, 65 vol.%(2)  
 6-Kevlar 49 aramid/934 epoxy, 67 vol.%(2)

Fig. 6.2.4 Temperature dependence of inplane shear modulus,  $G_{12}$ , of uniaxial glass-, boron-, graphite-, and aramid-reinforced epoxy laminates. Vol.% = fiber volume fraction. Refs.: (1) Schramm and Kasen (1977a); (2) Kasen, Schramm, and Beck (1980)

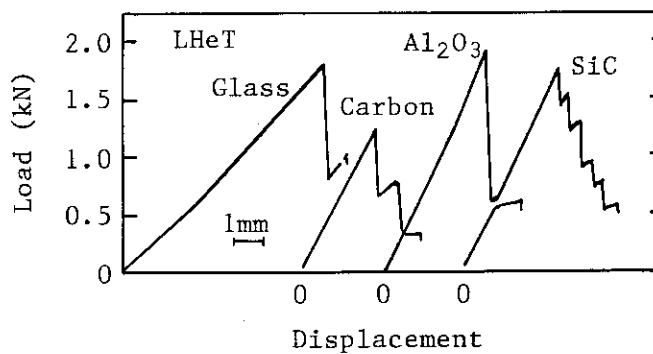


Fig. 6.2.5 Load-displacement curves obtained in four-point flexural test at LHeT

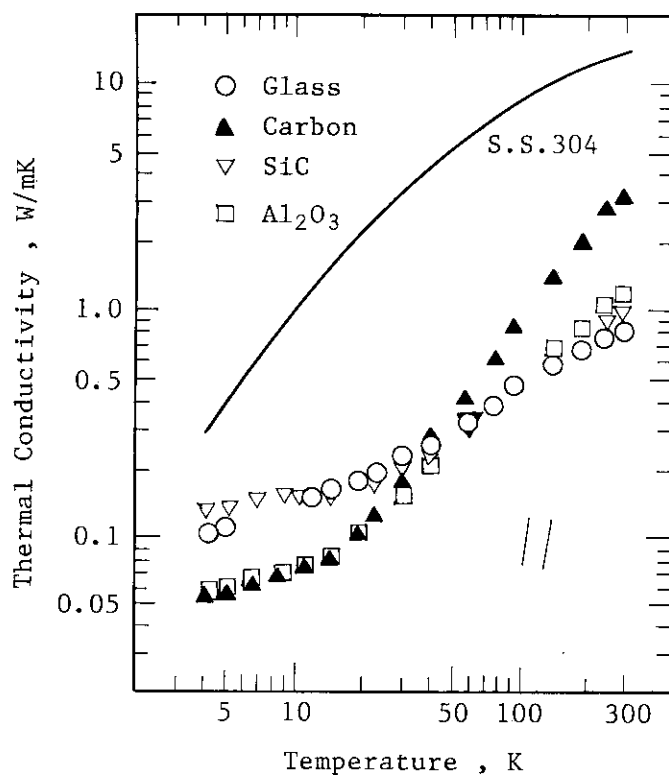


Fig. 6.2.6 Temperature dependence of thermal conductivity in fiber direction

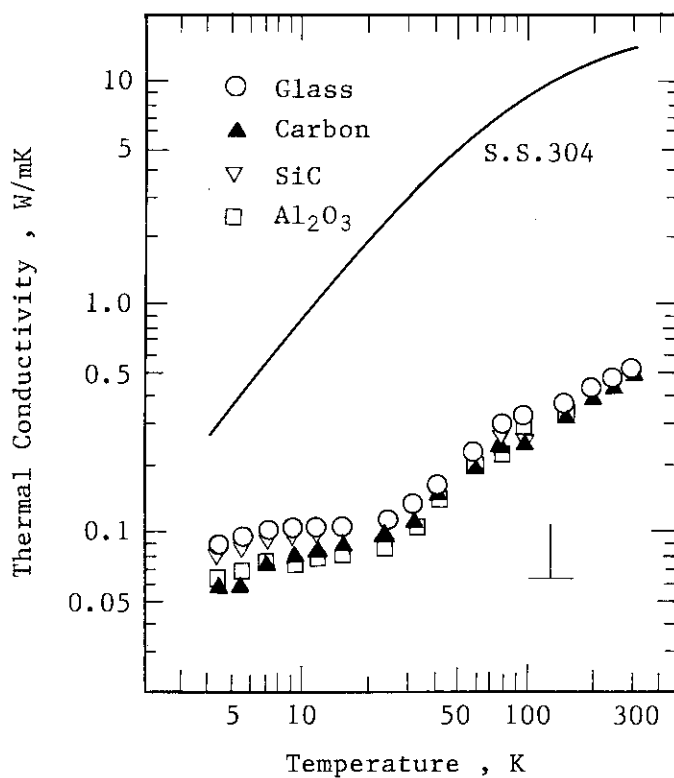
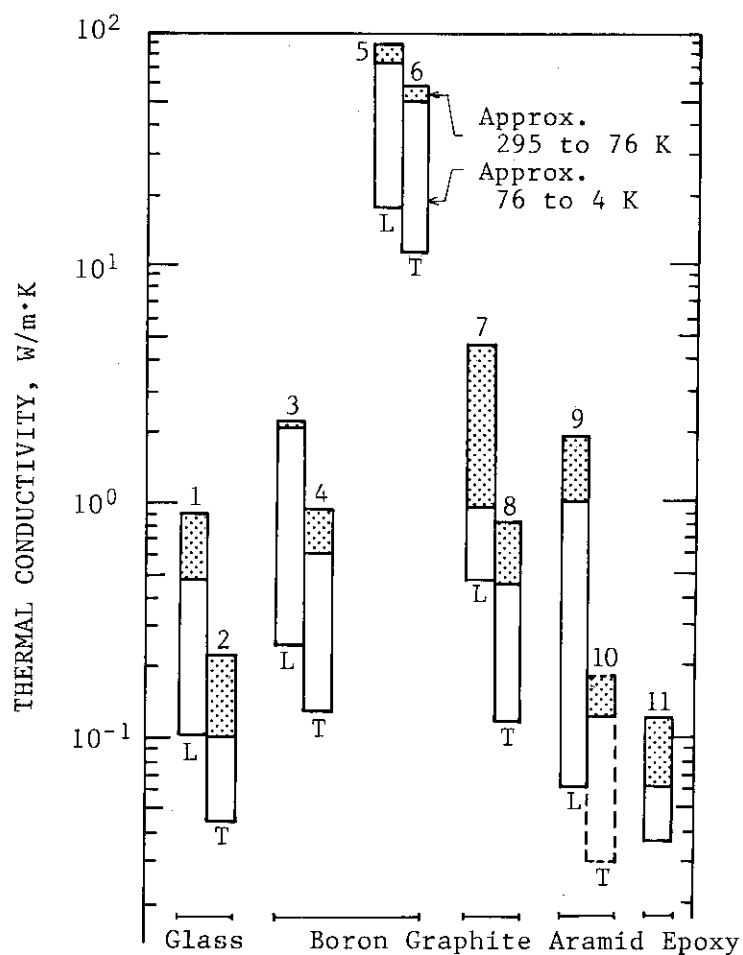


Fig. 6.2.7 Temperature dependence of thermal conductivity in transverse direction



- 1-S glass/epoxy, 65 vol.%(1)  
 2-S glass/epoxy, 63 vol.%(2)  
 3&4-140 $\mu$ m (5.6 mil) boron/epoxy,  
 52 vol.%(3)  
 5&6-140 $\mu$ m (5.6 mil) boron/aluminum,  
 47 vol.%(3)  
 7-Graphite/epoxy(3)  
 8-Graphite/epoxy(2)  
 9-Aramid/epoxy(4)  
 10-Aramid/epoxy(2)  
 11-Bisphenol A epoxy(2)

Vol.% = fiber volume fraction. Refs.: (1) Hust and Arvidson (1978); (2) Dehlerup-Petersen and Perrot (1979); (3) Hust (1976); (4) Hust (1975).

Fig. 6.2.8 Temperature dependence of thermal conductivity of uniaxial laminates.  
 L=longitudinal, T=transverse.  
 Transverse conductivity of the aramid laminate assumed from fabric reinforced data

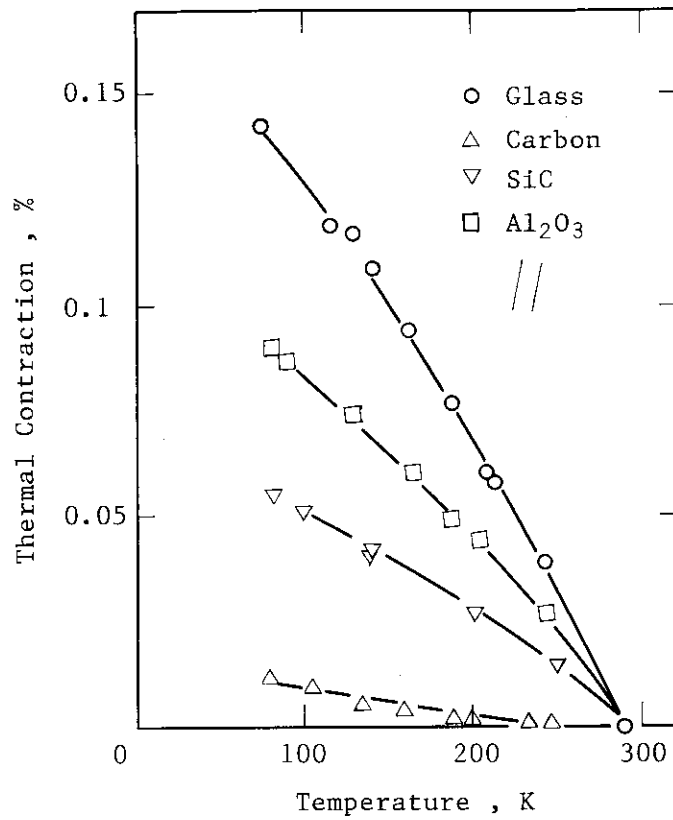


Fig. 6.2.9 Thermal contraction in fiber direction

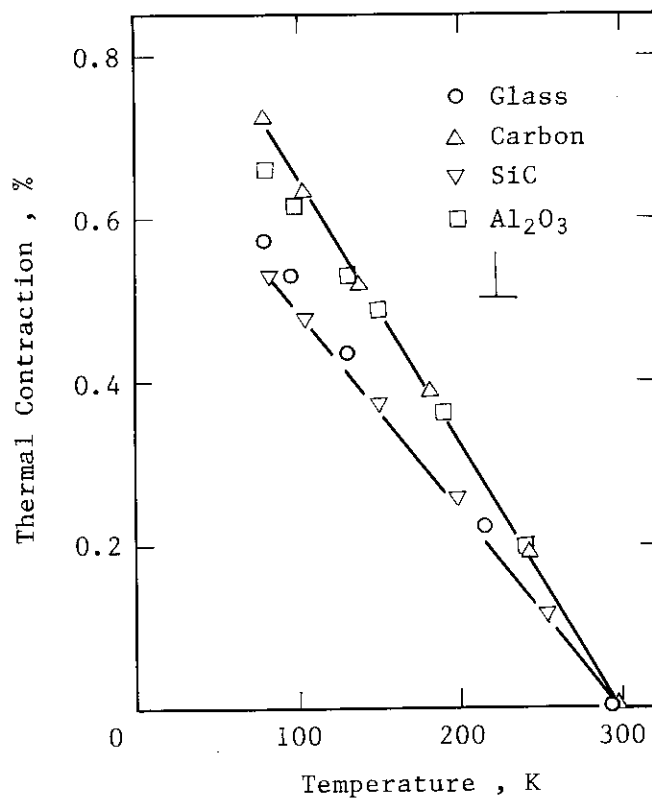
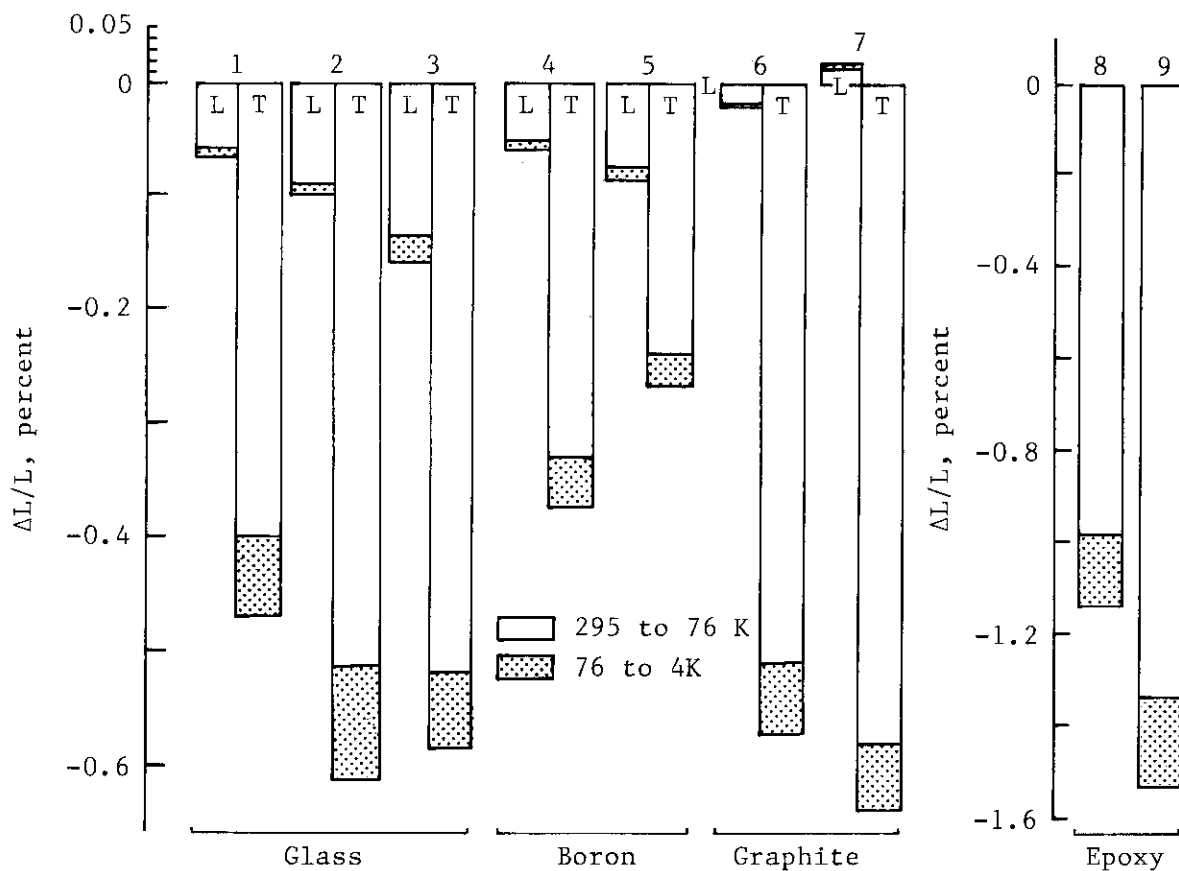


Fig. 6.2.10 Thermal contraction in transverse direction





## Glass Reinforcement

- 1-S-901/Resin 2, 66 vol.%(1)
- 2-R/bisphenol A, 63 vol.%(2)
- 3-E/bisphenol A, 50.6 vol.%(2)

## Boron Reinforcement

- 4-140μm(5.6 mil) B/2387 epoxy, 52 vol.%(1,3)
- 5-140μm(5.6 mil) B/6061 aluminum, 47 vol.%(1,3)

## Graphite Reinforcement

- 6-AS/Resin 2, 64 vol.%(1,3)
- 7-HM-S/bisphenol A, 55 vol.%(2)

## Epoxy Resins

- 8-Bisphenol A(2)
- 9-Resin 2(4)

Epoxy matrices are a conventional bisphenol A (Bis A) or a flexibilized formulation (Resin 2) (Soffer and Molho, 1967). Vol.% = fiber volume fraction. Refs.: (1) Schramm and Kasen (1977b); (2) Dahlerup-Petersen and Perrot (1979); (3) Schramm and Kasen (1977a); (4) Hust (1980).

Fig. 6.2.11 Temperature dependence of thermal expansion of uniaxial glass-, boron-, and graphite-reinforced laminates in the longitudinal (L) and transverse (T) directions

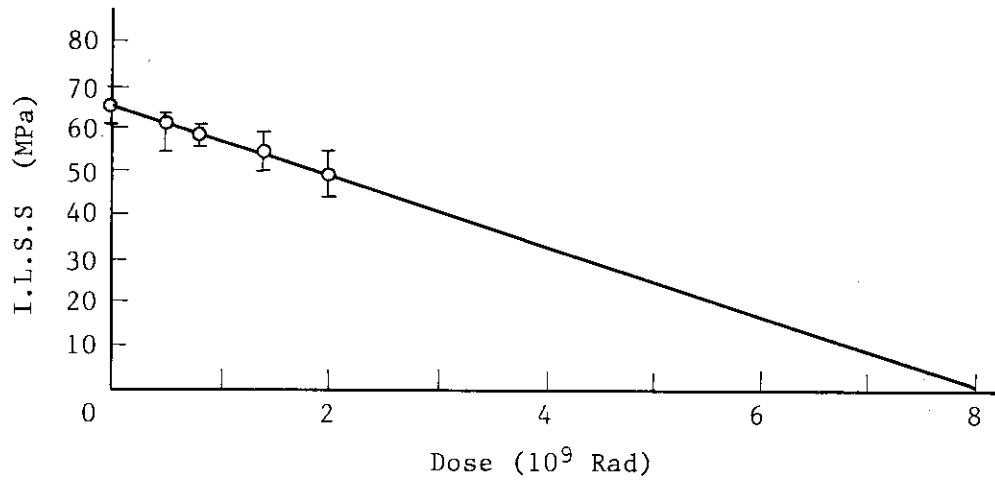


Fig. 6.2.12 Degradation of interlaminar shear strength induced by gamma irradiation

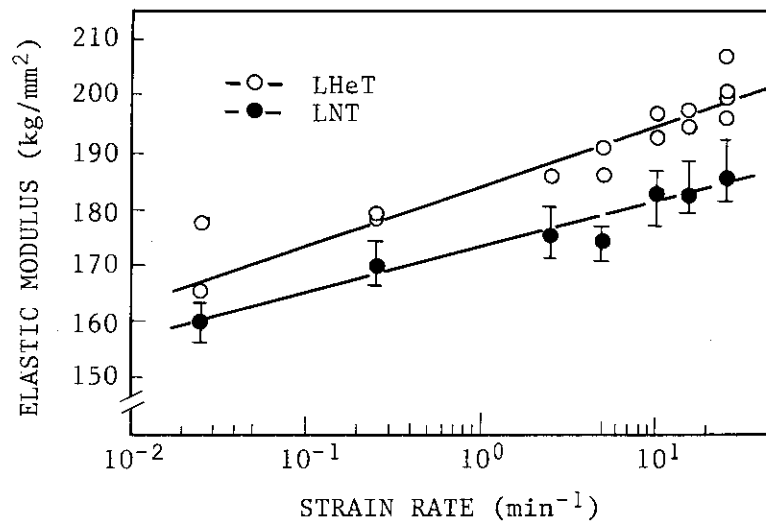


Fig. 6.2.13 Strain rate dependence of elastic modulus measured at LNT and LHeT

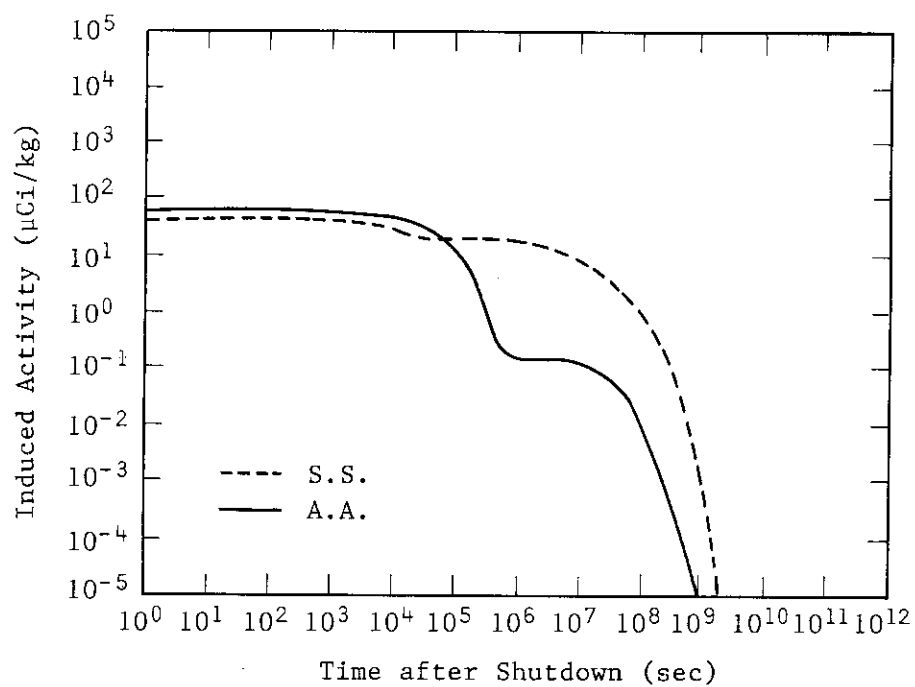


Fig. 6.2.14 Induced activity

### 6.3 Advantages of non-metallic structural materials for INTOR

#### (1) Reduction of activation level

As to induced radioactivity, aluminum has the almost same level as stainless steel in its initial stage. In the course of attenuation to 1/100, aluminium takes  $10^6$  sec, while stainless steel needs  $10^9$  sec. (ref.: 3) (See Fig. 6.2.14)

On the other hand, plastics are supposed to emit a smaller amount of induced radioactivity than metals. Based on the facts mentioned above, we can come to a conclusion that it will be possible to reduce the activation level to lower than 1/4 - 1/5 of the ratio of specific gravity, when employing composite materials having aluminium fiber, as structural materials.

There is no data about other composite materials, but further reduction of activation level can be expected.

#### (2) Estimation of eddy current loss

Eddy current loss is dependent on magnitude of magnetic flux change in elapsed time, shape and size of structural materials and electric resistance. Suppose FRP is used for structural materials, in place of stainless steel. The volume resistivity is  $5 \times 10^{-5}$  ohm·cm (at 4 K) and approx.  $2 \times 10^{17}$  ohm·cm, respectively for stainless steel and FRP. If the other conditions are identical, the eddy current loss for the structural materials can be reduced to approx.  $1/4 \times 10^{21}$ . Therefore, it is of great advantage to use non-metallic materials as structural materials.

#### (3) Improvement of PF penetration time

For the reasons mentioned in Appendix, no particular contribution is made to improvement of penetration time. Therefore, system benefits in this connection is extremely limited.

#### (4) Other points of improvement

The specific gravity of FRP is approx. 1.6 to 2 and this value is approx. 1/4 to 1/5 of that of stainless steel. Its specific heat is almost the same to that of stainless steel. Use of FRP will facilitate cooling down and reduce consumption of cooling-down LHe (coolant) to a half or less.

At the same time, the access time will be reduced to 1/1000 or less in accordance with decrease of induced radioactivity. These data,

however, are estimated on condition that all the major components of INTOR magnet system be composed of non-metallic materials. Taking this into consideration, our very urgent need is to complete high-rigidity advanced composite materials.

#### 6.4 Applicability of FRP to magnet component

As mentioned above, FRP has effective property as to reduce activation level and eddy current loss, but its Young's modulus is still lower level than stainless steel i.e., Young's modulus of GFRP is 20% of that of stainless steel, and the moduli of CFRP, SFRF and ALFRP etc. are 40% of that of stainless steel. So under present condition, FRP is applicable only to the components where much rigidity is not required.

But as the development of advanced composite materials, it can cause that FRP is applied to the magnet components. However following problems are pointed out in addition to increase of Young's modulus of FRP.

- ① reduction of Young's modulus and strength due to irradiation
- ② increase of shearing strength
- ③ accumulation of technical data of CFRP, SFRP and ALFRP, etc.
- ④ anisotropic property
- ⑤ connecting method

Before application of FRP to the magnet components, it is necessary to solve such problems.

## Appendix

Magnetic shielding effect of TF coil shear pannels against vertical field is estimated for the INTOR class tokamak reactor. Figure A.1 shows the magnetic shielding function  $M(s)$  (Ref. 4) (Laplace transfer function) defined as

$$M(S) = \sum_k \frac{s\tau_k}{1 + s\tau_k} m_k, \quad m_k = \frac{M'_{pk} M_{ik}}{M'_{pi} \tau_k}$$

where,  $M_{pk}$  : mutual inductance between plasma and the  $k$  th eddy current model,

$M_{pi}$  : mutual inductance between plasma and the  $i$  th PF coil,

$M_{ik}$  : mutual inductance between the  $i$  th PF coil and the  $k$  th eddy current mode,

$\tau_k$  : eigen time of the  $k$  th eddy current mode.

$M'$  represents the derivative of mutual inductance by plasma radial position.

The value of  $M(s)$  function is unity at  $s = \infty$  ( $t=0$ ), when passive structures completely surround a plasma. PF coil current must be increased by  $1/(1-M(s))$  times to generate the same field compared with the case of no passive structure (i.e. no magnetic shielding effect). PF coils are assumed to be installed at ( $R=8.2$  m,  $z=\pm 4.2$  m) out side TF coils in these calculations. Plasma major and minor radii are 5.0 m and 1.2 m, respectively. The magnetic shielding effect of shear pannels is not large as shown in Fig. 6.3.A-1, since shear pannels do not completely surround a plasma. The magnetic shielding effect against PF coils would be mainly due to blanket, shield and vacuum vessel. We also calculate the magnetic shielding effect against radial field. The shear pannels effect on the magnetic shielding is estimated to be much smaller than that against vertical field, since there are large windows between adjacent TF coils for ports and maintenance.

## References

- (1) T. Okada, et al.: Adv. Cryog. Eng., 32 (1986)  
"Thermal and mechanical properties of advanced composite materials at low temperatures."
- (2) Richard P. Reed and Alan F. Clark  
"Materials at low temperatures" American Society for Metals.  
ISBN: 0-87170-146-4
- (3) JAERI-M 7300 (1977)
- (4) A. Kameari and S. Niikura, Nuclear Engineering and Design/Fusion 2 (1985) 365-373.

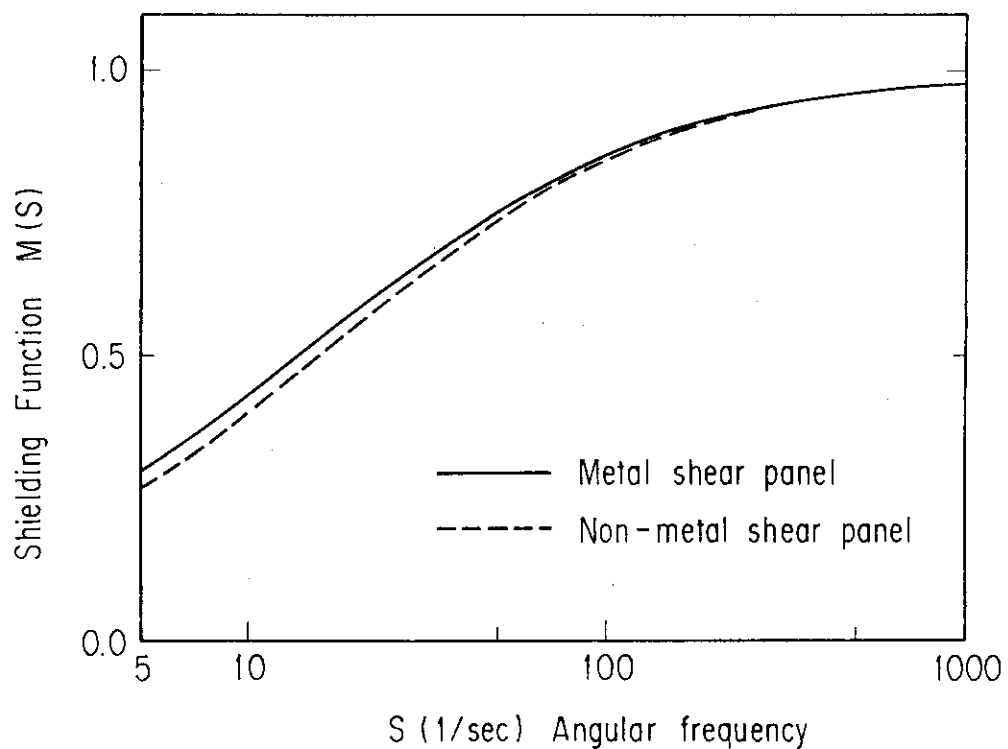


Fig. 6.3.A-1 Shielding function